THESIS

COFILIN-ACTIN RODS, A HIPPOCAMPAL PATHOLOGY IN MOUSE MODELS OF HUMAN DEMENTIAS, FORM FROM DIFFERENT INDUCERS THROUGH A COMMON MOLECULAR PATHWAY

Submitted by

Isaac W. Babcock

Department of Biochemistry and Molecular Biology

In partial fulfillment of the requirements

For the Degree of Master of Science

Colorado State University

Fort Collins, Colorado

Summer 2020

Master's Committee

Advisor: James R. Bamburg

Santiago Di Pietro
Mark D. Zabel

ABSTRACT

COFILIN-ACTIN RODS, A HIPPOCAMPAL PATHOLOGY IN MOUSE MODELS OF HUMAN DEMENTIAS, FORM FROM DIFFERENT INDUCERS THROUGH A COMMON MOLECULAR PATHWAY

Dementia is a diverse group of diseases leading to abnormal loss of cognitive function. Without effective therapeutics, these diseases are truly emotionally and financially devastating for every community. In addition, dementia is estimated to affect 150 million people worldwide by 2050 making it imperative to uncover the mechanisms leading to dementia from diverse causes. Most cases of dementia are sporadic and occur in an age-related manner but some have distinct initiating factors such as rare genetic mutations, or they develop as a result of viral infection or traumatic brain injury. Sporadic and familial dementias are classified under the same disease type if the same pathology and cognitive decline are present, yet therapeutics have been almost entirely based on the pathology of the familial forms and have had little success in halting progression, suggesting genetic factors may be sufficient to initiate neurodegeneration but do not address the underlying mechanisms that drive its progression. Aggregates of misfolded proteins deposited in insoluble extracellular plaques are a common hallmark for Alzheimer's dementia but do not correlate well with cognitive loss. Intracellular aggregates of misfolded proteins have a better correlation with cognitive dysfunction but whether these are the initiators of the decline or develop as a result of other functional abnormalities is still an unanswered question. Common cellular features of cognitive loss

are the excess of reactive oxygen species (ROS), excess cytokine production, and cytoskeleton abnormalities. The cytoskeleton, especially the dynamic non-equilibrium polymers of tubulin or actin, is necessary for neurons to create, maintain, or destroy neuronal connections, the basis of cognition. Cofilin is the major actin binding/severing protein which plays a dominant role in modulating local actin dynamics. Within neurites of a subpopulation (20-25%) of hippocampal neurons in culture, treatment with disease-associated peptides or proteins, such as the amyloid-β peptide in Alzheimer's disease or the proinflammatory cytokine TNFα, leads to formation of rod-shaped inclusions (rods) that contain cofilin and actin in a 1:1 ratio. Rods lead to synaptic loss and neuronal dystrophy through a pathway previously characterized to require the expression of the cellular prion protein (PrP^C) and NADPH oxidase (NOX).

The work undertaken in this thesis was designed to first develop methods that would allow us to address several issues related to the study of cofilin-actin rods in living cells and brain slices. These methods include an improved method for studying postnatal hippocampal slices in roller tubes for long term imaging in an enclosed system. We then optimized culture conditions for the survival of adult mouse brain slices which then permitted the study of brain tissue already undergoing the pathological changes associated with dementia. Because we wanted to be able to study synaptic connections in these adult slice cultures, we needed methods for random labeling of neurons to visualize dendritic spines but in a sparsely labeled culture or slice so individual neurons could be visualized. Thus, we developed a novel twist on the random diolistic membrane labeling method we call microcrystal labeling. Manual analysis of cultured neurons and slices for rod quantification is a tedious process and so we developed an unbiased semi-

automated method for rod quantification covering much bigger areas of analysis in a much shorter time period and applied this to cultures of dissociated neurons and brain slices.

We then undertook a collaborative study with Tom Kuhn and his graduate student, Lisa Smith, to examine rod formation in HIV-associated neurocognitive disorder (HAND), induced by the HIV envelope protein gp120. Many tropic forms of gp120 exist that used different receptors for the virus to gain cell entry. Using different tropic gp120 proteins and genetic and pharmacological approaches, we determined that gp120 tropic proteins utilize specific co-receptors, either CXCR4 or CCR5, to induce cofilin-actin rod formation in cultures of dissociated neurons and demonstrated that the gp120-induced rod formation from either receptor is dependent on PrP^C and a functional NOX.

In collaboration with two other groups, Marcia Liz and her student Marina da Silva at the University of Porto and Raymond Swanson at UCSF, we studied the role of rods in Parkinson's disease with Lewy Body dementia (PDD). Utilizing a mouse line with X-linked triplication of alpha-synuclein (α-Syn), a causative protein in PDD, we show that cofilin-rods form in the hippocampus concomitantly with the reported time-frame of cognitive loss. We quantified rod numbers and locations within the hippocampus and also showed that rod formation could be induced in wildtype neurons treated with preformed fibrils (PFF) of α-Syn. PFF-induced rod formation requires PrP^C and NOX. Furthermore, we demonstrated PFF-induced rod formation is blocked by antagonists of the CXCR4 and CCR5 receptors. We also utilized a novel octapeptide antagonist of X4 and R5 receptors, RAP310, and showed it to be very efficacious in inhibiting rods in both dissociated neuron and slice cultures in response to multiple rod inducers.

Similar studies to those using PFF were also carried out in the context of Alzheimer's dementia, using the causative, synaptotoxic Aβ dimer/trimer (Aβd/t), which has been shown to induce rods through PrP^c and NOX. We demonstrated the inhibition of Aβd/t-induced rods with X4 and R5 antagonists demonstrating that in mouse and in vitro models of AD, PDD, and HAND, causative proteins utilize the CCR5/CXCR4 chemokine receptors, the cellular prion protein, and NOX complex to induce cofilin-actin rods. We propose that rods are a common mechanism for promoting synapse loss in these dementias and that a common therapeutic approach might be possible.

ACKNOWLEDGEMENTS

It is incredible to think five years ago I was entering CSU as a freshman undergraduate totally naïve to the years to come. First I want to thank my parents because without there unconditional love, support, and confidence in me I would not be the person I am today and certainly would never reached out to Dr. Bamburg.

Mostly I want to thank Dr. Bamburg, his knowledge and experience has been the most amazing resource I could be fostered under. More importantly Dr. Bamburg's patience and kindness towards me has changed my life immensely. In Addition, I want to thank Laurie Minamide. Her friendship and generosity has been amazing. And her M&M's and treats fueled me through many days.

I would also like to thank all of the amazing scientists I have had the pleasure to work with. Dr Lubna Tahtamouni has been an incredible figure for me and has taught me so much about strength. Likewise, Dr. Thomas Kuhn has been a great pleasure to work with on experiments, learn from, and talk rock climbing. Also, I want to thank Alisa Shaw whom has taught me so much about experimental design and lab work. I want to thank Barbra Bernstein whom I learned much about literary searching and I also want to thank O'Neil Wiggan for being a great person to ask technical questions too.

I am forever thankful to Dr. Marcia Liz and Marina da Silva, of University of Porto Portugal, for including me in their research project allowing me the opportunity to do exciting research. I also want to thank Dr. Raymond Swanson, of UCSF, for he provided almost all of the mice and purified proteins for much of my research. Respectively I want to

acknowledge Drs. Mike Ruff and Chaoping Chen for providing us with the peptide drug Rap310 and maraviroc.

I want to thank Dr. Lisa Smith whom was a pleasure to work with while she was in Fort Collins. And is the key person who collected data presented within chapter 4. I also want to thank Dr. Marcello Pignataro who was a great friend to have in the lab and was an even better person to discuss experiments.

There are many students who have helped my research. Mainly, Ben Fixman, Maia Zollar, Zack Fleishhacker, Isheeta Govardhan.

While I am sure I have been a bother, I have had great experiences learning from my Advisors Dr. Mark Zabel and Dr. Santiago Di Pietro and I am forever thankful for their kindness and willingness to help me. I have greatly enjoyed the conversations I have had with each of them and they have both significantly influenced my scientific life.

Last, I want to thank my friends who have been incredibly supportive of me and my research endeavors and have always provided the best outlets for any frustration.

TABLE OF CONTENTS

LIST OF TABLES

LIST OF FIGURES

CHAPTER 1

BACKGROUND

This review covers many different aspects of neurodegenerative diseases and neuronal cell biology. As such, thousands of references would be needed if we were to cite every original contribution to the literature. Thus, for many areas covered in this chapter, we cite recent review articles that allow anyone wanting more in depth information to find it.

Organization of Neurons and Circuitry

Although quite variable in different brain regions, about half of all the cells comprising the brain are neurons (von Bartheld et al., 2016). Neurons are highly polarized cells with multiple intricate branched dendrites receiving chemical input and converting it to an electrical output that travels through the soma (cell body) and along an axon to communicate with cells within its network. The electrical signals that are encoded within circuits can store information (Grossberg, 2020). Connections between neurons occur at synapses, sites where neurotransmitters (NTs) are released from the axon terminus of a presynaptic neuron onto the postsynaptic specialization of the receiving neuron where receptors for the NTs are located (Dolphin and Lee, 2020). Each neuron has hundreds or even thousands of synapses and these can be either excitatory or inhibitory (Oldenberg and Ding. 2011). Within an electrical circuit there may be anywhere from a few neurons to hundreds of neurons and the output of anyone neuron is based on a summation of the multiple inputs, both inhibitory and excitatory (Farhy-Tselnicker and Allen, 2018). (Figure 1.1).

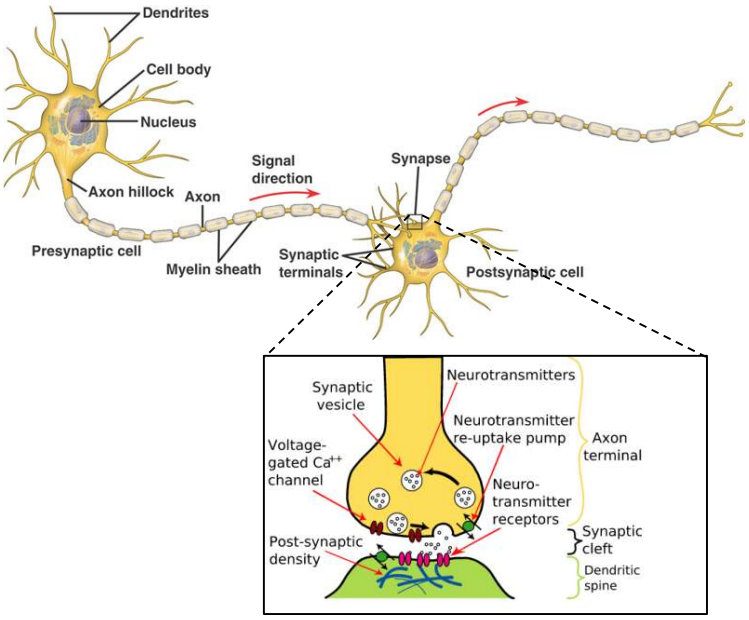

Figure 1.1. Neuronal structure and circuitry. Diagram of a neuron with a myelinated axon showing dendritic array for synaptic inputs and direction of action potential to another neuron. Boxed insert is a blow up of a synapse with the presynaptic terminus of an excitatory synapse over a dendritic spine. Adapted from An et al., 2017; Jaeger, 2015).

Different brain regions carry out specific tasks through unique neuron types and signaling circuits (Linaro et al., 2019). For example, cortical regions are specialized for visual input, auditory input, sensory input, smell, and taste and these inputs are integrated by other regions of the brain to control motor function, decision making and to form memories that are required for learning (Schultz et al., 2015). The encoding of a memory involves the strengthening or weakening of specific synapses within a circuit (Gandolfi et al., 2020). This can occur through the activation of NT receptors (Lutzu and Castillo, 2020) or by concentrating more receptors into the postsynaptic region underlying the site of neurotransmitter release (Metzbower et al., 2019). Although synaptic strength can change without any observable morphological alterations, a change in synaptic strength is often accompanied by the enlargement or shrinkage of the post synaptic specification of excitatory synapses, the dendritic spine (Kasai et al., 2010). The entorhinal cortex (EC) and the hippocampus (HC) are major regions that work together to organize and encode

sensory input that can be recalled as a memory (Hoesen et al., 1991; Klatt and Smeeton, 2019) (Figure 1.2).

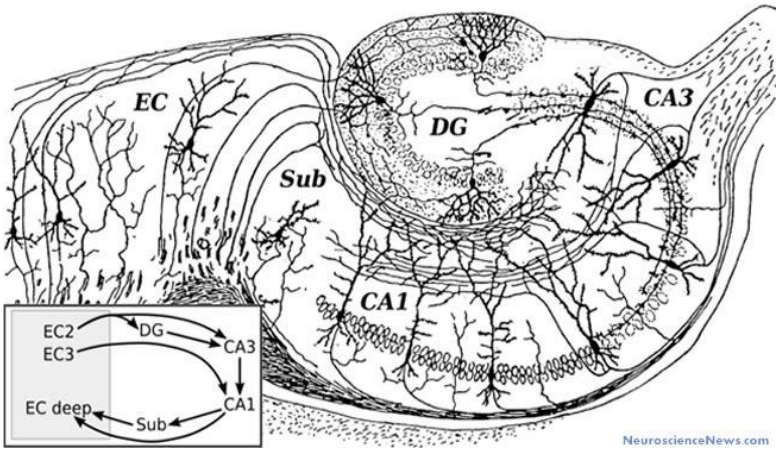

Figure 1.2. Entorhinal-hippocampal circuit drawn by Santiago Ramon y Cajal. Axons from the entorhinal cortex (EC) synapse on neurons of the dentate gyrus (DG) whose axons, called mossy fibers (MF) synapse with the Cornus Ammonis layer 3 (CA3). The axon tracts from CA3, called Shaffer collaterals, synapse on neurons of the CA1 region.

Development and Causes of Dementia

Dementia is the loss of cognitive function involved with memory and learning. During the development of dementia, specific brain regions lose synaptic connections resulting in an impaired ability to perform specific tasks (Schultz et al., 2015; Hoesen et al, 1991; Sengoku, 2020). Synapse loss and disruption of circuits occurs long before neuronal death (Masliah et al., 1994), which is found in late stages of virtually all neurodegenerative diseases. Some forms of dementia are genetic and are characterized by specific types of pathology. Other forms appear to be sporadic but if they develop the same pathology as a genetic form and follow the same type of cognitive decline, they are classified under the same disease type. Usually the genetic (familial) forms of dementia occur at earlier ages of onset than the sporadic forms (Shea et al., 2017). Onset of either form is rare in individuals under 45 years of age, suggesting that that there are age-related factors, such

as reduced mitochondrial function or increased reactive oxygen species (ROS) that contribute to the development of dementias (Mufson et al., 2016). Increased ROS production can come from mitochondrial dysfunction alone (Lejri et al., 2019), but the activation of ROS generating enzymes such as NADPH oxidases (Ansari and Scheff, 2011), and the decline in a cells ability to inactive and remove ROS (Casajus Pelegay et al., 2019) both play roles in age-related neurodegenerative diseases leading to a loss of synapses and development of dementia.

Alzheimer Disease (AD) is the most common form of dementia (Alzheimer's Disease, 2020). The first brain regions to show characteristic AD pathology, the entorhinal cortex (EC) and the hippocampus (Braak et al., 2011), are involved in memory and learning and thus memory impairment is one of the early indications of AD. Familial (genetic) AD constitutes less than 5% of all cases but most of the theories for initiation and progression of AD stem from our understanding of FAD mutations and their causative pathology (Selkoe and Hardy, 2016). However, it is important to remember that 95% of AD cases are sporadic, even though many of these have some genetic risk factors that can tie them back to the pathology of AD.

Parkinson ’s disease (PD) primarily affects motor function by the loss of dopamine releasing neurons in the substantia nigra in the brain stem (Bellucci et al., 2020). However, a subpopulation of PD patients develops the second most common form of dementia, Parkinson ’s disease with Lewy Body Dementia (PDD) (Fang et al., 2020). PDD shares some of the same pathology as AD and has many similar cognitive issues (Visanji et al., 2019). The majority of PD patients that develop PDD are those that overexpress α-synuclein, a major component of Lewy Bodies (Xu et al., 2015).

Frontal temporal dementia (FTD), less common than AD or PDD, is most often associated with genetic mutations (Perry and Miller, 2013). It shares some pathology and symptoms with both AD and PDD (Kneynsberg et al., 2017).

HIV-associated neurocognitive disorder (HAND) and Traumatic brain injury (TBI) are forms of dementia that do not have any familial correlate but do have a known disease initiating factor. HIV-infected individuals that have harbored the virus for long periods develop memory and cognitive deficits. The HIV virus resides in the brain and sheds viral proteins leading to systemic neuroinflammation (Smith et al, 2018). TBI, also a dementia caused by neuroinflammation (Dinet et al., 2019), arises from a physical insult to the brain. Depending on the location and extent of the insult, TBI can have a variety of cognitive symptoms and pathology, and some cases of TBI can initiate the future development of AD or PD (Xiong et al., 2018).

Molecular changes driving hypotheses for dementia: From studying the major pathologies associated with familial forms of dementia, we have gained insight into molecular pathways that have led to the pathology and these insights have fostered the development of hypotheses as to what causes the different dementias. For example, three different hypotheses have developed for trying to explain the development of AD. The Amyloid Hypothesis (Hardy and Higgins, 1992) is supported by genetic information from FAD patients of whom the majority have mutations in the gene for the single-pass membrane protein, amyloid precursor protein (APP) and/or in the expression of or in the genes encoding its molecular cleavage (Gandy et al., 1994; Mullan and Crawford, 1994). APP undergoes proteolytic cleavage in its ecto-and membrane spanning domains in two different ways. One mechanism utilizes α-secretase and γ-secretase, which together

generate soluble and easily cleared fragments (Turner et al., 2003). The second mechanism involves β-secretase (BACE) and γ-secretase, which together generate a small amyloidogenic peptide, amyloid-β (Aβ), of between 37 and 43 amino acids (Penke et al., 2020). Aβ can self-assemble into dimers and higher oligomers, which eventually form insoluble fibrils that deposit into extracellular amyloid plaques, one of the hallmarks of AD (Penke et al., 2020). The Tauopathy Hypothesis draws support from the finding of phosphorylated tau protein in neuropil threads and neurofibrillary tangles, which are also AD hallmarks (Penke et al., 2020; Watanabe et al, 2019). The normal function of tau is the binding and presumed stabilization and spacing of axonal microtubules (MT) (Chen et al., 1992; Best et al., 2019). Certain mutations in the gene encoding the tau protein are causative of Frontal Temporal Dementia (FTD), a form of dementia which usually presents without amyloid plaque pathology (Gozes, 2010). The third major hypothesis for AD is the Cytokine Hypothesis, which is based on an initial cascade of neuroinflammation that ultimately leads to synaptic loss and development of AD (Regen, et al., 2017). This hypothesis is supported by an increase in proinflammatory cytokines, microgliosis, and markers of oxidative stress in early AD (Taylor et al., 2018), as well as a genetic loss of function variant of TREM2, a single pass membrane protein of microglia, which results in disease state microglia activation and AD (Dean et al., 2019; Meilandt et al., 2020).

These three hypotheses are not mutually exclusive. Each has its merits. Interestingly, each protein thought to be causative is also observed in pathologies occurring in other forms of dementia. As mentioned, FTD arises from mutations in tau that lead to its hyperphosphorylation and the development of tau pathology. Pathology of

familial PDD overlaps considerably with Dementia with Lewy Bodies (Walker et al., 2019), deposits of α-synuclein, a protein that normally plays a role in neurotransmitter release (Sulzer and Edwards, 2019), but which can aggregate into beta sheets forming amyloid fibrils, similar in nature to the extracellular Aβ fibrils that form in AD (Sawada et al., 2020). α-Synuclein found within intracellular deposits is often phosphorylated on serine 129 (Wang et al., 2012). The Lewy Bodies found in PDD contain some cell debris, but to a large extent are composed of α-synuclein fibrils (Lashuel, 2020). Recent work suggests that Aβ peptides can stimulate aggregation of α-synuclein and vice versa (Köppen et al., 2020) suggesting that some cross-talk can account for overlapping disease pathologies.

Pertinent to the discussion of the roles of Aβ in AD and α-synuclein in PDD is the fact that extracellular, soluble, oligomeric but non-fibrillar forms of both proteins occur in the disease. Of great interest is the fact that each protein may form covalent dityrosine cross-links, Y10 in Aβ and Y39 in alpha-synuclein (Al-Hilaly et al., 2016; Vázquez de la Torre et al., 2018). Such covalent cross-linking may be catalyzed by low levels of copper bound to residues surrounding the tyrosine to be oxidized by molecular oxygen (Atwood et al., 2004) and may greatly enhance the synaptotoxicity of the species (Barnham et al, 2004; Davis et al., 2011). As discussed further below, signaling from these oligomeric species may have some common targets that lead to synaptic loss.

The development of HAND (aka AIDS-dementia) arises from the brain accumulation of the HIV envelope glycoprotein gp120, which is shed from the virus envelope (Canet et al., 2018). HAND occurs in about 50% of HIV-infected individuals even when the symptoms of AIDS are controlled by drugs that block HIV replication and preserve T-cells of the immune system (Eggers et al, 2017). In the brain, gp120 can

activate microglia and stimulate ROS production but its mechanism of inducing dementia is not fully understood (Smith et al., 2018). Activated microglia have been shown to prune synapses, but they also release proinflammatory cytokines and produce reactive oxygen species, either of which could also mediate dementia through direct effects on neurons (Walsh et al., 2014). In this respect, HAND is like dementia resulting from TBI, which also causes microglia activation and the resulting neuroinflammatory cascade. In severe TBI, the insulted region often becomes necrotic, similar to what occurs in the regions of ischemic brain damage following a stroke (Kumar Sahel et al., 2019). Stroke and TBI are acute and differ in many ways from the slower and age-related onset of dementia, yet there are pathological similarities discussed further in this introduction that may inform about common molecular mechanisms of synapse loss in all major forms of dementia.

The Synapse: Structure and Function

Dendritic spines, the postsynaptic structures of excitatory synapses in brain, are the sites where chemical signals in the form of neurotransmitters released from the presynaptic neuron, are turned into an electrical signal through the opening of ion channels (Kasai et al., 2010). Both excitatory and inhibitory neurotransmitters exist (Gandolfi et al., 2020). Glutamate is the major excitatory neurotransmitter in brain (Lutzu and Castillo, 2020). Neurons maintain large ion gradients across their membranes with high intracellular potassium ions and low intracellular sodium ions, the opposite of what is found outside the cell. This gradient is maintained through the action of an ATP consuming pump, the Na^+/K^+ ATPase. Transient opening of glutamate receptor ion channels allows monovalent ions to cross, causing a depolarization of the membrane, and initiating an electrical current (action potential) that is transmitted at a high rate along

the dendrite and axon (Stuart et al., 1997). The sensitivity of the post synaptic terminal to neurotransmitter stimulation depends on the organization and concentration of receptors within the postsynaptic density (Lutzu and Castillo, 2020; Kasai et al., 2010). Dendritic spines contain both ionotropic and metabotropic glutamate receptors (Lutzu and Castillo, 2020). The major ionotropic glutamate receptors, AMPAR and NMDAR, named for specific agonists of each subtype, allow ions to flow across the membrane and alter its electrical potential. AMPAR largely function for passage of monovalent sodium and potassium. Once the membrane potential declines, a voltage-dependent magnesium block is released from the NMDAR central pore and divalent Ca^{2+} ions, activators of numerous signaling cascades, can enter the cell (Lutzu and Castillo, 2020; Metzbower et al., 2019). Metabotropic glutamate receptors are G-protein coupled receptors that activate heterotrimeric G-proteins producing intracellular signaling cascades (Lutzu and Castillo, 2020). Other neurotransmitters, such as serotonin (5-HT) and acetylcholine also function through G-protein-coupled receptors. The process of receptor insertion into the post synaptic density that enhances the sensitivity of the post synaptic terminal in response to the same stimulus is termed long-term potentiation (LTP) and is thought to be essential in learning and the encoding of memory. A reduction in sensitivity from a set stimulus is termed long-term depression (LTD) (Lutzu and Castillo, 2020).

The Cytoskeleton and Synaptic Function

Dendritic spines are very dynamic structures that can change their size and shape in response to their activity (Mikhaylova et al., 2018). These dynamic changes are dependent on the cytoskeleton, particularly the ever-present actin cytoskeleton (Kasai et al., 2010; Yoshihara et al., 2009) but also the occasional penetration into spines of

microtubules (Yoshihara et al., 2009; Bucher et al., 2020). Microtubules and actin filaments are both polar non-equilibrium polymers that can maintain different critical concentrations at each end made possible by their hydrolysis of a nucleotide triphosphate (ATP for actin and GTP for microtubules) (Figure 1.3). Non-equilibrium polymers have different growth rates and different critical concentrations of monomer needed to maintain growth at each end. At a steady state concentration of monomer and polymer, non-equilibrium polymers can behave in two ways. Treadmilling of subunits can occur when the concentration of unassembled subunits (monomers for actin, α,β-tubulin dimers for microtubules) is too low to maintain growth at the "minus" end of the polymer but high enough to maintain growth at the polymer "plus" end (Carlier, 1998). Treadmilling can do work and it is responsible for the major force exerted by actin assembly that drives membrane protrusion in migrating cells (Svitkina and Borisy, 1999). Recycling of the actin subunits from the depolymerizing end of the actin filaments is the job of many proteins discussed in detail below. Treadmilling can also occur in microtubules, but is not a major behavior of microtubules in interphase cells (Rodionov and Borisy, 1997). Most microtubule minus ends are capped or stabilized in a manner such that they do not participate in dynamics. Dynamic instability is another non-equilibrium polymer behavior. It is the major behavior of microtubules and occurs when the level of GTP-tubulin subunits cannot maintain a stable cap on the growing microtubule plus end (Figure 1.3). This loss of the GTP-tubulin cap leads to a catastrophe in which the microtubule disassembles very quickly due to the wall strain energy that has accumulated during GTP hydrolysis of the subunits behind the cap (Kim and Rice, 2019). Although dynamic instability is a major behavior for actin filaments, it has been observed in bundles of F-actin, such as in

stereocilia of inner ear auditory and vestibular hair cells where only subunits of the actin bundle near the distal tip of the stereocilia undergo turnover (Roy and Perrin, 2018).

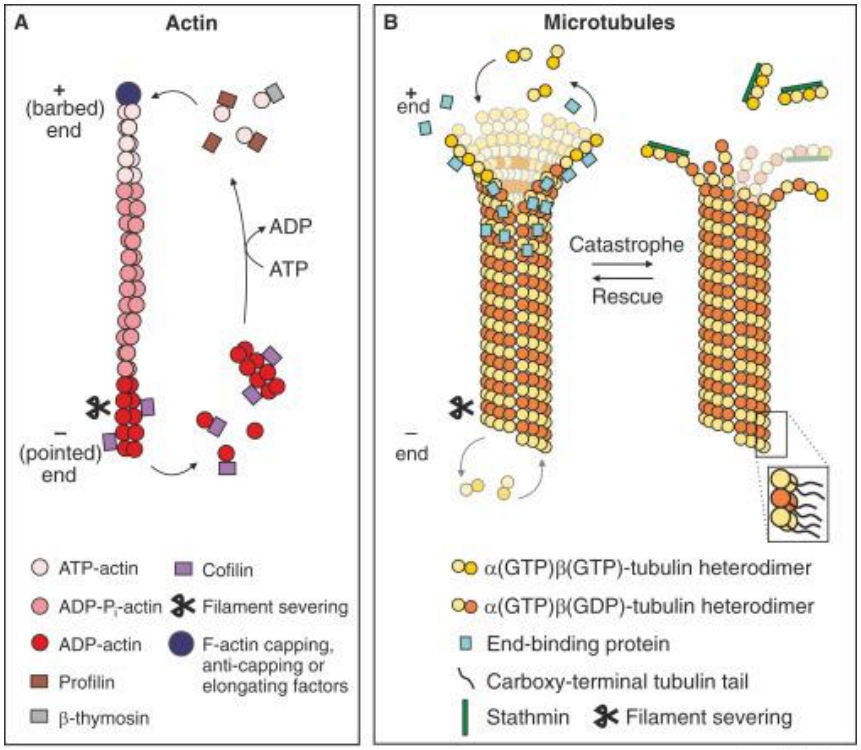

Figure 1.3 Cytoskeletal Dynamics. (A) Actin monomers contain either ATP or ADP but since they can exchange nucleotide with the cellular adenine nucleotide pool which is usually >90% ATP, it is mostly ATP-actin monomers that assemble into actin filaments. Hydrolysis of ATP occurs within seconds of filament incorporation, but dissociation of the inorganic phosphate follows more slowly. Thus, regions of F-actin contain ATP-actin, ADP-Pi-actin and ADP-actin creating a polar filament with higher ATP- and ADP-Pi-actin subunits toward the fast-growing (plus) end. (B) Microtubules assemble from polar dimers of α,β tubulin which creates a polar protofilament,. Microtubules typically contain 13 protofilaments in a straw shaped structure with a hollow core. Both α,β tubulin subunits have bound GTP but only the β subunit hydrolyzes GTP within a microtubule and this energy is stored as a conformational change (wall strain) between the protofilaments and is released during catastrophes when microtubules rapidly depolymerize from their (+)-end. Catastrophes are prevented by maintaining a cap of 50 to 70 assembled GTP-dimers at the growing end of the filament to prevent disassembly. From Coles and Bradke, 2015.

In addition to their behaviors described above in which assembly dynamics of actin filaments and microtubules drive cellular processes, more stable cytoskeletal networks interact with motor proteins to carry out transport of cargo and to generate tension when

bridged between opposite polarity filaments. Microtubules and their motors provide the major rapid transport system for vesicle and organelle movement within axons and dendrites (Guedes-Dias and Holzbauer, 2019). Included within this transport system are mitochondria, whose distributions within the long neurite processes are critical for maintenance of local energy levels (Khacho and Slack, 2018). Many microtubule-associated proteins (MAPs), such as tau and MAP2, play structural roles in spacing, positioning or stabilizing microtubules (Chen et al., 1992; Hahn et al., 2019 69). A small percentage (about 4%) of dendritic spines in fixed neurons show microtubule penetration but since spine penetration in dendrites of live cells is short lived, it is quite possible that many, if not most, spines have microtubule visitors delivering cargo, including mitochondria, at some unknown time interval (Hu et al., 2008; Gu and Zheng, 2009).

The Actin Cytoskeleton and Cofilin in Spine Dynamics

Actin filaments (F-actin) within spines are very dynamic (Bonilla-Quintana et al., 2020) and are often in branched arrays as a result of the presence of the ARP2/3 complex, which binds to the sides of existing F-actin and mimics an actin dimer producing growth of an actin branch off the mother filament (Svitkina and Borisy, 1999; Koribova and Svitkina, 2010). Disassembly of the branched network and turnover of the filament subunits is under control of many actin binding proteins, among them the dephosphorylated form of ADF/cofilin family proteins, which can bind an actin subunit within F-actin and induce a slight conformational change in its D-loop domain producing a slight torsional twist that results in filament severing (Huehn et al., 2020). However, ADF/cofilin can also bind cooperatively along F-actin (Hayden et l., 1993; McGough et al., 1997) in which all the subunits undergo a twist and create a stable ADF/cofilin

saturated-actin filament. In mammalian neurons, cofilin makes up >85% of the ADF/cofilin family proteins (Minamide et al., 2000; Garvalov et al., 2007) and hereafter will be the only member discussed. Other actin binding proteins, such as those in the coronin family, can help recruit cofilin to actin filaments (Mikati et al., 2015) whereas co-recruitment of the protein WDR1 (aka Aip1), helps cofilin to disassemble the filaments into cofilin-actin monomers (Ono, 2018), which can interact with the cyclase activating protein-1 (CAP1) to dissociate cofilin and aid in the exchange of ADP to ATP on the actin monomers (Zhang et al., 2020). Conversely, F-actin stabilizing proteins such as drebrin, a developmentally regulated brain actin binding protein, competes with cofilin for F-actin binding and is recruited into stable spines after cofilin undergoes inactivation through its phosphorylation by LIM kinase 1 (Mikhaylova et al., 2018; Bosch et al., 2014; Borovac et al., 2018). Cofilin is inactivated in binding to actin by phosphorylation on serine 3 by LIM kinase (Morgan et al., 1993; Agnew et al., 1995; Moriyama et al., 1996; Arber et al., 1998; Yang et al., 1998). Phospho-cofilin is dephosphorylated (reactivated) by phosphatases in the slingshot (SSH family) or chronophin (CIN) (Niwa et al., 2002; Gohla et al., 2005). Cofilin can also be held in an inactive state through binding to phosphatidyl-inositol phosphates (PIP and PIP2) (Yonezawa et al., 1990) where its release from the membrane by PLC isoforms can result in local activation (Mouneimne et al., 2006).

Both LTP and LTD are usually accompanied by cytoskeletal alterations. The role of the cytoskeleton in LTP can be best explained as a 4-step process that covers several hours. The first step of LTP involves the remodeling of the F-actin network through transient activation of cofilin (Gu et al., 2010; Rust, 2015). This can arise from either dephosphorylation of phospho-cofilin or the release of cofilin from binding to

phosphatidylinositol phosphates by phospholipase C (van Rheenen et al., 2007). Cofilin severed filaments create more nucleation sites for filament growth and help generate the Arp2/3- branched actin network within the spine (Korobova and Svitkina, 2010). Some branched actin networks protrude from the spine neck into the dendrite shaft where cortactin-bound F-actin directs MT penetration into the dendritic spine (Schatzle et al., 2018). Although cofilin alone will displace cortactin from actin filaments (unpublished results from Weed and Bamburg labs), after calcium entry during LTP, caldendrin a calcium-activated protein, enhances the ability of cortactin to stabilize F-actin in the presence of cofilin (Mikhaylova et al., 2018). This dynamic interplay between these proteins enhances spine growth in response to NMDAR activity and allows transient microtubule penetration for receptor vesicle/organelle trafficking. Receptors are trafficked to the post synaptic density where scaffolding proteins modulate the connectivity of the presynaptic and post synaptic site. Post synaptic density protein 95 (PSD-95) is the major excitatory post synaptic scaffolding protein and gephyrin is the major inhibitory post synaptic scaffolding protein (Handara and Kröger, 2019). PSD-95 plays many roles including stabilizing and altering NMDARs and AMPARs and stabilizes neuroligin-1's transsynaptic connection with neurexin (Jeong et al., 2019). PSD-95 also recruits homer, which is associated with stable spines, and shank, both of which play roles in calcium homeostasis and signaling in spines (Figure 1.4) (Sala et al., 2005).

The second step involves the inactivation (phosphorylation) of cofilin by LIM kinase, which is accompanied by the accumulation of drebrin and stabilization of the larger spine (Shirao et al., 2017; Saneyoshi et al., 2019). At this stage proteins such as CaMKII, which is activated by calcium/calmodulin, also stabilize filamentous actin within

spines (Wang et al., 2019). The incorporation of more AMPA receptors is a key event in LTP leading to enhanced depolarization of post synaptic compartments by the same amount of presynaptic neurotransmitter release (Moretto and Passafaro, 2018). The third step involves local translation of proteins that requires localized active mitochondria for energy (Rangaraju et al., 2019). The fourth step involves new gene transcription which depends in part upon translocation of CaM Kinase II-activated transcription factors from spines back to the nucleus (Dittmer et al., 2017). Actin dynamics in the nucleus also modulate transcription of LTP-related proteins (Zheng et al., 2009; Ifrim et al., 2015).

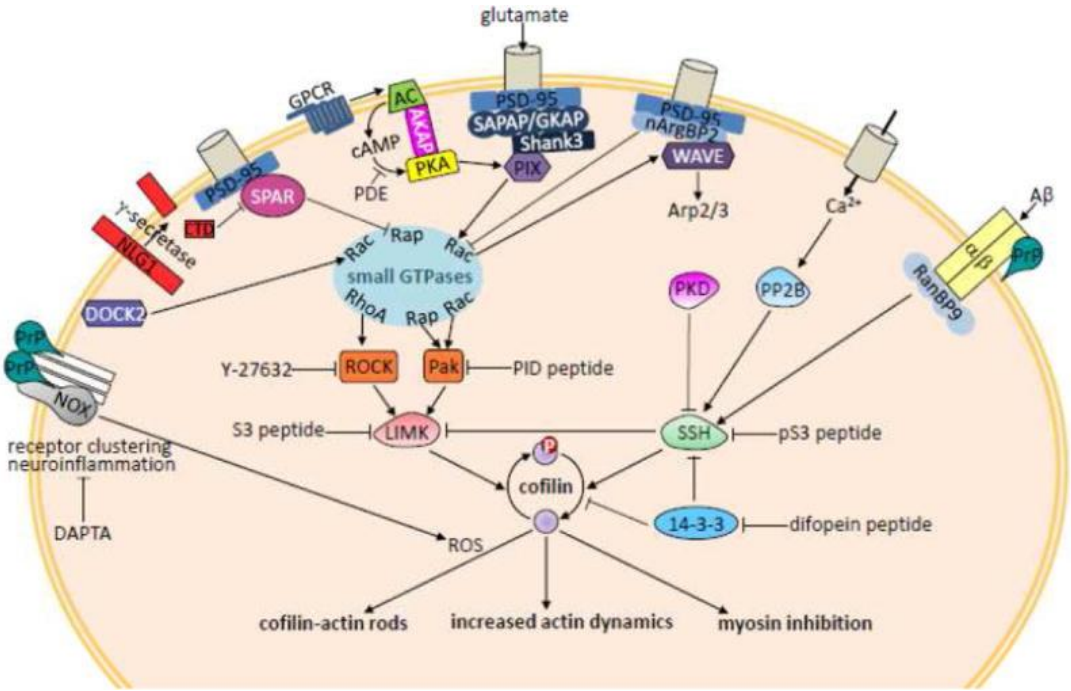

Figure 1.4. Some components of dendritic spines that impact cofilin activity and actin remodeling. Modulation of cofilin regulation with S3 and pS3 peptides corrects synaptic deficits in several neurodegenerative and psychiatric disorders (Shaw & Bamburg, 2016).

LTD on the other hand is accompanied by depolymerization of actin, spine shrinkage and removal of AMPAR from the postsynaptic membrane (Woolfrey et al, 2018; Hushchenko and Hotulainen, 2019). Cofilin activity is required for spine shrinkage in adult mice and for driving the actin dynamics in AMPAR endocytosis (Gu et al., 2010; Cao et

al., 2017; Pontrello et al., 2012; Calabrese et al., 2014). The removal of AMPAR requires phosphorylation of the AMPAR and subsequent clathrin-mediated endocytosis (Hanley, 2018). After a clathrin coat has formed at the site of receptor internalization, F-actin polymerization drives vesicle invagination with dynamin, a GTPase, required to complete the vesicle severing (Loebrich, 2014).

Transport Defects in Neurodegenerative Diseases: Alterations in the regulation of MAPs and ABPs result in defective axonal transport in almost all neurodegenerative diseases (Anggono and Huganir, 2012; Wang et al., 2014). Disrupted transport of vesicles, organelles and their associated proteins prevents the formation, stabilization and remodeling of synapses necessary for learning and memory (Maeder et al., 2014). In addition to direct effects within dendritic spines, F-actin acts as a scaffold for contractile forces necessary for mitochondria fission (Li et al., 2018). In AD brain mitochondrial dysfunction is rampant and is characterized by over production of reactive oxygen species (ROS) (Mancuso et al., 2009). AD brain has high levels of ROS, which has wide ranging affects, one of which is DNA damage. Alterations in cargo transport along microtubules in AD is hypothesized to exacerbate DNA damage through disrupted delivery of cargo for DNA damage repair, including actin and many ABPs (Mancuso et al., 2009; Poruchynsky et al, 2015; Chang et al., 2015; Schrank et al., 2018). Tau, the neurotoxic protein in FTD, helps stabilize and organize microtubule arrays. In FTD and AD, tau becomes hyperphosphorylated and aggregates in the soma and in neurites forming tau neurofibrillary tangles and neuropil threads, respectively. Early regions of tau to become phosphorylated in AD appear to be those sites involved in microtubule binding (Neddens et al., 2018); thus, it is not yet clear if release of tau from microtubules leads to their

destabilization or if microtubule destabilization leads to the release of tau. Furthermore, synaptic dysfunction may arise before these tauopathies appear. Tau is mistargeted in AD mice, with more of it going into dendrites and accumulating at dendritic spines (Ittner et al., 2010; Xia et al., 2015). Pathogenic tau also alters the location and activity of the mitochondrial fission proteins DRP1 (DuBoff et al., 2012) and relocates the axon initial segment, thus altering axon conductivity (Hatch et al., 2017). Resulting localized oxidative damage blocks mitochondrial transport leading to local energy rundown in regions of mitochondrial depletion (Grimm et al., 2018). Tau containing exosomes can transmit tau pathology to neighboring cells (Nisbet and Goetz, 2018). Significantly, soluble oligomers of tau (not fibrils) are released from cells, and these can disrupt synaptic plasticity in a cellular prion protein (PrP^C)-dependent manner (Ondrejcak et al., 2018). PrP^C expression is required for cognitive dysfunction in mouse models of all of the neurodegenerative diseases explored in this thesis and suggests that there may be a common membrane signaling platform that involves PrP^C which drives synaptic dysfunction. However the mechanism, the final result is improper axonal organelle trafficking affecting the delivery of neurotransmitters and the ability of axons to propagate signals (Hatchet al., 2017; Zhou et al., 2017). Defective axonal transport is one of the earliest changes seen in tauopathy models (Kneynsberg et al., 2017). Of additional interest, tauopathy model mice show abnormal cofilin function affecting microtubules (Woo et al., 2019).

Alpha-synuclein protein is an intrinsically disordered protein with an N-terminal membrane associated alpha-helix that plays a role in vesicle release at synaptic terminals (Eliezer, 2001; Burré et al., 2010). Alpha-synuclein can form into beta sheets resulting in amyloid fibrils. Pathological α-synuclein expression results in defective axonal transport

of essential proneuronal growth factors (Fang et al., 2017). In addition, extracellular fibrils of α-synuclein can lead to a variety of actin-dependent changes requiring the presence of PrP^C, as well as NADPH oxidase (NOX) to produce ROS (Hou et al., 2018; De Cecco and Legname, 2018; Zhong et al., 2018). Interestingly, Aβ oligomers can stimulate hyperphosphorylation of tau and the formation of tauopathies through a PrP^C-dependent signaling cascade (Kostylev et al., 2018); hyperphosphorylated tau enhances Aβ-mediated toxicity, via a mechanism that seems to be dependent on actin reorganization (Frost et al., 2015).

Cofilin-actin Rods

Aβ also induces cytoskeleton alterations in the form of cofilin-actin rods through a PrP^C- and NOX-dependent pathway (Walsh et al, 2014). Cofilin-actin rods (rods) were first observed in neurites of cultured neurons that were subjected to energetic or oxidative stress and these same structures were found in the hippocampus of AD subjects but not non-cognitively impaired subjects (Minamide et al., 2000). Rods are induced by synthetic Aβ oligomers (Maloney et al., 2005), but naturally secreted forms of Aβ, especially the more physiologically relevant dimer and trimer fraction (Aβd/t), are over 10^3 fold more active in inducing rods (Davis et al., 2011). Rods contain ADF/cofilin and actin in 1:1 ratio (Minamide et al., 2010) and the majority of the cofilin in rods is as a disulfide-linked dimer (Bernstein et al., 2012). In neurites containing rods, most of the cofilin is sequestered into rods (Walsh et al., 2014, Maloney ey al, 2005). Rods can directly block transport and inhibit distal synaptic function (Maloney et al., 2005; Cichon et al., 2012) or they can alter synaptic plasticity through sequestering of cofilin, or both. The cognitive deficits of AD model mice and the loss of LTP in brain slices from these model mice are both restored

upon reduction of cofilin-actin rod pathology by reducing cofilin expression (Woo et al., 2015A), reducing the expression of an upstream protein (RanBP9) involved in slingshot recruitment for activating cofilin (Woo et al., 2015B), or through the enhanced inactivation of cofilin by increasing its phosphorylation (Deng et al., 2016; Shaw and Bamburg, 2016). Reduction of cofilin pathology in a Tauopathy model mouse also restored cognition and LTP (Woo et al., 2019). The average level of phosphorylated cofilin in adult mouse brain is less than 5% of the total and changes in phosphorylation can be very rapid and highly localized making the overall state of cofilin phosphorylation misleading when studying its effects (Meberg et al., 1998); thus local phosphocycling and the inability of cofilin to enter this pool, rather than the absolute pool size of the dephospho-cofilin is probably a key to understanding its role in dementia.

Cofilin-Actin rods are a shared pathology in AD and stroke. The quick onset of dementia occurring from stroke gives unique insight into the biochemistry of neurodegeneration. In stroke two distinct brain regions can be observed, the infarct or necrotic region, and the peri-infarct or dying region peripheral to the infarct. The peri-infarct region is of interest because cells within it are not dead but are degenerating. Once a capillary or artery has been occluded by a clot, oxygen and nutrients are depleted from neurons fed by the capillary. After the clot has been cleared, reperfusion of nutrients will flood the neurons. It has been shown that rods form during the O_2 depletion in stroke and during the reperfusion in stroke (Shu et al., 2018), especially within the peri-infarct region (Won et al., 2018). Knockdown or deletion of NOX2 results in reduced rod formation and a delayed spreading of the infarct region into the peri-infarct (McCann et al., 2014), suggesting that rod formation dependent on NOX2 has a role in exacerbating neuronal

degeneration. In addition, an experimental therapeutic for stroke, hypothermia, which lowers the body temperature and reduces proinflammatory cytokine production resulting in preserved motor function and cognition, is accompanied by a significant reduction in rod formation mediated through the heat-shock protein (HSP) 70 (Kurisu et al., 2019). Previous work has shown that another HSP, HSP-90, complexes with the phospho-cofilin phosphatase chronophin (CIN) and that in neurons, CIN is released from HSP-90 in response to ATP-depletion and leads to rod formation (Huang et al., 2008). Transcranial imaging of cofilin in live mouse cortical neurons by two-photon microscopy showed improved motor ability once rods were reduced through enhancing cofilin phosphorylation with LIM kinase (Shu et all, 2018). Taken together with previous work showing reducing cofilin levels or activity also enhanced cognition in AD mice, rod formation may be a common mechanism in neurodegenerative diseases.

Although dementias arise from different causes and may have some unique pathologies, common factors seem to be the loss of dendritic spines, the presence of proinflammatory cytokines, and increased levels of reactive oxygen species. The latter two factors are cofilin-actin rod-inducing, suggesting rods could be a common mechanism for dendritic spine loss. Most therapeutic approaches for each form of dementia have focused on the specific pathology associated with that dementia, for example, reducing Aβ in brains of AD subjects. In spite of achieving some reduction in amyloid beta from the brain, new therapeutics for AD have shown benefit only if performed during early stages of mild cognitive impairment with little to no change in the progression of cognitive decline for those patients already in AD. None of the current FDA approved drugs for AD stem the progression of dementia and, at best, only delay the progression of decline for a few

months. The failure of therapeutics is due to a fundamental lack of understanding of the cause of the synaptic dysfunction. Work from our lab and others has shown the importance of PrP^c and a functional NOX enzyme for cofilin-actin rod formation and that rods are a common pathology induced by Aβ and proinflammatory cytokines (Walsh et al., 2014).

Results from studies investigating the role of reactive microglia in synaptic loss have suggested that their HIV-co-receptors CCR5 and CXCR4 might be involved in mediating synaptic loss (Maung et al., 2012; Victoria et al., 2017). Indeed, inhibitors of CCR5, maraviroc (aka Selzentry®), and of CXCR4, AMD3100 (aka Plerixafor®) or a natural inhibitory ligand, CXCL12, enhanced cognition and synaptic plasticity in subjects following stroke and those with HIV-associated neurocognitive disorder (Maung et al., 2012; Victoria et al., 2017; Festa et al., 2020; Joy et al., 2019). In our work presented below we show that the HIV gp120 protein, the protein responsible for HAND, as well as some soluble component in sonicated preparations of α-synuclein fibrils (PDD), induce cofilin-actin rods in the same subpopulation of rodent hippocampal neurons, through a PrP^C- and NOX-dependent pathway. The non-additive response when multiple rod-inducers are used suggest the pathway is identical to that used by Aβ and TNFα. Furthermore, we show that cofilin-actin rods from any of these inducers can be blocked by the CXCR4 inhibitor AMD3100, as well as by a small peptide inhibitor, Rap310, a possible dementia therapeutic. We also show that rodent neurons express both CXCR4 and CCR5 receptors on their surface, suggesting rod-inducers work directly on neurons.

References

Agnew BJ, Minamide LS, Bamburg JR. Reactivation of phosphorylated actin depolymerizing factor and identification of the regulatory site. *J Biol Chem*. 1995;270(29):17582-17587. doi:10.1074/jbc.270.29.17582

Al-Hilaly YK, Biasetti L, Blakeman BJ, et al. The involvement of dityrosine crosslinking in α-synuclein assembly and deposition in Lewy Bodies in Parkinson's disease. *Sci Rep*. 2016;6:39171. Published 2016 Dec 16. doi:10.1038/srep39171

Alzheimer's Association. 2020 Alzheimer's disease facts and figures. Alzheimers Dement. 2020;10.1002/alz.12068. doi:10.1002/alz.12068

An H, Ehsan AM, Zhou Z, Yi, Y. (2017) Electrical Modeling and Analysis of 3D Synaptic Array using Vertical RRAM Structure. Conference Paper through Research Gate

Anggono V, Huganir RL. Regulation of AMPA receptor trafficking and synaptic plasticity. *Curr Opin Neurobiol*. 2012;22(3):461-469. doi:10.1016/j.conb.2011.12.006

Ansari MA, Scheff SW. NADPH-oxidase activation and cognition in Alzheimer disease progression. *Free Radic Biol Med*. 2011;51(1):171-178. doi:10.1016/j.freeradbiomed.2011.03.025

Arber S, Barbayannis FA, Hanser H, et al. Regulation of actin dynamics through phosphorylation of cofilin by LIM-kinase. *Nature*. 1998;393(6687):805-809. doi:10.1038/3172

Atwood CS, Perry G, Zeng H, et al. Copper mediates dityrosine cross-linking of Alzheimer's amyloid-beta. *Biochemistry*. 2004;43(2):560-568. doi:10.1021/bi0358824

Augustinack JC, Schneider A, Mandelkow EM, Hyman BT. Specific tau phosphorylation sites correlate with severity of neuronal cytopathology in Alzheimer's disease. *Acta Neuropathol*. 2002;103(1):26-35. doi:10.1007/s004010100423

Barnham KJ, Haeffner F, Ciccotosto GD, et al. Tyrosine gated electron transfer is key to the toxic mechanism of Alzheimer's disease beta-amyloid. *FASEB J*. 2004;18(12):1427-1429. doi:10.1096/fj.04-1890fje

Bellucci A, Bubacco L, Longhena F, et al. Nuclear Factor-κB Dysregulation and α-Synuclein Pathology: Critical Interplay in the Pathogenesis of Parkinson's Disease. *Front Aging Neurosci*. 2020;12:68. Published 2020 Mar 24. doi:10.3389/fnagi.2020.00068

Bernstein BW, Shaw AE, Minamide LS, Pak CW, Bamburg JR. Incorporation of cofilin into rods depends on disulfide intermolecular bonds: implications for actin regulation and neurodegenerative disease. *J Neurosci*. 2012;32(19):6670-6681. doi:10.1523/JNEUROSCI.6020-11.2012

Best RL, LaPointe NE, Liang J, et al. Tau isoform-specific stabilization of intermediate states during microtubule assembly and disassembly. *J Biol Chem*. 2019;294(33):12265-12280. doi:10.1074/jbc.RA119.009124

Bonilla-Quintana M, Wörgötter F, Tetzlaff C, Fauth M. Modeling the Shape of Synaptic Spines by Their Actin Dynamics. *Front Synaptic Neurosci*. 2020;12:9. Published 2020 Mar 10. doi:10.3389/fnsyn.2020.00009

Borovac J, Bosch M, Okamoto K. Regulation of actin dynamics during structural plasticity of dendritic spines: Signaling messengers and actin-binding proteins. *Mol Cell Neurosci*. 2018;91:122-130. doi:10.1016/j.mcn.2018.07.001

Bosch M, Castro J, Saneyoshi T, Matsuno H, Sur M, Hayashi Y. Structural and molecular remodeling of dendritic spine substructures during long-term potentiation. *Neuron*. 2014;82(2):444-459. doi:10.1016/j.neuron.2014.03.021

Braak H, Thal DR, Ghebremedhin E, Del Tredici K. Stages of the pathologic process in Alzheimer disease: age categories from 1 to 100 years. *J Neuropathol Exp Neurol*. 2011;70(11):960-969. doi:10.1097/NEN.0b013e318232a379

Bucher M, Fanutza T, Mikhaylova M. Cytoskeletal makeup of the synapse: Shaft versus spine. *Cytoskeleton (Hoboken)*. 2020;77(3-4):55-64. doi:10.1002/cm.21583

Burré J, Sharma M, Südhof TC. α-Synuclein assembles into higher-order multimers upon membrane binding to promote SNARE complex formation. *Proc Natl Acad Sci U S A*. 2014;111(40):E4274-E4283. doi:10.1073/pnas.1416598111

Calabrese B, Saffin JM, Halpain S. Activity-dependent dendritic spine shrinkage and growth involve downregulation of cofilin via distinct mechanisms. *PLoS One*. 2014;9(4):e94787. Published 2014 Apr 16. doi:10.1371/journal.pone.0094787

Canet G, Dias C, Gabelle A, et al. HIV Neuroinfection and Alzheimer's Disease: Similarities and Potential Links?. *Front Cell Neurosci*. 2018;12:307. Published 2018 Sep 11. doi:10.3389/fncel.2018.00307

Cao F, Zhou Z, Pan X, et al. Developmental regulation of hippocampal long-term depression by cofilin-mediated actin reorganization. *Neuropharmacology*. 2017;112(Pt A):66-75. doi:10.1016/j.neuropharm.2016.08.017

Carlier MF. Control of actin dynamics. *Curr Opin Cell Biol*. 1998;10(1):45-51. doi:10.1016/s0955-0674(98)80085-9

Casajus Pelegay E, Puzzo F, Yilmazer A, Cagin U. Targeting Mitochondrial Defects to Increase Longevity in Animal Models of Neurodegenerative Diseases. *Adv Exp Med Biol*. 2019;1134:89-110. doi:10.1007/978-3-030-12668-1_5

Chang CY, Leu JD, Lee YJ. The actin depolymerizing factor (ADF)/cofilin signaling pathway and DNA damage responses in cancer. *Int J Mol Sci*. 2015;16(2):4095-4120. Published 2015 Feb 13. doi:10.3390/ijms16024095

Chen J, Kanai Y, Cowan NJ, Hirokawa N. Projection domains of MAP2 and tau determine spacings between microtubules in dendrites and axons. *Nature*. 1992;360(6405):674-677. doi:10.1038/360674a0

Cichon J, Sun C, Chen B, et al. Cofilin aggregation blocks intracellular trafficking and induces synaptic loss in hippocampal neurons. *J Biol Chem*. 2012;287(6):3919-3929. doi:10.1074/jbc.M111.301911

Coles CH, Bradke F. Coordinating neuronal actin-microtubule dynamics. *Curr Biol*. 2015;25(15):R677-R691. doi:10.1016/j.cub.2015.06.020

Davis RC, Marsden IT, Maloney MT, et al. Amyloid beta dimers/trimers potently induce cofilin-actin rods that are inhibited by maintaining cofilin-phosphorylation. *Mol Neurodegener*. 2011;6:10. Published 2011 Jan 24. doi:10.1186/1750-1326-6-10

Dean HB, Roberson ED, Song Y. Neurodegenerative Disease-Associated Variants in TREM2 Destabilize the Apical Ligand-Binding Region of the Immunoglobulin Domain. *Front Neurol*. 2019;10:1252. Published 2019 Nov 26. doi:10.3389/fneur.2019.01252

De Cecco E, Legname G. The role of the prion protein in the internalization of α-synuclein amyloids. *Prion*. 2018;12(1):23-27. doi:10.1080/19336896.2017.1423186

Deng Y, Wei J, Cheng J, et al. Partial Amelioration of Synaptic and Cognitive Deficits by Inhibiting Cofilin Dephosphorylation in an Animal Model of Alzheimer's Disease. *J Alzheimers Dis*. 2016;53(4):1419-1432. doi:10.3233/JAD-160167

Dinet V, Petry KG, Badaut J. Brain-Immune Interactions and Neuroinflammation After Traumatic Brain Injury. *Front Neurosci*. 2019;13:1178. Published 2019 Nov 12. doi:10.3389/fnins.2019.01178

Dittmer PJ, Wild AR, Dell'Acqua ML, Sather WA. STIM1 Ca^{2+} Sensor Control of L-type Ca^{2+}-Channel-Dependent Dendritic Spine Structural Plasticity and Nuclear Signaling. *Cell Rep*. 2017;19(2):321-334. doi:10.1016/j.celrep.2017.03.056

Dolphin AC, Lee A. Presynaptic calcium channels: specialized control of synaptic neurotrans-mitter release. *Nat Rev Neurosci*. 2020;21(4):213-229. doi:10.1038/s41583-020-0278-2

DuBoff B, Götz J, Feany MB. Tau promotes neurodegeneration via DRP1 mislocalization in vivo. *Neuron*. 2012;75(4):618-632. doi:10.1016/j.neuron.2012.06.026

Eggers C, Arendt G, Hahn K, et al. HIV-1-associated neurocognitive disorder: epidemiology, pathogenesis, diagnosis, and treatment. *J Neurol*. 2017;264(8):1715-1727. doi:10.1007/s00415-017-8503-2

Eliezer D, Kutluay E, Bussell R Jr, Browne G. Conformational properties of alpha-synuclein in its free and lipid-associated states. *J Mol Biol*. 2001;307(4):1061-1073. doi:10.1006/jmbi.2001.4538

Fang C, Lv L, Mao S, Dong H, Liu B. Cognition Deficits in Parkinson's Disease: Mechanisms and Treatment. *Parkinsons Dis*. 2020;2020:2076942. Published 2020 Mar 24. doi:10.1155/2020/2076942

Fang F, Yang W, Florio JB, et al. Synuclein impairs trafficking and signaling of BDNF in a mouse model of Parkinson's disease. *Sci Rep*. 2017;7(1):3868. Published 2017 Jun 20. doi:10.1038/s41598-017-04232-4

Farhy-Tselnicker I, Allen NJ. Astrocytes, neurons, synapses: a tripartite view on cortical circuit development. *Neural Dev*. 2018;13(1):7. Pub. 2018 May 1. doi:10.1186/s13064-018-0104-y

Festa LK, Irollo E, Platt BJ, Tian Y, Floresco S, Meucci O. CXCL12-induced rescue of cortical dendritic spines and cognitive flexibility. *Elife*. 2020;9:e49717. Published 2020 Jan 23. doi:10.7554/eLife.49717

Frost B, Götz J, Feany MB. Connecting the dots between tau dysfunction and neurodegeneration. *Trends Cell Biol*. 2015;25(1):46-53. doi:10.1016/j.tcb.2014.07.005

Gandolfi D, Bigiani A, Porro CA, Mapelli J. Inhibitory Plasticity: From Molecules to Computation and Beyond. *Int J Mol Sci*. 2020;21(5):1805. Published 2020 Mar 6. doi:10.3390/ijms21051805

Gandy S, Caporaso G, Buxbaum J, Frangione B, Greengard P. APP processing, A beta-amyloidogenesis, and the pathogenesis of Alzheimer's disease. *Neurobiol Aging*. 1994;15(2):253-256. doi:10.1016/0197-4580(94)90125-2

Garvalov BK, Flynn KC, Neukirchen D, et al. Cdc42 regulates cofilin during the establishment of neuronal polarity. *J Neurosci*. 2007;27(48):13117-13129. doi:10.1523/JNEUROSCI.3322-07.2007

Gohla A, Birkenfeld J, Bokoch GM. Chronophin, a novel HAD-type serine protein phosphatase, regulates cofilin-dependent actin dynamics. *Nat Cell Biol*. 2005;7(1):21-29. doi:10.1038/ncb1201

Gozes I. Tau pathology and future therapeutics. *Curr Alzheimer Res*. 2010;7(8):685-696. doi:10.2174/156720510793611628

Grimm A, Cummins N, Götz J. Local Oxidative Damage in the Soma and Dendrites Quarantines Neuronal Mitochondria at the Site of Insult. *iScience*. 2018;6:114-127. doi:10.1016/j.isci.2018.07.015

Grossberg S. Developmental Designs and Adult Functions of Cortical Maps in Multiple Modalities: Perception, Attention, Navigation, Numbers, Streaming, Speech, and Cognition. *Front Neuroinform*. 2020;14:4. Published 2020 Feb 6. doi:10.3389/fninf.2020.00004

Gu J, Zheng JQ. Microtubules in Dendritic Spine Development and Plasticity. *Open Neurosci J*. 2009;3:128-133. doi:10.2174/1874082000903020128

Gu J, Lee CW, Fan Y, et al. ADF/cofilin-mediated actin dynamics regulate AMPA receptor trafficking during synaptic plasticity. *Nat Neurosci*. 2010;13(10):1208-1215. doi:10.1038/nn.2634

Guedes-Dias P, Holzbaur ELF. Axonal transport: Driving synaptic function. *Science*. 2019;366(6462):eaaw9997. doi:10.1126/science.aaw9997

Hahn I, Voelzmann A, Liew YT, Costa-Gomes B, Prokop A. The model of local axon homeostasis - explaining the role and regulation of microtubule bundles in axon maintenance and pathology. *Neural Dev*. 2019;14(1):11. Published 2019 Nov 9. doi:10.1186/s13064-019-0134-0

Handara G, Kröger S. Alternative Splicing and the Intracellular Domain Mediate TM-agrin's Ability to Differentially Regulate the Density of Excitatory and Inhibitory Synapse-like Specializations in Developing CNS Neurons. *Neuroscience*. 2019;419:60-71. doi:10.1016/j.neuroscience.2019.09.011

Hanley JG. The Regulation of AMPA Receptor Endocytosis by Dynamic Protein-Protein Interactions. *Front Cell Neurosci*. 2018;12:362. Published 2018 Oct 11. doi:10.3389/fncel.2018.00362

Hardy JA, Higgins GA. Alzheimer's disease: the amyloid cascade hypothesis. *Science*. 1992;256(5054):184-185. doi:10.1126/science.1566067

Hatch RJ, Wei Y, Xia D, Götz J. Hyperphosphorylated tau causes reduced hippocampal CA1 excitability by relocating the axon initial segment. *Acta Neuropathol*. 2017;133(5):717-730. doi:10.1007/s00401-017-1674-1

Hayden SM, Miller PS, Brauweiler A, Bamburg JR. Analysis of the interactions of actin depolymerizing factor with G- and F-actin. *Biochemistry*. 1993;32(38):9994-10004. doi:10.1021/bi00089a015

Hlushchenko I, Hotulainen P. Chemical LTD, but not LTP, induces transient accumulation of gelsolin in dendritic spines. *Biol Chem*. 2019;400(9):1129-1139. doi:10.1515/hsz-2019-0110

Hou L, Bao X, Zang C, et al. Integrin CD11b mediates α-synuclein-induced activation of NADPH oxidase through a Rho-dependent pathway. *Redox Biol*. 2018;14:600-608. doi:10.1016/j.redox.2017.11.010

Hu X, Viesselmann C, Nam S, Merriam E, Dent EW. Activity-dependent dynamic microtubule invasion of dendritic spines. *J Neurosci*. 2008;28(49):13094-13105. doi:10.1523/JNEUROSCI.3074-08.2008

Huang TY, Minamide LS, Bamburg JR, Bokoch GM. Chronophin mediates an ATP-sensing mechanism for cofilin dephosphorylation and neuronal cofilin-actin rod formation. *Dev Cell*. 2008;15(5):691-703. doi:10.1016/j.devcel.2008.09.017

Huehn AR, Bibeau JP, Schramm AC, Cao W, De La Cruz EM, Sindelar CV. Structures of cofilin-induced structural changes reveal local and asymmetric perturbations of actin filaments. *Proc Natl Acad Sci U S A*. 2020;117(3):1478-1484. doi:10.1073/pnas.1915987117

Ifrim MF, Williams KR, Bassell GJ. Single-Molecule Imaging of PSD-95 mRNA Translation in Dendrites and Its Dysregulation in a Mouse Model of Fragile X Syndrome. *J Neurosci*. 2015;35(18):7116-7130. doi:10.1523/JNEUROSCI.2802-14.2015

Ittner LM, Ke YD, Delerue F, et al. Dendritic function of tau mediates amyloid-beta toxicity in Alzheimer's disease mouse models. *Cell*. 2010;142(3):387-397. doi:10.1016/j.cell.2010.06.036

Jaeger S. Detecting Disease in Radiographs with Intuitive Confidence. *ScientificWorldJournal*. 2015;2015:946793. doi:10.1155/2015/946793

Jeong J, Pandey S, Li Y, Badger JD 2nd, Lu W, Roche KW. PSD-95 binding dynamically regulates NLGN1 trafficking and function. *Proc Natl Acad Sci U S A*. 2019;116(24):12035-12044. doi:10.1073/pnas.1821775116

Joy MT, Ben Assayag E, Shabashov-Stone D, et al. CCR5 Is a Therapeutic Target for Recovery after Stroke and Traumatic Brain Injury. *Cell*. 2019;176(5):1143-1157.e13. doi:10.1016/j.cell.2019.01.044

Kasai H, Fukuda M, Watanabe S, Hayashi-Takagi A, Noguchi J. Structural dynamics of dendritic spines in memory and cognition. *Trends Neurosci*. 2010;33(3):121-129. doi:10.1016/j.tins.2010.01.001

Khacho M, Slack RS. Mitochondrial dynamics in the regulation of neurogenesis: From development to the adult brain. *Dev Dyn*. 2018;247(1):47-53. doi:10.1002/dvdy.24538

Kim T, Rice LM. Long-range, through-lattice coupling improves predictions of microtubule catastrophe. *Mol Biol Cell*. 2019;30(12):1451-1462. doi:10.1091/mbc.E18-10-0641

Klatt S, Smeeton NJ. Visual and Auditory Information During Decision Making in Sport [published online ahead of print, 2019 Dec 28]. *J Sport Exerc Psychol*. 2019;1-11. doi:10.1123/jsep.2019-0107

Kneynsberg A, Combs B, Christensen K, Morfini G, Kanaan NM. Axonal Degeneration in Tauopathies: Disease Relevance and Underlying Mechanisms. *Front Neurosci*. 2017;11:572. Published 2017 Oct 17. doi:10.3389/fnins.2017.00572

Köppen J, Schulze A, Machner L, et al. Amyloid-Beta Peptides Trigger Aggregation of Alpha-Synuclein In Vitro. *Molecules*. 2020;25(3):580. Published 2020 Jan 29. doi:10.3390/molecules25030580

Korobova F, Svitkina T. Molecular architecture of synaptic actin cytoskeleton in hippocampal neurons reveals a mechanism of dendritic spine morphogenesis. *Mol Biol Cell*. 2010;21(1):165-176. doi:10.1091/mbc.e09-07-0596

Kostylev MA, Tuttle MD, Lee S, et al. Liquid and Hydrogel Phases of PrP^{C} Linked to Conformation Shifts and Triggered by Alzheimer's Amyloid-β Oligomers. *Mol Cell*. 2018;72(3):426-443.e12. doi:10.1016/j.molcel.2018.10.009

Kumar Sahel D, Kaira M, Raj K, Sharma S, Singh S. Mitochondrial dysfunctioning and neuroinflammation: Recent highlights on the possible mechanisms involved in Traumatic Brain Injury. *Neurosci Lett*. 2019;710:134347. doi:10.1016/j.neulet.2019.134347

Kurisu K, You J, Zheng Z, Won SJ, Swanson RA, Yenari MA. Cofilin-actin rod formation in experimental stroke is attenuated by therapeutic hypothermia and overexpression of

the inducible 70 kD inducible heat shock protein (Hsp70). *Brain Circ*. 2019;5(4):225-233. Published 2019 Dec 27. doi:10.4103/bc.bc_52_19

Lashuel HA. Do Lewy bodies contain alpha-synuclein fibrils? and Does it matter? A brief history and critical analysis of recent reports. *Neurobiol Dis*. 2020;141:104876. doi:10.1016/j.nbd.2020.104876

Lejri I, Agapouda A, Grimm A, Eckert A. Mitochondria- and Oxidative Stress-Targeting Substances in Cognitive Decline-Related Disorders: From Molecular Mechanisms to Clinical Evidence. *Oxid Med Cell Longev*. 2019;2019:9695412. Published 2019 May 12. doi:10.1155/2019/9695412

Li GB, Zhang HW, Fu RQ, et al. Mitochondrial fission and mitophagy depend on cofilin-mediated actin depolymerization activity at the mitochondrial fission site. *Oncogene*. 2018;37(11):1485-1502. doi:10.1038/s41388-017-0064-4

Linaro D, Ocker GK, Doiron B, Giugliano M. Correlation Transfer by Layer 5 Cortical Neurons Under Recreated Synaptic Inputs *In Vitro*. *J Neurosci*. 2019;39(39):7648-7663. doi:10.1523/JNEUROSCI.3169-18.2019

Loebrich S. The role of F-actin in modulating Clathrin-mediated endocytosis: Lessons from neurons in health and neuropsychiatric disorder. *Commun Integr Biol*. 2014;7:e28740. Published 2014 Apr 3. doi:10.4161/cib.28740

Lutzu S, Castillo PE. Modulation of NMDA Receptors by G-protein-coupled receptors: Role in Synaptic Transmission, Plasticity and Beyond [published online ahead of print, 2020 Feb 24]. *Neuroscience*. 2020;S0306-4522(20)30105-6. doi:10.1016/j.neuroscience.2020.02.019

Maeder CI, Shen K, Hoogenraad CC. Axon and dendritic trafficking. *Curr Opin Neurobiol*. 2014;27:165-170. doi:10.1016/j.conb.2014.03.015

Maloney MT, Minamide LS, Kinley AW, Boyle JA, Bamburg JR. Beta-secretase-cleaved amyloid precursor protein accumulates at actin inclusions induced in neurons by stress or amyloid beta: a feedforward mechanism for Alzheimer's disease [published correction appears in J Neurosci. 2006 Jan 4;26(1):354]. *J Neurosci*. 2005;25(49):11313-11321. doi:10.1523/JNEUROSCI.3711-05.2005

Mancuso M, Calsolaro V, Orsucci D, et al. Mitochondria, cognitive impairment, and Alzheimer's disease. *Int J Alzheimers Dis*. 2009;2009:951548. Published 2009 Jul 6. doi:10.4061/2009/951548

Masliah E, Mallory M, Hansen L, DeTeresa R, Alford M, Terry R. Synaptic and neuritic alterations during the progression of Alzheimer's disease. *Neurosci Lett*. 1994;174(1):67-72. doi:10.1016/0304-3940(94)90121-x

Maung R, Medders KE, Sejbuk NE, Desai MK, Russo R, Kaul M. Genetic knockouts suggest a critical role for HIV co-receptors in models of HIV gp120-induced brain injury. *J Neuroimmune Pharmacol*. 2012;7(2):306-318. doi:10.1007/s11481-011-9328-x

McCann SK, Dusting GJ, Roulston CL. Nox2 knockout delays infarct progression and increases vascular recovery through angiogenesis in mice following ischaemic stroke with reperfusion. *PLoS One*. 2014;9(11):e110602. Published 2014 Nov 6. doi:10.1371/journal.pone.0110602

McGough A, Pope B, Chiu W, Weeds A. Cofilin changes the twist of F-actin: implications for actin filament dynamics and cellular function. *J Cell Biol*. 1997;138(4):771-781. doi:10.1083/jcb.138.4.771

Meberg PJ, Ono S, Minamide LS, Takahashi M, Bamburg JR. Actin depolymerizing factor and cofilin phosphorylation dynamics: response to signals that regulate neurite extension. *Cell Motil Cytoskeleton*. 1998;39(2):172-190. doi:10.1002/(SICI)1097-0169(1998)39:2<172::AID-CM8>3.0.CO;2-8

Meilandt WJ, Ngu H, Gogineni A, et al. Trem2 Deletion Reduces Late-Stage Amyloid Plaque Accumulation, Elevates the Aβ42:Aβ40 Ratio, and Exacerbates Axonal Dystrophy and Dendritic Spine Loss in the PS2APP Alzheimer's Mouse Model. *J Neurosci*. 2020;40(9):1956-1974. doi:10.1523/JNEUROSCI.1871-19.2019

Metzbower SR, Joo Y, Benavides DR, Blanpied TA. Properties of Individual Hippocampal Synapses Influencing NMDA-Receptor Activation by Spontaneous Neurotransmission. *eNeuro*. 2019;6(3):ENEURO.0419-18.2019. Published 2019 May 29. doi:10.1523/ENEURO.0419-18.2019

Mikati MA, Breitsprecher D, Jansen S, Reisler E, Goode BL. Coronin Enhances Actin Filament Severing by Recruiting Cofilin to Filament Sides and Altering F-Actin Conformation. *J Mol Biol*. 2015;427(19):3137-3147. doi:10.1016/j.jmb.2015.08.011

Mikhaylova M, Bär J, van Bommel B, et al. Caldendrin Directly Couples Postsynaptic Calcium Signals to Actin Remodeling in Dendritic Spines. *Neuron*. 2018;97(5):1110-1125.e14. doi:10.1016/j.neuron.2018.01.046

Minamide LS, Striegl AM, Boyle JA, Meberg PJ, Bamburg JR. Neurodegenerative stimuli induce persistent ADF/cofilin-actin rods that disrupt distal neurite function. *Nat Cell Biol*. 2000;2(9):628-636. doi:10.1038/35023579

Minamide LS, Maiti S, Boyle JA, et al. Isolation and characterization of cytoplasmic cofilin-actin rods. *J Biol Chem*. 2010;285(8):5450-5460. doi:10.1074/jbc.M109.063768

Morgan TE, Lockerbie RO, Minamide LS, Browning MD, Bamburg JR. Isolation and characterization of a regulated form of actin depolymerizing factor. *J Cell Biol*. 1993;122(3):623-633. doi:10.1083/jcb.122.3.623

Moretto E, Passafaro M. Recent Findings on AMPA Receptor Recycling. *Front Cell Neurosci*. 2018;12:286. Published 2018 Sep 3. doi:10.3389/fncel.2018.00286

Moriyama K, Iida K, Yahara I. Phosphorylation of Ser-3 of cofilin regulates its essential function on actin. *Genes Cells*. 1996;1(1):73-86. doi:10.1046/j.1365-2443.1996.05005.x

Mouneimne G, DesMarais V, Sidani M, et al. Spatial and temporal control of cofilin activity is required for directional sensing during chemotaxis. *Curr Biol*. 2006;16(22):2193-2205. doi:10.1016/j.cub.2006.09.016

Mufson EJ, Ikonomovic MD, Counts SE, et al. Molecular and cellular pathophysiology of preclinical Alzheimer's disease. *Behav Brain Res*. 2016;311:54-69. doi:10.1016/j.bbr.2016.05.030

Mullan M, Crawford F. The molecular genetics of Alzheimer's disease. *Mol Neurobiol*. 1994;9(1-3):15-22. doi:10.1007/BF02816100

Neddens J, Temmel M, Flunkert S, et al. Phosphorylation of different tau sites during progression of Alzheimer's disease. *Acta Neuropathol Commun*. 2018;6(1):52. Published 2018 Jun 29. doi:10.1186/s40478-018-0557-6

Nisbet RM, Götz J. Amyloid-β and Tau in Alzheimer's Disease: Novel Pathomechanisms and Non-Pharmacological Treatment Strategies. *J Alzheimers Dis*. 2018;64(s1):S517-S527. doi:10.3233/JAD-179907

Niwa R, Nagata-Ohashi K, Takeichi M, Mizuno K, Uemura T. Control of actin reorganization by Slingshot, a family of phosphatases that dephosphorylate ADF/cofilin. *Cell*. 2002;108(2):233-246. doi:10.1016/s0092-8674(01)00638-9

Oldenburg IA, Ding JB. Cholinergic modulation of synaptic integration and dendritic excitability in the striatum. *Curr Opin Neurobiol*. 2011;21(3):425-432. doi:10.1016/j.conb.2011.04.004

Ondrejcak T, Klyubin I, Corbett GT, et al. Cellular Prion Protein Mediates the Disruption of Hippocampal Synaptic Plasticity by Soluble Tau *In Vivo*. *J Neurosci*. 2018;38(50):10595-10606. doi:10.1523/JNEUROSCI.1700-18.2018

Ono S. Functions of actin-interacting protein 1 (AIP1)/WD repeat protein 1 (WDR1) in actin filament dynamics and cytoskeletal regulation. *Biochem Biophys Res Commun*. 2018;506(2):315-322. doi:10.1016/j.bbrc.2017.10.096

Penke B, Szűcs M, Bogár F. Oligomerization and Conformational Change Turn Monomeric β-Amyloid and Tau Proteins Toxic: Their Role in Alzheimer's Pathogenesis. *Molecules*. 2020;25(7):1659. Published 2020 Apr 3. doi:10.3390/molecules25071659

Perry DC, Miller BL. Frontotemporal dementia. *Semin Neurol*. 2013;33(4):336-341. doi:10.1055/s-0033-1359316

Pontrello CG, Sun MY, Lin A, Fiacco TA, DeFea KA, Ethell IM. Cofilin under control of β-arrestin-2 in NMDA-dependent dendritic spine plasticity, long-term depression (LTD), and learning. *Proc Natl Acad Sci U S A*. 2012;109(7):E442-E451. doi:10.1073/pnas.1118803109

Poruchynsky MS, Komlodi-Pasztor E, Trostel S, et al. Microtubule-targeting agents augment the toxicity of DNA-damaging agents by disrupting intracellular trafficking of DNA repair proteins. *Proc Natl Acad Sci U S A*. 2015;112(5):1571-1576. doi:10.1073/pnas.1416418112

Rangaraju V, Lauterbach M, Schuman EM. Spatially Stable Mitochondrial Compartments Fuel Local Translation during Plasticity. *Cell*. 2019;176(1-2):73-84.e15. doi:10.1016/j.cell.2018.12.013

Regen F, Hellmann-Regen J, Costantini E, Reale M. Neuroinflammation and Alzheimer's Disease: Implications for Microglial Activation. *Curr Alzheimer Res*. 2017;14(11):1140-1148. doi:10.2174/1567205014666170203141717

Rodionov VI, Borisy GG. Microtubule treadmilling in vivo. *Science*. 1997;275(5297):215-218. doi:10.1126/science.275.5297.215

Roy P, Perrin BJ. The stable actin core of mechanosensory stereocilia features continuous turnover of actin cross-linkers. *Mol Biol Cell*. 2018;29(15):1856-1865. doi:10.1091/mbc.E18-03-0196

Rust MB. ADF/cofilin: a crucial regulator of synapse physiology and behavior. *Cell Mol Life Sci*. 2015;72(18):3521-3529. doi:10.1007/s00018-015-1941-z

Sala C, Roussignol G, Meldolesi J, Fagni L. Key role of the postsynaptic density scaffold proteins Shank and Homer in the functional architecture of Ca2+ homeostasis at dendritic spines in hippocampal neurons. *J Neurosci*. 2005;25(18):4587-4592. doi:10.1523/JNEUROSCI.4822-04.2005

Saneyoshi T, Matsuno H, Suzuki A, et al. Reciprocal Activation within a Kinase-Effector Complex Underlying Persistence of Structural LTP. *Neuron*. 2019;102(6):1199-1210.e6. doi:10.1016/j.neuron.2019.04.012

Sawada M, Yamaguchi K, Hirano M, et al. Amyloid Formation of α-Synuclein Based on the Solubility- and Supersaturation-Dependent Mechanism. *Langmuir*. 2020;36(17):4671-4681. doi:10.1021/acs.langmuir.0c00426

Schätzle P, Esteves da Silva M, Tas RP, et al. Activity-Dependent Actin Remodeling at the Base of Dendritic Spines Promotes Microtubule Entry. *Curr Biol*. 2018;28(13):2081-2093.e6. doi:10.1016/j.cub.2018.05.004

Schrank BR, Aparicio T, Li Y, et al. Nuclear ARP2/3 drives DNA break clustering for homology-directed repair. *Nature*. 2018;559(7712):61-66. doi:10.1038/s41586-018-0237-5

Schultz H, Sommer T, Peters J. The Role of the Human Entorhinal Cortex in a Representational Account of Memory. *Front Hum Neurosci*. 2015;9:628. Published 2015 Nov 20. doi:10.3389/fnhum.2015.00628

Selkoe DJ, Hardy J. The amyloid hypothesis of Alzheimer's disease at 25 years. *EMBO Mol Med*. 2016;8(6):595-608. Published 2016 Jun 1. doi:10.15252/emmm.201606210

Sengoku R. Aging and Alzheimer's disease pathology. *Neuropathology*. 2020;40(1):22-29. doi:10.1111/neup.12626

Shaw AE, Bamburg JR. Peptide regulation of cofilin activity in the CNS: A novel therapeutic approach for treatment of multiple neurological disorders. *Pharmacol Ther*. 2017;175:17-27. doi:10.1016/j.pharmthera.2017.02.031

Shea YF, Chu LW, Lee SC, Chan AO. The first case series of Chinese patients in Hong Kong with familial Alzheimer's disease compared with those with biomarker-confirmed sporadic late-onset Alzheimer's disease. *Hong Kong Med J*. 2017;23(6):579-585. doi:10.12809/hkmj176845

Shirao T, Hanamura K, Koganezawa N, Ishizuka Y, Yamazaki H, Sekino Y. The role of drebrin in neurons. *J Neurochem*. 2017;141(6):819-834. doi:10.1111/jnc.13988

Shu L, Chen B, Chen B, et al. Brain ischemic insult induces cofilin rod formation leading to synaptic dysfunction in neurons. *J Cereb Blood Flow Metab*. 2019;39(11):2181-2195. doi:10.1177/0271678X18785567

Smith LK, Kuhn TB, Chen J, Bamburg JR. HIV Associated Neurodegenerative Disorders: A New Perspective on the Role of Lipid Rafts in Gp120-Mediated Neurotoxicity. *Curr HIV Res*. 2018;16(4):258-269. doi:10.2174/1570162X16666181003144740

Stuart G, Schiller J, Sakmann B. Action potential initiation and propagation in rat neocortical pyramidal neurons. *J Physiol*. 1997;505 (Pt 3)(Pt 3):617-632. doi:10.1111/j.1469-7793.1997.617ba.x

Sulzer D, Edwards RH. The physiological role of α-synuclein and its relationship to Parkinson's Disease. *J Neurochem*. 2019;150(5):475-486. doi:10.1111/jnc.14810

Svitkina TM, Borisy GG. Arp2/3 complex and actin depolymerizing factor/cofilin in dendritic organization and treadmilling of actin filament array in lamellipodia. *J Cell Biol*. 1999;145(5):1009-1026. doi:10.1083/jcb.145.5.1009

Taylor JM, Moore Z, Minter MR, Crack PJ. Type-I interferon pathway in neuroinflammation and neurodegeneration: focus on Alzheimer's disease. *J Neural Transm (Vienna)*. 2018;125(5):797-807. doi:10.1007/s00702-017-1745-4

Turner PR, O'Connor K, Tate WP, Abraham WC. Roles of amyloid precursor protein and its fragments in regulating neural activity, plasticity and memory. *Prog Neurobiol*. 2003;70(1):1-32. doi:10.1016/s0301-0082(03)00089-3

Van Hoesen GW, Hyman BT, Damasio AR. Entorhinal cortex pathology in Alzheimer's disease. *Hippocampus*. 1991;1(1):1-8. doi:10.1002/hipo.450010102

van Rheenen J, Song X, van Roosmalen W, et al. EGF-induced PIP2 hydrolysis releases and activates cofilin locally in carcinoma cells. *J Cell Biol*. 2007;179(6):1247-1259. doi:10.1083/jcb.200706206

Vázquez de la Torre A, Gay M, Vilaprinyó-Pascual S, et al. Direct Evidence of the Presence of Cross-Linked Aβ Dimers in the Brains of Alzheimer's Disease Patients. *Anal Chem*. 2018;90(7):4552-4560. doi:10.1021/acs.analchem.7b04936

Victoria ECG, de Brito Toscano EC, de Sousa Cardoso AC, et al. Knockdown of C-C Chemokine Receptor 5 (CCR5) is Protective Against Cerebral Ischemia and Reperfusion Injury. *Curr Neurovasc Res*. 2017;14(2):125-131. doi:10.2174/1567202614666170313113056

Visanji NP, Lang AE, Kovacs GG. Beyond the synucleinopathies: alpha synuclein as a driving force in neurodegenerative comorbidities. *Transl Neurodegener*. 2019;8:28. Published 2019 Sep 4. doi:10.1186/s40035-019-0172-x

von Bartheld CS, Bahney J, Herculano-Houzel S. The search for true numbers of neurons and glial cells in the human brain: A review of 150 years of cell counting. *J Comp Neurol*. 2016;524(18):3865-3895. doi:10.1002/cne.24040

Walker L, Stefanis L, Attems J. Clinical and neuropathological differences between Parkinson's disease, Parkinson's disease dementia and dementia with Lewy bodies - current issues and future directions. *J Neurochem*. 2019;150(5):467-474. doi:10.1111/jnc.14698

Walsh KP, Minamide LS, Kane SJ, et al. Amyloid-β and proinflammatory cytokines utilize a prion protein-dependent pathway to activate NADPH oxidase and induce cofilin-actin rods in hippocampal neurons. *PLoS One*. 2014;9(4):e95995. Published 2014 Apr 23. doi:10.1371/journal.pone.0095995

Wang Q, Chen M, Schafer NP, et al. Assemblies of calcium/calmodulin-dependent kinase II with actin and their dynamic regulation by calmodulin in dendritic spines. *Proc Natl Acad Sci U S A*. 2019;116(38):18937-18942. doi:10.1073/pnas.1911452116

Wang X, Huang T, Bu G, Xu H. Dysregulation of protein trafficking in neurodegeneration. *Mol Neurodegener*. 2014;9:31. Published 2014 Aug 25. doi:10.1186/1750-1326-9-31

Wang Y, Shi M, Chung KA, et al. Phosphorylated α-synuclein in Parkinson's disease. *Sci Transl Med*. 2012;4(121):121ra20. doi:10.1126/scitranslmed.3002566

Watanabe H, Bagarinao E, Yokoi T, et al. Tau Accumulation and Network Breakdown in Alzheimer's Disease. *Adv Exp Med Biol*. 2019;1184:231-240. doi:10.1007/978-981-32-9358-8_19

Won SJ, Minnella AM, Wu L, et al. Cofilin-actin rod formation in neuronal processes after brain ischemia. *PLoS One*. 2018;13(10):e0198709. Published 2018 Oct 16. doi:10.1371/journal.pone.0198709

Woo JA, Zhao X, Khan H, et al. Slingshot-Cofilin activation mediates mitochondrial and synaptic dysfunction via Aβ ligation to β1-integrin conformers. *Cell Death Differ*. 2015A;22(6):1069-1070. doi:10.1038/cdd.2015.41

Woo JA, Boggess T, Uhlar C, et al. RanBP9 at the intersection between cofilin and Aβ pathologies: rescue of neurodegenerative changes by RanBP9 reduction. *Cell Death Dis*. 2015B;6(3):1676. Published 2015 Mar 5. doi:10.1038/cddis.2015.37

Woo JA, Liu T, Fang CC, et al. Activated cofilin exacerbates tau pathology by impairing tau-mediated microtubule dynamics. *Commun Biol*. 2019;2:112. Published 2019 Mar 22. doi:10.1038/s42003-019-0359-9

Woolfrey KM, O'Leary H, Goodell DJ, et al. CaMKII regulates the depalmitoylation and synaptic removal of the scaffold protein AKAP79/150 to mediate structural long-term depression. *J Biol Chem*. 2018;293(5):1551-1567. doi:10.1074/jbc.M117.813808

Xia D, Li C, Götz J. Pseudophosphorylation of Tau at distinct epitopes or the presence of the P301L mutation targets the microtubule-associated protein Tau to dendritic spines. *Biochim Biophys Acta*. 2015;1852(5):913-924. doi:10.1016/j.bbadis.2014.12.017

Xiong Y, Mahmood A, Chopp M. Current understanding of neuroinflammation after traumatic brain injury and cell-based therapeutic opportunities. *Chin J Traumatol*. 2018;21(3):137-151. doi:10.1016/j.cjtee.2018.02.003

Xu W, Tan L, Yu JT. Link between the SNCA gene and parkinsonism. *Neurobiol Aging*. 2015;36(3):1505-1518. doi:10.1016/j.neurobiolaging.2014.10.042

Yang N, Higuchi O, Ohashi K, et al. Cofilin phosphorylation by LIM-kinase 1 and its role in Rac-mediated actin reorganization. *Nature*. 1998;393(6687):809-812. doi:10.1038/31735

Yonezawa N, Nishida E, Iida K, Yahara I, Sakai H. Inhibition of the interactions of cofilin, destrin, and deoxyribonuclease I with actin by phosphoinositides. *J Biol Chem*. 1990;265(15):8382-8386.

Yoshihara Y, De Roo M, Muller D. Dendritic spine formation and stabilization. *Curr Opin Neurobiol*. 2009;19(2):146-153. doi:10.1016/j.conb.2009.05.013

Zhang H, Ramsey A, Xiao Y, et al. Dynamic Phosphorylation and Dephosphorylation of Cyclase-Associated Protein 1 by Antagonistic Signaling through Cyclin-Dependent Kinase 5 and cAMP Are Critical for the Protein Functions in Actin Filament Disassembly and Cell Adhesion. *Mol Cell Biol*. 2020;40(4):e00282-19. Published 2020 Jan 30. doi:10.1128/MCB.00282-19

Zheng B, Han M, Bernier M, Wen JK. Nuclear actin and actin-binding proteins in the regulation of transcription and gene expression. *FEBS J*. 2009;276(10):2669-2685. doi:10.1111/j.1742-4658.2009.06986.x

Zhong Z, Grasso L, Sibilla C, Stevens TJ, Barry N, Bertolotti A. Prion-like protein aggregates exploit the RHO GTPase to cofilin-1 signaling pathway to enter cells. *EMBO J*. 2018;37(6):e97822. doi:10.15252/embj.201797822

Zhou L, McInnes J, Wierda K, et al. Tau association with synaptic vesicles causes presynaptic dysfunction. *Nat Commun*. 2017;8:15295. Published 2017 May 11. doi:10.1038/ncomms15295

CHAPTER 2

MODIFIED ROLLER TUBE METHOD FOR PRECISELY LOCALIZED AND REPETITIVE INTERMITTENT IMAGING DURING LONG-TERM CULTURE OF BRAIN SLICES IN AN ENCLOSED SYSTEM[1]

Preface

The first three authors contributed equally to this work. I joined this project after Ben Fixman had developed the method for adhering the coverslip to the roller tube. My contributions led to many of the images used in the final manuscript, especially the use of the NeuO for neuronal viability studies and preparation and use of lentiviral vectors for expressing the rod reporter. Although publication of this article preceded the start of my BS/MS degree program, many of the following chapters utilize methods that are described in detail in this chapter and thus it is included to give a complete picture of my research experience.

Summary:

Cultured rodent brain slices are useful for studying the cellular and molecular behavior of neurons and glia in an environment that maintains many of their normal *in vivo* interactions. Slices obtained from a variety of transgenic mouse lines or use of viral

[1]Fixman, BB, Babcock IW, Minamide LS, Shaw AE, Oliveira da Silva MI, Runyan AM, Maloney MT, Field JJ, Bamburg JR. (2017) Modified roller tube method for precisely localized and repetitive intermittent imaging during long-term culture of brain slices in an enclosed system. *JoVE* e56436 (2017) doi:10.3791/56436

vectors for expression of fluorescently tagged proteins or reporters in wild type brain slices allow for high-resolution imaging by fluorescence microscopy. Although several methods have been developed for imaging brain slices, combining slice culture with the ability to perform repetitive high-resolution imaging of specific cells in live slices over long time periods has posed problems. This is especially true when viral vectors are used for expression of exogenous proteins since this is best done in a closed system to protect users and prevent cross contamination. Simple modifications made to the roller tube brain slice culture method that allow for repetitive high-resolution imaging of slices over many weeks in an enclosed system are reported. Culturing slices on photoetched coverslips permits the use of fiducial marks to rapidly and precisely reposition the stage to image the identical field over time before and after different treatments. Examples are shown for the use of this method combined with specific neuronal staining and expression to observe changes in hippocampal slice architecture, viral-mediated neuronal expression of fluorescent proteins, and the development of cofilin pathology, which was previously observed in the hippocampus of Alzheimer's disease (AD) in response to slice treatment with oligomers of amyloid-β (Aβ) peptide.

Introduction

Primary culture of dissociated neurons from regions of rodent brain is an important tool used by researchers to observe responses to pathologically implicated stimuli. However, such studies have the disadvantage of looking at neurons in only 2D and without their glial support system. Furthermore, unless grown under conditions of very high density (640 neurons/mm^2 or about 16% of surface area) in which it becomes

impossible to follow the random outgrowth of a dendrite or axon for more than a short distance from its cell body, hippocampal neuronal viability over 4 weeks declines significantly (Brewer et al., 1993), limiting the use of dissociated cultures for extended studies of age-related pathologies. The culturing of slices prepared from rodent brain is an attractive option that overcomes these limitations by maintaining an organized cell architecture and viability for weeks or months. Conditions for maintaining many different regions of rodent brain in slice culture have been described (Humpel, 2015).

Two major methods are widely used for long-term culture of brain slices: culturing on membranes at the air-liquid interface (Stoppini et al., 1991) or culturing on coverslips in sealed tubes allowed to rotate in a roller incubator to provide aeration (Gähwiler, 1981). Slices cultured on membranes can be directly imaged with high-resolution fluorescence microscopy using an upright microscope and water immersion objectives (Gogolla et al., 2006). Alternatively, slices cultured on membranes have been transferred to glass bottom dishes to achieve good resolution of dendritic spines using an inverted microscope (De Roo and Ribic, 2017). However, both methods of imaging slices grown on membranes are open systems that require medium changes and often use antifungal and/or antibiotics to prevent or reduce contamination (Gogolla et al., 2006; De Roo and Ribic, 2017). Slices on a membrane at the air-medium interface maintain excellent morphology and survival, but returning to precise locations during repetitive imaging at high magnification is extremely difficult unless the experiment is following only small groups of cells expressing a fluorescent marker. Although slices grown on membranes have been used with viral-mediated expression of transgenes (Gogolla et al., 2006; De Roo and Ribic, 2017), biosafety protocols may require an enclosed culture system be employed

for certain viral vectors that are used for expressing fluorescently tagged proteins and reporters of cell physiology. Furthermore, immersion objectives require decontamination between samples that will be followed in culture (Gogolla et al., 2006). One major application of membrane interface cultures is combining high-resolution imaging with electrophysiology at single time points (Lee et al., 2016). The roller tube method with coverslips inside the plastic tube does not permit any electrophysiology or high-resolution imaging without removing the coverslip. Thus, this method has been most often applied to long-term studies in which post-fixation observations have been made (Davis et al., 2009).

Described here is a method that utilizes the roller tube culture technique but on drilled-out tubes with slices on coverslips that can be imaged repetitively for as long as the cultures are maintained. The enclosed system requires no medium change for imaging and utilizes photoetched coverslips to provide fiducial marks that allow imaging at high magnification, after days or weeks, the precise fields previously imaged. We apply this method to examine changes in the rodent hippocampus, a major brain region involved in memory and learning. The rodent hippocampus is often studied as a model for pathological or age-related changes observed during development of cognitive impairment (Clark and Squire, 2013), such as those that occur in AD. Our method is particularly well suited to study pathological changes that develop within a single slice over time in response to environmental changes, such as increases in Aβ peptides, which is characteristic of AD (Davis et al., 2009). One pathology associated with human and rodent AD brain is the presence of cofilin-actin aggregates and rods, the latter containing bundles of filaments in which cofilin and actin are in a 1:1 molar ratio (Minamide et al.,

2000; Rahman et al., 2014; Bamburg and Bernstein, 2016). Rods have been observed in fixed slices of rat hippocampus following Aβ treatment, as well as within a live rodent brain slice expressing cofilin-GFP subjected to hypoxia (Davis et al., 2009), and they may contribute to the synaptic dysfunction seen in AD and stroke. Here we use this new culturing method to observe the time course and distribution within slices of expressed exogenous chimeric fluorescent proteins introduced by different viruses. We then utilize the neuronal specific expression of a cofilin reporter construct to follow the development of cofilin rod and aggregate pathology in hippocampal slices in response to treatment with soluble Aβ oligomers ($A\beta_o$).

Methods

Animal Protocols: Animal use follows approved breeding and animal use protocols (IACUC approved protocol #17-7411A) that conform to the Animal Care and Use Guidelines of Colorado State University.

NOTE: The protocol below describes the preparation and culture method for the long-term incubation and intermittent imaging of hippocampal slices. A single hippocampal slice is attached to a specially prepared photoetched coverslip using a plasma clot, and then the coverslips are sealed onto the flat side of a drilled-out roller tube, which is maintained in a roller incubator. Plasma clots are dissolved with plasmin before viral infection for fluorescent protein expression and high-resolution imaging. A fluorescent neuronal vital dye is used to image neurons within slices. Modifications to this method as well as development of other methods used in this thesis are described in Chapter 3.

Preparation of Roller Tube Rack: The template shown in Figure 2.1A is printed to the size shown on the scale bar. With a nail, punch small holes (large enough for a fine point marker) in the template centered on the holes. Set the template on the bottom of a 15 cm tissue culture dish (nominal diameter of 14 cm) and mark the position of the holes.

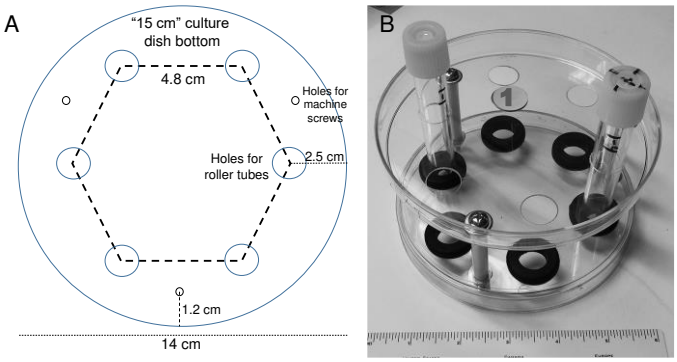

Figure 2.1. Preparation of roller tube rack. A) Template for marking hole positions for drilling out the 15 cm tissue culture dish bottoms. If the figure is printed to the size of the scale bar shown, it can be cut out and used for marking the positions on a 15 cm culture dish for drilling the holes shown. B) Completed roller tube rack with two tubes inserted. Each rack is numbered on a sticker easily visible on the top of the rack.

Repeat this on a second dish. With drill bits designed for use on plastic, drill six 1.5 cm diameter holes on each dish in a hexagonal array (4.8 cm center-to-center) with hole centers 2.5 cm from the edge of the dish. Drill three holes (3 mm in diameter) 12 mm from the edge that are placed equidistantly between two of the larger holes as shown in Figure 1A. To assemble to roller tube holder, face the bottoms of each dish towards each other and place a 2.5 inch long machine screw (3/16 inch diameter) with a flat washer through one of the small holes followed by a second flat washer, a piece of polyethylene tubing (spacer, 4.7 cm), another flat washer, the second tissue culture dish, another flat washer, a locking washer, and a nut. Repeat with the other two machine screws, and tightening only loosely until all three machine screws are in place. Then tighten the nuts securely. Work the grommets (5/16 inch thick, 5/8 inch hole diameter) into the holes of the bottom

dish to obtain the final roller tube rack (Figure 2.1B; shown with two tubes in place). Place a sticker with a unique number on each rack.

Preparation of Roller Tubes: To facilitate making many tubes that have the coverslip in the same position, we first made a jig for drilling the hole in roller tubes. Drill a 1.5 cm hole 8 cm deep in the center **side** of a 2 x 4 x 5.5 inch wooden block at an angle such that the flat side of the roller tube will be nearly parallel with the block face when inserted (Figure 2.2A). Enlarge the hole using a round wood file to both widen and taper the hole to allow tube insertion (roller tubes are slightly larger in diameter near the cap end) (Figure 2.2B).

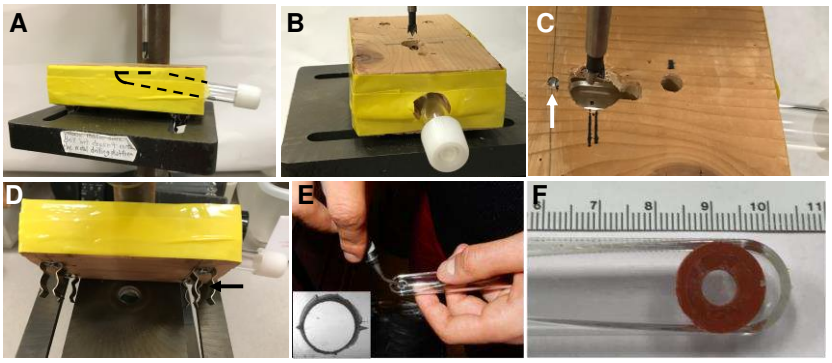

Figure 2.2. Preparation of the roller culture tubes. A) Front view of roller tube inserted in a jig on a drill press for drilling out the 6 mm hole in the tube. Dashed line shows position of the flat sided roller tube in the jig. B) End view of jig with tube inserted and drill bit aligned over hole. C) Top view of hole in jig for drilling out roller tubes with 6 mm drill bit. White arrow shows position of cut-off nail inserted as a stop for positioning tubes and black double lines are for bit alignment. D) Spring clips (black arrow) installed on bottom of jig to securely hold it in position when drilling tubes. E) After drilling out hole, edges are smoothed with a deburring tool and grooves are cut on the inner side of the hole (inset shows hole viewed through a dissection microscope) to enhance medium draining from the hole during tube rotation F) Culture tube with hole aligned to one in the silicone rubber adhesive to which the coverslip will be attached.

Drill a 1.5 cm diameter vertical hole, 5.5 cm from the side of the block, and centered over the side hole (Figure 2C). When the side hole is tapered enough, insert a roller tube that is marked at the desired spot to center the hole for the slice and position the tube so the marked spot is centered in the 1.5 cm vertical hole. Remove the tube and measure the distance from the spot to the end of the tube. Mark this distance from the center of

the hole in the jig and insert a nail to provide a stop to correctly position the tube for drilling (arrow in Figure 2.2C). Use a hacksaw to cut the nail off flush with the surface of the wood block to prevent injury. Add spring clips on the bottom of the jig if there is a drill press with slots that allow it to be anchored (Figure 2.2D black arrow). Otherwise, use C-clamps to hold the jig securely onto the drill press.

Using the jig described above to hold and position a flat sided 11 cm plastic culture tube with the flat side up (Figure 2.2A), drill a 6 mm diameter hole with the center 1.0 cm from the bottom and centered between the sides of the tube. A drill bit designed for plastic should be used. With a swiveling deburring tool, smooth the edges of the hole (Figure 2.2E) and make 4 grooves on the inside edge of the hole (Figure 2.2E, inset) to facilitate draining of the hole during tube rotation. Prepare double-sided adhesive silicone rubber Secure Seal discs, 12 mm diameter with a 6 mm central hole. Precut discs are available by special order. Otherwise, discs can be prepared using a 12 mm hole punch from sheets of non-toxic double-sided adhesive Secure Seal®, after which the center hole can be punched with a standard one-hole paper punch (6 mm diameter). Rinse the drilled tubes with 70% ethanol, air dry them in a biological safety cabinet, and sterilize the tubes and the adhesive discs for 40 min under the UV lamp (30 W at 70 cm average distance) in the biological safety cabinet. **Caution:** To avoid UV exposure, wear eye protection and close the cabinet before turning on the UV lamp. Reposition the tubes and discs after 20 min so that all exposed surfaces are sterilized. Under sterile conditions, peel off the white backing from an adhesive disc and affix the silicone rubber to the outside of a tube, aligning the holes (Figure 2.2F).

Preparation of coverslips: Clean 12 mm diameter photoetched (10x10 mm array of center numbered squares) German glass coverslips. Hold the coverslip gently with forceps and dip in absolute ethanol, followed by water, followed by absolute ethanol again, and finally pass the coverslip through a flame to burn off the ethanol. Allow coverslips to cool. Holding the coverslip with forceps, dip into 2% 3-aminopropyltri-ethoxysilane in acetone for 10 s. Rinse the coverslips with ultrapure water and allow to air dry. Set the coverslips on sterile filter paper inside of a biological safety cabinet and turn on the UV light. Expose each side of the coverslips for 20 min.

Preparation of Hippocampal Slices: Before starting the dissection, prepare halves of double-edged razor blades for the tissue chopper. Fold the blades lengthwise carefully with fingers and snap in half. Rinse the blade halves with acetone using a cotton swab to clean them, followed by rinsing in absolute ethanol and air drying. Before mounting a half blade on the tissue chopper, sterilize it by rinsing with 70% ethanol.

Following protocols approved by the institutional Animal Care and Use Committee, euthanize a 4-7 day old mouse or rat pup and remove the head with scissors or guillotine. NOTE: The brain slice culture protocol is independent of mouse or rat strain or genotype. Many transgenic mouse lines with different genetic backgrounds have been used. Rinse the head with 70% ethanol, and place it in a 60 mm Petri dish. Until the final mounting of the brain slice onto the roller tube, all of the following steps are performed in a laminar flow hood to maintain sterility.

Using a #21 surgical blade, make a sagittal cut through the skin and skull. With a #5 Dumont forceps, peel back the skin and skull to expose the brain. With closed forceps, gently tease out the whole brain, releasing it by pinching with the forceps through the

brain stem behind the cerebellum. Place the brain in a sterile 60 mm dish containing 4 °C Gey's Balanced Salt Solution/0.5% glucose (GBSS/glucose).

Using a dissection microscope to visualize the brain (Figure 2.3A), place the brain dorsal side up and cut off the front third of the brain and the cerebellum with a surgical blade (Figure 2.3B). With forceps, hold the trimmed brain posterior side up and ventral side against the side of the Petri dish for stability. Gently tease away meninges around the sagittal midline and remove the midbrain tissue using a fine tipped Dumont #5 forceps (Figure 2.3C, dashed circle). Make two cuts along the side of the brain to spread it open (Figure 2.3C, dashed lines). Once the brain is placed dorsal side down and spread open, the hippocampal fissure should be visible (Figure 2.3D, arrow). Transfer the spread open brain to a piece of polychlorotrifluoroethylene (Aclar®) plastic film and position it for slicing on the stage of a McIlwaine tissue chopper. Wet the blade with GBSS/glucose and chop the hippocampus into ~250 µm thick slices. With a transfer pipette, flush the sliced brain off the plastic film into a fresh 60 mm dish containing GBSS/glucose (Figure 2.3E). Gently pinch off and tease away, with fine tipped forceps, the remaining meninges and other non-hippocampal tissue (Figure 2.3F) from the slices (Figure 2.3G, H).

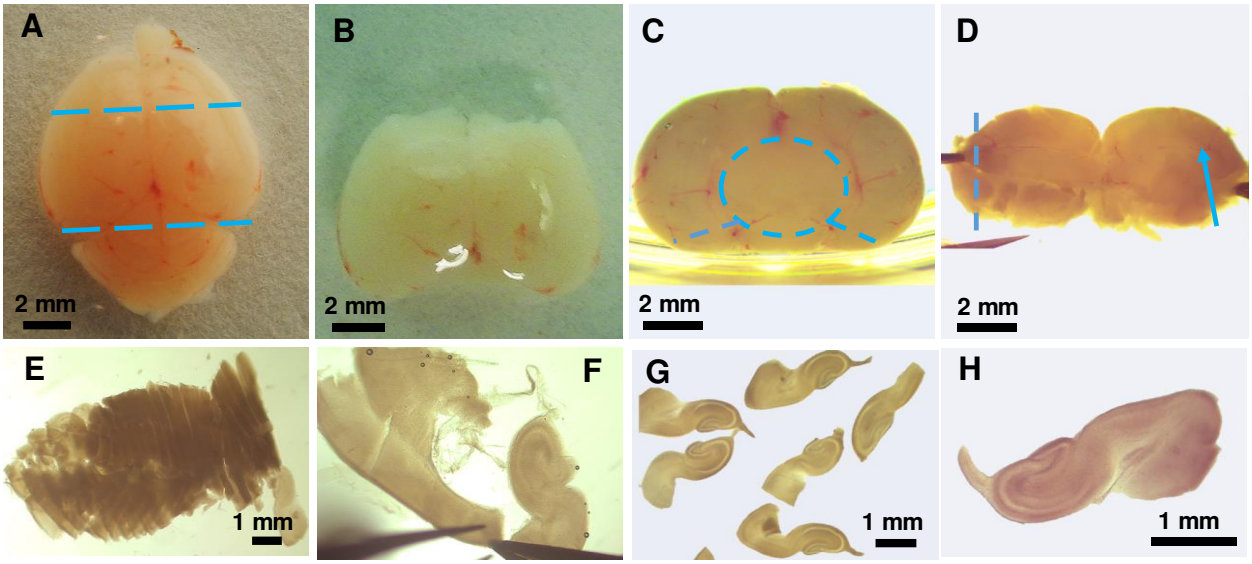

Figure 2.3. Preparation of hippocampal brain slices. Photos taken with a dissection microscope showing: A) Intact mouse brain. Position of cuts to remove forebrain and cerebellum are shown as blue dashed lines. B) After removal of forebrain and cerebellum; C) Piece of brain in B is flipped 90° with posterior region (toward the cerebellum) facing up. Positioning the piece next to the side of the dish helps with the removal of the midbrain (blue dashed circle) which can be teased away from the remaining hippocampus, thalamus and hypothalamus. Two cuts with the forceps (blue dashed lines) allow the remaining piece containing the hippocampus from both hemispheres to be spread flat. D) The flattened brain piece showing the blood vessel running along hippocampal fissure (blue arrow). This tissue is placed on plastic film and transferred to the tissue chopper for slicing in the direction of the dashed line. E) Sliced tissue showing slightly more than half the hippocampus after being returned to GBSS/glucose. F) Final dissection of the hippocampus and cleaning of the slices to remove non-hippocampal material. G) Several floating slices after final clean-up. H) Enlarged photo of a single slice for transfer to coverslip.

Plating Slices: Once slices have been obtained, place 2 µL of chicken plasma on the center of the photoetched side of a prepared coverslip. Spread the plasma slightly to achieve a 3-4 mm diameter spot. NOTE: The photoetched side is the top side of the coverslip when viewed through a dissection microscope such that the numbers are correctly oriented. Transfer 1 brain slice with a sterile narrow-tip spatula (Figure 2.4A) to the plasma spot (Figure 2.4B). Use closed forceps to keep the slice on the spatula tip while lifting the slice from the GBSS/glucose. Touch the spatula to the plasma spot on the

coverslip, and with closed forceps, push the slice onto the coverslip. Mix 2.5 µL of plasma with 2.5 µL of thrombin in a separate tube. Quickly place 2.5 µL of this mixture over and around the slice and pipet up and down gently to mix it (Figure 2.4B). NOTE: The plasma will clot within 10-15 s, so this must be done quickly. If slice adhesion is a problem, mix 5 µL plasma with 5 µL thrombin and use 4-5 µL on the slice, removing some after mixing so that the slice lies flat on the coverslip. Remove the clear plastic covering from the exposed side of the silicone rubber adhesive previously affixed to a roller tube and place the coverslip with the brain slice onto the adhesive aligning the slice within the hole (Figure 2.4C). To ensure adhesion, apply soft, even pressure to the coverslip with your thumb by pressing the coverslip down evenly and holding it for about 1 min while transferring the tube to a biological safety cabinet. In a biological safety cabinet, add 0.8 mL of complete Neurobasal A culture medium (Table of Materials) to each tube (Figure 2.4D). Flow a 5% CO_2/95% air mixture through a sterile cotton-plugged Pasteur pipette held securely by a clamp. Flush the roller tube with the gas mixture and rapidly cap the tube as it is withdrawn from around the pipette. Label the tubes with the slice number and rack number. Insert tubes into a roller rack, ensuring they are geometrically balanced. If there is an odd number of tubes, add blank tubes to balance. Place the racks in a 35 °C roller incubator set for a rotation rate of about 10-13 RPH (about 5-6 min per revolution) (Figure 2.4E). To keep the medium in the bottom of the tubes, tilt the roller incubator back approximately 5° by raising its front on a board. Enter the slice and tube number onto a spreadsheet, which is used to record all information of slice treatments and observation dates.

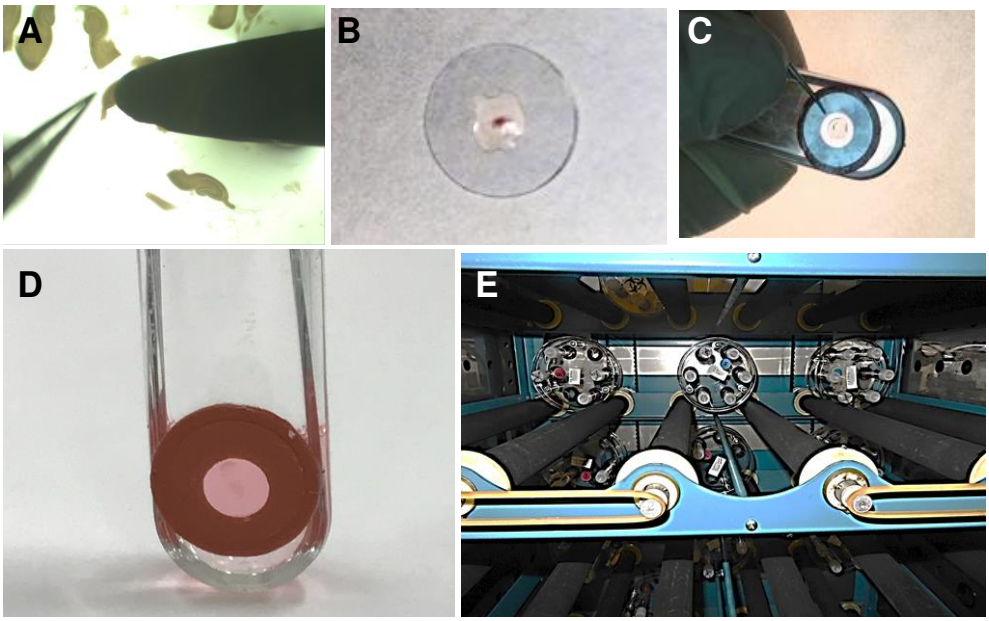

Figure 2.4. Plating slices. A) A mouse hippocampal slice is removed from the culture dish on the tip of spatula using the tip of forceps to help lift it free of solution. B) The slice is placed flat in the center of a photoetched and treated 12 mm coverslip on 2 µL of chick plasma and another 2.5 µL of a 1:1 plasma/thrombin mixture is added to generate a clot. C) After the clot is set (about 1-2 min), the covering is removed from the silicone rubber adhesive circle on a roller tube and the coverslip is positioned with the clot centered into the hole and then the coverslip is pressed in place with a thumb. Hold in position form about 1 min. D) Add 0.8 ml of complete culture medium. E) Roller tube holders inside of large roller incubator with front raised to tilt 5º to keep medium at the bottom of the tubes.

Slice maintenance: Slice medium is changed every 3 days with complete Neurobasal A medium. At approximately day 6 in culture (6 DIV), add 1 µL (0.002 U) of active plasmin to each tube to remove the thrombin clot. After the clots dissolve completely (usually within a few hours), remove the medium and replace with fresh medium without plasmin. If necessary, slices can be incubated with plasmin overnight and the medium changed the next day. Slices are usually incubated for at least 7-10 days before use in experiments with medium aspirated and replaced at 3 day intervals and tubes flushed with 5% CO_2/95% air before replacing in roller incubator.

Use of Viral Vectors for Transgene Expression: NOTE: Expression of transgenes in neurons of slice cultures is achieved either by using brains from genetically engineered

rodents or by introducing the transgene by infection with recombinant replication deficient viruses. Adenoviruses (AV), adeno-associated viruses (AAV), and recombinant lentivirus vectors have all been used in our hippocampal slice cultures for expression of different fluorescent protein chimeras in brain slices.

Prepare replication deficient AV for expressing the RNA of interest according to methods described elsewhere (He et al., 1998; Minamide et al., 2003). Titer the viruses for infectious U/mL by the serial dilution method using an antibody to a virally expressed protein as described (Minamide et al., 2003). To observe cofilin aggregates and cofilin-actin rod formation, utilize the cofilin-R21Q-mRFP cDNA (plasmid #51279) (Mi et al., 2013). NOTE: The synapsin 1 promoter is an excellent choice for neuronal specific expression in slices (Kügler et al., 2003), whereas the cytomegalovirus promoter is useful for driving high expression levels in many cell types (He et al., 1998).

Prepare AAV by co-transfection of transfer plasmid containing the gene of interest and a rep/cap plasmid, with or without a helper plasmid, into HEK293 packaging cells, which supply the viral E1 gene, as previously described (Wang et al., 2011; Matsushita et al., 1998). NOTE: Recombinant AAV can also be made for targeted insertion into the host cell genome (Ward and Walsh, 2012). For the transfer plasmid, we use human cofilin 1 with a C-terminal mRFP1 fluorescence protein tag (plasmid #50856) cloned into a synapsin promoter-containing AAV plasmid downstream from the calcium sensor GCaMP5 (Akerboom et al., 2012). A piece of DNA encoding the P2A self-cleaving peptide sequence is inserted by PCR between GCaMP5G and cofilin-RFP during the preparation of the transfer plasmid to provide expression of both proteins from a single AAV transcript (Kim et al, 2011).

Prepare recombinant lentivirus vectors by co-transfection of transfer plasmid containing the gene or cDNA of interest and integration signals, along with a third-generation lentivirus packaging mixture that divides the viral gag, pol, rev, and vsv-g genes onto three separate plasmids (Benskey et al., 2016; Huang and Chen, 2010). For the transfer plasmid, use a single step cloning system (Bordat et al., 2015) to assemble the synapsin promoter and cofilin-R21Q-mRFP cDNA (from plasmid #51279) into pLKO.1-GFP (plasmid #30323), with the synapsin promoter and cofilin-R21Q-mRFP replacing the hPGK promoter and GFP cDNA, respectively. Transfect the final plasmid into HEK293T cells by calcium phosphate as previously described (Huang and Chen, 2010). Collect medium from four 10 cm dishes, concentrate to 500 µL using 150K-cutoff centrifugal concentrators, and store the final lentivirus at -80°C in small aliquots after quick freezing in liquid nitrogen. Thaw an aliquot only once for infecting cells.

The volume of each virus type prepared above to achieve the degree of expression desired is determined by setting up a number of different slice cultures to follow the expression of the transgenes after infection with various volumes of virus. Typically, 1-10 µL of virus is used per slice.

Slice Treatments: To infect the slices with virus work in a biological safety cabinet approved for virus work at the biological safety level appropriate for the vector. Mix an aliquot of the virus (usually 1-10 µL) with 0.8 mL of complete medium. Aspirate the medium from the slice using a sterile Pasteur pipette into a collection trap containing bleach. A secondary trap is always used between the first trap and the vacuum source. Replace this medium with the virus-containing aliquot prepared above, return the culture tubes to a rack, and place in the incubator. After 2-5 days of incubating the slices with

virus, work in a biological safety cabinet to remove the virus-containing medium with a sterile transfer pipette and place it into a bottle containing an approved antiviral agent to kill virus.

Staining of neurons with vital dye: Prepare and store aliquots of NeuO, a neuronal specific fluorescent vital dye (Er et al., 2015), by quick freezing 4 µL of aliquots in liquid nitrogen at a concentration of 100 µM and store these at -20 °C. Do not freeze/thaw the dye more than once. To label neurons for visualization by fluorescence microscopy, thaw one aliquot of the neuronal vital dye and dilute to 4 mL in complete Neurobasal medium (final dye concentration is 100 nM). Remove the medium from slices by aspiration (or with a transfer pipette if the medium contains virus) and replace it with 0.8 mL of the medium containing 100 nM neuronal vital dye. Return the slices to the roller apparatus in the incubator. After incubating the slices for 2 h, aspirate the dye-containing medium and replace it with 0.8 mL of fresh complete medium working in a biological safety cabinet. NOTE: Labeling of neurons in slices with vital dye requires several hours of incubation. The first images are usually taken 24 h after dye treatment. Although neurons are specifically labeled, there is background fluorescence that declines over 2-3 days to give better neuronal imaging. Intensity of the vital dye declines after 72 h. To follow changes in slice morphology and neuronal viability over time, relabel the slices every 7 days.

Slice Imaging by Fluorescence Microscopy: View slices on an inverted microscope. For brightest fluorescence imaging, exchange culture medium 24 h before imaging with complete Neurobasal A medium without the Phenol Red pH indicator.

NOTE: For experiments reported here, slices are viewed on an inverted spinning disc confocal fluorescence microscope equipped with a linear encoded x, y stage with piezo z control and a sensitive high-resolution digital camera.

Transfer the tube with the slice culture to be imaged from the roller tube apparatus to the custom-made tube holder (Figure 2.5A), which is placed in the stage adapter (Figure 2.5B), to keep the coverslip perpendicular to the objective and maintain the slice in the same orientation during repetitive imaging sessions over long intervals. Push the slider on the stage adapter tight against the tube to hold the tube in position (Figure 2.5B). Maintain slice temperature at 35 °C during imaging by use of heating strips and a thermoregulatory controller built into the custom-made stage adapter (Figure 2.5C).

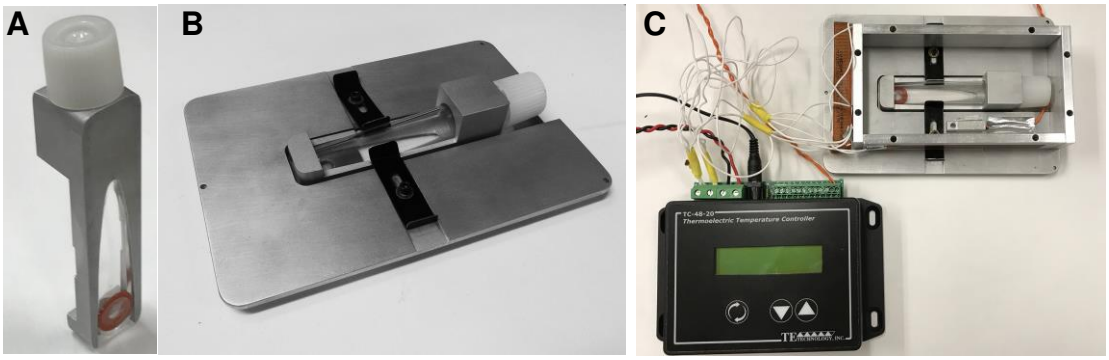

Figure 2.5. Tube holder and imaging stage adapter. A) Tube holder that positions the tube such that the coverslip is maintained in position for imaging. (B) Tube holder mounted in a microscope stage adapter plate. Sliders on side hold tube securely for imaging. (C) Stage adapter with tube holder and side panels added containing heating strips connected to a thermoelectric temperature controller. Once tubes are mounted and positioned, a solid top to the box can be added to help hold temperature during imaging. Orange wire is thermocouple lead. Plans for the design and building of the stage adapter and heater are available at: https://vpr.colostate.edu/min/custom-machining/roller-tube-holder/

Using a low power (e.g. 4X) objective and bright field transillumination, focus on the photoetched grid pattern (Figure 2.6A) under the slice. For the initial imaging session, quickly scan around the slice to locate and record the grid number for the various regions in which higher magnification imaging is desired (*e.g.*, cornu ammonis (CA)1, CA3,

dentate gyrus (DG), *etc.*). Move the stage to the first grid square containing a region of interest. Switch to the 20X air objective and locate a fiducial mark (*e.g.*, tip of an etched number) (Figure 2.6B). Switch to a higher power objective (40X or 60X), localize the fiducial mark, and then record the x and y position of the stage. Move the stage to find the field(s) of interest nearby and record their x and y offsets from the fiducial mark (Figure 2.6B, arrow). Repeat in other grid areas if desired. NOTE: These off-set positions from the fiducial mark allow consistent pinpointing of the same coverslip location when the slice is reimaged, even though the original x, y setting of the fiducial mark changes when the tube or stage adapter are removed and replaced.

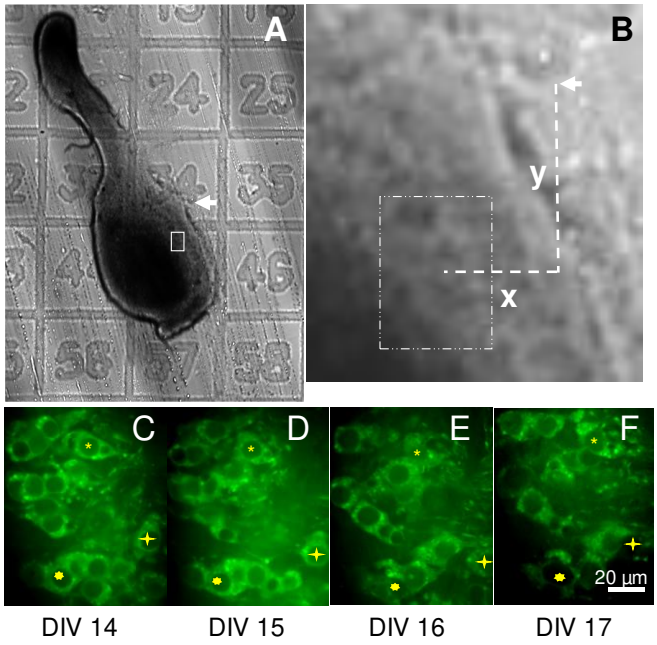

Figure 2.6. A) Hippocampal slice on photoetched coverslip (1 mm squares) with subiculum unfolded (tail) viewed with 4x objective and bright field illumination. Curvature of plastic roller tube helps create an oblique illumination that enhances the visualization of the grid. The box shows the position and size of a 60x field. B) A view of the same slice with a 20x objective for finding the fiducial mark as the tip of the bottom of the 4 from square 34. The y and x offsets are shown to reproducibly locate the center of the desired box for higher magnification confocal imaging. C-F) A slice labeled with neuronal vital dye 13 DIV was imaged using a 60x objective and making a 30 µm projection image on 4 consecutive days (14-17 DIV). Identical neurons were imaged each day. The position of the nucleus in each of three neurons is marked with a different symbol. They are more easily identified by scrolling through image stacks as their 3D position changes slightly.

Capture an image Z-stack within each selected field using either the microscope objective control or a piezo stage control, if available. NOTE: Image planes are usually obtained at intervals of 0.5 µm to 2 µm, depending on the size and desired resolution of the image features. Building a quality 3D image requires that image features extend over multiple planes of acquisition, and so to visualize smaller features, smaller intervals are required between planes. Keep the total imaging time for each slice as short as possible. NOTE: Most imaging sessions reported here were under 18 min/slice. However, we have imaged some slices ten or more times, and even as long as 40 min in a single session, without apparent harm in the long-term survival of the slice.

Results

To determine how accurately fiducial marks can be utilized to reimage the same cells within the same fields over time, we examined slices grown on photoetched coverslips (Figure 2.6A). Neurons were visualized by staining with a vital dye (100 nM for 2 h does not stain non-neuronal cells), which disappears from neurons over time without harming the cells (Er et al., 2015). We identified a fiducial mark in a single grid square (Figure 2.6A, B), found a region of vital dye-labeled neurons 24 h after labeling, recorded the x and y offset positions from the fiducial mark (Figure 2.6B), and collected, using a 60X objective, confocal image stacks of this region, repeating the imaging on 4 consecutive days. The maximum projection images of a 30 µm image stack taken in the same location are shown (Figure 2.6C-F). Although some morphological changes occur within the region over 4 days, the identical cells (several of which are marked) can be followed over time. The fluorescence intensity of the vital dye declined over time but

neurons were still clearly identifiable 4 days after labeling. Although most of the neuronal vital dye fluorescence was diffuse within the cytoplasm, some punctate staining was always observed, which became more noticeable as background fluorescence declined. In unhealthy slices, a punctate staining of non-neuronal cells was also observed as slices deteriorated. These results demonstrate that identified cells in slices can be repetitively imaged by using fiducial marks to find them.

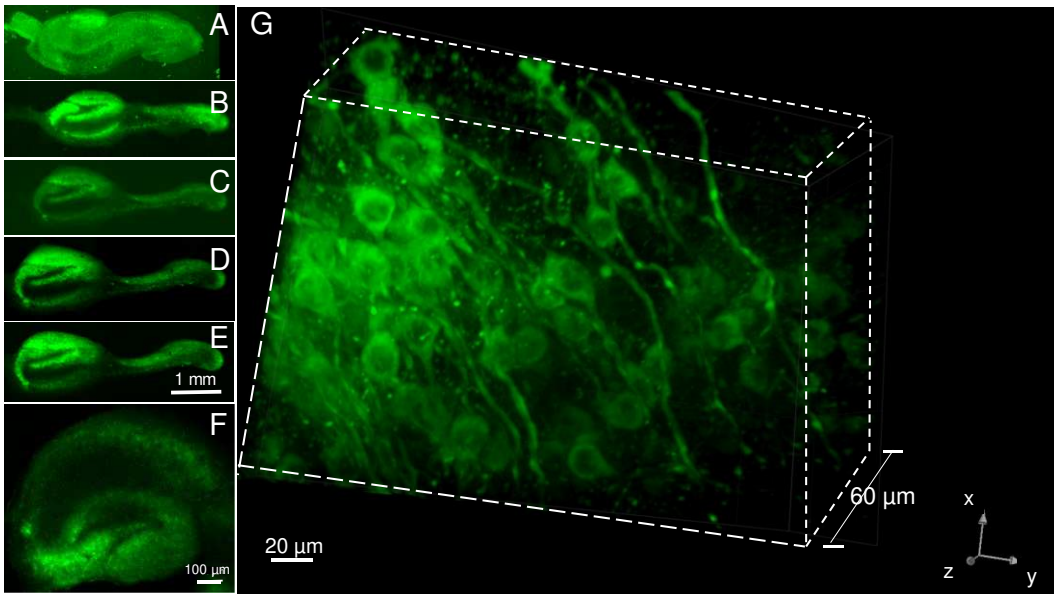

Figure 2.7. A) Neuronal vital dye stained slice in plasma clot taken 24 h after plating with 4x objective. Dye (100 nM) was added when the slice was first placed in the roller tube holder and washed out 2 hr later. Subiculum is curled around hippocampus in the clot. B-E) After clot dissolution by plasmin added at 6 DIV, the slice was reloaded 5 times with the vital dye 24 h in advance of imaging at weekly intervals. Images shown were collected at 8, 21, 28 and 35 DIV (B-E respectively). F) Hippocampal slice cultured for 3 weeks and stained with neuronal vital dye 24 h in advance of imaging with 4x objective. G) Confocal stack of images on same slice as in F showing a 3D view of 61 planes taken at 1 µm intervals. Neuronal vital dye clearly labels both neurites and cell body but it is excluded from the nucleus.

To examine time-dependent changes in neuronal organization and viability within slices during long-term culture, we followed the same slices over 5 weeks, labeling with fluorescent neuronal vital dye once per week 24 h before imaging. Multiple rounds of staining with this vital dye over several weeks increased accumulation of aggregates.

Neurons within freshly plated slices that were still in plasma clots were loaded with dye and imaged at one day *in vitro* (1 DIV). The same slices were imaged again weekly for 5weeks. Images obtained from a single slice with a 4x objective are shown (Figure 2.7A-E). The pyramidal cell layers of the CA and DG regions are brightly labeled when excited at 488 nm and fluorescence emission measured at > 620 nm. Over a 5-week period of observing 19 slices, three slices came off the coverslip and two others lost their typical morphology and became opaque, an indication of their death. Thus, a survival rate of about 70% for experiments should be considered, and extra slices prepared to assure an adequate number for analysis. Slices were prepared at a nominal thickness setting on the tissue chopper of 300 μm. After 5 weeks in culture, we measured the slice thickness by imaging neuronal vital dye-stained slices from the coverslip up through the slice with a 40X oil objective on a spinning disc confocal microscope. Loss of focus of neurons occurred at an average of 257 nm (n = 5 slices with multiple locations used per slice), demonstrating that very little thinning of the slice had occurred from the time of plating. We could not accurately measure the slice thickness by fluorescence microscopy at the time of plating because the vital dye entrapped in the plasma clot gave diffuse fluorescence making it difficult to accurately measure the position at which loss of focus occurred. However, 3D images of neurons within slices are easily obtained in slices after the plasma clot is removed. The 21 DIV slice, shown at low magnification in Figure 2.7F, was imaged with a 60X objective on a confocal microscope (1 μm steps) 3 days after loading with the neuronal vital dye. A 60 μm 3D image was built from the focal planes (Figure 2.7G). Neurons and their neurite processes that are labeled with the vital dye can

be followed in 3D. Morphology and 3D structure of slices were well-maintained over at least 3 months, and the longest times were used in the current study.

Major changes in the morphology of a previously imaged position also occurred in some slices, suggesting that movement of the slice on the coverslip may take place. Certainly, over longer intervals between imaging it became more difficult to know with certainty that the cells in the field being imaged were identical to the ones observed in previous imaging sessions. Thus, maximum projection images of confocal stacks of vital dye-labeled slices acquired at the identical location with the 60x objective at weekly intervals spanning 4 weeks (Figure 2.8) show that neuronal viability is well maintained but that it is difficult to identify a specific neuron over time when images are obtained with long time intervals between sessions. Presumably the pattern of cells labeled with multiple fluorophores would be more easily recognized, as are cells in localized groups when observed by scrolling through an image stack.

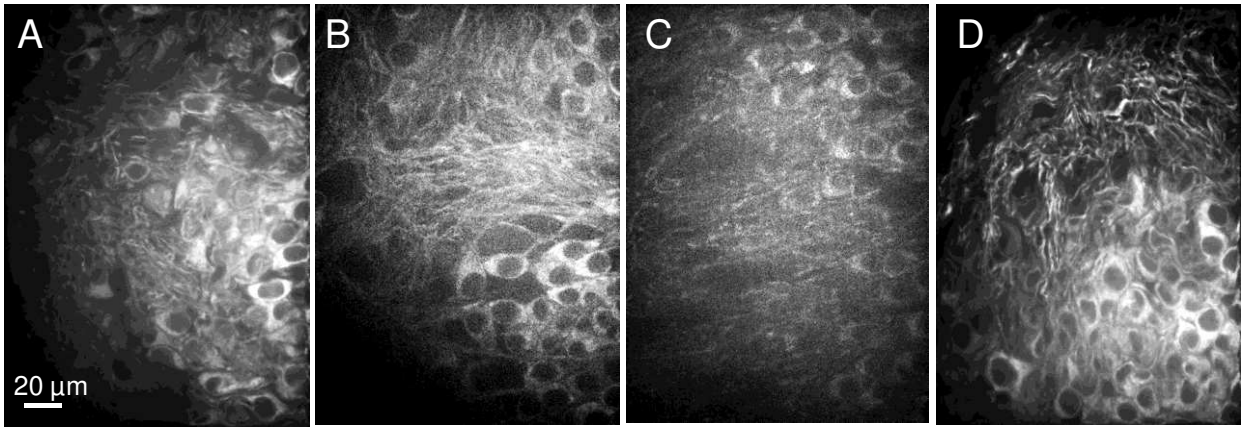

Figure 2.8. Repetitive imaging of identical neurons over several days. Maximum projection images of 30 µm confocal image stacks of the same field of cells (by positioning) from vital dye-labeled slices taken at 12, 20, 30 and 40 DIV (A-D, respectively). It is difficult to repetitively identify individual cells over the longer time frames in projection images. However, even over these long periods, identification of the same cells is often possible by scrolling through the image stacks or building 3D images that can be rotated, such as shown in Figure 2.7G.

To assess the usefulness of different viral vectors for introduction of exogenous genes in neurons of hippocampal slices, we compared slice infectivity using AV, AAV, and recombinant lentiviral vectors, each expressing different fluorescent tags or using different promoters to drive expression. AV (2 x 10^7 infectious U/slice) expressing cofilin-mRFP behind a strong, non-cell specific CMV promoter was used to infect a mouse hippocampal slice that had been cultured 9 weeks on coverslips. Expression of cofilin-mRFP was found throughout the slice at 5 days post-infection, with expression most intense around the slice periphery as observed with a 4x objective (Figure 9A).

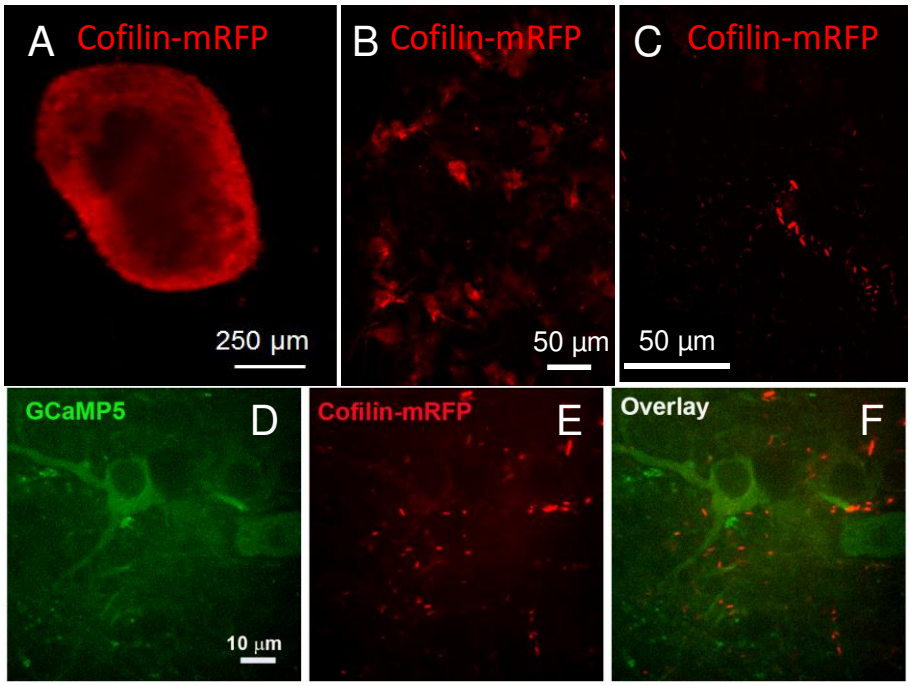

Figure 2.9. Viral-mediated expression of fluorescent proteins. A) Hippocampal slice cultured for 9 weeks and infected with adenovirus for expressing cofilin-mRFP behind a CMV promoter. Expression was found throughout slice at 5 days post-infection but fluorescence was brightest near the slice periphery. B) Same slice showed expression in cells deeper within the slice when viewed with 20X objective. Image is a projection from a stack of 20 images spaced 2 µm apart. C) The same slice was examined after 17 weeks in culture (8 weeks post-infection) and cofilin mRFP was observed in rod shaped aggregates as seen in this projection image from a 70 µm stack of 23 images, 3 µm apart, taken with a 40X objective. D-F) Mouse hippocampal slice infected at 9 weeks in culture with an AAV expressing a GCaMP5-(P2A)-cofilin-mRFP behind a synapsin promoter. Fluorescence was visible in both red and green channels after 10 days. A single plane image of the slice showing the expression of (D) GCaMP5, a calcium sensitive reporter, (E) many cofilin-containing rods, and F) an overlay image.

Cells within the slice expressing cofilin-mRFP were also observed with a 20X objective (Figure 2.9B) with some bright punctate staining and also diffuse expression in both neurons and non-neuronal cells. After 17 weeks in culture (8 weeks post-infection), spontaneous cofilin-rods had formed in some cells, presumably driven by overexpression of wild type cofilin mRFP (Figure 2.9C) (Bernstein et al., 2006; Cichon et al., 2012).

We also demonstrated that AAV (10^{10} particles) could be used for expression in slices. Images of slices infected at 9 weeks in culture with AAV, in which a neuronal specific synapsin promoter drove expression of GCaMP5-cofilin-mRFP with a self-cleaving P2A peptide sequence in the linker of the translated polyprotein (Kim et al., 2011), were captured 8 weeks post-infection (17 weeks in culture). In neurons expressing the GCaMP5 and cofilin-mRFP, some cofilin rods/aggregates formed (Figure 2.9D-F). The fluorescence intensity of the rods/aggregates was so strong that very little fluorescence of a diffuse cofilin-mRFP could be observed without complete saturation and blossoming of the cofilin fluorescence image of rods. Spontaneous cofilin rods appear in neurons in which wild-type cofilin-fluorescent protein chimeras have been over-expressed (Bernstein et all, 2006; Cichon et al., 2012), as well as in stressed neurons (Minamide et al., 2000). Based on the titers of adenovirus, which are determined on the basis of infectivity (Minamide et al., 2003) and the particle counts used for determining AAV titer, about 100 to 500 fold higher particle numbers of AAV are needed to obtain approximately the same infectivity/expression in slices compared to AV.

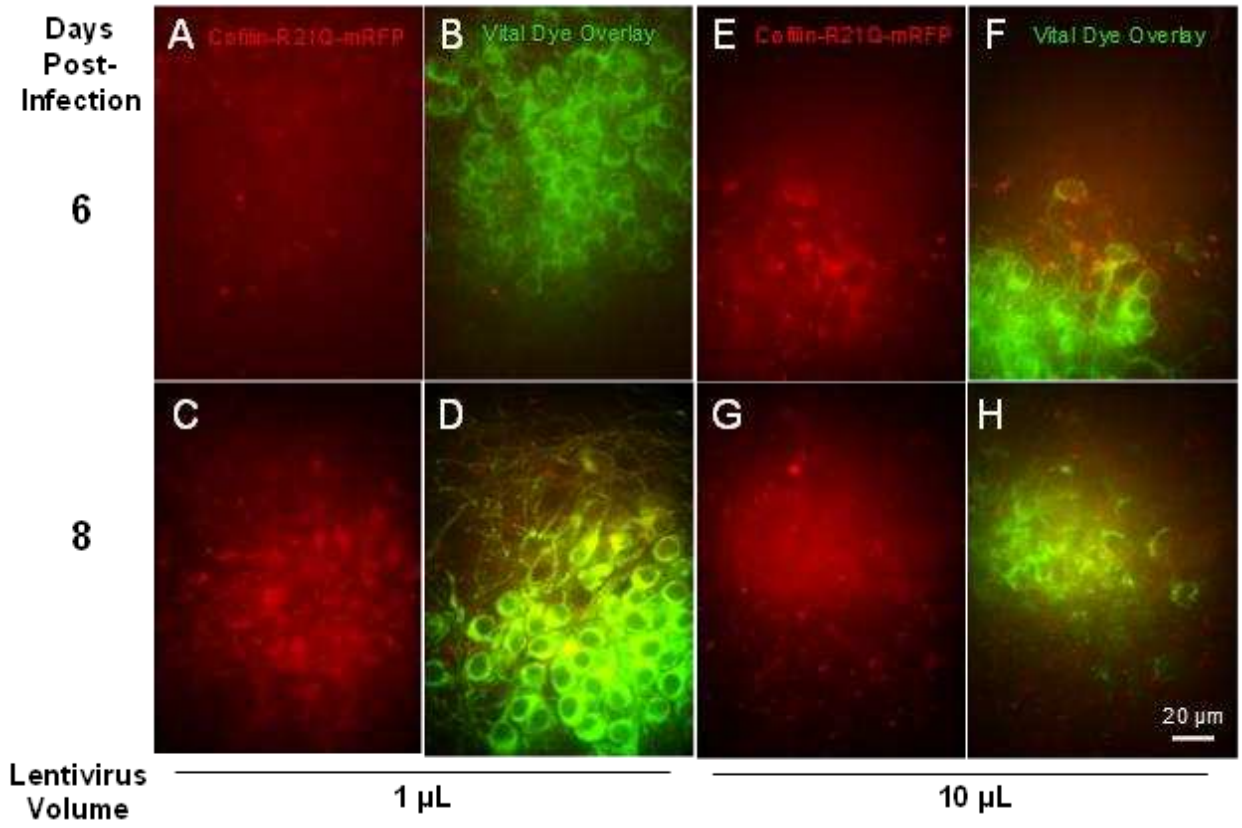

Figure 2.10. Expression of cofilin-R21Q-mRFP driven by a synapsin promoter in neurons infected with recombinant lentiviral vectors. Detection of a weak fluorescence signal is first observed by about 3-4 day post-infection using 10 µL of virus and becomes usable by 5-6 days (E) as seen in these images acquired with a 60x objective. Although it takes longer to achieve the same levels of expression with 1 µL of virus, by 8 days post-infection a similar high percentage of neurons (vital dye labeled) were expressing the cofilin-R21Q-mRFP. Only 27% of neurons expressed the mRFP at 6 days post-infection with 1 µL (A-B) but this increased to 85% (C-D) by 8 days.

To follow recombinant lentivirus-mediated expression of fluorescent proteins in slices, slices were infected at 6 DIV with 1, 3, 10, and 30 µL aliquots of a recombinant lentivirus for neuronal-specific expression (synapsin promoter) of cofilin-R21Q-mRFP, developed as a live cell imaging probe for cofilin-actin rod formation (Mi et al., 2013). Slices were labeled with neuronal vital dye at 11 DIV and imaged in specific regions for the dye and cofilin-R21Q-mRFP expression on 12 and 14 DIV. The slice infected with the 30 µL aliquot of virus did not survive for imaging but triplicate slices treated with the other

volumes of virus showed a dose-dependent expression of mRFP. Figure 2.10 shows images of slices infected with 1 µL and 10 µL of lentivirus at 6 and 8 days post-infection. Multiple regions of two different slices were quantified for co-staining of neurons with the vital dye and mRFP expression.

For slices infected with 1 µL of lentivirus, about 28% of neurons expressed mRFP at 6 days post-infection, increasing to 85% by 8 days post-infection. For slices infected with 10 µL of lentivirus, about 58% of neurons expressed mRFP at 6 days post-infection, increasing to 86% by 8 days post-infection. Thus, 1 µL of the lentivirus was sufficient to provide widespread slice infectivity and neuronal expression by 8 days post-infection.

To demonstrate that this culture system is useful in following development of cofilin pathology, slices infected with lentivirus for expressing cofilin-R21Q-mRFP in neurons were left untreated or treated with various concentrations (1 µM, 333 nM, and 100 nM) of synthetic human Aβ protein that had undergone incubation to form oligomers (Stine et al., 2003). Results from previous studies demonstrated that synthetic Aβo induce cofilin-actin rods in up to 25% of dissociated hippocampal neurons (Maloney et al., 2005; Davis et al., 2011; Walsh et al., 2014). All three slices treated with the 1 µM concentration of Aβ came loose from the coverslip in the first 24 h, whereas all vehicle treated slices (control) and those treated with the 333 nM and 100 nM concentrations of Aβ survived for the two weeks that they were followed. The same cellular regions (CA1, CA3, and DG) in a slice treated with 100 nM Aβo were imaged (60x objective) over several days. Control slices that were infected on 6 DIV with lentivirus for synapsin promoter-driven cofilinR21Q-mRFP expression had diffuse cellular mRFP expression by 15 DIV (Figure 2.11A). Slices exposed to 100 nM Aβo at 14 DIV and imaged at 15 DIV showed that the distribution of

cofilin-R21Q-mRFP became punctate, appearing in both rod shaped structures and aggregates (Figure 2.11B). These structures became even more prominent 6 days after Aβ-treatment (Figure 2.11C, which is the same field of cells as Figure 2.11B). In many places rich in neurites where neuronal cell somas are absent (Figure 2.11D), punctate and rod-like arrays of cofilinR21Q-mRFP developed (arrows in Figure 2.11C), similar to the distribution of cofilin-actin rods previously reported within neurites of Aβ-treated neurons in culture (Maloney et al., 2005; Davis et al., 2011; Walsh et al., 2014).

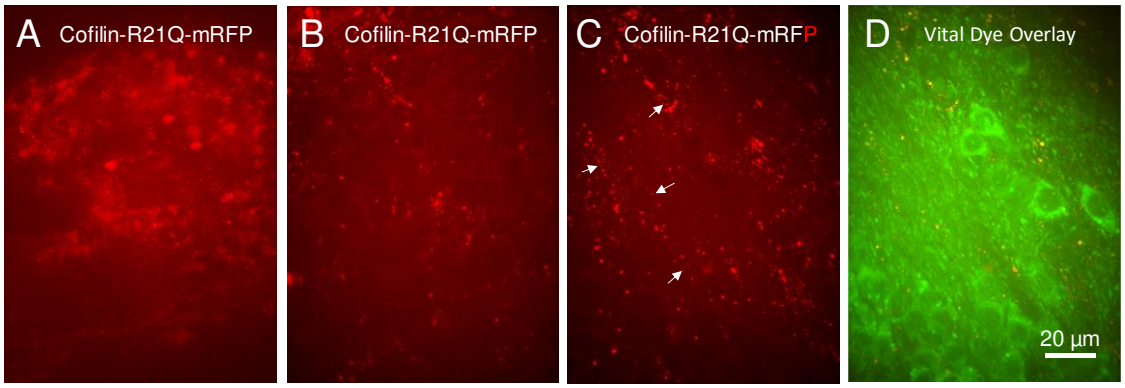

Figure 2.11. Amyloid-β oligomer-induced cofilin pathology in mouse hippocampal slices. All images taken as 30 µm image stacks with a 60x objective and are shown as maximum projection images. Slices were infected with cofilin-R21Q-mRFP at 6 DIV. A) 15 DIV slice treated on 14 DIV with vehicle (DMSO/HAMS F12 medium used to generate $A\beta_o$). B) Slice 15 DIV treated with 100 nM $A\beta_o$. C) Same field as in B taken at 20 DIV and shown in (D) as an overlay with neuronal vital dye label. Arrows show linear arrays of cofilin aggregates and rods in the region of the slice containing neurites but few cell bodies.

Thus, this new method for culturing and observing hippocampal slices will allow users to determine the long-term viability of cells in which cofilin aggregates and rods form and the reversibility of the pathology at various stages of development, and to easily perform dose-response measurements on reagents that could block or reverse the formation of cofilin pathology in a more *in vivo*-like cellular organization.

Discussion

The roller tube method described here allows for long-term culturing and high-resolution live imaging of sliced brain tissue. One major issue with the slice technique as applied here is in the mounting and maintenance of slices. Coverslip coatings that support slice adhesion, promote slice thinning by enhancing the outgrowth of neurites and migration of cells out of the slice; thus, we avoided the use of these substrates. The insertion of amino groups onto the glass by treatment with 3-aminopropyltriethoxysilane improved the adherence of slices, but too little or too much chicken plasma on the coverslip can also cause adherence problems leading to slice loss. The volume of plasma needed for proper adhesion is dependent on the size of the cultured brain slice, and thus is greater for rat hippocampal slices, which are about 4 times larger in area than mouse brain slices. If too much plasma clots under the slice, cell adhesion to the coverslip is impaired and treatment with plasmin will loosen the slice so that it either changes position or detaches completely. However, too little plasma in the clot may lead to slice loss during the first few days of rotation in the incubator. In a recent experiment involving 39 slices, three were lost but some of those lost may have resulted from slice damage occurring during the slicing process. Nevertheless, we usually prepare about 50% more slices than the estimated number needed for the experiment. The second leading cause of culture problems is leakage of medium around the coverslip seal. This problem worsens when coverslips are not held firmly in position for at least 1 min after affixing them to the seal. Heat from the thumb used to apply pressure most likely helps complete the adhesion. Leakage that does occur is often through tiny air channels under the coverslip that can be observed with a dissection microscope. These usually disappear upon using

prolonged thumb pressure. Loss of about 2% of cultures due to slow leakage can be expected and thus it is recommended to wait 10 days after setting up the cultures before performing viral infections. Excessive thumb pressure, especially if produced unevenly across the coverslip, can also cause the coverslip to crack. If breakage is an issue, pressing the tubes down flat onto a rubber mouse pad warmed in an incubator might help to provide more even pressure across the coverslip.

Previously described methods for brain slice culture on membranes at the air-liquid interface (open system) or on a glass coverslip inside of a sealed plastic tube (closed system) are very effective for long-term slice survival, but each method has its strengths and weaknesses. Slice cultures on membranes at the air liquid interface are advantageous for combined electrophysiological studies with immersion objectives for high resolution imaging (Lee et al., 2016), but have drawbacks in finding the exact field of cells for reimaging over time, as well as potential user exposure and objective contamination when using viral-mediated gene expression. Use of viruses for expression of transgenes is safer and easier to perform in a closed system where contamination of microscope objectives is not an issue. Our modified roller tube method gives access of the slice for high-resolution imaging, although it is not amenable to electrophysiological studies.

Slice culture conditions have been established for many regions of the rodent brain (Humpel, 2015), but here we utilize only hippocampus because it is one of the most widely studied brain regions and changes that occur in the hippocampus are of great interest in studies of cognitive impairment. The pyramidal cell layers of the CA and DG regions maintain their organization over several weeks in culture and can be readily observed

morphologically. We have utilized a newly developed fluorescent neuronal viability marker (Er et al., 2015), which has fluorescence properties that allow it to be used to monitor neuronal viability and organization within hippocampal slices over periods of days to months but also is compatible with the use of many other fluorescent proteins and reporters. Although not optimal for NeuO fluorescence (Er et al., 2015), we can excite at NeuO at 488 nm and measure emission at >617 nm. Fiducial marks on the photoetched coverslips helped locate the same cells repetitively over many days of culture and allowed us to image identical regions of the slices over many weeks. Virtually no significant thinning of the slices occurred on the modified glass coverslips during 5 weeks in culture, the longest time point for which we obtained slice thickness measurements.

AV, AAV, and recombinant lentivirus vectors work well for expressing exogenous genes in slices. Lentivirus with a neuronal specific promoter is particularly useful for obtaining expression in a very high percentage (> 85%) of neurons within 8 days post-infection. Furthermore, we show that the cofilin-actin rod pathology associated with development of cognitive deficits in human AD (Minamide et al., 2000; Rahman et al., 2014) and Aβ overexpressing mouse AD models (Woo et al., 2015) can be monitored in slice cultures treated with relatively low concentrations (100 nM) of synthetic human $A\beta_o$. We envision that future applications of this method will include characterizing new therapeutics to reverse cofilin-actin rod pathology and/or correct dendritic spine abnormalities that occur in many neurological disorders (Shaw and Bamburg, 2017).

References

Akerboom J, Chen TW, Wardill TJ, et al. Optimization of a GCaMP calcium indicator for neural activity imaging. *J Neurosci*. 2012;32(40):13819-13840. doi:10.1523/JNEUROSCI.2601-12.2012

Bamburg JR, Bernstein BW. Actin dynamics and cofilin-actin rods in alzheimer disease. *Cytoskeleton (Hoboken)*. 2016;73(9):477-497. doi:10.1002/cm.21282

Benskey MJ, Manfredsson FP. Lentivirus Production and Purification. *Methods Mol Biol*. 2016;1382:107-114. doi:10.1007/978-1-4939-3271-9_8

Bernstein BW, Chen H, Boyle JA, Bamburg JR. Formation of actin-ADF/cofilin rods transiently retards decline of mitochondrial potential and ATP in stressed neurons. *Am J Physiol Cell Physiol*. 2006;291(5):C828-C839. doi:10.1152/ajpcell.00066.2006

Bordat A, Houvenaghel MC, German-Retana S. Gibson assembly: an easy way to clone potyviral full-length infectious cDNA clones expressing an ectopic VPg. *Virol J*. 2015;12:89. Published 2015 Jun 14. doi:10.1186/s12985-015-0315-3

Brewer GJ, Torricelli JR, Evege EK, Price PJ. Optimized survival of hippocampal neurons in B27-supplemented Neurobasal, a new serum-free medium combination. *J Neurosci Res*. 1993;35(5):567-576. doi:10.1002/jnr.490350513

Cichon J, Sun C, Chen B, et al. Cofilin aggregation blocks intracellular trafficking and induces synaptic loss in hippocampal neurons. *J Biol Chem*. 2012;287(6):3919-3929. doi:10.1074/jbc.M111.301911

Clark RE, Squire LR. Similarity in form and function of the hippocampus in rodents, monkeys, and humans. *Proc Natl Acad Sci U S A*. 2013;110 Suppl 2(Suppl 2):10365-10370. doi:10.1073/pnas.1301225110

Davis RC, Maloney MT, Minamide LS, Flynn KC, Stonebraker MA, Bamburg JR. Mapping cofilin-actin rods in stressed hippocampal slices and the role of cdc42 in amyloid-beta-induced rods. *J Alzheimers Dis*. 2009;18(1):35-50. doi:10.3233/JAD-2009-1122

Davis RC, Marsden IT, Maloney MT, et al. Amyloid beta dimers/trimers potently induce cofilin-actin rods that are inhibited by maintaining cofilin-phosphorylation. *Mol Neurodegener*. 2011;6:10. Published 2011 Jan 24. doi:10.1186/1750-1326-6-10

De Roo M, Ribic A. Analyzing Structural Plasticity of Dendritic Spines in Organotypic Slice Culture. *Methods Mol Biol*. 2017;1538:277-289. doi:10.1007/978-1-4939-6688-2_19

Er JC, Leong C, Teoh CL, et al. NeuO: a fluorescent chemical probe for live neuron labeling. *Angew Chem Int Ed Engl*. 2015;54(8):2442-2446. doi:10.1002/anie.201408614

Gähwiler BH. Organotypic monolayer cultures of nervous tissue. *J Neurosci Methods*. 1981;4(4):329-342. doi:10.1016/0165-0270(81)90003-0

Gogolla N, Galimberti I, DePaola V, Caroni P. Long-term live imaging of neuronal circuits in organotypic hippocampal slice cultures. *Nat Protoc*. 2006;1(3):1223-1226. doi:10.1038/nprot.2006.169

He TC, Zhou S, da Costa LT, Yu J, Kinzler KW, Vogelstein B. A simplified system for generating recombinant adenoviruses. *Proc Natl Acad Sci U S A*. 1998;95(5):2509-2514. doi:10.1073/pnas.95.5.2509

Huang L, Chen C. Autoprocessing of human immunodeficiency virus type 1 protease miniprecursor fusions in mammalian cells. *AIDS Res Ther*. 2010;7:27. Published 2010 Jul 28. doi:10.1186/1742-6405-7-27

Humpel C. Organotypic brain slice cultures: A review. *Neuroscience*. 2015;305:86-98. doi:10.1016/j.neuroscience.2015.07.086

Kim JH, Lee SR, Li LH, et al. High cleavage efficiency of a 2A peptide derived from porcine teschovirus-1 in human cell lines, zebrafish and mice. *PLoS One*. 2011;6(4):e18556. doi:10.1371/journal.pone.0018556

Kügler S, Kilic E, Bähr M. Human synapsin 1 gene promoter confers highly neuron-specific long-term transgene expression from an adenoviral vector in the adult rat brain depending on the transduced area. *Gene Ther*. 2003;10(4):337-347. doi:10.1038/sj.gt.3301905

Lee KF, Soares C, Thivierge JP, Béïque JC. Correlated Synaptic Inputs Drive Dendritic Calcium Amplification and Cooperative Plasticity during Clustered Synapse Development. *Neuron*. 2016;89(4):784-799. doi:10.1016/j.neuron.2016.01.012

Maloney MT, Minamide LS, Kinley AW, Boyle JA, Bamburg JR. Beta-secretase-cleaved amyloid precursor protein accumulates at actin inclusions induced in neurons by stress or amyloid beta: a feedforward mechanism for Alzheimer's disease [published correction appears in J Neurosci. 2006 Jan 4;26(1):354]. *J Neurosci*. 2005;25(49):11313-11321. doi:10.1523/JNEUROSCI.3711-05.2005

Matsushita T, Elliger S, Elliger C, et al. Adeno-associated virus vectors can be efficiently produced without helper virus. *Gene Ther*. 1998;5(7):938-945. doi:10.1038/sj.gt.3300680

Mi J, Shaw AE, Pak CW, et al. A genetically encoded reporter for real-time imaging of cofilin-actin rods in living neurons. *PLoS One*. 2013;8(12):e83609. Published 2013 Dec 31. doi:10.1371/journal.pone.0083609

Minamide LS, Striegl AM, Boyle JA, Meberg PJ, Bamburg JR. Neurodegenerative stimuli induce persistent ADF/cofilin-actin rods that disrupt distal neurite function. *Nat Cell Biol*. 2000;2(9):628-636. doi:10.1038/35023579

Minamide LS, Shaw AE, Sarmiere PD, et al. Production and use of replication-deficient adenovirus for transgene expression in neurons. *Methods Cell Biol*. 2003;71:387-416. doi:10.1016/s0091-679x(03)01019-7

Rahman T, Davies DS, Tannenberg RK, et al. Cofilin rods and aggregates concur with tau pathology and the development of Alzheimer's disease. *J Alzheimers Dis*. 2014;42(4):1443-1460. doi:10.3233/JAD-140393

Shaw AE, Bamburg JR. Peptide regulation of cofilin activity in the CNS: A novel therapeutic approach for treatment of multiple neurological disorders. *Pharmacol Ther*. 2017;175:17-27. doi:10.1016/j.pharmthera.2017.02.031

Stine WB Jr, Dahlgren KN, Krafft GA, LaDu MJ. In vitro characterization of conditions for amyloid-beta peptide oligomerization and fibrillogenesis. *J Biol Chem*. 2003;278(13):11612-11622. doi:10.1074/jbc.M210207200

Stoppini L, Buchs PA, Muller D. A simple method for organotypic cultures of nervous tissue. *J Neurosci Methods*. 1991;37(2):173-182. doi:10.1016/0165-0270(91)90128-m

Walsh KP, Minamide LS, Kane SJ, et al. Amyloid-β and proinflammatory cytokines utilize a prion protein-dependent pathway to activate NADPH oxidase and induce cofilin-actin rods in hippocampal neurons. *PLoS One*. 2014;9(4):e95995. Published 2014 Apr 23. doi:10.1371/journal.pone.0095995

Wang L, Blouin V, Brument N, Bello-Roufai M, Francois A. Production and purification of recombinant adeno-associated vectors. *Methods Mol Biol*. 2011;807:361-404. doi:10.1007/978-1-61779-370-7_16

Ward P, Walsh CE. Targeted integration of a rAAV vector into the AAVS1 region. *Virology*. 2012;433(2):356-366. doi:10.1016/j.virol.2012.08.015

Woo JA, Boggess T, Uhlar C, et al. RanBP9 at the intersection between cofilin and Aβ pathologies: rescue of neurodegenerative changes by RanBP9 reduction. *Cell Death Dis*. 2015;6(3):1676. Published 2015 Mar 5. doi:10.1038/cddis.2015.37

CHAPTER 3

DEVELOPMENT AND APPLICATION OF METHODS FOR STUDYING NEURODEGENERATIVE EFFECTS OF COFILIN-ACTIN ROD INDUCERS IN CULTURES OF DISSOCIATED NEURONS AND HIPPOCAMPAL SLICES

Introduction

In Chapter 2 we reported the development of a brain slice culture method for long-term intermittent live imaging of brain slices obtained from postnatal (P5 to 9) mouse or rat pups in an enclosed system in which viruses can be used to express fluorescently tagged proteins of interest. After publishing this method, we ran out of the various reagents needed to continue the work but with the new reagents we could not repeat the procedure. Among the problems that developed were: 1) thrombin-treated plasma failed to clot within a reasonable time and therefore slices were not staying attached; 2) slices that did stay attached did not do well in the new complete Neurobasal A medium and often lost gross morphology within a week in culture; 3) adult brain hippocampal slices failed to survive in culture under any conditions. These problems prevented us from doing studies on aging mice that were from an established neurodegenerative disease mouse model in which the disease did not manifest until 6 months of age.

Additionally, spontaneous formation of rods occurred sporadically in dissociated neuronal cultured and created difficulties in studying rods induced by specific disease-related factors, as well as to make use of transgenic and knock-out lines of mice. Spontaneous rods also became a problem in rat hippocampal neuronal cultures, thus

preventing us from doing any quantitative work on rod induction. Although suppliers of our cell culture reagents reported no alterations had been made in the composition of the neurobasal medium used for many years in our lab, suppliers of the various component of the medium had changed and this suggested to us that impurities in the components might be responsible for the problems encountered. Many other labs have faced this same problem and searched for solutions. In particular, the Wolosker lab looked for components of commercial neurobasal medium that induced toxicity in brain slice cultures and discovered high D-serine levels (above 2% of total serine). Further work in their lab showed D-ser is an excitotoxic agent working via NMDA receptors (Wolosker, 2018). Another group compared the amounts of all the components within various commercial media used for culturing primary neurons and established another medium, available commercially as BrainPhys®, which was optimized for electrophysiology of cultured human neurons (Bardy et al., 2015). Each of these studies suggested to us that we would be better off starting with our own medium components of high purity to prepare a homemade neurobasal (HNB) medium in which spontaneous rod formation is minimized but in which a rod response to disease-related inducers could still be observed. Most previous studies using long-term culture of embryonic neurons to their fully differentiated state (>20 days in vitro (DIV)) also involved co-culturing with glial cells or using glial conditioned medium (Meberg and Miller, 2003). Thus, we also incorporated this conditioning with our HNB to try and obtain long-term survival of brain slice cultures.

In addition to the culture issues, manually counting of rods is too time consuming and without extensive experience, is inconsistent between investigators. Thus, we developed tools for an automated and unbiased analysis of rods in both dissociated

neuronal cultures and in brain slices. A confounding issue with this analysis is that neuronal growth cones contain rod-like actin bundles that co-stain for cofilin, raising the question as to whether or not these are rods, and if they are not rods based upon their dynamic behavior, can we remove them from an automated rod analysis?

One of our goals in studying rod formation is to understand the effects of rods on synaptic function, measured in terms of dendritic spine morphology and density. Spines cannot be visualized and classified if every neuron is expressing a fluorescent tag because even in dissociated cell cultures, dendritic density prevents clear imaging of individual spines. Visualizing spines in brain slices is even more difficult. To obtain only a limited number of labeled neurons in which spines have been visualized, the Golgi staining method or the expression of a fluorescent protein in subpopulations of neurons has been used. Unfortunately, these methods may not be random in their neuronal selection and thus are not unbiased for spine visualization. Furthermore, using mice in which a subpopulation of neurons is expressing a fluorescent protein driven by a special promoter (e.g. Thy1-EGFP mouse), selects for a specific population of neurons that might not be representative of the whole (Faw et al., 2018). Even viral infection of neurons in culture may not be truly random since viral uptake depends on receptor expression. To overcome this problem, random labeling of neurons with the fluorescent lipid dye, DiI, has been used. Reported DiI labeling methods for neurons utilize a gene gun to propel microbeads into the neuronal or slice cultures to obtain dye transfer to the membrane, referred to as diolistic labeling (Foster Olive et al., 2018). Although random labeling is achieved, the method requires a gene gun and considerable work in optimizing conditions

for particle acceleration. We desired to develop a gentler method for application of DiI crystals to neurons.

This chapter will present methods we developed to help solve the above issues. Most of the issues regarding culture medium and slice survival were carried out by Laurie Minamide, a senior research associate in our lab. I worked with her to test how the various changes in medium worked in the systems I was using. Using fluorescence recovery after photobleaching (FRAP), I showed that cofilin-actin bundles in growth cones were quite different in behavior from rods. In a collaboration with Tom Kuhn, a visiting professor in the lab, we figured out a way to stain growth cones and remove the rod-like structures within them from rod analysis. I then developed and provide results that show the application of an unbiased rod analysis algorithm that can be applied to cultures of dissociated neurons and a modified version that can be used with hippocampal slices. Also presented is our random and unbiased DiI membrane labeling method that can be applied to both living and fixed cultures of either dissociated neurons or brain slices and can be used to visualize dendritic spines.

Methods

Animals: All animals were handled according to National Research Council's Guidelines to Care and Use of Laboratory Animals as approved by the Colorado State University Institutional Animal Care and Use Committee protocols 17-7541A, 17-7411A and 18-7779A. Mice used for these studies were C57BL/6 wild type. Rats were Sprague-Dawley.

Preparation and freezing of dissociated hippocampal or cortical neurons: Timed-pregnant mice (E16.5) or rats (E18) were euthanized, embryos removed, euthanized and submerged in cold dissection saline (1x Hanks balanced salt solution, 10 mM HEPES). The brains are quickly removed and placed in fresh cold dissection saline. Hippocampi are isolated under sterile conditions using a stereo dissection microscope in a laminar flow hood. All remaining steps were done under conditions to maintain sterility. Trypsin-EDTA (Gibco) is added to the hippocampi for 10 min and then the trypsin solution is removed and replaced with Homemade Neurobasal medium (HNB, described below) containing 55% Hyclone Fetal Bovine Serum (FBS) and triturated. After allowing any clumps to settle, the supernatant containing the dissociated cells is removed, cells are counted with a hemocytometer and diluted with HNB, FBS and DMSO to a final concentration of 10^6 cells per ml in HNB containing 50% FBS and 10% DMSO. Aliquots of 250 µL or 500 µL were placed in 1 ml liquid nitrogen storage vials and put into a polystyrene container with a lid. The container was placed into a -80^o C freezer overnight in which cells cool at the rate of about 1^o C per minute. After overnight freezing, vials were transferred to liquid nitrogen storage.

Plating and maintaining dissociated neuronal cultures: Coverslips, either 12 mm plain (Deckglaser Cover Glasses) or 12 mm photoetched (Bellco Biotechnology) are dipped in 100% ethanol (Pharmaco), sterile H_2O, 100% ethanol, blotted with a Kimwipe and flamed dry. In a biological safety cabinet, coverslips are placed in 24 well plates (Corning Incorporated REF3524) and UV sterilized for 20 min. A 0.1 mg/ml solution of Poly-D-Lysine (PDL) in 50 mM Borate buffer, pH 8.4 is syringe filtered through a 0.2 µm Supor Membrane (PALL Life Sciences FE4855) using a 5 ml syringe. Sterile PDL solution (200

µL) is placed on each coverslip and allowed to sit for a minimum of 2 h and a maximum of 24 h before washing 3x wash with phosphate buffered saline (PBS; 140mM NaCl, 8 mM NaH_2PO_4, 2.7 mM KCl, pH 7.2) and allowed to dry. Alternatively, the center 8 wells of glass bottom 24 well plates (Cellvis P24-1.5H-N, Lot#: 190828), were coated with sterile PDL and neurons cultured directly in these wells, selected because the outer wells on a 24 well dish cannot be scanned completely using the Keyence microscope. Frozen neuron aliquots are thawed quickly and diluted with HNB to decrease FBS to 10% and DMSO to <2%. Neurons are plated on the coverslips or within wells of the 24 well plate at 20,000 to 80,000 per well (113 mm^2 area of coverslip or 201 mm^2 area of well in glass bottom 24 well plates) and the plate is incubated in a humidity controlled 37° C incubator in an atmosphere of 5% CO_2 and 95% air for 2 h. Medium is then removed from each well and replaced with complete HNB without FBS. Culture medium is completely changed every 2 days. For long-term culture (over 7 days) 5-Fluoro-2'-deoxyuridine (FUdR) is added to 1 µM on day 4 (DIV 4) and removed on DIV 5 to minimize growth of non-neuronal cells.

Organotypic slice cultures: Obtaining postnatal hippocampal slices is done according to protocol in chapter 2. New methods for their mounting and culturing along with the preparation and culturing of adult brains slices are described here. Prior to starting a dissection, prepare the coverslips for mounting the slices. If slices are to be used for treatments that will be followed by fixation and immunostaining, they are adhered to 12 mm x 24 mm coverslips to be inserted inside a roller tube. If slices are to be mounted for live observation, they are adhered to 12 mm diameter round coverslips. Prior to dissection, wash coverslips as described in Chapter 2 and after UV sterilization apply 50

µl of 0.1 mg/ml PDL in borate buffer (pH 8.4) to coverslips under sterile conditions and allow them to dry completely.

Obtaining hippocampal slices from adult mice: Adult mice (4-12 month) are euthanized in a chamber saturated with isoflurane (about 2 min prior to placing a mouse in the chamber). A toe pinch reflex test is done to ensure anesthesia is complete before performing a pneumothorax with a scalpel blade. The mouse is then decapitated. Under sterile conditions in a laminar flow hood the brain is quickly removed using scissors, a scalpel blade, and blunt tipped forceps, and placed into a 35 mm petri dish. The brain is submerged in cold Hibernate A (BrainBits® Lot#061719) containing 2% B27 supplement (Gibco Ref#17504-044 Lots# 209041, 2121058). With a scalpel or tweezers, the brain is cut sagittal at the corpus colosseum to obtain two hemispheres. Working with one hemisphere at a time tease out the brainstem. Looking at the interior of the superior caudal aspect of the cortex a white commissure should be observed with a fissure below. The tissue attached to the commissure is the hippocampus. A thin spatula is used to slide under the fissure and flip the hippocampus out of the cortex. Cut the commissure with narrow forceps to release the hippocampi from the cortex. Have ready 2% low-melt agarose dissolved in Gey's balanced salt solution heated and then cooled to about 40° C. The hippocampus is placed on an Aclar® strip and melted agarose solution is applied over the tissue to keep it flat on the Aclar®. Caution should be taken to ensure the agarose is not too hot. Once the agarose has solidified, place the tissue onto the McIlwaine Tissue Chopper. Use blunt forceps to hold the Aclar® flat to the base of the chopper and cut adult slices at 150 µm thickness. P5-10 mice are dissected as in Chapter 2 and can be embedded in agarose for chopping but is unnecessary. Post-natal slices have been used

at thicknesses between 150 and 300 µm but for studies in this chapter postnatal slices were cut at 250 µm. After the tissue is sliced, a P1000 pipette is used to flow Hibernate A/ B27 dissection solution over the sliced hippocampus to flush it into a 35 mm dissection dish containing hibernate/B27. Slices are separated and pieces of extraneous tissue removed using fine forceps.

Modifications for adhering slices to coverslips: Before placing a slice onto a coverslip, the coverslip is dipped 2x in Gey's Balanced Salt Solution (GBSS) and the edge blotted on a Kimwipe® to slightly dry. A P1000 pipet with a cut tip is used to transfer a slice to the coverslip and a P200 pipet is used to remove excess liquid from around the slice. Slices are adhered to the coverslip with a hydrogel (Vitrogel 3D, TWG001; The Well Bioscience). The volume of the hydrogel depends on the size of the slice being mounted but usually is between 5 µL and 10 µL, the larger volume being required for larger septal adult mouse hippocampal slices. The hydrogel polymerizes in the presence of ionic solutions and is applied directly on-top of each slice. The gel will polymerize sufficiently within 1 min to hold the tissue in place during rotation in the incubator. Two forms of Vitrogel were tested: Vitrogel 3D and RGD Vitrogel 3D, the latter of which contains the integrin-binding peptide sequence. Both hydrogels work for mounting adult slices and postnatal slices. Multiple slices (2-6) can be plated on one 12 mm x 24 mm coverslip intended for fixation whereas only one slice can be used with the 12 mm x 12 mm coverslips intended for live imaging.

*Viral infection of cultures: C*ultures of dissociated neurons were infected with adenoviruses for expression behind strong CMV promoters of either cofilin-R21Q-RFP and/or Actin-GFP on DIV 3 at an MOI of 100. Medium was changed on DIV 5 and experiments were on DIV 6.

Glia conditioned medium: Glial cells were obtained from P4 mice and frozen stocks were maintained in liquid nitrogen (Meberg and Miller, 2003). For making glial conditioned medium (GCM), thaw a vial of glia and plate cells on 10 cm culture dishes (Corning bioscience) in HGDMEM containing 10% FBS. Cells are grown to about 60 to 70% confluency and the medium is removed and discarded. Cells are washed with a few ml of complete HNB medium and 10.5 ml of complete HNB medium is added to the glia for overnight incubation to generate GCM. If more than 10 ml of GCM is needed for feeding cells or slices, additional plates of glia are maintained. After harvesting GCM, medium on glia is replaced with complete HNB and this cycle can be repeated with the same plates of glia for at least 3 weeks provided the glia look healthy and do not proliferate (remain at 70% confluency). Conditioned medium is centrifuged at 300 rpm for 3 min to pellet any floating cells and the supernatant is used immediately on slice cultures. In some cases, GCM was stored at 4° C overnight before use.

Modifications in roller tube culturing methods: By switching from plasma clots to Vitrogel for adhering slices, it was no longer necessary to perform plasmin treatments for clot removal. If slices are plated on Secure Seal® discs for live imaging, ~600ul of glia conditioned medium (GCM) is used for culture. For internal coverslips (12 mm x 24 mm) in roller tubes, multiple slices can be used, and their variable location requires that the amount of GCM is adjusted so that all slices are covered when the tube is vertical. After GCM is added, tubes are flushed for 10 s with 5% CO_2/ 95% air and quickly capped. One day after dissection a complete medium change (with gas flushing) is performed. Medium changes are then done every-other day accompanied by a CO_2/air flush.

DiI microlabeling of neurons flor visualizing dendritic spines

Preparing crystal formation liquid: Prepare 2 ml of 0.7 mg/ml DiI in 70% ethanol and aliquot into four 1.7 ml microfuge tubes to dry in a laminar flow hood. Store at -80º C until needed.

Preparing surfaces of materials to resist DiI binding: Coat the lid of a 10 cm plastic culture dish with 5 ml of 2% 3-aminopropyltriethoxysilane solution in 70% ethanol (APES) for 15 seconds. Perform a 3x wash with room temp sterile H_2O and allow to air dry. Fill a p20, p200, and a p1000 pipette tip to 20 µl, 100 µl, and 500 µl respectively with the APES solution. Let sit for 15 s to coat with the APES and then pipette up and down in H_20 3x. Perform this procedure of coating and washing with 5 ml APES in a 15ml conical tube, and 500ul with the airbrush (AWAKA Neo Airbrush). Coat airbrush by loading and softly spraying 500 µl of APES through the airbrush to ensure APES is in contact with airbrush for 15 s and repeat 3x with H_2O. (NOTE: For other airbrush uses, the APES coating in the airbrush should be removed with hot H_2O). Take the APES coated 10 cm dish lid and add 5 ml of Gey's balanced salt solution. Ensure the Gey's solution is covering the entire lid. In a biosafety cabinet set up the airbrush apparatus (Figure 3.1) and expose to UV for 30 min. Ensure airbrush is spraying liquid by passing 500 µl H_2O until completely dry. Place dish lid containing 5 ml of Gey's onto bullseye of airbrush set up. Dissolve one aliquot of DiI in 0.5 ml heptane. Load 100 µl of heptane dye solution into the airbrush with APES coated pipette tip. Spray solution into the dish. Wait one minute to allow crystals to form and heptane to evaporate, then spray another 100 ul of heptane dye solution. Wait one minute and repeat 3 x until heptane dye solution is gone. If there is not adequate time between spritzing or if too large a volume is used, the droplets of heptane will coalesce,

and smaller numbers of large crystals will be formed. After the last spritz wait 1 min then using a p1000 APES-coated tip, remove the Gey's/DiI crystal solution and place it in APES coated 15ml conical tubes.

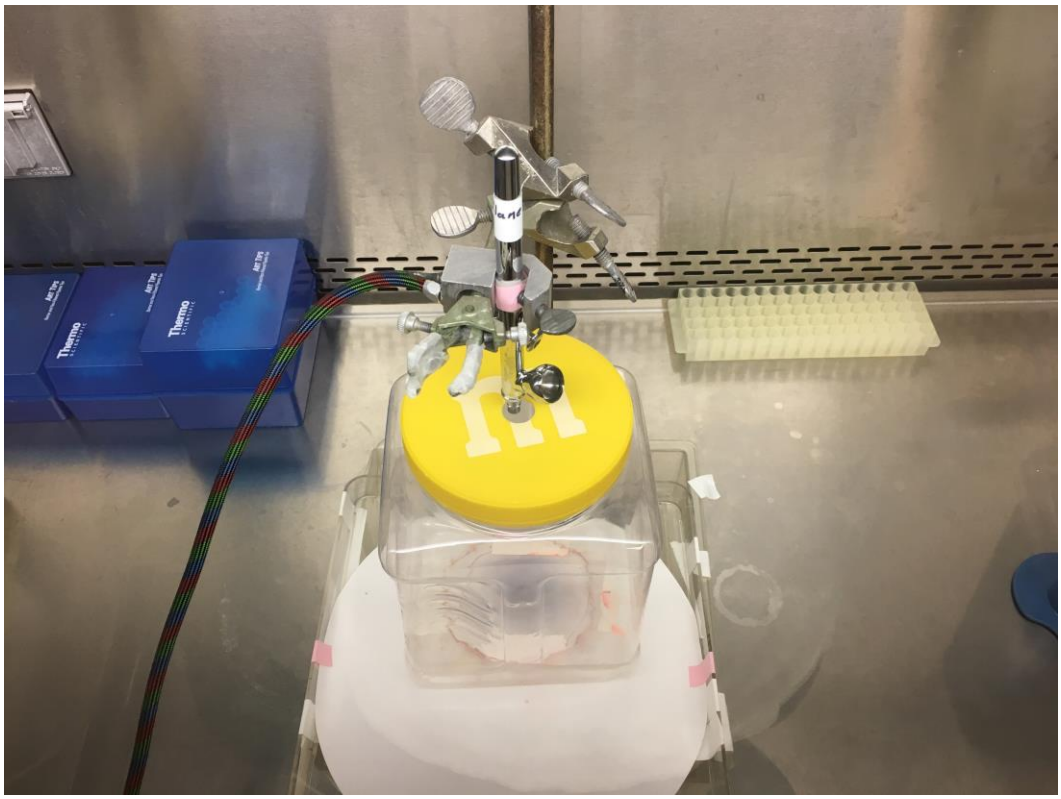

Figure 3.1. Airbrush mounted on ring-stand and inserted through a hole drilled in the plastic lid of an empty plastic contained. The entire apparatus is in a biological safety cabinet for UV sterilization and for spritzing cells and brain slices. The container has a large hole cut in the base with filter paper underneath to catch any excess DiI spray. Height from tip of airbrush to bottom is about 8 inches.

Applying Crystals to Culture: These step needs to be performed as quickly as possible to ensure tissue does not dry.

Brain slices: Cut a p1000 tip so that you can pipette a brain slice into the tip without damage. Pipette the brain slice onto an Aclar® strip. Pipette off as much liquid as possible then quickly spray the tissue with 50 µl of Gey's crystal suspension loaded into the

airbrush. Apply fresh dissection solution to the tissue then pipette the tissue up and plate as wanted.

Cultures of dissociated neurons: Pipette 8 µl of Gey's crystal suspension into culture using an APES coated P20 pipette tip. Gently swirl and let sit for at least 6 h before imaging.

Fluorescence labeling and Immunostaining: Slice cultures were fixed in 37° C, 4% formaldehyde in PBS for 1 h and permeabilized with 100% -20° C methanol for 15 min. Dissociated neurons were fixed in 37° C, 4% formaldehyde in PBS for 20 min and permeabilized with 100% -20° C methanol for 3 min. Vitrogel was removed under PBS from on top of slices by gently lifting it off with forceps while working under a dissection microscope. All cultures were blocked for 1 h in TBS+1% BSA +5% goat serum before immunostaining. Primary antibody solution in TBS +1% BSA was incubated at 4° C overnight. Cofilin was immunostained with affinity purified rabbit 1439 antibody at 2 ng/µl (Shaw et al., 2004), Map2 with Chicken ant-mouse Map2 (Abcam 92434) at 1:300, and growth cones with mouse anti-chicken tectum 2G13 (Novus Biologicals, Ref NB600-785) at 1:75 (Stettler et al., 1999). After 5 TBS washes (dissociated neurons) or 10 TBS washes (slices), secondary antibody in TBS +1% BSA was applied and incubated at room temperature for 2 h. Goat anti-rabbit and goat anti-chicken antibodies (Alexa 488 or 561) were used on cultured slices and dissociated neurons at 1:500. Goat anti-mouse IgY (Alexa 647) was used on cultured dissociated neurons at 1:500. After 5 TBS washes (dissociated neurons) or 10 (slices), Prolong Diamond Antifade (Invitrogen Ref P36961) was applied to coverslips of neurons (3 µl) or slices (8 µl) for mounting.

Data acquisition: Slice imaging for cofilin pathology was performed using the quick focus capture function on the Keyence Wide Field BZ-710 microscope with 40x plan apo objective. A central point on the slice is identified at low magnification and using the Keyence software navigation feature the central point can be found at 40x, this will be the central point from which a 7 by 7 or 9 by 9 stitched image is obtained, which covers about 75% of a 12 mm diameter coverslip. A Z-stack range is selected to encompass all the planes in focus across the hippocampus with a step size of 2 µm. Filter cubes for image acquisition are 350ex/370em, 480ex/500em, 560ex/590em. Z-Stacks at each field are acquired with each filter cube before moving on to the next x,y location. Cultures of dissociated neurons were captured in fewer planes and used the 647ex/670em filter cube for the growth cone antibody. Images are stitched in their respective channel with adjusted shading selected to decrease waffling of the montage image.

Imaging of dendrites and dendritic spines in hippocampal slices and cultures of dissociated neurons was performed on an Olympus IX83 microscope with a Yokagawa spinning disk confocal system using either the 488 or 561 lasers with 2x, 60x, or 100x objectives. Z-stacks were obtained with a step size of 0.1 or 0.2 µm.

Imaging for FRAP experiments was performed on the spinning disc confocal microscope with a phasor light illumination system (3I, Denver, CO). A 100x, 1.45 na objective was used for photobleaching with either the 488 nm or 561 nm lasers at 100% power for 0.5 s. Single plane images of both emissions were acquired every 5 s using an exposure of 100 ms with laser power at 20%. Acquisition duration was 20 min or until fluorescence recovery plateaued as observed via real-time Slidebook fluorescence recovery graphs.

Automated rod analysis: Images of fixed dissociated neurons immunostained for cofilin, growth cone antigen (2G13 antibody) (Stettler et al., 1998) and DAPI stained are captured across the entire coverslip in 3 wavelengths on the Keyence microscope using a 40x objective and are stitched into three single images that are then exported and opened in ImageJ. Macro functions are then applied for a local threshold and shape/size segmentation using the “analyze particles” function for both the cofilin and growth cone antibodies. Cofilin stained material within the growth cone regions as well as within the cell soma are eliminated from analysis and cofilin stained puncta that fall within the shape/size parameters set to include all rods but exclude large aggregates are quantified. A coverslip region of 49 fields (7x7) covers the majority of area within a drilled dish. In the absence of using a neuronal specific stain, such as Neu N (Tsai et al., 2000), neurons identified morphologically can be counted per field and their abundance compared to total DAPI stained nuclei within that field. Rod index can then be estimated. ImageJ script is in Supplementary Material, Chapter 3.S1.

Brain hippocampal slices (150 um thick) cultured on coverslips in roller tubes are fixed, methanol permeabilized and immunostained for cofilin plus DAPI for staining nuclei. Slice health was often evaluated by Map2 staining of dendrites. The entire slice is scanned in 3D at 40x for each wavelength on the Keyence microscope, stitched, and the projection image exported to ImageJ for analysis. Fields within each of 5 regions of the hippocampus (dentate gyrus, mossy fiber tract, CA1, CA3 and subiculum) were manually selected, added to the ImageJ ROI manager from the DAPI stain positioning (unbiased for cofilin), and were chosen between multiple slices to be as identical in position as possible. Rod quantification was then carried out using an unbiased script that applied

local thresholds and segmentation macros to eliminate background and large aggregates from the area used to quantify the remaining cofilin-stained puncta using the analyze particles function. Planes to be quantified were separated by 2 μm (10 x 0.2 μm per plane) to eliminate most duplication in rod counting assuming a random 3D distribution (mean angle of 45°) of 3 μm rods. ImageJ script is in Supplementary Material, Chapter 3.S2. Data was then exported to excel for statistical analysis.

Statistical Analysis: Relevant statistical analysis is included in each figure legend.

Results

Improving adherence of slices to coverslips: Vitrogel has many advantages over plasma for mounting slices on coverslips. It is transparent and does not need to be removed for live imaging of slices starting immediately after plating (Fig. 3.2 A). Vitrogel works to

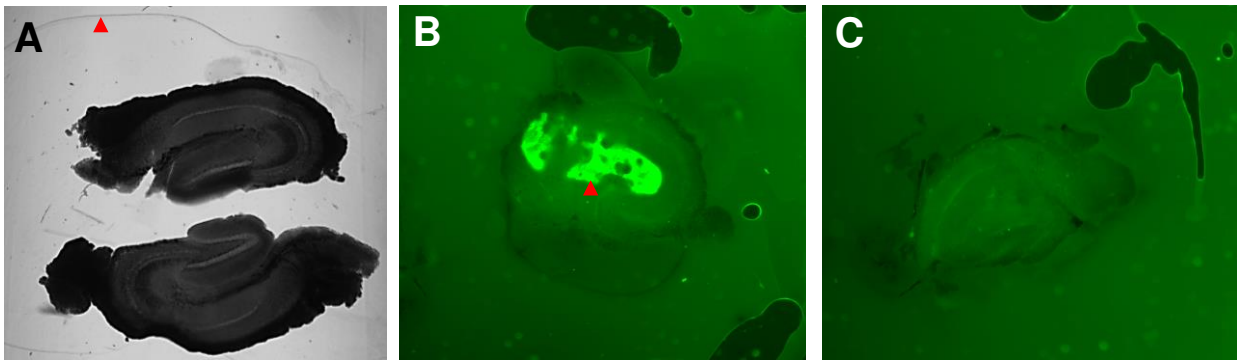

Figure 3.2. Vitrogel 3D hydrogel for mounting sensitive tissue on coverslips for culture, live imaging, and immunostaining. (A) Brightfield image of live hippocampal slices embedded in Vitrogel. Red arrow points to the edge of the Vitrogel overlay. (B) Fluorescence image (488 nm) showing slice after immunostaining with Vitrogel between the slice and coverslip showing up in the 488 nm channel (red arrow). (C) Fluorescence image (488 nm) of immunostained slice (DAPI and 561 nm fluors) with Vitrogel manually removed from slice tissue.

maintain adhesion of slices even if the slices die and lose their characteristic morphology and it can remain present during fixation and immunostaining without interference.

However, if it penetrates under the slice, it can reduce the efficiency of washing away non-specifically bound fluorescently tagged secondary antibodies and thus leave a residual fluorescence as observed in Figure 3.2 B. However, the Vitrogel does not appear to penetrate the tissue before it sets. This is advantageous as well, because it allows the Vitrogel overlay to be removed from both living and immunostained slice (Fig. 3.2C).

Optimizing culture medium for adult hippocampal slice culture: To overcome the problems with commercial neurobasal medium, we purchased all of the medium components with analytical grade purity including amino acids of the highest L-amino acid content available and prepared neurobasal medium with the composition of commercial NB medium (Table 3.1, adjusted items highlighted). We also adjusted the NaCl content of the medium to bring it to 300 mOsM. Higher purity of the components and adjusted osmolarity did result in enhanced survival of our postnatal slices, but it did not eliminate the problem with spontaneous rods in dissociated neuronal cultures. We next evaluated medium in which we varied the content of L-cysteine, which was as low as 10 µM and as high as 260 µM in different published papers of hippocampal neuronal culture medium. Reducing the L-cysteine from that found in commercial NB (260 µM) to 50 to 100 µM, significantly reduced spontaneous rods (Fig. 3.3A). To determine the optimal concentration of L-cysteine to reduce spontaneous rods but permit a consistent result with PrP^C-dependent rod initiators, we tested amounts between 100 and 260 µM. We found that at 175 µM L-cysteine we have low spontaneous rods yet produce a significant rod response when in the presence of stressors (Fig. 3.3B). Although we occasionally find high spontaneous rods, we have performed many replicated experiments in triplicate without interference.

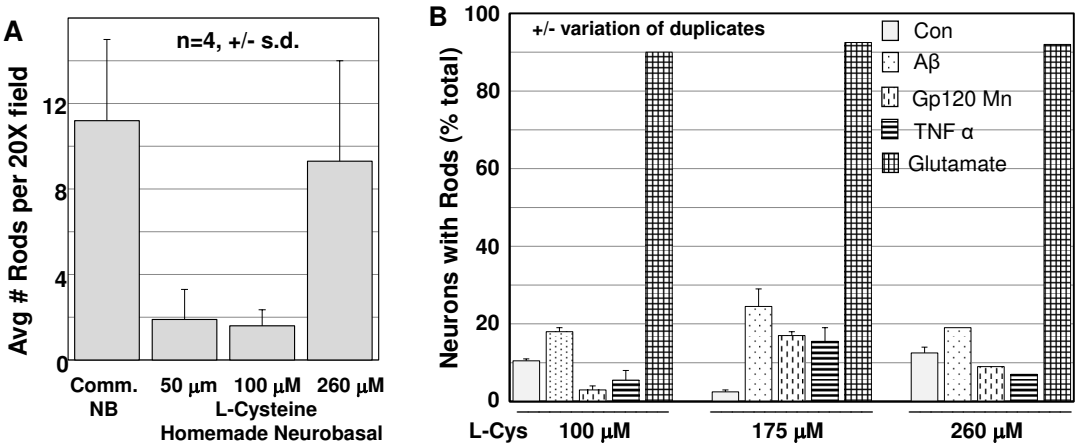

Figure 3.3. Effects of L-cysteine concentration on spontaneous and induced rod formation in dissociated hippocampal neurons. (A) Rods quantified per field in DIV6 cultures grown in commercial NB (260 µM L-cys) or Homemade NB. Data is from 4 coverslips and error bars are standard deviation. (B) Percent neurons with rods (control=spontaneous rods) induced by neurodegenerative signals or glutamate. Averages of duplicate samples with range shown by bar. Overnight treatments: Aβ synthetic oligomer (1 µM); gp120MN (500 pM); TNFα (50 ng/ml). Glutamate (200 µM) was used for 30-60 min.

Glia conditioned medium for culturing adult brain slices: Reports have shown that astrocytes help maintain adult neurons in vitro (Withers et al., 2000) and that the health of brain slices measured by maintenance of long Map2-immunostained dendrites correlates with the health of GFAP stained astrocytes (Schwarz et al., 2017). Because of the established circuitry that connects the hippocampus to other brain regions, loss of some neurites following hippocampal dissection is expected. To follow the long-term health of slices in culture, we utilized Map2 immunostaining of dendritic arrays of hippocampal slices to assess their preservation. The loss of Map2 immunostained dendritic arrays in the CA3 region of adult hippocampal slices maintained in HNB for six days compared to those fixed immediately after slicing showed a dramatic loss of total dendrites and a fragmentation of those that remained (Figure 3.4A).

Table 3.1 Components of Commercial NB, BrainPhys and Homemade NB Media

	NB	B-Phys	HNB
Components	Conc **mM**	Conc **mM**	Conc **mM**
Glycine	0.4	0.002	0.4
L-Alanine	0.02247191	0.002	0.0225
L-Arginine HCl	0.39810428	0.3	0.4
L-Asparagine-H2O (anhyd)	0.005533333	0.05	0.0055
L-Cysteine	**0.2603306**	**0.1**	**0.175**
L-Histidine HCl-H2O*	0.2	0.15	0.2
L-Isoleucine	0.8015267	0.416	0.8015
L-Leucine	0.8015267	0.451	0.8015
L-Lysine HCl	0.7978142	0.499	0.7978
L-Methionine	0.20134228	0.116	0.2013
L-Phenylalanine	0.4	0.215	0.4
L-Proline	0.06747826	0.06	0.0675
L-Serine	0.4	0.002	0.4
L-Threonine	0.79831934	0.449	0.7983
L-Tryptophan	0.078431375	0.0441	0.0784
L-Tyrosine	0.39779004	0.214	0.3978
L-Valine	0.8034188	0.452	0.8034
Choline chloride	0.028571429	0.0641	0.02857
D-Calcium pantothenate	0.008385744	0.0047	0.008386
Folic Acid	0.009070295	0.00601	0.00907
Niacinamide	0.032786883	0.0166	0.03279
Pyridoxal hydrochloride	0.019607844	0.00986	0.01961
Riboflavin	0.00106383	0.000582	0.001064
Thiamine HCl	0.011869436	0.00644	0.01187
i-Inositol	0.04	0.07	0.04
D-Glucose (Dextrose)	**25**	**2.5**	**2.5**
Sodium Chloride	**68.965515**	**121**	**122**
Potassium Chloride	5.3333335	4.2	5.333
Magnesium Chloride 6H2O	0.8136842	0	0.8137
Sodium Phosphate monobasi	0.9057971	0.45	0.9058
Phenol Red	0.021519661	0.021519661	0.02152
HEPES	10.92437	5	10.92
Sodium Pyruvate	**0**	**0.5**	**0.2273**
Vitamin B12	5.02E-06	5.00E-04	5.02E-06
Zinc Sulfate 7H2O	6.74E-04	0.0015	6.74E-04
Ferric Nitrate (Fe(NO3)3-9H2O	2.48E-04	1.24E-04	2.48E-04
Calcium Chloride (anhy)	1.8018018	1.1	1.8018
Sodium Bicarbonate	26.190475	29	26.1905

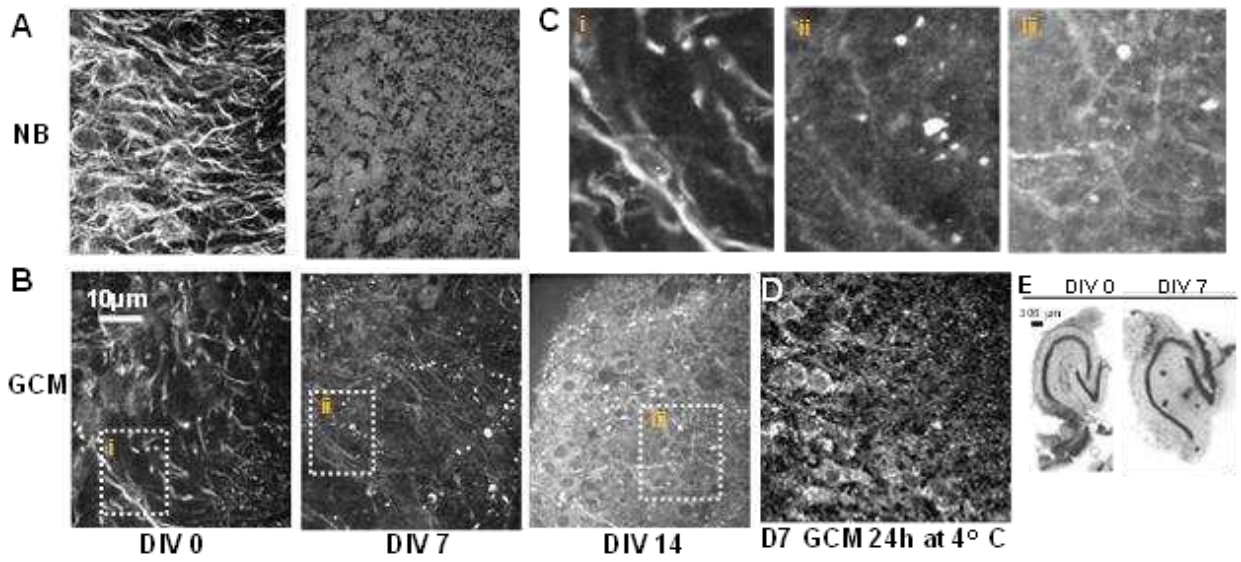

Figure 3.4. Map2 immunostaining of dendrites in CA3 region of adult mouse hippocampal slices fixed immediately (DIV 0) or cultured in roller tubes for DIV shown. (A) Slice cultured 7 DIV in HNB shows loss of dendrites compared to slice fixed immediately after dissection. (B) Adult mouse hippocampal slice fixed immediately (DIV 0) or cultured in GCM for 7 DIV (middle) or 14 DIV (right). Boxed regions are shown at higher magnification in (C). Although some loss of Map2 staining occurs, much is maintained even through 14 DIV. (D) GCM stored overnight at 4° C does not support adult slice health. (E) Gross slice morphology (DAPI stain) is well maintained during culture in GCM. Hippocampus tapers from septal to temporal region. Slice on right is septal and that on left is medial.

However, if the HNB medium was conditioned overnight using glia cultures (GCM), we saw a marked improvement in the health of the slice with well-defined dendritic tracts being observed even after 14 DIV (Figure 3.4 B,C) and gross slice morphology is well maintained (Figure 3.4 E). Although it has been reported that GCM is stable in storage at 4° C for 3 days after collection (Ruiz et al., 2012), this may apply only to certain uses. We found that GCM that was harvested and held overnight at 4° C before use lost its beneficial effects in maintaining Map2 dendritic arrays in adult slice cultures (Fig. 3.4 D).

Automated cofilin pathology analysis: Cofilin-actin rods are distinct in brightness and shape. Using ImageJ scripts to batch macro functions we segmented images obtained with a 40x objective of fluorescently tagged cofilin in neurons by local threshold intensity and shape/size exclusion to contain only cofilin rods and growth cones (Figure 3.5).

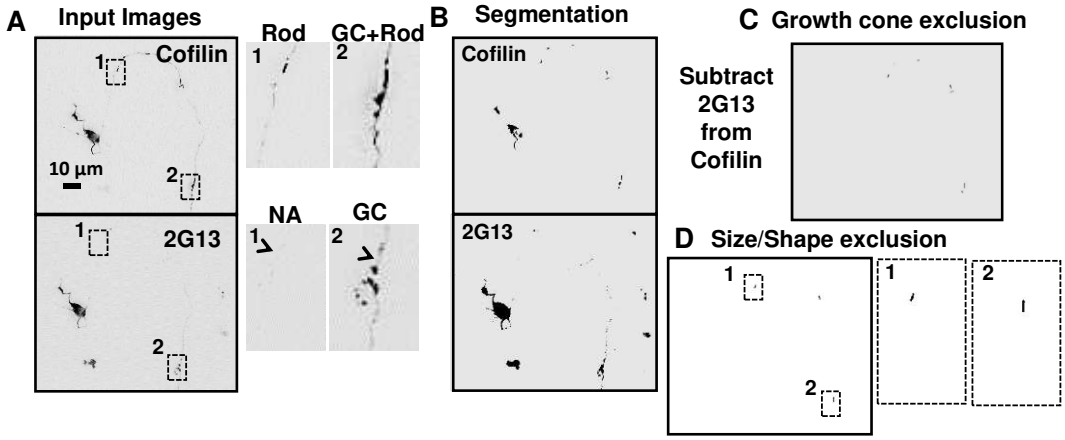

Figure 3.5. Steps in semi-automated rod analysis of cultured neurons using growth cone exclusion (inverted images). (A) Two images of the same field immunostained for cofilin and growth cones (2G13) with boxed areas 1 and 2 showing magnified regions in identical locations between two panels. (1) Contains a cofilin-stained rod (location is arrowhead in lower set); (2) contains a cofilin-stained growth cone and rod (arrowhead). (B) Images are segmented using Bernstein's local contrast threshold in ImageJ to isolate only the objects of greatest local contrast in the cofilin channel and to isolate all 2G13 stained objects. The 2G13 image is dilated to ensure subtraction of growth cones and extending filopodia. (C) Resulting image from subtracting 2G13 image from cofilin image. (D) A second size/shape exclusion results in an image containing cofilin rods. Magnification of boxed regions show the rods that are counted automatically within the algorithm.

To validate that cofilin stained structures discriminated as rods or growth cones are different structures, we performed FRAP experiments using WT cofilin tagged with RFP. We bleached growth cones and rods and recorded the recovery of fluorescence. The cofilin-RFP in rods had negligible recovery over long time periods whereas cofilin-RFP associated with actin bundles in growth cones recovered within 1 min confirming that these morphologically similar structures are very different (Figure 3.6 A, B).

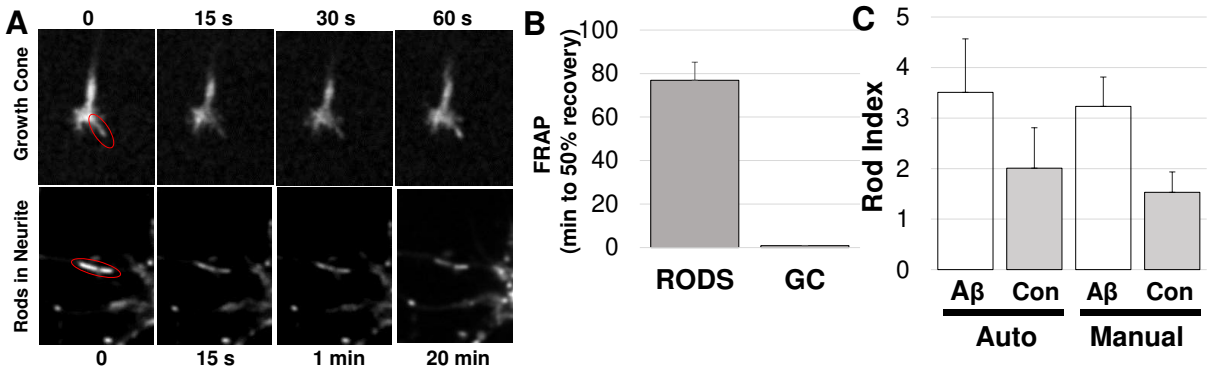

Figure 3.6. Turnover of cofilin on actin bundles in growth cones and rods and comparison of rod quantification between manual and automated analysis. (A) Images of fluorescence recovery after photobleaching (FRAP) in red oval for cofilin-RFP along actin bundles in growth cones (top row) and rods within neurites of DIV7 hippocampal neurons treated 24 h with Aβd/t (bottom row). Laser intensity and duration was intended to achieve about an 80% bleach. (B) FRAP recovery times to 50% of starting value from 5 independent observations each of rods and growth cones. Bar shows range of times determined from extrapolation of curves from 20 min time point. (C) Rod index scores of neuronal cultures either untreated (con) or treated overnight with Aβd/t and scored using the automated analysis method or done manually. Error bars are s.d. from triplicate samples.

To further validate the automated method, we compared results obtained by comparing rod index values (rods/neuron) from an automated count of cultures compared to a manual count. In this particular experiment we had an elevated number of spontaneous rods but these were compared to cultures treated with the rod-inducing amyloid-β dimer/trimers (Figure 3.6C). Both methods of analysis gave very similar results, but the automated unbiased analysis was completed on both samples within a few minutes instead of one hour for the manual analysis. Similar thresholding principles can be applied to images of brain tissue immunolabeled for cofilin to identify cofilin rods and puncta (Figure 3.7). Imaging was performed on both the Keyence wide field microscope acquiring fields with the 40x objective (Fig. 3.7A-E) and on the spinning disc confocal microscope in which rods are quantified in 30 µm Z-stacks taken with the 60 x objective (Figure 3.7F).

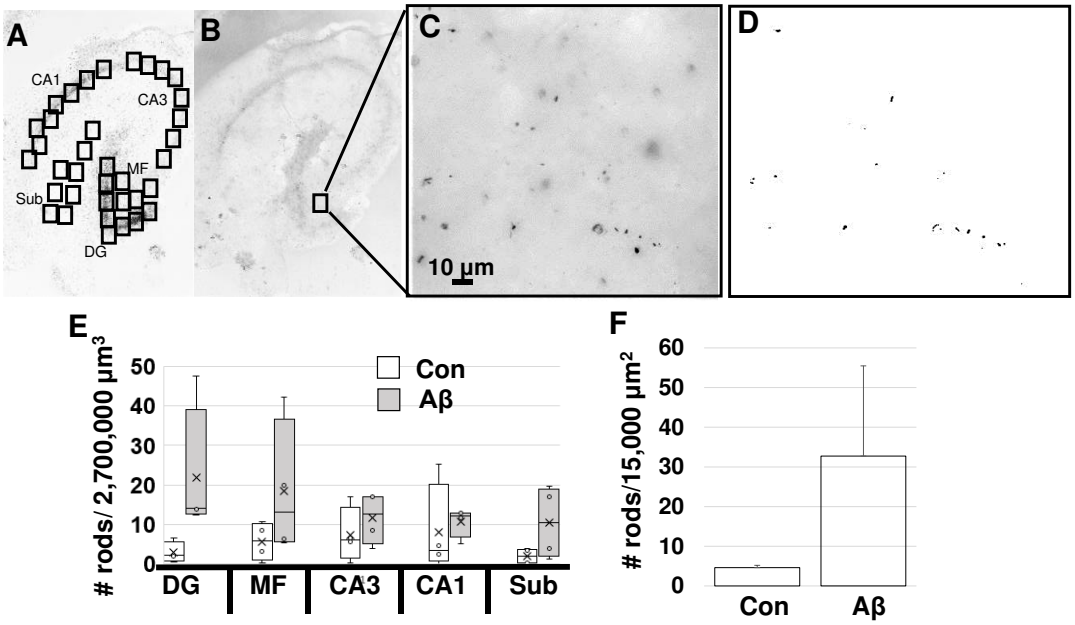

Figure 3.7. Semi-automated rod localization and quantitative analysis in slices. (A) The rod analysis program prompts the user to select 36 regions of interests (ROI) from a projection image of a DAPI stained slice from a Keyence multichannel 3D 9x9 scanned image obtained with a 40x objective. Boxes display typical placement of ROI's over hippocampal pyramidal layers and the subiculum area with each area labeled. DG, CA1, CA3 and Sub have 8 ROIs and MF tract has 4. (B) Projection image of the same cofilin immunostained slice is opened. (C) An individual 3D image of the cofilin staining is made for each ROI selected from the DAPI image. The images are then segmented using a local median threshold with a radius the size of manually predetermined measured rods. (D) Image after threshold and an additional size exclusion analysis showing rods. (E) Box plot shows number of rods per ROI (2,700,000 μm^3) averaged between the ROIs on each slice and then between 4 separate slices for untreated and 4DIV Aβd/t-treated slices from a 4 month WT mouse. Bars show the range for middle 50% of the values with X being the mean and the cross bar the median. Error bars represent the range of highest and lowest slice averages. (F) Plot showing same sets of slices as analyzed in E but using the confocal microscope with 60x objective and only showing the DG region. The semi-automated rod analysis program can quantify rods more accurately from confocal images.

Because rod orientation might be vertical and thus remain as a round puncta rather than an elongated rod shape, we do not apply the shape exclusion in slice analysis. Rod numbers in different regions of the hippocampus (Figure 3.7A) were quantified in the full volume of the 3D slice (150 µm thick) both in untreated control slices from 4 month WT mice and in slices treated 4 DIV with 1 nM amyloid-β dimers/trimers (Aβd/t) (Figure 3.7E) (see Chapter 6). The dentate gyrus and mossy fiber tracts are the most sensitive to

forming rods in the presence of Aβd/t. Rather than use a projection image for the 30 μm Z-stack of rods from the spinning disc confocal microscope, we analyzed every plane for rod content. Rod numbers calculated from the 0.2 μm step size of image planes on the confocal were corrected for objects that extended over multiple planes by assuming rods have a random orientation within the slice and that rod average length, based upon 3D reconstructions, is 3 μm, meaning we analyzed image planes separated by 2 μm which accounts for random orientation. Rod numbers within the dentate gyrus calculated from the spinning disc confocal image are shown in Figure 3.7F.

Labeling dendritic spines with DiI: We modified the Diolistic labeling method to eliminate the gene gun (Foster Olive et al., 2018) and call this method DiI microlabeling. DiI microlabeling entails forming crystals of DiI by evaporation of organic solvent on an aqueous surface. An inexpensive airbrush (AWAKA) available at art stores is used spray droplets of heptane DiI onto a balanced salt solution to form DiI crystals ranging from ~2-30 μm. The crystals in the salt solution can be sprayed onto slices or added into cultures of live neurons to randomly label those that contact a sedimented crystal. There are several forms of membrane dyes that can be used for this type of work and which different in their fluorescence spectrum. We have used DiI and DiA most often (Figure 3.8).

Discussion

For many years we utilized commercial neurobasal medium for hippocampal and cortical neuronal cultures with very little spontaneous rod formation. In about 2015, the

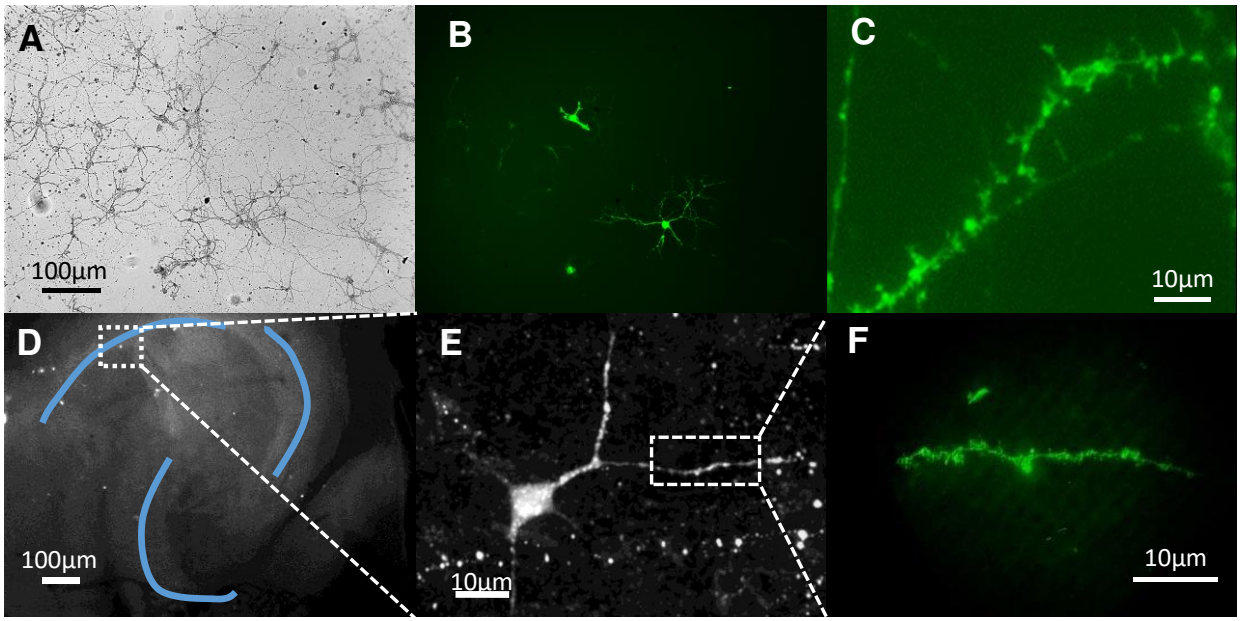

Figure 3.8. DiA microlabeling in a variety of neuronal culture settings. (A) Bright field image (10x objective on Keyence) showing a live culture of DIV 21 mouse neurons containing a highly intercalated network of neuronal processes that have been labeled with DiA. (B) Same field as in (A) but showing random bright labeling of a few neurons in the 488 fluorescence channel 48h post labeling by pipetting 8 µl of DiA crystal solution into culture well. (C) High magnification (100 x objective) of DiA-labeled dendrite showing dendritic spine architecture. (D) Microlabeling of a 12-month-old adult hippocampal slice to which crystals were applied by airbrush on day of making slices (DIV 0). Blue lines trace the pyramidal cells layers of CA and DG. On DIV 7 the slice was fixed and imaged showing sparse distribution of crystals within the tissue (crystals appear as bright puncta in the image obtained with 4x objective). (E) Higher magnification (zoomed image obtained with 40x objective) of boxed region in D obtained in 488 nm channel on the confocal microscope showing labeled neuron in a maximum projection image. (F) 2D image of a 3D reconstructed image stack taken with 100x objective of the boxed region of the neuron identified in panel (E). Dendritic spines are visible along within the randomly labeled neuron after 8 DIV of slice culture.

problems with spontaneous rods became very severe but manufacturers of the medium claimed the contents had not changed. After finding many other labs were also having difficulty with neuronal growth, we decided to purchase components from sources we trusted and make our own medium. In addition to obvious benefits shown here in being able to reduce spontaneous rods and maintain survival of organotypic slices of adult rodent hippocampus, we discovered other benefits as well. The medium is much less

expensive per liter, concentrated stock of many components can be made and quick frozen in aliquots so only a few ingredients need to be made fresh, and specific components can be eliminated. For example, we can prepare a low fluorescent and low fluorescence-quenching medium by eliminating riboflavin, folic acid, tryptophan, and phenol red to improve the signal to noise for fluors excited at low wavelengths.

Cofilin-actin rod quantification has always been performed manually by scanning cofilin immunostained cultures. However, the question of what rod-like cofilin-stained structures count as rods has always been a problem for novices, especially in young cultures of dissociated neurons or in postnatal slices. Growth cones of neurons often contain bundles of actin associated with cofilin that look very much like the cigar-shaped rods in neurites. Here we show that the dynamics of cofilin in rods differs greatly from that in actin-cofilin structures in growth cones in which the proteins turnover within seconds rather than hours. Even for well-trained individuals, the tedium of manually rod counting is unwelcome. Thus, developing an automated unbiased program for the identification of cofilin rods in immunostained neurons or slice cultures was of high priority for creating an unbiased and consistent method for rod quantification. The rod analysis segmentation described in this thesis is probably not as accurate in counting rod numbers as manual counting by someone experienced in doing this analysis, but it is able to process substantially more data in a consistent manner. Nearly all rod data in this thesis was collected using automated unbiased analyses.

In vitro studies on adult rodent hippocampal slice cultures are rarely performed because of the rapid loss of dendritic morphology. The lack of success is partially due to culture medium conditions as well as the inevitable atrophy from the loss of established

circuitry during dissection. Using Map2 staining as a readout of dendrite integrity, we show that adult slice cultures can be maintained for at least 2 weeks by eliminating D-serine, optimizing L-cysteine concentration and medium osmolarity, and culturing in fresh GCM. These advances allow us to culture brain slices from neurodegenerative mouse models at critical periods during which the mice are undergoing cognitive dysfunction. It is important to note the health of the glia cultures before and during medium conditioning and to use GCM immediately after harvesting it from the glia. Although the Map2 staining in our adult slices declines in intensity during culture, even after two weeks we find wild type adult slices with long dendritic processes. We certainly do not claim that these are fully healthy slices since slow degeneration must continue to occur. However, it provides us with a method to test both exacerbation of degeneration or protection from degeneration of adult neurons in an in vitro environment over which we have total control. This is a major advance for studies on age-related neurodegenerative diseases.

Adhering slices to the coverslips with Vitrogel maintains their attachment even though degeneration might be occurring, thus allowing one to follow these changes. High resolution light and fluorescence microscopy can be done on slices as soon as they are attached since the Vitrogel is optically clear. Even in the presence of Vitrogel, slices can be fixed and immunostained but careful removal of the Vitrogel after fixation is also possible enhancing permeabilization and immunostaining. One negative consequence of using Vitrogel over a plasma clot, which is removed by plasmin treatment, is the inability to patch neurons for electrophysiology. During patch clamping, back-pressure is applied to a neuron to patch the cell's membrane and Vitrogel interferes. There is the possibility to remove the Vitrogel from living slices but this has not yet been tested for patching.

Lastly, we describe a novel method to use DiI to sparsely and randomly label neurons in slices or cultures of dissociated neurons that are alive or fixed. Investigation of dendritic spine density and morphology is typically visualized using either Golgi staining, a long method only of use on fixed tissue and not random, or expression of a fluorescent protein within a subpopulation of neurons. The latter method often uses the Thy-1 promoter to drive GFP expression in a subset of neurons or viral-induced expression of a fluorescent protein. Neither of these methods is truly random and so this type of spine visualization is often compared to results from diolisitic labeling, which is random by nature. The traditional diolistic labeling method requires a gene gun to accelerate particles carrying DiI. It is often difficult to work out conditions to deposit these beads within neurons without damage. Here, we simplify this labeling procedure by using an airbrush to generate a solution of optimal sized crystals that can be applied to brain slices using the airbrush or to cultures of dissociated neurons simply by addition of the crystal suspension to the medium. When we first started using DiI we found that by spraying an ethanol solution with an airbrush onto a sheet of parafilm, small rectangular crystals of DiI formed during solvent evaporation. These crystals could be placed onto a brain slice using a micromanipulator and label those cells in which it came into contact. We realized that the same crystal formation could be done at the liquid-liquid interface between heptane and a balanced salt solution (or medium). As the heptane evaporates, the DiI crystallizes and the crystals sediment into the aqueous solution. Coating pipette tips, microfuge tubes, and the airbrush with a charged molecule such as APES is necessary to ensure that DiI does not stick to the plastic surfaces. Spraying the aqueous medium containing crystals onto coverslips containing brain slices or cultured cells is

forceful and holding coverslips to the bottom of a chamber through capillary action during spraying is helpful. This spray force also ensures quick penetration of crystals onto the tissue or cells and limits time when the cultures or tissue are not in medium. This novel system is inexpensive, can easily be adapted to most labs, requires minimal troubleshooting, and effectively labels dendritic spines in a variety of culture settings.

References

Bardy C, van den Hurk M, Eames T, et al. Neuronal medium that supports basic synaptic functions and activity of human neurons in vitro [published correction appears in Proc Natl Acad Sci U S A. 2015 Jun 23;112(25):E3312]. *Proc Natl Acad Sci U S A*. 2015;112(20):E2725-E2734. doi:10.1073/pnas.1504393112

Faw TD, Lerch JK, Thaxton TT, Deibert RJ, Fisher LC, Basso DM. Unique Sensory and Motor Behavior in Thy1-GFP-M Mice before and after Spinal Cord Injury. *J Neurotrauma*. 2018;35(18):2167-2182. doi:10.1089/neu.2017.5395

Foster Olive M, Del Franco AP, Gipson CD. Diolistic Labeling and Analysis of Dendritic Spines. *Methods Mol Biol*. 2018;1727:179-200. doi:10.1007/978-1-4939-7571-6_14

Meberg PJ, Miller MW. Culturing hippocampal and cortical neurons. *Methods Cell Biol*. 2003;71:111-127. doi:10.1016/s0091-679x(03)01007-0

Ruiz C, Casarejos MJ, Gomez A, Solano R, de Yebenes JG, Mena MA. Protection by glia-conditioned medium in a cell model of Huntington disease. *PLoS Curr*. 2012;4:e4fbca54a2028b. Published 2012 Jul 2. doi:10.1371/4fbca54a2028b

Schwarz N, Hedrich UBS, Schwarz H, et al. Human Cerebrospinal fluid promotes long-term neuronal viability and network function in human neocortical organotypic brain slice cultures. *Sci Rep*. 2017;7(1):12249. Published 2017 Sep 25. doi:10.1038/s41598-017-12527-9

Shaw AE, Minamide LS, Bill CL, Funk JD, Maiti S, Bamburg JR. Cross-reactivity of antibodies to actin- depolymerizing factor/cofilin family proteins and identification of the major epitope recognized by a mammalian actin-depolymerizing factor/cofilin antibody. *Electrophoresis*. 2004;25(15):2611-2620. doi:10.1002/elps.200406017

Stettler O, Bush MS, Kasper M, Schlosshauer B, Gordon-Weeks PR. Monoclonal antibody 2G13, a new axonal growth cone marker. *J Neurocytol*. 1999;28(12):1035-1044. doi:10.1023/a:1007044207002

Tsai TH, Chen SL, Chiang YH, et al. Recombinant adeno-associated virus vector expressing glial cell line-derived neurotrophic factor reduces ischemia-induced damage. *Exp Neurol*. 2000;166(2):266-275. doi:10.1006/exnr.2000.7505

Withers GS, Higgins D, Charette M, Banker G. Bone morphogenetic protein-7 enhances dendritic growth and receptivity to innervation in cultured hippocampal neurons. *Eur J Neurosci*. 2000;12(1):106-116. doi:10.1046/j.1460-9568.2000.00889.x

Wolosker H. The Neurobiology of d-Serine Signaling. *Adv Pharmacol*. 2018;82:325-348. doi:10.1016/bs.apha.2017.08.010

CHAPTER 4

DIRECT INTERACTION OF HIV GP120 WITH NEURONAL CXCR4 AND CCR5 RECEPTORS INDUCES COFILIN-ACTIN ROD PATHOLOGY VIA A CELLULAR PRION PROTEIN- AND NOX-DEPENDENT MECHANISM[1]

Preface

This Chapter contains work that was initiated in our laboratory by Professor Thomas Kuhn in 2013 during which he and a former student, Keifer Walsh, identified cofilin-actin rods in neurons treated with the HIV gp120 envelop protein. This work developed into the primary thesis work of his graduate student, Lisa K. Smith at the University of Alaska Fairbanks, focused on responses of different tropic forms of gp120 and their receptors. She was the primary author of the chapter. My contribution to the work presented here was helping to resolve culture conditions, presented in more detail in Chapter 3, characterization of the lack of microglia and quantification of other glia in cultures of dissociated neurons, preparation and use of the amyloid-β d/t fraction, and characterization in cultured E18 rat neurons of the inhibition of gp120-induced rod formation by the CCR5 antagonist maraviroc. I am indebted to Chaoping Chen for obtaining the maraviroc for my studies on rat neurons. I am indebted to Raymond Swanson for providing the Iba-1 antibody microglia immunostaining.

[1]To be submitted: Lisa K. Smith, Isaac W. Babcock, Laurie S. Minamide, Alisa E. Shaw, Keifer P. Walsh, James R. Bamburg, Thomas B. Kuhn. Title not yet determined.

Summary

Nearly 50% of individuals with long-term HIV infection are affected by the onset of progressive HIV-associated neurocognitive disorders (HAND). HIV infiltrates the central nervous system (CNS) early during primary infection where it establishes persistent infection in microglia (resident macrophages) and astrocytes that in turn release inflammatory cytokines, small neurotoxic mediators, and viral proteins. While the molecular mechanisms underlying pathology in HAND remain poorly understood, synaptodendritic damage has emerged as a hallmark of HIV infection of the CNS. Here, we report that the viral envelope glycoprotein gp120 induces the formation of aberrant, rod-shaped cofilin-actin inclusions (rods) in cultured mouse hippocampal neurons via a /signaling pathway common to other neurodegenerative stimuli including oligomeric, soluble amyloid-β and proinflammatory cytokines. Synaptic function is impaired preferentially in the distal proximity of rods within dendrites. Our studies demonstrate gp120 binding to either chemokine co-receptor CCR5 or CXCR4 is capable of inducing rod formation, and signaling through this pathway requires active NADPH oxidase presumably through the formation of superoxide (O^{2-}) and the expression of cellular prion protein (PrP^{C}). These findings link gp120-mediated oxidative stress to the generation of rods, which may underlie early synaptic dysfunction observed in HAND.

Introduction

HIV infection of the CNS is characterized by the induction of inflammatory and neurotoxic insults, including the activation of microglia and astrocytes, suspected to stimulate a progressive synaptic degeneration manifested in cognitive decline. Despite

the prevalence of HIV-associated neurocognitive disorders (HAND) the underlying molecular and cellular mechanisms promoting pathogenesis remain poorly understood but are thought to consist of a combination of direct viral infection of the cells of the CNS and indirect neurotoxicity mediated by inflammatory cytokines, metabolites, and effects of viral proteins including the envelope glycoprotein gp120. Gp120 is a potent neurotoxin with roles in a number of indirect and direct neurotoxic pathways including the release of excitatory molecules, reactive oxygen species (ROS), and pro-inflammatory cytokines from activated microglia and astrocytes (indirect) as well as NMDAR mediated excitotoxicity and co-receptor mediated neuronal apoptosis arising from the direct interaction of gp120 with receptors expressed on the neuronal membrane (Lipton et al., 1991; Bell, 1998; Kaul et al., 2001; Chen et al., 2002; Wang et al., 2003; Lewerenz and Maher, 2015).

Gp120 facilitates viral entry to host cells via its interaction with primary host-cell receptor CD4 and chemokine co-receptors CCR5 (R5) and CXCR4 (X4) at host-cell lipid raft domains (Kozak et al., 2002). Gp120 co-receptor preference categorizes distinct strains of HIV on the basis of cellular tropism, with macrophage tropic (R5) strains binding CCR5 receptors, T-cell tropic (X4) strains preferentially binding CXCR4 receptors, and dual-tropic (R5/X4) strains binding both co-receptors (Wilen et al., 2012). Binding of gp120 to cellular receptors induces coalescence of lipid raft domains into large, stable platforms, a proposed mechanism for clustering receptors and components of receptor-activated signaling cascades observed in a number of CNS dysfunctions, including CNS aging and trauma, as well as Alzheimer's disease (Jana and Pahan, 2004). Indeed, in neurons, gp120 was found to enlarge and stabilize raft domains in a CXCR4-dependent

pathway involving the redox-sensitive translocation of neutral sphingomyelinase 2 (nSmase2) to the membrane and the forward trafficking, surface expression, and clustering of NMDA receptors to enlarged raft domains (Cremesti et al., 2002; Jana and Pahan, 2004). These studies are consistent with macro domain formation promoted by the release of ceramide from nSmase2-mediated hydrolysis of sphingomyelin to activate signaling in response to various agonists and stress signals. Specifically, a redox-sensitive translocation of nSmase2 is mediated by gp120 stimulating a lipid-raft localized NADPH-oxidase 2 (NOX2) with a subsequent production of superoxide (O^{2-}) radicals in neurons (Jana and Pahan, 2004).

The interaction of proteins with lipid-raft localized receptors as a mechanism of regulating pathologic signaling has been observed for a number of neurodegenerative diseases, most notably in Alzheimer's disease where soluble, stable amyloid-β dimers and trimers ($A\beta_{d/t}$) interact with the lipid raft-anchored cellular prion protein PrP^{C} to stimulate a pathway mediated by activated NOX leading to the formation of rod-shaped bundles of filaments composed of a 1:1 complex of cofilin-actin (Iskander et al., 2004; Minamide et al., 2010; Walsh et al., 2014). These rod-like inclusions are generated in response to oxidative stress conditions and arise from the oxidation of active (dephosphorylated form) cofilin in stressed neurons to form intermolecular disulfide cross-linked cofilin (Bernstein et al., 2013). Rods have been described during the progression of Alzheimer's and other neurodegenerative diseases where they contribute to cytoskeletal abnormalities and synaptic dysfunction through the disruption of normal actin dynamics, the blocking of neuronal transport, and the sequestration of cofilin (Maloney et

al., 2005; Minamide et al., 2000; Gu et al., 2010; Rahman et al., 2012; Cichon et al., 2012).

Given the similarities in the neuronal response to HIV gp120 and that of $A\beta_{d/t}$ it is feasible that gp120-sensitive production of O^{2-} mediated by NOX2 is similarly inducing the downstream formation of cofilin-actin rods. Here, we present evidence that gp120 signaling through chemokine co-receptors CCR5 and CXCR4 induces the formation of cofilin-actin rods via a pathway common to $A\beta_{d/t}$ and proinflammatory cytokines comprised of PrP^C and NOX2.

Methods

Ethics Statement: All animals were handled according to the guidelines provided by the National Research Council for the Care and Use of Laboratory Animals as approved by the Colorado State University Institutional Animal Care and Use Committee (IACUC approved protocol #17-7411A).

Reagents: All chemical reagents were obtained from Sigma-Aldrich Co. (St. Louis, MO) unless indicated otherwise. Tissue culture reagents and immunocytochemistry reagents were from ThermoFisher (Waltham, MA). Maraviroc and AMD3100 are from Santa Cruz. HIV gp120 proteins: MN and IIIB tropic forms (Immuno Diagnostics); CM and LAV tropic forms (ProSpec Proteins); BAL (NIH #4961). Primary antibodies: rabbit 1439 anti-cofilin antibody (2 ng/ml, affinity purified) (Shaw et al., 2004); mouse monoclonal actin antibody (C4; ThermoFisher); rabbit anti-CXCR4 (1:250-500; AIDS Reagent Bank, NIH #11232); rabbit anti-CCR5 (1:250-500; AIDS Reagent Bank NIH #11236); rabbit monoclonal

antibody to microglia (Iba-1, Abcam 178846) a generous gift from Dr. R.A. Swanson, UCSF; and mouse monoclonal antibody to glial fibrillary acidic protein (GFAP) (ThermoFisher, MA5-15086). Alex dye-secondary antibodies were from ThermoFisher.

Source of Neurons: Mouse neurons were obtained from either wildtype C57BL/6, PrP^C null (C57BL/6J-Prnp−/−; Talen) or $p47^{PHOX}$ null (B6N.129S2-Ncf1tm1Shl/J p47 phox -/-; JAX 027331) lines. Rat neurons were from Sprague-Dawley rats.

Neuronal Cell Culture: Hippocampal and cortical neuron cultures were prepared either from freshly dissected E16.5 fetal mouse or E18 fetal rat brains according to published methods (Barlett and Banker, 1984) or from cell stocks of these dissociated neurons slow frozen at 10^6 cells/ml (hippocampal neurons) or 10^7 cells/ml (cortical neurons) in 50% fetal bovine serum (FBS) and homemade Neurobasal medium (HNB, see below). Briefly, round glass coverslips (12 mm diameter, #1 German, Carolina Biologicals Supply Co.) inserted into 24 well plates were coated with 100 µg/ml poly-D-lysine in pH 8.4 borate buffer (30 min, RT), washed 3 times with ultrapure water, and air dried. Dissociated neurons were plated at a density of 40,000 neurons per well (0.5 ml medium per well) in 10 % FBS (Hyclone, VWR Radnor, PA)-supplemented complete growth medium composed of HNB (made from all components of commercial NB but with highly purified L-serine and adjusted to final concentrations of 175 µM L-cysteine, 2.5 mM glucose and to 300 mOsM with NaCl), Glutamax used at 25 µl/10 ml, 50 U/ml penicillin, 50 µg/ml streptomycin, and N21-MAX (R&D Systems) at 1 ml/50 ml. Cultures are maintained at 37° C in a humidified incubator under 5% CO_2. After 1-2 h, serum-containing medium was removed, replaced with complete growth medium (1 ml/well) and exchanged every 3 days.

Adenovirus Preparation: Recombinant, replication deficient adenovirus for the expression of EGFP-PrP^c, lacZ-GFP, and $DNp22^{PHOX}$ (a dominant negative from of the small membrane NOX subunit $p22^{PHOX}$) were made using the AdEasy system (He et al., 1998; Minamide et al., 2003). Virus titer was determined by immunostaining against E2A of infected HEK293 cells as previously described (Minamide et al., 2003). Titers were expressed as focus-forming units (ffu/ml) and were usually about 10^9 ffu/ml. Recombinant adenoviruses were stored at -80° C.

Adenovirus infection of neurons: Replication deficient, recombinant adenovirus was added to neurons 4 days after plating (days in vitro, DIV) at 30 to 200 multiplicity-of-infection (MOI) to express either EGPF-PrP^c, lacZ-GFP, or $DNp22^{PHOX}$. Infection was executed concomitant with a full medium exchange.

Rod Induction in neuronal cultures: Rod induction was initiated at 6 DIV over a time period of 16 h unless indicated otherwise. After a complete medium exchange (1 ml/well), doses between 250 pM and 750 pM of dual tropic gp120MN, monotropic X4 (gp120IIIB) or monotropic R5 (gp120Bal) were added in complete growth medium. Amyloid-β dimer/trimers ($Aβ_{d/t}$) were isolated from medium of 7PA2 cells as previously described (Walsh et al., 2002; Cleary et al., 2005; Davis et al., 2011) and used at ~1 nM final concentration (monomer equivalent) determined from Western blots with monomeric synthetic Aβ standards.

Culture Treatments: Maraviroc (R5 inhibitor, 100 nM), AMD3100 (X4 inhibitor, 50 nM) or TG6-227 (NOX inhibitor, kindly provided by Dr. J.D. Lambeth, Emory University) were added to some cultures 1 h prior to addition of gp120 and maintained for the duration of the experiment.

Immunolabeling of rods and chemokine receptors: Following treatments, neurons were fixed in 4% formaldehyde, 0.1% glutaraldehyde in warm (37° C at addition) phosphate buffered saline (PBS) for 30 min at room temperature. Cultures were washed 3 times with PBS and permeabilized with methanol (chilled to -20° C) for 3 min. After several washes with Tris buffered saline (TBS), cultures were treated with blocking buffer (5% goat serum, 1% BSA in TBS) for 1 h prior to the addition of primary antibodies overnight (4° C). After 3 washes with TBS, Alexa-488 or Alexa-564 secondary antibodies (1:1000) were applied for 1 h (room temperature), followed by 3 washes in TBS, and coverslips were then mounted onto glass slides with ProLong Gold Antifade containing DAPI (Molecular Probes, Eugene Or).

Immunolabeling of Iba-1: Following fixation in 4% formaldehyde in warm (37° C at addition) phosphate buffered saline (PBS) for 30 min at room temperature for cultures of dissociated neurons and 1h for slice cultures. Neurons were permeabilized with methanol (chilled to -20° C) for 3 min or antigen retrieved in boiling sodium citrate buffer (10 mM Sodium citrate, 0.05% Tween 20, pH 6.0) for 45 min. The same antigen retrieval was used for some slice cultures while others were methanol permeabilized for 15 min. Cultures were blocked in 10% Donkey serum in TBS 1% BSA solution (Fisher Sci., normal donkey serum ref#: 17000121) Application of primary antibody for rabbit affinity purified cofilin 1439 was at 2 ng/ul (Shaw et al., 2004), goat polyclonal to Iba-1 was at 1:500 (ab107159), and mouse monoclonal GFAP was at 1:500 (MA5-15086) overnight at 4° C in 1% BSA/TBS solution. Following TBS washes, highly cross adsorbed secondary antibody (1:500; Fisher Sci, Donkey anti-goat Alexa 647, Donkey anti-rabbit Alexa 561, Donkey anti-mouse Alexa 488) plus DAPI for 2 hr followed by 3 washes in TBS, and

coverslips were then mounted onto glass slides with ProLong Gold Antifade (Molecular Probes, Eugene OR). In our hands we did not see any distinct differences in Iba-1 staining, in slices, after antigen retrieval or methanol permeabilization (Supplementary Material, Chapter 4, S4.1).

Rod quantification: Immunolabeled neurons were imaged on an inverted fluorescence microscope using a 40x air objective and scored by an individual blinded to the treatments or by more than one individual. For most experiments, at least 100 neurons per coverslip were scored for the presence of rods with triplicates for each condition and three independent experiments. Neuronal processes in the vicinity of non-neuronal cells and rod-like staining in growth cones were disregarded in the analysis. Scoring in low density cultures was performed by calculating the percent of isolated neurons with rods, whereas in higher density cultures, rod index was scored by counting the number of rods per total nuclei (DAPI) per field of view.

Statistical Analysis: Quantification of all experiments were performed with at least triplicate samples for each condition and repeated in at least three independent experiments. Independent group averages (from triplicates) were used to calculate the standard deviations shown on plots. Significant differences among treatments and between treatments and controls were tested using by one-way ANOVA with Tukey's or Dunnett's posthoc-analysis using Graph Pad Prism software (GraphPad Software, Inc.).

Results

Gp120 interacts with neurons to induce actin-cofilin rods in a dose- and time-dependent manner.

Prior to experiments examining gp120-mediated rod induction, we first addressed the issue of spontaneous rod formation in neuronal cultures. Through many years of experiments scoring rods in neuronal cultures, untreated controls generally had fewer than 5% of neurons with "spontaneous" rods (e.g. Walsh et al., 2014), in recent years this number became much more variable and often exceeded 25%, with rods/cell (rod index) of 0.5 to 1.0, totally unacceptable in our experiments. As the increase in spontaneous rods is likely due to culture stress, we sought to improve culture conditions to reduce spontaneous rods. By using a complete growth medium based on homemade neurobasal (HNB) medium made with L-serine purchased from a supplier with low D-serine contamination, low glucose (2.5 mM), L-cysteine at 175 µM, and a physiological osmolarity of 300 mOsM (see Chapter 3), in most experiments we reduced neurons with spontaneous rods to 5% or less and lowered the rod index to less than 0.2 rods/neuron (see Chapter 2). Neuronal cultures were maintained in complete growth medium utilizing NB as a basal medium for all experiments reported here, with the exception of those examining the role of NOX activity.

Gp120 was demonstrated previously to be a potent generator of ROS (Walsh et al., 2004; Guo et al., 2013; Louboutin and Strayer, 2014). Given the requirement of oxidized cofilin for the formation of cofilin:actin rods, we examined whether gp120 is capable of inducing rod formation in cultured mouse hippocampal neurons. Neurons at DIV 6 were treated with increasing concentrations of dual-tropic $gp120_{MN}$ for 18 hours

before being fixed, immunostained for actin and/or cofilin, and evaluated for rod formation (Figure 4.1A). For each concentration tested, dual-tropic gp120 induced rod formation significantly above the untreated control in a dose-dependent manner (Figure 4.1B).

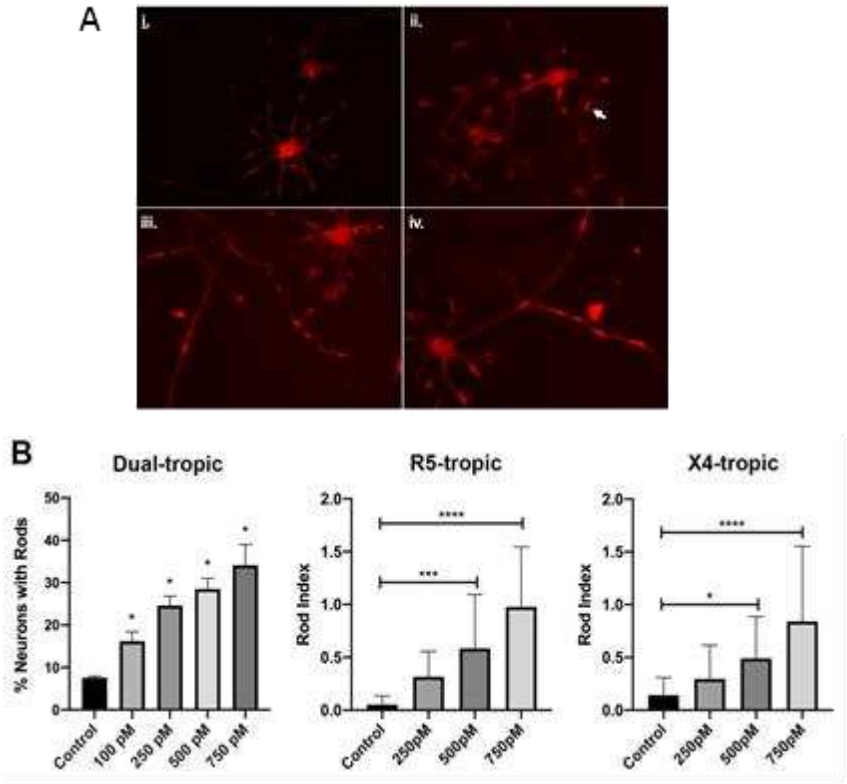

Figure 4.1. Tropic forms of gp120 induce dose-dependent rod formation. E16 mouse hippocampal neurons were grown 6 DIV and treated over night with dual- R5- and X4-tropic forms of gp120. A) Neurons treated with 250 pM dual-tropic $gp120_{MN}$ (ii), R5-tropic $gp120_{CM}$ (iii), X4-tropic $gp120_{IIIB}$ (iv) or untreated (i) for 16 hours then immunostained for cofilin and imaged. Each of the gp120 strains induced robust rod formation (*arrow indicates rod in ii)*. B) Hippocampal neurons were treated with increasing concentrations of dual-, R5-, and X4- tropic strains of gp120 proteins and processed as described above. Rods were induced in a dose-dependent manner. *p<0.05; ***p<0.005; ****p<0.001 from one-way ANOVA with Tukey's or Dunnett's posthoc-analysis using Graph Pad Prism software.

As dual-tropic gp120 is capable of binding to both R5 and X4 receptors, we further evaluated the ability of mono-tropic gp120 strains to induce rod formation. Neurons exposed to increasing concentrations of X4- and R5-tropic gp120 ($gp120_{IIIB}$ and $gp120_{BaL}$) for 18 h demonstrated rod formation significantly above control at concentrations of 500

and 750 pM for both strains tested, suggesting that both co-receptors are capable of initiating gp120-mediated rod formation (Figure 4.1B).

We next examined the time course of dual-tropic gp120 mediated rod formation. Mouse hippocampal neurons were treated with 500 pM dual-tropic gp120 and the percent of neurons forming rods increased over time, reaching significance above control by 6 h and half-maximum rod induction at 8 to 9 h (Figure 4.2A).

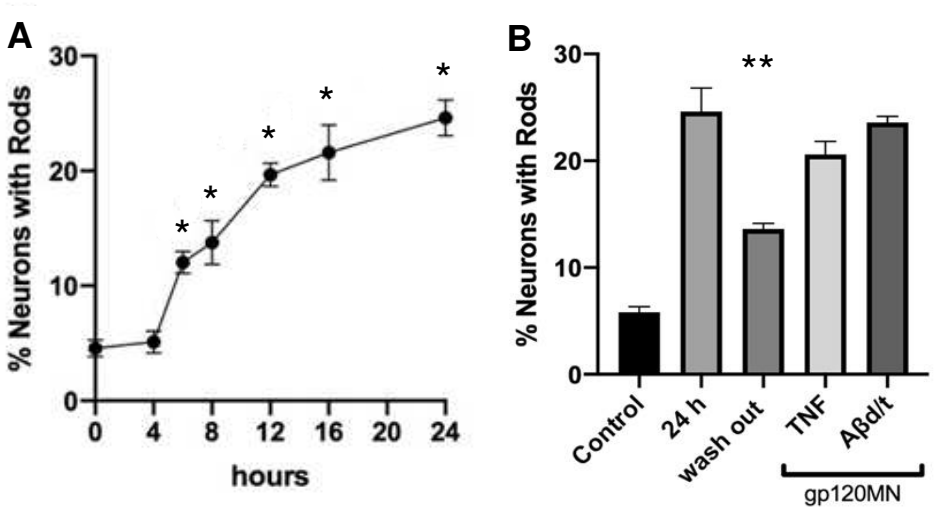

Figure 4.2. Time course of rod formation, reversal and lack of additive effects of rod-inducers. A) Percent of neurons expressing rods was quantified at 4, 6, 8, 12, 16, and 24 hours post exposure to 500 pM dual-tropic $gp120_{MN}$. *$p<0.05$ compared to 0 time point by one-way ANOVA with Tukey's posthoc-analysis using Graph Pad Prism software. B) Wash-out of $gp120_{MN}$ after 24 h significantly reduced rod formation (**$p<0.01$). No additive effect was observed upon incubation with both $gp120_{MN}$ and TNF-α or amyloid-β. gp*+TNF = 500 pM* $gp120_{MN}$ *& 50 ng/mL TNF-*α*, gp+*Aβ*d/t= 500 pM gp120 + 0.2 nM* Aβ*d/t.*

Previous studies have demonstrated that almost all neurons can form rods when subjected to energy depletion (Minamide et al., 2000) but rods are induced in a maximum of 20-25% of cultured mouse hippocampal neurons by $A\beta_{d/t}$ and the proinflammatory cytokine TNFα when used separately or in combination (Walsh et al., 2014), suggesting that both inducers are eliciting rod formation through the same pathway (Walsh et al., 2014). To determine if dual-tropic $gp120_{MN}$ is also inducing rods through this same

pathway, mouse hippocampal neurons were treated for 24 h with 500 pM dual tropic gp120 alone or in combination with either 50 ng/ml TNFα or 1 nM $A\beta_{d/t}$ before immunostaining and rod quantification. Rods were observed in 20-25% of dual-tropic gp120-treated neurons alone or in combination with $A\beta_{d/t}$ or TNFα (Figure 4.2B). Interestingly, we also found dual-tropic gp120-mediated rod formation to be reversible since washing out gp120 after a 22 h exposure significantly reduced the percentage of neurons with rods detected 2 h post washout (Figure 4.2B), similar to what was observed for TNFα-induced rods (Walsh et al., 2014). We observe similar rod induction by gp120 in mouse cortical neurons (dual-tropic gp120), as well as a time-dependent formation of rods in rat cortical neurons with R5 or X4-tropic gp120 (Supplementary Material, Chapter 4, S4.2). Notably, in rat cortical neurons, gp120 signaling through CXCR4 appears to be a more potent inducer of rod formation. Taken together, these findings suggest that gp120, $A\beta_{d/t}$, and TNFα all induce rod formation in a subpopulation of hippocampal neurons through what is likely a common pathway, and that continuous exposure to gp120 is required for the persistence of gp120-induced rods.

Rodent hippocampal neurons express CCR5 and CXCR4 chemokine receptors.

We next assessed the role of individual co-receptors in the induction of rods. Though most cell types in the human CNS express either chemokine receptor, there has been less consistent evidence of R5 expression on neuronal cells (Bell, 1998; Gabuzda and Wang, 2000; Canto-Nogues et al., 2005; Sorce et al., 2011). To confirm that both X4 and R5 are indeed expressed in rodent hippocampal neurons, both mouse and rat neurons were cultured to DIV7, fixed, and immunostained for each receptor on their surface (no permeabilization). Both receptors are widely expressed in rodent

hippocampal neurons on the soma as well as on all neurites (Figure 4.3A; Supplementary Material, Chapter 4, S4.3). As levels of CCR5 expression in mouse neurons have been reported to increase following exposure extrinsic stress insults (Joy et al., 2019), we tested whether gp120 exposure may also upregulate R5 membrane expression. Mouse hippocampal neurons were treated with 250 pM of R5 and X4-tropic gp120 for 16 h before being fixed and immunostained for R5 or X4. However, no increase in expression of either receptor was detected (data not shown).

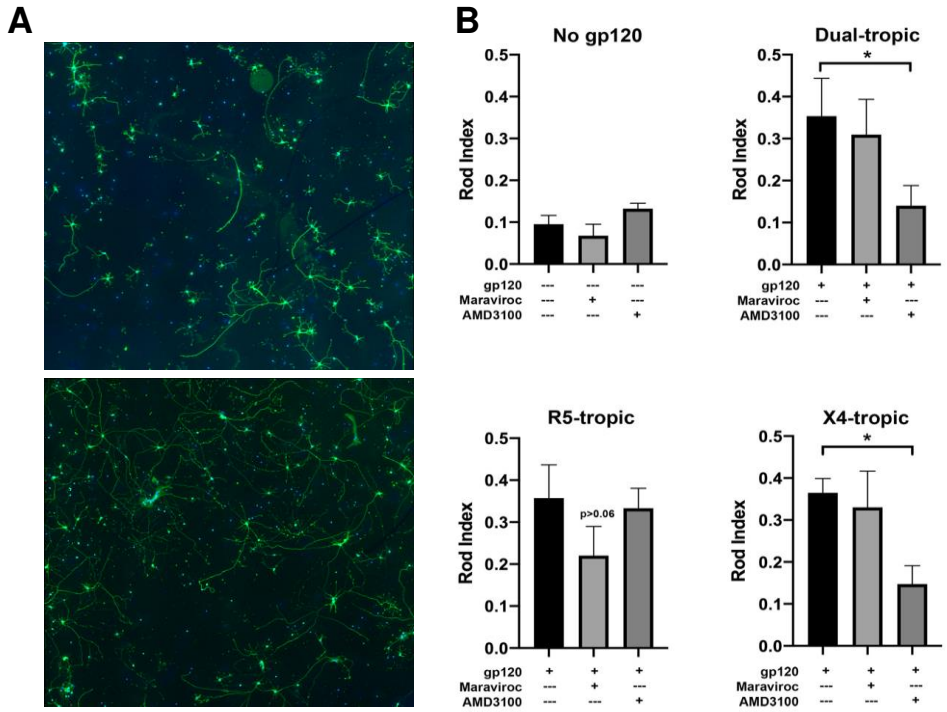

Figure 4.3. Mouse neurons express CXCR4 and CCR5 receptors. Antagonists of these receptors block rod induction by receptor-tropic gp120. A) Mouse hippocampal neurons (DIV7) immunostained for CCR5 (i) and CXCR4 (ii). B) Neurons were pre-treated with 100 nM maraviroc or 50 nM AMD3100 for 1h prior to gp120 exposure and maintained throughout 16-hour treatment. CXCR4 inhibitor AMD3100 blocked rod induction by X4-binding strains of gp120. CCR5 inhibitor maraviroc reduced rods in cells treated with R5-binding gp120 tropic strains but not as significantly as the CXCR4 inhibitor. *$p<0.05$ from one-way ANOVA with Tukey's or Dunnett's posthoc-analysis using Graph Pad Prism software.

Inhibition of X4 with receptor-specific antagonist AMD3100 blocks rod formation.

Whereas gp120 binding to R5 and X4 co-receptors is required for facilitating viral envelope fusion with the host membrane, interactions with other neuronal receptors, including N-methyl-D-aspartate receptors (NMDAR) and nicotinic acetylcholine receptors (nAChR) have been reported (Bracci et al., 1992; Xu et al., 2011; Ballester et al., 2012; Capó-Vélez et al., 2018). Having demonstrated that gp120 co-receptors are present in the membrane of rodent hippocampal neurons, we sought to confirm that it is the interaction of gp120 with these specific chemokine receptors that triggers rod formation. To this end, we exposed 6 DIV cultured mouse hippocampal neurons to 250 pM R5, X4, or dual tropic gp120 in the presence of 100 nM maraviroc and 50 nM AMD3100, receptor specific inhibitors for R5 and X4, respectively (Scholten et al., 2012). In neurons exposed to R5-tropic gp120, there was a measurable decrease in rod index in cultures exposed to maraviroc but it fell slightly short of the 95% significance level (Figure 4.3B). Rod index was restored to control levels in neurons exposed to X4-tropic gp120 in the presence of AMD3100, suggesting that gp120-mediated signaling through X4 may be a more potent activator of rod induction (Figure 4.3B). Neither maraviroc nor AMD3100 significantly affected rod induction in cultures exposed to the opposite receptor-binding gp120 strain. For dual-tropic gp120, only AMD3100 significantly reduced the number of rods, confirming the observation that neuronal rod induction is more sensitive to gp120 signaling through X4 (Figure 4.3B). Indeed, for both dual- and X4-tropic gp120, blocking X4 with AMD3100 returned rods to basal levels supporting the hypothesis that rod induction by gp120 is occurring through a CXCR4-mediated signal transduction pathway.

Gp120 mediates rod formation through a cellular prion protein PrP^C-dependent pathway that requires the NOX activation.

Rod induction by Aβ dimers and trimers (Aβ$_{d/t}$) and proinflammatory cytokines occurs through a PrP^c-dependent signaling pathway linking these ligands to the activation of NOX (Walsh et al., 2014). We hypothesized that gp120-mediated rod induction also requires membrane expression of PrP^C and active NOX. To test this hypothesis, we exposed hippocampal neurons from PrP^C-null mice to all three gp120 tropic strains. Unsurprisingly, none of the tested strains of gp120 induced rod formation (Figure 4.4A).

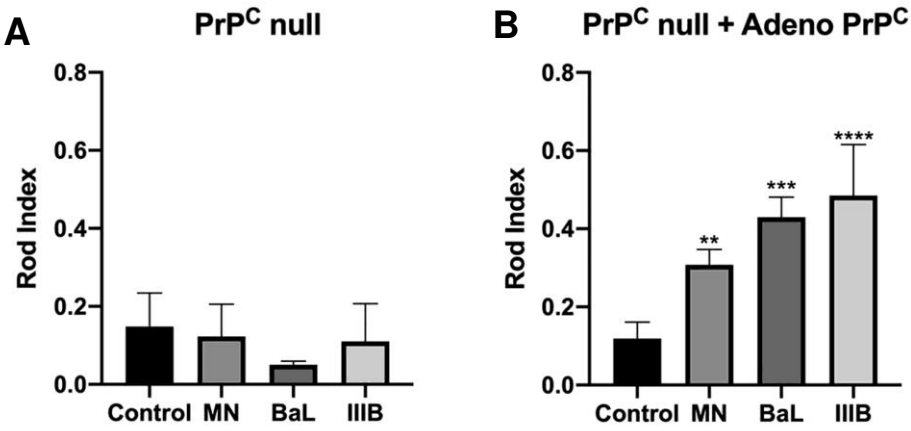

Figure 4.4. Gp120-induced rods requires the expression of cellular prion protein (PrP^C). A) E16 mouse hippocampal neurons cultured from a PrP^C-null mouse were exposed to each of the gp120 strains (250 pM, 16 h) and rod index calculated. None of the gp120 strains tested induced rod formation in PrPc-null neurons above control. B) PrP^C-null neurons were then infected with adenovirus expressing EGFP-PrP^C to drive re-expression of the protein. Infected cells were then exposed to 250 pM gp120 as described above and rod index calculated. In infected cells re-expressing PrP^C, all three strains of gp120 tested induced rod formation significantly above control. **p<0.01; ***p<0.005; ****p<0.001 from one-way ANOVA with Tukey's or Dunnett's posthoc-analysis using Graph Pad Prism software.

To verify the requirement of PrP^C expression for gp120-mediated rod formation, we infected PrP^C-null hippocampal neurons with adenovirus expressing EGFP-PrP^C

driven by a CMV promotor that has previously been demonstrated to drive the expression of functional PrP^C at the membrane surface (Haigh et al., 2005). In neurons re-expressing PrP^C, 18 h treatment with 250 pM of each tropic strain of gp120 induced a significant increase in rod formation over control (Figure 4.4B). Having confirmed the essential role of PrP^C in mediating gp120 induced rod formation, we next sought to confirm the requirement for active NOX.

Active NOX2, a superoxide (O^{2-}) generating multi-subunit enzyme, is comprised of two membrane subunits ($gp91^{PHOX}$, $p22^{PHOX}$) and three cytosolic components ($p47^{PHOX}$, $p67^{PHOX}$, and $p40^{PHOX}$) in addition to the ancillary small GTPase Rac1. To test the requirement for NOX activity in rod induction by gp120, we employed a combination of pharmacological, molecular, and genetic approaches to block NOX activity. First, we used the NOX inhibitor TG6-227 (kindly provide by Dr. David Lambeth, Emory University GA) and exposed cells to dual-tropic gp120. We found rod formation was significantly reduced in TG6-227-treated neurons when compared to controls (Figure 4.5A).

Next, we infected mouse hippocampal neurons with adenovirus expressing the dominant-negative mutant of the NOX small membrane subunit $p22^{PHOX}$ ($DNp22^{PHOX}$) at 30 and 100 MOI (multiplicity of infection) to inhibit NOX activation. $DNp22^{PHOX}$-expressing hippocampal neurons showed no increase in rod induction when exposed to 500 pM dual-tropic gp120 at either MOI tested (Figure 4.5B). In contrast, both control neurons and those infected with adenovirus expressing the lacZ reporter (control infected) responded to dual-tropic gp120 with a nearly 4-fold increase in rods (Figure 4.5B). Lastly, we showed that the absence of the cytosolic membrane subunit $p47^{PHOX}$ ($p47^{PHOX}$-null mouse line) prevented rod formation induced by each gp120 strain (Figure 4.5C). Together these

results demonstrate the inhibition of NOX activity is sufficient to block gp120-induced rod formation.

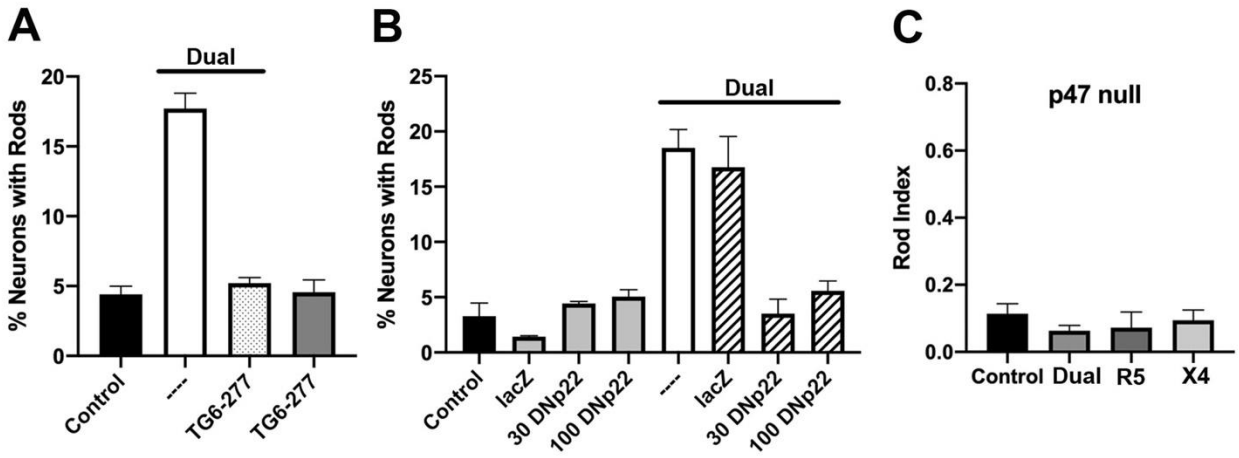

Figure 4.5. Gp120-induced rods occurs via a NOX mediated pathway. NOX activity was inhibited using pharmacologic, molecular and genetic approaches. A) The NOX inhibitor TG6-277 blocks dual-tropic gp120 mediated rod formation. B) Adenoviral infection of mouse hippocampal neurons with virus expressing dominant-negative mutant of NOX2 membrane subunit $p22^{PHOX}$ blocked dual-tropic gp120-induced rod formation at both MOIs tested. LacZ is infection control, not different from uninfected culture. C) Hippocampal neurons from a cytosolic subunit $p47^{PHOX}$ knock-out mouse were exposed to gp120 and evaluated for rod formation. None of the three strains of gp120 tested induced rod formation above control levels in $p47^{PHOX}$-null neurons.

Discussion

Here we describe for the first time HIV gp120-mediated induction of cofilin-actin rods as a novel mechanism potentially underlying synaptic dysfunction in HAND. Mouse hippocampal neurons were found to significantly increase both the percentage of neurons with rods as well as the number of rods in neurites following gp120 exposure. Rod induction requires gp120 interaction with R5 or X4 chemokine receptor and occurs through a pathway dependent on both PrP^C and NOX.

Cofilin:actin rod induction within neurites is a well-documented neuronal response to neurodegenerative stimuli including mitochondrial dysfunction, ischemia/reperfusion, NMDA receptor mediated excitotoxicity, and the PrPc/NOX-dependent stimuli that include $A\beta_{d/t}$, pro-inflammatory cytokines, and now, gp120 (Minamide et al., 2000; Chen et al., 2012; Walsh et al., 2014; Shu et al., 2018; Won et al., 2018).

Common to all rod inducers is the increased production of ROS in neurons exposed to these stimuli. We provide evidence that for gp120, activation of NOX, which produces ROS, is causal to rod formation supported by the absence of rod induction in cultures exposed to gp120 after preventing NOX activity through pharmacological inhibition, the introduction of dominant-negative mutation in the $p22^{PHOX}$ membrane subunit, or the gene-knockout of cytosolic subunit $p47^{PHOX}$. Furthermore, we demonstrate that PrP^C-null mouse hippocampal neurons do not generate rods in response to gp120 exposure. However, re-expressing PrP^C successfully recovered the potency of gp120 to induce rods in these cells. Notably, the neurotoxic $A\beta_{d/t}$ also requires NOX and is further dependent on the expression of PrP^C for induction of rods (Walsh et al., 2014).Taken together, these results provide evidence that rod induction via the PrP^C/NOX-dependent pathway may be a common mechanism underlying synaptic loss observed for a number of neurodegenerative diseases, including Alzheimer's disease and HAND.

HIV infection in the CNS appears restricted to microglia and macrophages while causing injury and apoptotic death in neurons (Jordan et al., 1991; Bell, 1998; Gerngross and Fischer, 2015). As such, there has been some debate as to the mechanisms of neurotoxicity— whether neuronal injury observed in HAND is the result of indirect effects mediated by the release of neurotoxic, proinflammatory host factors from infected or

activated glial cells, or rather the result of a direct neurotoxic effect of soluble HIV proteins shed from infected host cells and virus. Gp120 is a potent neurotoxin implicated in promoting neurodegeneration through a combination of both indirect and direct actions (Kaul and Lipton, 1999; Wallace, 2006; Mocchetti et al., 2012; Smith et al., 2018). Gp120 has been shown to trigger the release of pro-inflammatory and pro-apoptotic cytokines, including TNFα, from infected macrophages and activated microglia, in an indirect mechanism of neuroinflammation (Guo et al., 2013; Festa et al., 2015; Planès et al., 2018). Mechanisms of direct neurotoxicity are mediated by gp120 interactions with host receptors at the neuronal membrane (Catani et al., 2000). In addition to its R5 and X4 co-receptors, gp120 has also been demonstrated to directly interact with neuronal NMDAR and α7-nAChR leading to increased intracellular calcium and induction of apoptosis (Bracci et al., 1992; Corasaniti et al., 1998).

Dissociated mouse hippocampal cultures are virtually devoid of microglia cells (see Supplementary Material, Chapter 4, S4.1) yet contain approximately 40% GFAP-positive astrocytes. Previous studies in our lab showed that medium from these cultures have levels of the most common proinflammatory cytokines, e.g. TNFα, IL-1β, IL-6, that are 10 fold or more below the lowest level known to induce rods (Walsh et al., 2014). This suggested to us that gp120 might be interacting directly with chemokine co-receptors on the neuronal membrane to activate the PrP^C/NOX-mediated pathway of rod induction. Our results support rod formation results from the direct interaction of gp120 and neuronal R5 or X4 receptors. Interestingly, while signaling through either R5 or X4 induced a significant increase in rod index, there appear to be differences in the strength of induction associated with individual receptors. Blocking either receptor from interacting with gp120

led to a reduction in rods induced by receptor-tropic gp120 strains tested; however, only AMD3100 inhibition of the X4 receptor significantly reduced rod induction to levels of untreated controls for both dual-tropic and X4-tropic strains of gp120. We did not observe a significant decline in rod production for cultures treated with maraviroc to block rod formation by dual-tropic or R5-tropic gp120. Indeed, it appears that blocking gp120/R5-interactions with maraviroc achieves only a partial inhibition of rod induction. Though maraviroc treatment did achieve a reduction in rods, widespread cytotoxicity was observed in neuronal cultures treated with an initial concentration of 20 μM for inhibition of R5. To avoid neuron loss, the concentration of maraviroc was reduced to 100 nM, a concentration used widely in the literature. At 100 nM, we observed a small reduction in gp120 induced rod formation without apparent cytotoxicity. However, it is possible that at this lower maraviroc concentration we are not fully inhibiting R5 receptors, the remainder of which can then activate rod induction in response to gp120 binding. This is supported by results from dissociated rat neuron experiments where we did not notice cytotoxicity at 5 μM maraviroc but were able to prevent gp120-induced rod formation (Supplementary Material, Chapter 4, S4.3). Notably, inhibiting R5 with maraviroc had no effect on rod formation activated by the gp120 X4 tropic forms. Likewise, X4 inhibition with AMD3100 had no effect on R5-mediated rod induction. Thus, rod induction activated by different tropic-strains of gp120 is indeed receptor specific and independently activated by each receptor.

HAND in the post-cART era is no longer characterized by neuronal loss and brain atrophy; rather, neuronal synaptopathy has emerged as a hallmark of HIV-mediated neurotoxicity (Wenzel et al., 2019a). There is increasing evidence to support that

impairments in neuronal cytoskeleton structure and function underlie synaptopathy observed in HAND and that it is the action of neurotoxic HIV proteins driving these impairments (Avdoshina et al., 2017; Avdoshina et al., 2019; Wenzel et al., 2019b). Though gp120 has been demonstrated to play a role in synaptic dysfunction and dendritic simplification thought to underlie cognitive impairments observed in HAND, the mechanisms underlying gp120-mediated synaptic damage are not well understood (Masliah et al., 1997; Iskander et al., 2004; Smith et al., 2018). The activation of a PrP^C/NOX-mediated pathway of rod induction is one potential mechanism for gp120-induced synaptic dysfunction involving the perturbation of neuronal cytoskeleton dynamics.

Persistent rods have been observed during the progression of Alzheimer's and other neurodegenerative diseases (Minamide et al., 2000; Chen et al., 2012; Rahman et al., 2014). In these pathologies, rods have been demonstrated to induce synapse loss by the interruption of vesicular transport due to occluded neurites (Maloney et al., 2005; Cichon et al., 2012). Rods have further been linked to synaptic dysfunction via sequestration of cofilin from dendritic spines where it has a role in post-synaptic plasticity (Gu et al., 2010; Rust MB et al., 2015).

Thus, synaptopathy observed in HAND may arise from cytoskeletal aberrations induced by gp120 signaling through R5 and X4 in the form of cofilin-actin rods. Interestingly, a recent study reported dendritic simplification and cognitive flexibility in a transgenic rat model of HIV-1 infection can be rescued with the intracebroventricular administration of chemokine CXCL12 (aka SDF-1 alpha), the endogenous ligand for the X4 receptor (Festa et al., 2020). Presumably, CXCL12 outcompetes gp120 to bind

CXCR4, not only preventing gp120-associated synaptic toxicity, but also appearing to activate a pathway that seemingly reverses dendritic damage observed in HAND. Two different ligands signaling through X4 to generate opposite outcomes is not unheard of. Indeed, CXCL12 and gp120 signaling through X4 has previously been reported to differentially activate the spontaneous activity of Cajal-Retzius cells to opposite outcomes (Marchionni et al., 2012). In this study, the authors propose the ability of CXCL12 and gp120 to modulate excitability of these cells in opposite directions resulting from the activation of distinct pools of intracellular calcium by each ligand. In the case of gp120/CXCL12 signaling and dendritic spine morphology, it may be that gp120 and CXCL12 signaling through X4 similarly activate different intracellular targets to modulate cytoskeletal effects.

Our results provide evidence to support potential therapeutics for targeting rod formation to ameliorate not only HAND but also pathologic rod formation in response to several neurodegenerative stimuli, including Aβ and proinflammatory cytokines. Our results demonstrate gp120 co-receptor antagonists, specifically AMD3100 inhibition of X4, would be a potential mechanism to block rod formation. Further, Festa *et al.* (2020) demonstrated CXCL12-mediated rescue of dendritic spines suggesting gp120 co-receptor agonists should also be considered for their potential to activate protective pathways against gp120-mediated toxicity.

The importance of membrane architecture as a regulator of protein function in the gp120-mediated pathway to rod formation cannot be understated. Membrane lipid raft domains serve not only as critical sites of interaction for chemokine receptors, but are also essential for the appropriate receptor conformation to support co-receptor function

(Nguyen and Taub, 2002; Jana and Pahan, 2004). Recent studies have attributed a 'chaperone-like' allosteric function for cholesterol in stabilizing structural elements of integral membrane proteins through a cholesterol recognition/interaction amino acid consensus sequence, with demonstrable alterations of protein function by modulating cholesterol interactions (Fantini, 2003; Fantini and Barrantes, 2013). Notably, putative cholesterol binding sites have been identified in the structure of both R5 and X4, supporting the necessity of lipid raft localization for proper receptor function (Zhukovsky et al., 2013; Legler et al., 2017). Further, both PrP^C and NOX2 are localized to raft domains where raft composition similarly affects conformational stability and enzyme activity (Taylor and Hooper, 2006; Jin et al., 2011; Botto et al., 2014). Lipid rafts have been implicated in the pathology of several neurodegenerative disorders, including Parkinson's, Huntington's, and Alzheimer's disease where altered raft composition appears to underlie changes in signal transduction contributing to pathogenesis (Sonnino et al., 2014; Grassi et al., 2019). As gp120-induced rod formation requires signaling not only through lipid-raft localized receptors, but also the involvement of proteins tied to raft domains, membrane architecture becomes an important potential target for drug discovery and therapeutics directed against HAND.

References

Avdoshina V, Taraballi F, Tasciotti E, Üren A, Mocchetti I. (2019) Helix-A peptide prevents gp120-mediated neuronal loss. Molecular Brain 12:61.

Avdoshina V, Caragher SP, Wenzel ED, Taraballi F, Mocchetti I, Harry GJ. (2017) The viral protein gp120 decreases the acetylation of neuronal tubulin: potential mechanism of neurotoxicity. Journal of neurochemistry 141:606-613.

Ballester LY, Capo-Velez CM, Garcia-Beltran WF, Ramos FM, Vazquez-Rosa E, Rios R, Mercado JR, Melendez RI, Lasalde-Dominicci JA. (2012) Up-regulation of the neuronal nicotinic receptor alpha7 by HIV glycoprotein 120: potential implications for HIV-associated neurocognitive disorder. The Journal of biological chemistry 287:3079-3086.

Bamburg JR, Bernstein BW, Davis RC, Flynn KC, Goldsbury C, Jensen JR, Maloney MT, Marsden IT, Minamide LS, Pak CW, Shaw AE, Whiteman I, Wiggan O. (2010) ADF/cofilin-actin rods in neurodegenerative diseases. Current Alzheimer research 7:241-250.

Bartlett WP, Banker GA. (1984) An electron microscopic study of the development of axons and dendrites by hippocampal neurons in culture. I. Cells which develop without intercellular contacts. *J Neurosci*. 1984;4(8):1944-1953.

Bell JE. (1998) The neuropathology of adult HIV infection. Revue neurologique 154:816-829.

Botto L, Cunati D, Coco S, Sesana S, Bulbarelli A, Biasini E, Colombo L, Negro A, Chiesa R, Masserini M, Palestini P. (2014) Role of lipid rafts and GM1 in the segregation and processing of prion protein. PLoS One 9:e98344.

Bracci L, Lozzi L, Rustici M, Neri P. (1992) Binding of HIV-1 gp120 to the nicotinic receptor. FEBS Lett 311:115-118.

Canto-Nogues C, Sanchez-Ramon S, Alvarez S, Lacruz C, Munoz-Fernandez MA. (2005) HIV-1 infection of neurons might account for progressive HIV-1-associated encephalopathy in children. Journal of molecular neuroscience : MN 27:79-89.

Capó-Vélez CM, Morales-Vargas B, García-González A, Grajales-Reyes JG, Delgado-Vélez M, Madera B, Báez-Pagán CA, Quesada O, Lasalde-Dominicci JA. (2018) The alpha7-nicotinic receptor contributes to gp120-induced neurotoxicity: implications in HIV-associated neurocognitive disorders. Scientific Reports 8:1829.

Catani MV, Corasaniti MT, Navarra M, Nisticò G, Finazzi-Agrò A, Melino G. (2000) gp120 induces cell death in human neuroblastoma cells through the CXCR4 and CCR5

chemokine receptors. *J Neurochem*. 2000;74(6):2373-2379. doi:10.1046/j.1471-4159.2000.0742373.x

Chen B, Jiang M, Zhou M, Chen L, Liu X, Wang X, Wang Y. (2012) Both NMDA and non-NMDA receptors mediate glutamate stimulation induced cofilin rod formation in cultured hippocampal neurons. Brain Res 1486:1-13.

Chen W, Sulcove J, Frank I, Jaffer S, Ozdener H, Kolson DL. (2002) Development of a human neuronal cell model for human immunodeficiency virus (HIV)-infected macrophage-induced neurotoxicity: apoptosis induced by HIV type 1 primary isolates and evidence for involvement of the Bcl-2/Bcl-xL-sensitive intrinsic apoptosis pathway. Journal of virology 76:9407-9419.

Corasaniti, M. Tiziana, et al. (1998) Mechanisms of Neurotoxicity Induced by the HIV-1 Coat Protein, gp120, in Human Neuroblastoma Cells in Culture. In "*Nitric Oxide and the Cell: Proliferation, Differentiation, and Death*" S. Moncada et al. (Eds), Princeton University Press, Princeton New Jersey, 1998, pp. 157–170.

Cremesti AE, Goni FM, Kolesnick R. (2002) Role of sphingomyelinase and ceramide in modulating rafts: do biophysical properties determine biologic outcome? FEBS Letters 531:47-53.

Fantini J. (2003) How sphingolipids bind and shape proteins: molecular basis of lipid-protein interactions in lipid shells, rafts and related biomembrane domains. Cellular and Molecular Life Sciences CMLS 60:1027-1032.

Fantini J, Barrantes FJ. (2013) How cholesterol interacts with membrane proteins: an exploration of cholesterol-binding sites including CRAC, CARC, and tilted domains. Frontiers in physiology 4:31-31.

Festa L, Gutoskey CJ, Graziano A, Waterhouse BD, Meucci O. (2015) Induction of Interleukin-1β by Human Immunodeficiency Virus-1 Viral Proteins Leads to Increased Levels of Neuronal Ferritin Heavy Chain, Synaptic Injury, and Deficits in Flexible Attention. The Journal of Neuroscience 35:10550-10561.

Festa LK, Irollo E, Platt BJ, Tian Y, Floresco S, Meucci O. (2020) CXCL12-induced rescue of cortical dendritic spines and cognitive flexibility. eLife 9:e49717.

Gabuzda D, Wang J. (2000) Chemokine receptors and mechanisms of cell death in HIV neuropathogenesis. Journal of neurovirology 6 Suppl 1:S24-32.

Gerngross L, Fischer T. (2015) Evidence for cFMS signaling in HIV production by brain macrophages and microglia. Journal of neurovirology 21:249-256.

Goyal P, Pandey D, Brünnert D, Hammer E, Zygmunt M, Siess W. (2013) Cofilin Oligomer Formation Occurs In Vivo and Is Regulated by Cofilin Phosphorylation. PLoS ONE 8:e71769.

Grassi S, Giussani P, Mauri L, Prioni S, Sonnino S, Prinetti A. (2020) Lipid rafts and neurodegeneration: structural and functional roles in physiologic aging and neurodegenerative diseases. *J Lipid Res*. 2020;61(5):636-654. doi:10.1194/jlr.TR119000427

Gu J, Lee CW, Fan Y, Komlos D, Tang X, Sun C, Yu K, Hartzell HC, Chen G, Bamburg JR, Zheng JQ. (2010) ADF/Cofilin-Mediated Actin Dynamics Regulate AMPA Receptor Trafficking during Synaptic Plasticity. Nat Neurosci 13:1208-1215.

Guo L, Xing Y, Pan R, Jiang M, Gong Z, Lin L, Wang J, Xiong G, Dong J. (2013) Curcumin protects microglia and primary rat cortical neurons against HIV-1 gp120-mediated inflammation and apoptosis. PLoS One 8:e70565.

Haigh CL, Edwards K, Brown DR. (2005) Copper binding is the governing determinant of prion protein turnover. Mol Cell Neurosci 30:186-196.

Holten DJ, Canals M, Maussang D, et al. (2012) Pharmacological modulation of chemokine receptor function. *Br J Pharmacol*. 2012;165(6):1617-1643. doi:10.1111/j.1476-5381.2011.01551.x

Iskander S, Walsh KA, Hammond RR. (2004) Human CNS cultures exposed to HIV-1 gp120 reproduce dendritic injuries of HIV-1-associated dementia. Journal of neuroinflammation 1:7-7.

Jana A, Pahan K. (2004) Human immunodeficiency virus type 1 gp120 induces apoptosis in human primary neurons through redox-regulated activation of neutral sphingomyelinase. The Journal of neuroscience : the official journal of the Society for Neuroscience 24:9531-9540.

Jin S, Zhou F, Katirai F, Li P-L. (2011) Lipid raft redox signaling: molecular mechanisms in health and disease. Antioxid Redox Signal 15:1043-1083.

Jordan CA, Watkins BA, Kufta C, Dubois-Dalcq M. (1991) Infection of brain microglial cells by human immunodeficiency virus type 1 is CD4 dependent. Journal of virology 65:736-742.

Joy MT, Ben Assayag E, Shabashov-Stone D, Liraz-Zaltsman S, Mazzitelli J, Arenas M, Abduljawad N, Kliper E, Korczyn AD, Thareja NS, Kesner EL, Zhou M, Huang S, Silva TK, Katz N, Bornstein NM, Silva AJ, Shohami E, Carmichael ST. (2019) CCR5 Is a Therapeutic Target for Recovery after Stroke and Traumatic Brain Injury. Cell 176:1143-1157.e1113.

Kaul M, Lipton SA. (1999) Chemokines and activated macrophages in HIV gp120-induced neuronal apoptosis. Proceedings of the National Academy of Sciences of the United States of America 96:8212-8216.

Kaul M, Garden GA, Lipton SA. (2001) Pathways to neuronal injury and apoptosis in HIV-associated dementia. Nature 410.

Kozak SL, Heard JM, Kabat D. (2002) Segregation of CD4 and CXCR4 into distinct lipid microdomains in T lymphocytes suggests a mechanism for membrane destabilization by human immunodeficiency virus. Journal of virology 76:1802-1815.

Legler DF, Matti C, Laufer JM, Jakobs BD, Purvanov V, Uetz-von Allmen E, Thelen M. (2017) Modulation of Chemokine Receptor Function by Cholesterol: New Prospects for Pharmacological Intervention. Mol Pharmacol 91:331-338.

Lewerenz J, Maher P. (2015) Chronic Glutamate Toxicity in Neurodegenerative Diseases—What is the Evidence? Frontiers in Neuroscience 9:469.

Lipton SA, Sucher NJ, Kaiser PK, Dreyer EB. (1991) Synergistic effects of HIV coat protein and NMDA receptor-mediated neurotoxicity. Neuron 7:111-118.

Louboutin J-P, Strayer D. (2014) Role of Oxidative Stress in HIV-1-Associated Neurocognitive Disorder and Protection by Gene Delivery of Antioxidant Enzymes. Antioxidants 3:770-797.

Marchionni I, Beaumont M, Maccaferri G. (2012) The chemokine CXCL12 and the HIV-1 envelope protein gp120 regulate spontaneous activity of Cajal-Retzius cells in opposite directions. J Physiol 590:3185-3202.

Masliah E, Heaton RK, Marcotte TD, Ellis RJ, Wiley CA, Mallory M, Achim CL, McCutchan JA, Nelson JA, Atkinson JH, Grant I. (1997) Dendritic injury is a pathological substrate for human immunodeficiency virus-related cognitive disorders. HNRC Group. The HIV Neurobehavioral Research Center. Ann Neurol 42.

Minamide LS, Striegl AM, Boyle JA, Meberg PJ, Bamburg JR. (2000) Neurodegenerative stimuli induce persistent ADF/cofilin-actin rods that disrupt distal neurite function. Nature cell biology 2:628-636.

Mocchetti I, Bachis A, Avdoshina V. (2012) Neurotoxicity of human immunodeficiency virus-1: viral proteins and axonal transport. Neurotoxicity research 21:79-89.
Nguyen DH, Taub D (2002) CXCR4 Function Requires Membrane Cholesterol: Implications for HIV Infection. The Journal of Immunology 168:4121-4126.

Nguyen DH, Taub D. (2002) Cholesterol is essential for macrophage inflammatory protein 1 beta binding and conformational integrity of CC chemokine receptor 5. *Blood*. 2002;99(12):4298-4306. doi:10.1182/blood-2001-11-0087

Planès R, Serrero M, Leghmari K, BenMohamed L, Bahraoui E. (2018) HIV-1 Envelope Glycoproteins Induce the Production of TNF-α and IL-10 in Human Monocytes by Activating Calcium Pathway. Scientific Reports 8:17215.Sc

Rust MB. (2015) ADF/cofilin: a crucial regulator of synapse physiology and behavior. *Cell Mol Life Sci*. 2015;72(18):3521-3529. doi:10.1007/s00018-015-1941-z

Shaw AE, Minamide LS, Bill CL, Funk JD, Maiti S, Bamburg JR. (2004) Cross-reactivity of antibodies to actin- depolymerizing factor/cofilin family proteins and identification of the major epitope recognized by a mammalian actin-depolymerizing factor/cofilin antibody. *Electrophoresis*. 2004;25(15):2611-2620. doi:10.1002/elps.200406017

Shu L, Chen B, Chen B, et al. (2019) Brain ischemic insult induces cofilin rod formation leading to synaptic dysfunction in neurons. *J Cereb Blood Flow Metab*. 2019;39(11):2181-2195. doi:10.1177/0271678X18785567

Smith LK, Kuhn TB, Chen J, Bamburg JR. (2018) HIV Associated Neurodegenerative Disorders: A New Perspective on the Role of Lipid Rafts in Gp120-Mediated Neurotoxicity. Current HIV research 16:258-269.

Sonnino S, Aureli M, Grassi S, Mauri L, Prioni S, Prinetti A. (2014) Lipid rafts in neurodegeneration and neuroprotection. Molecular neurobiology 50:130-148.

Sorce S, Myburgh R, Krause K-H. (2011) The chemokine receptor CCR5 in the central nervous system. Progress in Neurobiology 93:297-311.

Taylor DR, Hooper NM. (2006) The prion protein and lipid rafts (Review). Molecular Membrane Biology 23:89-99.

Wallace DR. (2006) HIV neurotoxicity: potential therapeutic interventions. J Biomed Biotechnol 2006:65741-65741.

Walsh KA, Megyesi JF, Wilson JX, Crukley J, Laubach VE, Hammond RR. (2004) Antioxidant protection from HIV-1 gp120-induced neuroglial toxicity. Journal of Neuroinflammation 1:8.

Walsh KP, Minamide LS, Kane SJ, Shaw AE, Brown DR, Pulford B, Zabel MD, Lambeth JD, Kuhn TB, Bamburg JR. (2014) Amyloid-β and Proinflammatory Cytokines Utilize a Prion Protein-Dependent Pathway to Activate NADPH Oxidase and Induce Cofilin-Actin Rods in Hippocampal Neurons. PLoS ONE 9:e95995.

Wang Z, Pekarskaya O, Bencheikh M, Chao W, Gelbard HA, Ghorpade A, Rothstein JD, Volsky DJ. (2003) Reduced expression of glutamate transporter EAAT2 and impaired glutamate transport in human primary astrocytes exposed to HIV-1 or gp120. Virology 312:60-73.

Wenzel ED, Avdoshina V, Mocchetti I. (2019a) HIV-associated neurodegeneration: exploitation of the neuronal cytoskeleton. Journal of neurovirology 25:301-312.

Wenzel ED, Speidell A, Flowers SA, Wu C, Avdoshina V, Mocchetti I. (2019b) Histone deacetylase 6 inhibition rescues axonal transport impairments and prevents the neurotoxicity of HIV-1 envelope protein gp120. Cell death & disease 10:674-674.

Wilen CB, Tilton JC, Doms RW. (2012) HIV: cell binding and entry. Cold Spring Harbor perspectives in medicine 2.

Won SJ, Minnella AM, Wu L, et al. (2018) Cofilin-actin rod formation in neuronal processes after brain ischemia. *PLoS One*. 2018;13(10):e0198709. Published 2018 Oct 16. doi:10.1371/journal.pone.0198709

Xu H, Bae M, Tovar-y-Romo LB, Patel N, Bandaru VV, Pomerantz D, Steiner JP, Haughey NJ. (2011) The human immunodeficiency virus coat protein gp120 promotes forward trafficking and surface clustering of NMDA receptors in membrane microdomains. The Journal of neuroscience : the official journal of the Society for Neuroscience 31:17074-17090.

Zhukovsky MA, Lee PH, Ott A, Helms V. (2013) Putative cholesterol-binding sites in human immunodeficiency virus (HIV) coreceptors CXCR4 and CCR5. Proteins 81:555-567.

CHAPTER 5

ALPHA-SYNUCLEIN INDUCES A REVERSIBLE COFILIN-ACTIN ROD PATHOLOGY IN NEURONS IN VITRO AND IN VIVO THROUGH A PRP^C- AND NOX-DEPENDENT PATHWAY MEDIATED BY CXCR4/CCR5[1]

Preface

Work contained in this chapter is a collaborative project with Marcia Liz and her student Marina da Silva, University of Porto, Portugal. Marina spent several months in our lab at the beginning of the time I started my undergraduate lab work. Her project was also a collaboration with the laboratory of Tiago Outeiro, Max Planck Institute for Experimental Medicine, Goettingen, Germany. The project was to determine if cofilin-actin rods were a pathology in alpha-synuclein overexpressing mice. Our laboratory has an ongoing collaboration with the lab of Ray Swanson, UCSF, to study cofilin-actin rods in stroke. The Swanson lab also works with PD mice and we facilitated the sharing with Marina sections of brain tissue from mice in which alpha-synuclein preformed fibrils (PFF) had been injected. Marina identified rods within the hippocampus of these animals and this finding resulted in our application of adult hippocampal slice cultures to study the role of rods in PDD. We obtained Thy-1-alpha-synuclein mice and PFF from the Swanson lab.

[1]Manuscript will be submitted with the following authors: M. I. Oliveira da Silva, I. W. Babcock, M. Santejo, L.S. Minamide, A.E. Shaw, S. J. Won, E. Castillo, T. Outeiro, R.A. Swanson, J.R. Bamburg, M.A. Liz. Univ. Porto, Porto, Portugal; Colorado State University; University of California, San Francisco; Max Planck Institute, Goettingen, Germany.

Summary

Alpha-synuclein is the major protein of Lewy Bodies, intracellular amyloid deposits found in the hippocampus of subjects with Lewy body dementia. Lewy Body dementia affects cognition in an age-dependent manner and often accompanies a familial form of Parkinson's disease with dementia (PDD) that arises from mutations in alpha-synuclein or its increased expression, most often arising from the duplication of the alpha-synuclein gene. Alpha-synuclein can adopt a β-amyloid structure that aggregates into oligomers and eventually into insoluble fibrils that deposit into Lewy Bodies. Degeneration of hippocampal neurons in mice overexpressing alpha-synuclein requires expression of the cellular prion protein (PrP^C) and functional NADPH oxidase (NOX). Cofilin, a major F-actin binding and severing protein, also plays a degenerative role through its ability to form within dendrites and axons of neurons, rod-shaped bundles of cofilin-actin (1:1) filaments (rods) that cause distal atrophy and synaptic dysfunction. Exposure of neurons to extracellular factors associated with inducing dementia, such as amyloid-β in AD, proinflammatory cytokines in neuroinflammation, or the viral envelope gp120 protein in HIV-associated neurocognitive disorder (HAND), activates a PrP^C- and NOX-dependent signaling pathway leading to rod formation. Preliminary results from our collaborators showed that rod formation was induced in brains of mice injected with preformed fibrils (PFF) of alpha-synuclein. Here we utilized slices from the hippocampus of adult wild type (WT) and alpha-synuclein-expressing mice, fixed immediately after preparation or cultured in roller tubes for up to 12 days, to follow age-dependent development of rod pathology, and to determine if rod formation is enhanced by exposure of slices to sonicated PFF. Results from an unbiased semi-automated quantification of rod pathology in both slices and cultures of dissociated neurons demonstrated that: (1) rod formation

occurs in an age dependent manner in alpha-synuclein overexpressing mice but not in age matched WT mice; (2) treatment with PFF exacerbates rod formation in slices from the younger alpha-synuclein mice and induced rods in the slices from the WT mice at all ages; (3) rod formation induced by PFF is dependent on PrP^C and NOX; and (4) rod formation is inhibited in neurons by treatments with antagonists of co-receptors CXCR4 and CCR5, which also inhibit rod formation induced by the other diseases associated factors mentioned above.

Introduction

The most prevalent form of dementia following Alzheimer's disease is dementia with Lewy bodies (DLB). Lewy bodies are cytoplasmic inclusions first identified in Parkinson's disease subjects in dopaminergic neurons in the substantia nigra pars compacta of the brainstem, but have also been identified in other brain areas such as the hippocampus, and cortex (Byrne et al. 1991; Adamowicz et al., 2017). Lewy bodies are primarily composed of the 140 amino acid protein alpha-synuclein (α-Syn) (Spillantini et al., 1998; Meade et al., 2019) as amyloid fibrils (Guerrero-Ferreira et al., 2020).

Parkinson's disease with Lewy Body dementia (PDD) is especially prevalent in patients with an autosomal dominant mutation resulting in duplication of the α-Syn gene (SNCA) or those that overexpress a missense mutation in α-Syn (Polymeropoulos et al., 1997; Lesage et al., 2013; Kiely et al., 2013; Konno et all, 2016; Book et al., 2018; Araki et al., 2019). However, other mutations leading to PD may work upstream of α-Syn but still result in PDD (Kitada et al., 1998).

α-Syn is an intrinsically disordered protein with an N-terminal membrane associated alpha-helix that has a role in vesicle release at synaptic terminals (Eliezer, 2001; Burré et al., 2010). Upon contact with a lipid micelle or bilayer, the N-terminal region restructures into an alpha-helical domain. However, it also can fold into stable beta-sheet structures that aggregate into fibrils and deposit into inclusions called Lewy bodies (Singh et al., 2011). Autosomal dominant mutations in α-Syn resulting in PDD are located in the region of amino acids 45-57 and affect the ability of one amyloid folded α-Syn associating with another. (Zarranz et al., 2004; Appel-Cresswell et al., 2013; Baba et al., 1998; Fares et al., 2014; Polymeropoulos et al., 1997; Yoshino et al., 2017). A point mutation in the SNCA gene leading to expression of a G51D form of alpha-synuclein, the most severe form of familial PDD, results in alpha-synuclein oligomers preferring to stay as oligomers rather than progressing to fibrils (Fares et al., 2014). This finding bears a striking similarity to the Alzheimer-like dementia in subjects with the Osaka ΔE693 mutation in the amyloid precursor protein (APP) leading to production of AβΔE22 which remains as soluble dimers or small oligomers and leads to early and severe dementia without amyloid plaques (Tomiyama et al., 2008). Together, these findings suggest that major forms of dementia are induced by soluble oligomers of amyloidogenic peptides.

As with all amyloid-associated dementias, the mechanim(s) behind α-Syn-induced synaptic dysfunction and neurodegeneration is not well understood (Kim et al., 2014). Neurons can secrete endogenous α-Syn suggesting it could act extracellularly (Emmanouilidou et al., 2010). Soluble α-Syn species have been postulated to regulate mGluR5 and NMDARs producing neurotoxic signaling (Ferreira et al, 2017) similar to the pathway suggested for Aβ oligomer-induced neurodegeneration (Walsh et al., 2014). Yet

most research has focused on the mechanism of α-Syn prion-like propagation of fibrils (Kim et al., 2014). It is still controversial as to how secreted or intracellular α-Syn aggregates contribute to synaptic dysfunction but it has been suggested that secreted α-Syn can induce intracellular fibril formation. It is hypothesized that the secreted alpha-synuclein leads to neurodegeneration because of its ability to induce intracellular fibril formation (Kim et al., 2014).

In AD, defects in both the actin and microtubule cytoskeletal networks have been described. Alleviating the defects in actin results in enhanced cognition in mouse models suggesting the cytoskeleton plays a critical role in amyloid-based dementias (Shaw and Bamburg, 2017). Neurons rely on the cytoskeleton to carry out their essential functions including vesicle transport, synaptic dynamics and plasticity, and energetic homeostasis through mitochondrial fission and distribution (Bamburg and Bloom, 2009; Bamburg and Bernstein, 2016). Disorganized microtubules and Tau-containing neurofibrillary tangles occur in AD. In addition, altered actin filament structures including actin cofilin-actin rods are present in AD brain (Minamide et al., 2000). These changes may be responsible for the alterations in dendritic spines that are contemporaneous with the decline in synaptic efficacy during AD progression (Herms and Dorostkar, 2016). Amyloid-β (Aβ) oligomers, especially the dimer/trimer fraction, induce rod-like inclusions of bundled filaments containing cofilin:actin in a 1:1 molar ratio (Minamide et al., 2010). Furthermore, rod formation induced by Aβ is dependent on PrP^C and a functional NOX (Walsh et al., 2014) and both appear to be required for α-Syn-induced actin cytoskeletal alterations (Hou et al., 2018; Zhong et al., 2018), suggesting that α-Syn may induce rod formation through the same molecular pathway as Aβ.

To test this hypothesis, we used adult organotypic hippocampal slices from male mice overexpressing α-Syn (X-linked expression) along with their age matched wild-type littermates to follow rod formation and rod location in the hippocampus from 4, 7, and 10.5 month mice. We further treated slices with PFF or amyloid beta to see if rod formation is exacerbated in α-Syn-expressing mice or induced in wild-type slices. In addition, we examined the role of PrP^C and NOX in the rod signaling pathway initiated by PFF by using cultured neurons from mice lacking either PrP^C (PrP^C KO) or a functional NOX complex (p47 KO). Finally, we tested the effect of a peptide called RAP310, an antagonist of the CCR5 and CXCR4 co-receptors identified in Chapter 4 as mediating the gp120 rod response, in preventing or reversing rod formation from added PFF in both cultured adult brain slices and dissociated neurons.

Methods

Animals: All animals were handled according to National Research Council's Guidelines to Care and Use of Laboratory Animals as approved by the Colorado State University Institutional Animal Care and Use Committee protocols 17-7541A, 17-7411A and 18-7779A. The lines of mice used are: Line61 Thy-1-α-Syn mice (Chesselet et al, 2012); C57BL6/DBA2 50:50 background as breeding stock for the Line61 mice; p47 null mice ($p47^{phox-/-}$) JAX stock number 027331 B6N.129S2-Ncf1tm1Shl/J); PrP^C null mice ($PrP^{-/-}$) TALEN (Nuvolone et al., 2016); C57BL6 wild type mice. Breeding pairs of Line61 and p47 null mice were generously provided by Dr. Ray Swanson, University of California, San Francisco. $PrP^{-/-}$ mice were generously provided by Mark Zabel, Prion Research Center, Colorado State University.

Genotyping of the Line61, Thy-1-α-Syn (SNCA triplicate gene) was performed from tissue obtained from ear notching at weening (P20-21). The ear notch is placed in 25 mM NaOH/ 0.2 mM EDTA, pH 12.0 and heated to 95° C for 1 h. Samples are then vortexed, cooled to room temperature and neutralization buffer (75 µL 40 mM Tris, pH 5.0) is gently mixed into the tubes. After 1 min, samples are centrifuged at 4,000 rpm for 3 min and the supernatant containing the DNA is removed. The forward and reverse primers (GACGGGTGTGACAGCAGTAGCC) and (GATGATGGCATGCAGCACTGG), respectively, were added for PCR (1x Phire buffer, 0.2mM dsNTPs, 0.7x Orange G, Phire Hot Start II 0.4 µL/ 20 µL reaction, initial denaturation at 98° C for 30 s, followed by 36 repeated cycles of 98 ° C for 5 s then 67 ° C for 5 s then 72° C 13 s with a final extension at 72 ° C for 2 min and held at 4 ° C) used to produce a DNA product of 350 base pairs indicative of the inserted Thy1-α-Syn gene.

Adult mouse hippocampal slice cultures: Dissection and culturing of adult brain slices was performed as described in Chapter 3. Ages of WT and α-Syn overexpressing mice were within a few days of each other and were obtained at approximately 4, 7 and 10.5 months of age. If dissections spanned multiple days, WT and α-Syn mice were always paired together on each day. Duration of time from euthanasia to culture never spanned more than 2 hrs with brains and slices kept cold during this entire period. Each mouse yielded 24 slices from the hippocampus of hemisphere and the entire contralateral hippocampus was quick frozen and stored at -80° C in case it was needed for other uses. For every experiment comparing rods in slices between genotypes, coverslips contained mixtures of medial, temporal and septal slices for each treatment or comparison group. Treatments

were started on either DIV 7 or 8 and continued for 4 days. Medium was changed every other day requiring one reapplication of the treatment with medium change.

Specifics for each group are listed below.

Mice at 4 months: Cultures of hippocampal slices (48, 2/coverslip) were obtained from 2 male alpha-synuclein mice and an identical number from 2 male WT mice. The added glial conditioned medium (GCM) was used fresh and changed completely every other day.

Mice at 7 months: Cultures of hippocampal slices (48, 2/coverslip) were obtained from 2 male alpha-synuclein mice and an identical number from 2 male WT mice. In addition, 24 slices of each genotype were obtained from two $p47^{PHOX-/-}$, two $PrP^{-/-}$, and two WT C57DB/J6 (genotype control). The GCM was harvested from glial cultures and held overnight at 4^{o} C prior to changing on slice cultures every other day.

Mice at 10.5 months: Cultures of hippocampal slices (48, 2/coverslip) were obtained from 2 male alpha-synuclein mice and an identical number from 2 male WT mice. The added glial conditioned medium (GCM) was used fresh and changed completely every other day.

Cultures of dissociated mouse hippocampal neurons: Dissociated neurons from timed pregnant WT, p47 KO, and PrP^{C} KO mice were obtained from embryos taken at E16.5 and cultured on coverslips in wells of 24 well plates as described in Chapter 3. Neurons were plated at 30,000 cells per well in 10% FBS in HNB for 2 h then changed to complete HNB medium (1 ml) without FBS. Medium was completely changed on DIV 2 and DIV 5, with treatments occurring on DIV 6 and fixation 16h later on DIV 7.

Preparation of α-Syn preformed fibrils: Human α-Syn preformed fibrils (PFF) were a generous gift from Drs. Ray Swanson and Erica Castello at the University of California, San Francisco. PFF were prepared according to the protocol established by the Michael J Fox Foundation for Parkinson's Research (Patterson et al., 2019). Briefly, human α-Syn monomers (RP-003, Proteos) were diluted to 5 mg/ml in 0.01M phosphate buffered saline (PBS) containing 0.03% sodium azide to prevent bacterial growth. Monomers were shaken at 1000 rpm in an orbital shaker at 37° C for 7 days to induce the formation of PFF. Images of monomers and PFF taken by negative staining transmission electron microscopy (Supplementary Material, Chapter 5, S5.1) were kindly provided to us by Erica Castello. Aliquots (12 µl) were rapidly frozen in liquid nitrogen, shipped to CSU on dry ice, and stored at -80° C. An aliquot was thawed, diluted 1:50 in PBS to 0.1 mg/ml and small, single use aliquots of 100X final concentration were rapidly frozen in liquid nitrogen. Upon use an aliquot is thawed, sonicated in bath sonicator at room temperature for 5 min and added to neuron or slice cultures at 1 µg/ml. Controls cultures were treated with an equal volume of the PFF storage buffer (PBS + 0.03% sodium azide) diluted 1:50 in PBS.

Culture and slice treatments with antagonists of CXCR4 and CCR5: Cultures of hippocampal slices and dissociated neurons were treated alone or in the presence of PFF with the following receptor antagonists: Maraviroc, an antagonist of CCR5 (see Chapter 4), was dissolved to 20 mg/ml in 70% ethanol, with a dilution to 50 µg/ml in PBS before dilution to 50 ng/ml in culture; AMD3100, an antagonist of CXCR4 (see Chapter 4), was dissolved to 5 mg/ml in PBS and also diluted to 50 µg/ml before addition to cultures at 50 ng/ml. Rap310 (all D amino acid octapeptide ASTTTNYT; Creative BioPeptides, Inc.)

was diluted from a 10^{-6} M stock in water to 10^{-9} M in glial conditioned medium (GCM) and used at a 1:100 dilution in cultures to obtain a final concentration of 10^{-11} M.

Fixation and Immunostaining:

Slices and cultures of dissociated neurons were fixed, permeabilized and immunostained as described in Chapter 3.

Slices from 4 month mice: DIV 0 and DIV 7 slices were immunostained for cofilin, Map2, and GFAP. DAPI was used to stain chromatin. Treated slices (DIV 12) were immunostained for cofilin, GFAP, and microglia (Iba1 antibody). DAPI was also applied.

Slices from 7 month mice: DIV 0 and DIV 7 slices were immunostained for cofilin, Map2, and Iba1. DNA was labeled with DAPI. Treated slices (DIV 12) were immunostained for cofilin and nuclei stained with DAPI.

Slices from 10.5 month mice: All slices were immunostained for cofilin and Map2 with DNA stained with DAPI.

Cultures of dissociated neurons were immunostained for cofilin and the growth cone antigen with 2G13 monoclonal antibody. DNA was labeled with DAPI.

Microscopy and image analysis: Neurons were imaged on the Keyence microscope with a 40x air objective as described in Chapter 3. The percent of cells that are neurons was determined manually and rods were counted in stitched images of the coverslip along with total nuclei using the unbiased semi-automated procedure described in Chapter 3. Rods per nucleus were converted to rods per neuron based on the percent of neurons determined manually to obtain rod index values. To obtain percent neurons with rods we

manually scored coverslips on the Nikon Diaphot 300 microscope using the 60x Nikon plan apo oil objective (NA 1.4).

Slices were imaged on the Keyence microscope with a 40x air objective as described in Chapter 3 for mapping the location of cofilin pathology. Rod quantification was performed using the Olympus Spinning Disk Confocal with the 60x oil objective. Rods in every field were counted using the unbiased semi-automated procedure described in Chapter 3.

Statistical analysis: Method of Statistical analysis described in figure legends. Statistical comparisons were performed with PPM software from SAS and are shown using the following symbols for p values. * $p<0.05$, ** $p<0.01$, # $p<0.005$, and ## $p<0.001$. NS = not significant.

Results

Cofilin-containing rods form in α-Syn mice during development of cognitive impairment. Thy-1-α-synuclein (Line 61) mice are cognitively normal at 4 months (Chesselet et al., 2012) but show significant hippocampal-dependent learning and memory deficits by 6 months. To determine if α-Syn overexpressing mice form cofilin-containing rods contemporaneously with cognitive defects, we fixed DIV 0 hippocampal slices from WT and α-Syn mice at 4, 7 and 10.5 months and immunostained for cofilin and Map2, as well as with DAPI. Images were captured and processed for rods using the unbiased and semi-automated procedure described in Chapter 3. Even without quantification, it was obvious that much greater cofilin immunostained rods accumulated in the α-Syn overexpressing mice than in the same age WT mice (Figure 5.1). We initially focused on

the dentate gyrus, a region of the hippocampus that was shown previously to develop abundant rods in response to amyloid-β (Davis et al., 2011). WT mice had low rod abundance that did not change significantly between 4 and 10.5 months when quantified as either rod numbers per unit area (Figure 5.1B) or rod area as a percentage of total field area (Figure 5.1C).

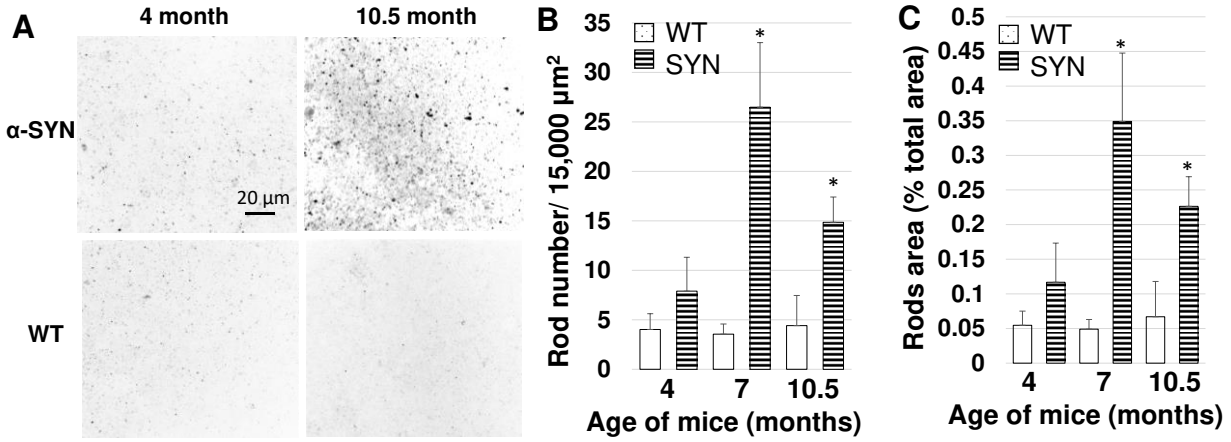

Figure 5.1. Comparison of cofilin rod response in the dentate gyrus of wild type and α-Syn overexpressing mice during aging. (A) Inverted fluorescence images of rods in a comparable field from the dentate gyrus of α-Syn overexpressing mice and WT mice sacrificed at 4 month, before onset of cognitive deficits, and at 10.5 months. Images have been processed for rod identification in slices using the method described in Chapter 3. (B) Rod response quantified using the unbiased semiautomatic method for counting rod numbers per field in 8 fields from each of two mice for each genotype in each age group. (C) Same data expressed in terms of rod areas as a percent of total field area. The error bars are standard deviation and the differences between WT and α-Syn mice of each age were from a 2 way ANOVA with Tukey's posthoc text for variance. Values of significance: *7m SYN p=0.018; *10m SYN p=0.0239.

Characterization of rod localization within brain slices: We performed rod quantification using the semi-automatic and unbiased algorithm for 5 areas within the hippocampus of WT and α-Syn mice at 10.5 months of age, a time at which the α-Syn mice were showing visible abnormal behavior. From 4 of the regions, CA1, CA3, DG, and Sub, we obtained 8 contiguous fields and 4 fields from the MF region from each of 4 slices (Figure 5.2A). At least two different mice were used for each data set and slices within each set

represented medial, septal and temporal locations. The rod numbers in every region of the slices from the 10.5 month α-Syn mice except the subiculum are significantly elevated over the same age WT mice (Figure 5.2B).

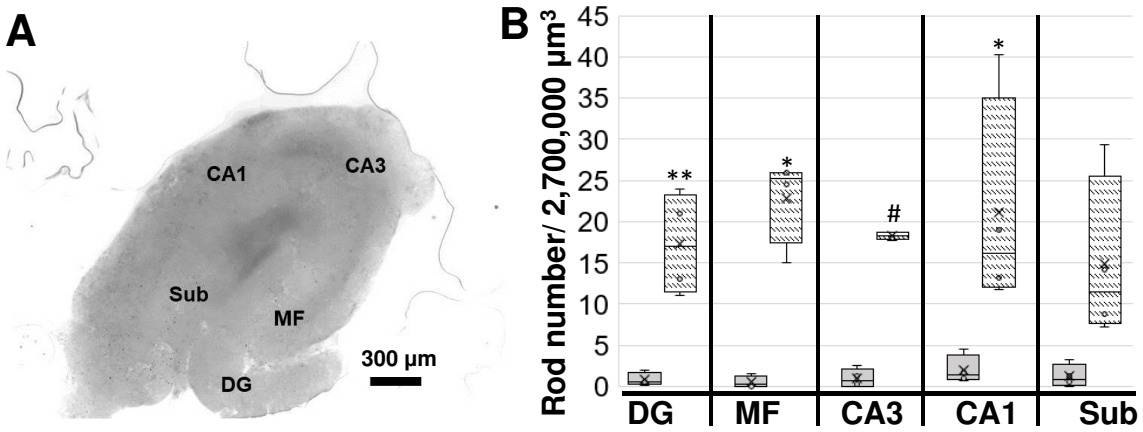

Figure 5.2. Localization and quantification of rods in the hippocampus of WT and α-Syn mice from unbiased semi-automatic analysis of cofilin immunostaining. (A) Cofilin immunostained brain slice obtained with a 2x objective on the Keyence microscope. A DAPI stained image (not shown) was used to localize the different regions labeled as CA1 and CA3 (Cornu Ammonis 1 and 3), MF (mossy fiber tract), DG (dentate gyrus), and Sub (subiculum). (B) Rod numbers per volume shown were calculated from 3D images through the entire slice (150 µm thick) using the full focus maximum projection capture. Because of background fluorescence the rod numbers are very much under estimated in Keyence images. In each area, WT slice is on left and α-Syn slices have the herringbone pattern. Bars show the range for middle 50% of the values with X being the mean and the cross bar the median. Error bars represent the range of highest and lowest slice averages. Significance calculated by 2 way ANOVA of each α-Syn group compared to its WT set. *=$p<0.05$; **=$p<0.01$; #=$p<0.001$. p value for subiculum is 0.085.

Characterization of adult brain slice integrity during roller tube culture. Slice morphology and dendritic arrays in the CA3 region were examined in DIV 0 and DIV 7 slices following fixation and immunostaining for Map2 and cofilin along with DAPI staining (Figure 5.3). Both WT and α-Syn slices from 4 month mice retained their overall morphology and Map2 dendritic arbors during the 7 days in culture, although the Map2 staining intensity decreased and there was a decline in the number of Map2 branches. WT slices from 7 and 10.5 month mice were similar to those from 4 month at both DIV 0 and DIV 7, whereas

slices from the 7 and 10.5 month α-Syn mice showed a clear decline in the density of dendritic arbors over the 7 days in culture even though their gross morphology appeared normal (Figure 5.3). More detailed analysis of the Map2 staining in the DIV 0 slices from 7 month and 10.5 month α-Syn mice showed that Map2 staining was present but only through about 25% of the Z-stack sections at 7 month and less than 10% of the Z-stack sections in the 10.5 month mouse.

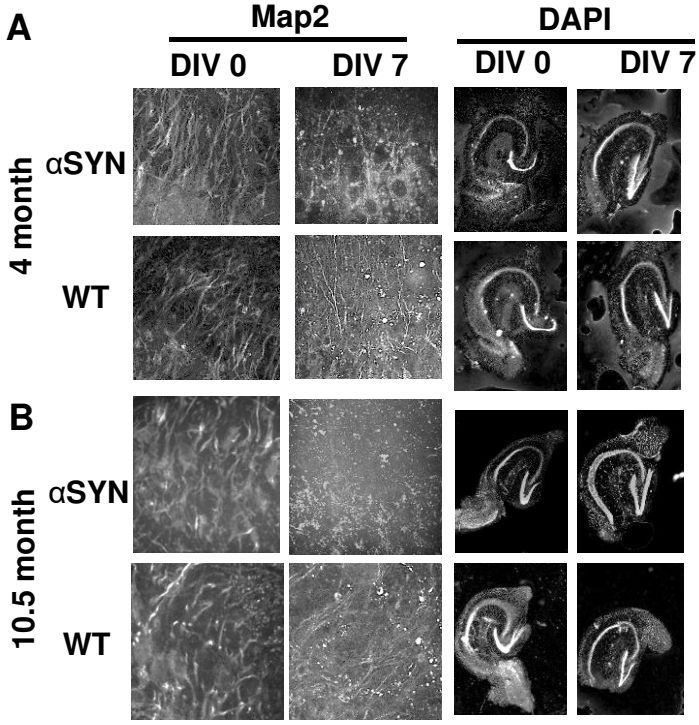

Figure 5.3. Evaluation of brain slice health in culture by Map2 and DAPI staining. (A) Both WT and α-Syn mice maintain dendrites and gross morphology over 7 DIV. (B) WT slices from 10.5 month mice maintain dendrites similar to 4 month slices whereas α-Syn slices lose almost all Map2 staining of longer dendrites even while keeping gross morphology. Map2 images are from confocal microscope with 60X objective and DAP images are from Keyence with 2x objective.

To determine if the loss of dendrites seen in the α-Syn slices cultured 7 DIV might arise from continued rod formation, we quantified rods in the DIV 0 and DIV 7 slices (Figure 5.4). Rod numbers and rod areas were not significantly different between DIV 0 and DIV 7 in WT slices from 4 to 10.5 months and are also similar to the slices from 4 month α-

Syn mice. However rods continued to form in the slices from the 7 and 10.5 month α-Syn mice between DIV 0 and DIV 7, increasing two to three fold in both number (Figure 5.4A) and area (Figure 5.4B).

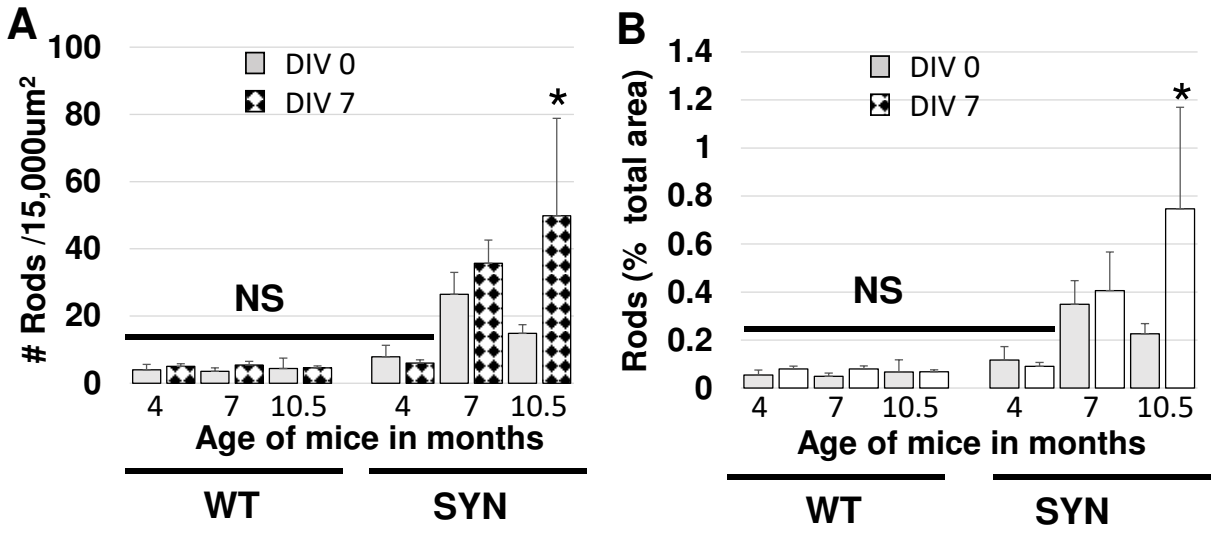

Figure 5.4. Changes in rod number and rod area during 7 days in culture for adult slices from WT and α-Syn mice of different ages. Rod numbers (A) and Rod areas (B) remain constant over the 7 DIV for WT slices from 4 to 10.5 month animals and are the same for the 4 month α-Syn slices. However, there is a doubling or tripling of rod numbers during 7 DIV for slices from the 7 and 10.5 month α-Syn mice. Data acquired by confocal imaging with 60x objective. n=2-4 slices for each time point. *=$p<0.021$ using 2 way ANOVA with Tukeys post hoc analysis. NS= no significant difference.

PFF induces rod formation in cultured hippocampal neurons: Cultures of dissociated WT mouse neurons (E16.5) were treated on DIV 6 with 1 μg/ml PFF or buffer control and analyzed on DIV 7 for rod formation (Figure 5.5). Approximately 20-23% of neurons formed rods compared with 5% or less in control treated cultures. Furthermore, the rod index (rods/neuron) was about 4 fold higher than control, similar to findings that have been previously reported for neurons treated with amyloid-β (see Chapter 6).

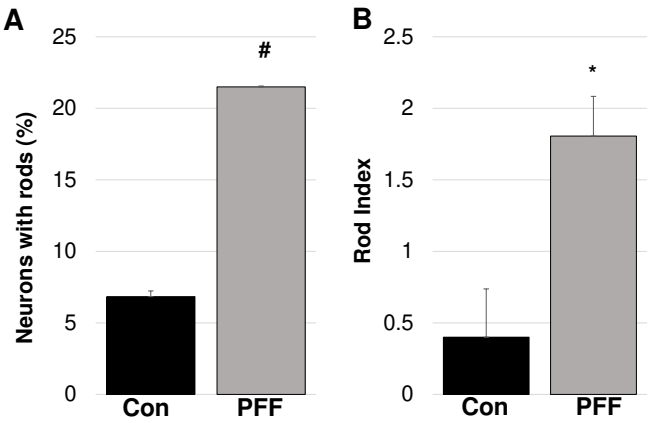

Figure 5.5. PFF induces cofilin rods in cultured hippocampal neurons. (A) Percent of neurons with rods was scored manually after overnight treatment of DIV 6 cultures with 1 µg/ml freshly sonicated PFF and immunostaining for cofilin and for growth cone antigen with 2G13 antibody. (B) Number of rods per neuron (Rod Index) was scored using the semi-automated growth cone exclusion method in chapter 3. (n=4, each repeat run in triplicate). # p=0.002; * p=0.013 by Students T-test.

We also used the dissociated neuronal cultures to validate that the PFF-induced rods are in fact cofilin-actin rods by dual immunostaining for cofilin and actin (Figure 5.6).

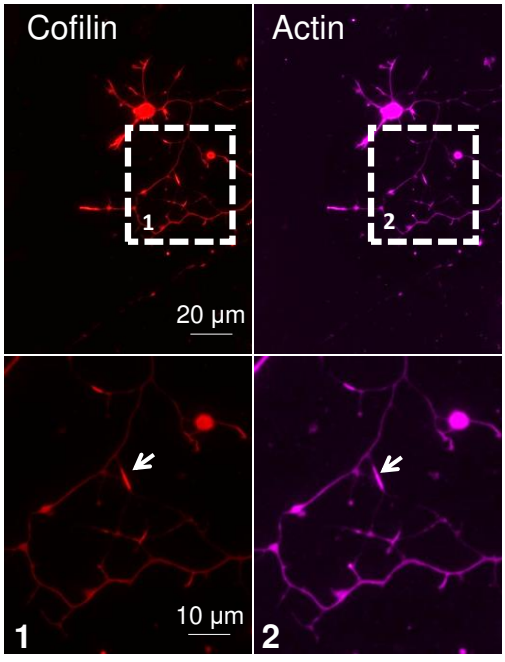

Figure 5.6. PFF-induced rods in hippocampal neurons contain both cofilin and actin. Neurons were cultured 6 DIV and treated overnight with 1 µg/ml PFF. After washing, fixation and permeabilization with 100% methanol, cofilin and actin were immunostained. Upper panels are lower magnification figure with boxed region of a rod shown at higher magnification below. I thank Tom Kuhn for obtaining this Figure.

PFF induces cofilin-actin rods in adult hippocampal slices: To determine if α-Syn PFF can induce rods in hippocampal slices, cultured WT and α-Syn brain slices from 4 and 10 month mice that were cultured for 7 or 8 DIV were treated with 1 μg/ml PFF or with the PFF buffer control. After 4 or 10 days, with culture medium (and PFF) changed every two days, slices were fixed and immunostained for cofilin and Map2, along with DAPI staining. None of the slices treated for 10 days with PFF survived. Each of the slices treated for 4 days with PFF were fixed and stained for cofilin, scanned in 3D, and both rod area and rod number were quantified (Figure 5.7).

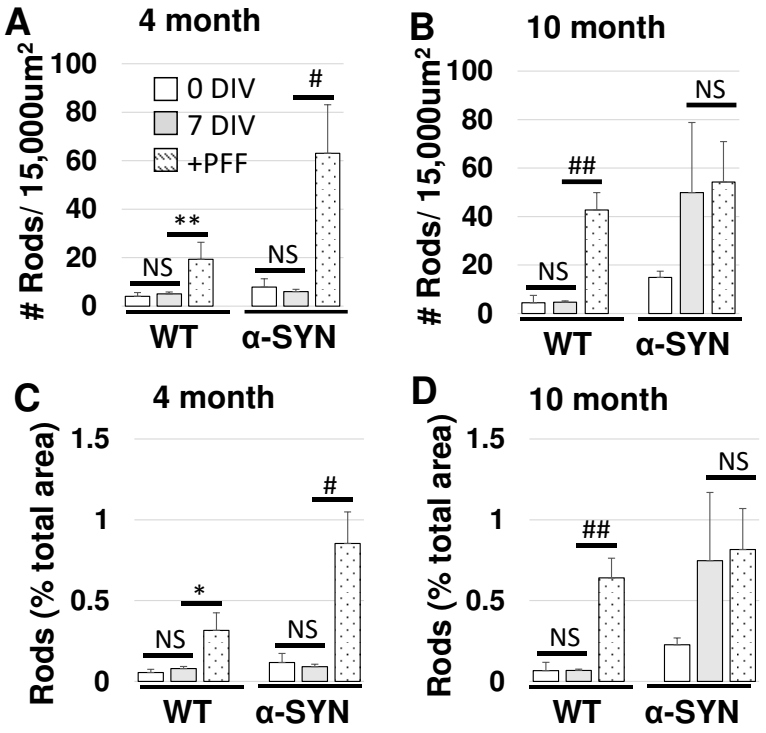

Figure 5.7. Quantification of rod number (upper panels) and rod area (lower panels) in adult WT and α-Syn slices from mice at the ages shown with or without treatment with 1 μg/ml PFF. Data is from confocal image stacks of 30 μm slice obtained with a 60x objective within the same region of the DG. n=4 for each treatment and age. Error bars are standard deviations. 2 way ANOVA with post hoc Students T-test comparing DIV 7 to PFF treatment gave the following p values: For rod numbers at 4 month WT p=0.0075, α-SYN p=0.0046, 10m WT p=0.00051, 10m SYN p=0.415. For rod areas: 4m WT p=0.0101, 4m αSYN p=0.00164, 10m WT p=0.0008, 10m α-SYN p=0.409.

WT slices all showed a significant increase in rods following PFF treatment with the 4 month α-Syn slices behaving the same. At 10 months, α-Syn slices had reached a maximum rod response that was not increased further by PFF-treatment.

PFF-treated WT slices have identical rod numbers and distribution as in 10 month slices from α-Syn mice: Knowing that PFF of α-synuclein induces rods in both cultures of neurons and slices, we asked if the distribution of rods in slices would differ between WT slices treated with PFF and those of a similar aged adult mouse expressing α-Syn. As found previously, rods in WT slices at DIV 0 are very low (Figure 5.8). Rod numbers in 10 month α-Syn slices are significantly above WT in all regions, but rod numbers and distribution in WT slices treated 4 DIV with PFF do not differ significantly from those endogenously over expressing α-Syn suggesting an identical rod forming neuronal population. This conclusion is supported by the plateau reached in rod formation in slices from α-Syn mice which is not increased following PFF treatment (Fig. 5.7).

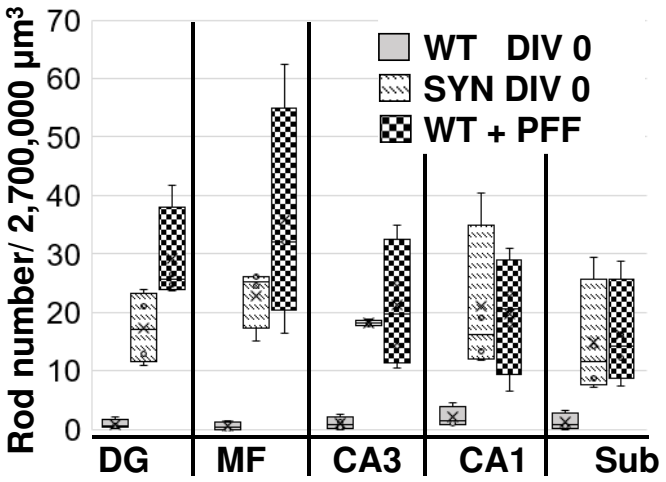

Figure 5.8. Comparison of rod numbers and distribution in brain slices of 10 month α-Syn mice with those from untreated and PFF-treated 10 month WT mice. Rod numbers determined by the semi-automatic and unbiased analysis algorithm. For each group, n=4 with 8 fields per slice in each region except MF, which had 4 fields. Error bars show range of the averages per slice with X the mean and the cross bar the median. PFF-treated WT and α-Syn expressing slices are all significantly above WT controls but are not significantly different from each other by 2 Way ANOVA with post hoc Student's T-Test.

Estimation of rods per length of dendrites: Given the numbers of rods we were quantifying in brain slices, we wanted to determine what these numbers related to in terms of rods per some unit length of dendrite or dendrite length per rod. To perform such an estimate we needed to obtain an estimate of the total dendritic lengths in a volume of tissue in which we quantified rods. We selected the CA3 region which had a well preserved Map2 immunostained dendritic arbor from WT DIV 0 slices. We used a 3D reconstruction of a confocal Z-stack to obtain the 2D single plane image shown in Figure 5.9A used to calculate the average Map2 stained area per 3500 μm^2. We then calculated the average width of a dendrite within this field (Figure 9B) and obtained the length from the area/width. In the figure shown, the average width is about 1.4 µm, the average area about 3500 μm^2 and the resultant dendritic length in the field is estimated as 2.5 mm.

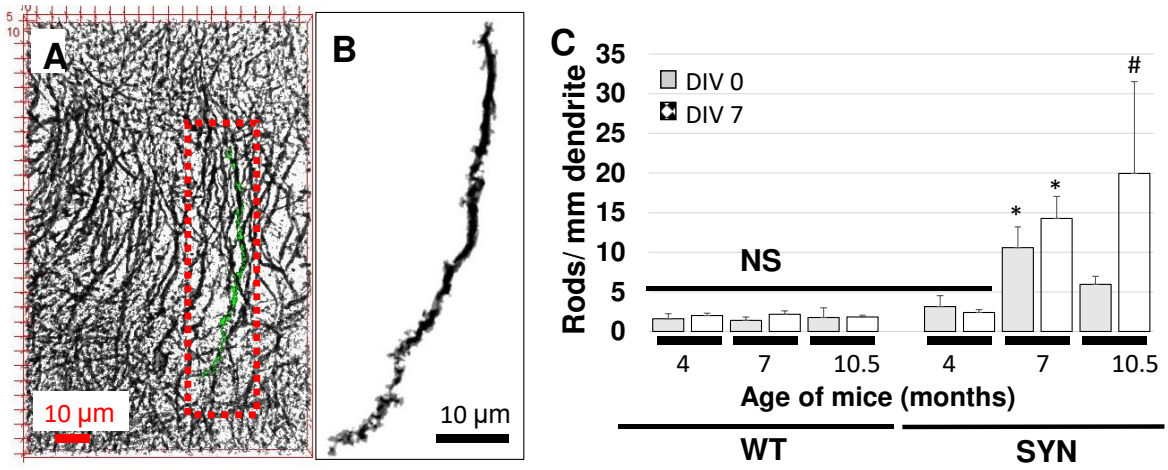

Figure 5.9. Determining rods per unit length of dendrites. (A) 3D reconstruction of a 60x 30 µm confocal Z-stack with 0.2 µm step size in the CA3 region of 7m DIV 0 WT slices showing intricate array of Map2-immunostained dendrites. 2D Single Z-plane image was used to calculate the average area of Map2 per field ~3500 μm^2. (B) Extracted tracing of a single dendrite within the boxed area in panel (A) overlayed in green. The ability to resolve dendritic spine architecture is useful for other ongoing projects explained elsewhere in this thesis. To obtain width of dendrites such as the one in (B), 5 equally spaced lines are drawn across it and the measurements averaged. This region contains proximal and secondary dendrites and 5 widths were averaged in each image stack. (C) Rod numbers per mm dendrite length from single confocal planes of WT and α-Syn mice of different ages, including before rod formation started in α-Syn mice (DIV 0 slice from a 4 month mouse). Rod numbers are corrected for overlap between planes.

In slices from all ages of WT mice and from 4 month α-Syn mice we identified at most 2 rods per mm of dendrite. In α-Syn mice by 7-10 months, one rod was found for every 50-70 µm of dendrite.

PFF-induced rods depend upon expression of PrP^c and a functional NADPH oxidase: Our previous studies identified PrP^C and NOX as required intermediates in Aβ-induced rod formation in neurons (Walsh et al., 2014). Others have since shown that PrP^c and NOX are required for the development of cognitive deficits in α-Syn mice, but it has not been demonstrated that α-synuclein PFF induces rods via the same pathway. Here we show that in cultured dissociated neurons PFF-induced rod formation is dependent upon PrP^C expression and NOX activity (Figure 5.10).

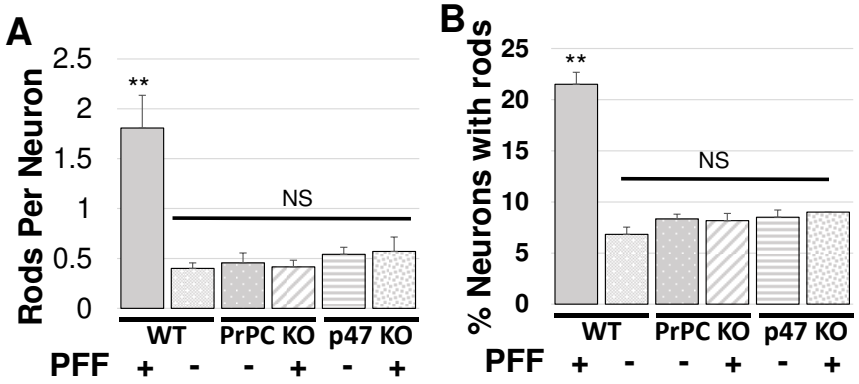

Figure 5.10. PFF-induced rods in neurons requires PrP^c and a functional NOX. Cultured dissociated neurons from WT, PrP^c KO, and p47 KO (p47 is an essential NOX subunit) mice treated with 1 µg/ml PFF overnight. (A) Number of rods per neuron (Rod Index) scored semi-automated using Keyence stitched data. (B) Percent neurons with rods scored manually on Nikon diaphot. Only the WT neurons form rods in response to PFF, suggesting expression of PrP^c and a functional NOX are necessary for PFF-induced rod formation (n=2, **p<0.01, 2 Way ANOVA with Tukey's post hoc test.

PFF-induced rod formation is dependent on the CXCR4 and CCR5 receptors: Since we showed PFF-induced rods required PrP^C and NOX activation, identical to what we found with Aβd/t and gp120-induced rods, we wanted to know if PFF worked through the

identical receptor signaling pathway involving CXCR4 and CCR5 receptors. Thus, we exposed cultures of dissociated E16.5 mouse neurons at DIV 6 (Figure 5.11 A) to PFF in the absence and presence of the CXCR4 antagonist AMD3100, the CCR5 antagonist maraviroc, or an octapeptide antagonist of both the X4 and R5 receptors called Rap310 for which we have previously determined a dose response for inhibiting Aβd/t-induced rods (EC_{50} of 10^{-13} M). We also exposed adult brains slices from WT mice to PFF or Aβd/t in the absence of presence of Rap310 (Figure 5.11 B,C). In all cases rod formation was significantly reduced by X4 and R5 antagonists. In addition, the ability of Rap310 to reduce rods to control levels when only added for the last 2 days of a 4 day treatment with either Aβ or PFF strongly suggests that rod reversal has occurred.

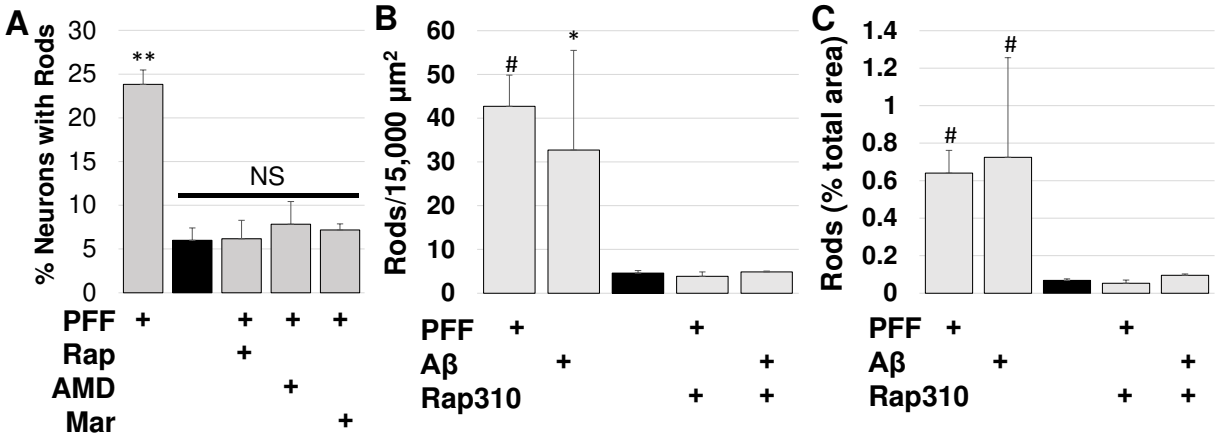

Figure 5.11. Antagonists of the CXCR4 and CCR5 receptors block rod formation induced by PFF and Aβd/t. (A) Cultures of E16.5 mouse hippocampal neurons were treated on DIV 6 with control PFF buffer (black bar), or with PFF plus or minus the addition of Rap310 (10 pM), Maraviroc (50 nM), or AMD310 (50 nM) and fixed and scored for rods on DIV 7. (A) Percent neurons with rods scored on Nikon Diaphot. (n=2, **p<0.01. Two-way ANOVA with post hoc Dunnet test for significance relative to control) (B, C) Hippocampal slices from 10 month WT mouse untreated (black bar) or treated with PFF or Aβ for 4 days in the presence or absence Rap310 at 10 pM for the last two days of stressor treatment. (B) Number of rods in the DG per 60x confocal field. (n=4. Comparison between untreated and: Aβ *p=0.049; PFF #p=0.0005, Rap310 NS.). (C) Rod area as a percent of total per 60x confocal field. (n=4, Comparison between untreated and: Aβ #p=0.0052, PFF #p=0.0008, +Rap310 NS. ANOVA with post hoc Student's T-test.

Discussion

There are two major hypotheses as to the mechanism by which alpha-synuclein overexpression mediates synaptic dysfunction. One of these is through intracellular accumulation of fibrils into Lewy bodies that ultimately lead to intracellular dysfunction through either direct effects on transport or via inhibition of normal protein homeostasis by blocking protein turnover pathways (Fang et al., 2017; Xu et al., 2016). A second hypothesis supports abnormal signaling pathways in neurons as a result of soluble forms of alpha-synuclein released into the extracellular environment (Emmanouilidou et al., 2010; Ferreira et al, 2017; Kim et al., 2014). These are not mutually exclusive mechanisms since extracellular signaling by alpha-synuclein might drive abnormal transport leading to accumulation of intracellular alpha-synuclein deposits or, conversely, intracellular accumulation of alpha-synuclein might drive its release in forms that can spread its effects through signaling. In this chapter we do demonstrate that the neuronal population that develops rods through duplication of the alpha-synuclein gene, appears to be the same neuronal population that as the one that response to PFF, since there is no added effect of PFF on rod formation in the α-Syn hippocampal slices taken from mice that have passed the 6 month age threshold for both motor and cognitive dysfunction.

Our results clearly show that sonicated PFF induces rod formation utilizing the identified components of the same signaling pathway utilized by Aβ and the HIV gp120 protein, all of which depend on PrPC, NADPH oxidase, CXCR4, and CCR5. We know rodent neurons express both the X4 and R5 receptors (Chapter 4), but it not clear if human neurons do the same. Indeed, neurons derived from human ES cells that develop into excitatory glutamatergic neurons express CXCR4 but do not express the CCR5

receptor, at least through their first 60 days after differentiation (Zhang et al., 2013). Thus, there may be differences in rod responses among different neuronal populations due to receptor expression profiles, or other factors in the signal transduction cascade to rod formation. Such differences might explain why only 20-25% of neurons form rods in response to any of the inducers using the PrP^C/NOX pathway, although 90% can form rods in response to excitotoxic glutamate or ATP-depletion (Minamide et al., 2000; Walsh et al., 2014).

Although we found increases in rod formation are contemporaneous with the loss of cognition and the decline in dendrites observed in culture slices, we are unable to provide a cause/effect relationship. The finding that Rap310 appears to be able to stop and reverse rod formation suggests that it can be used to further test this relationship. By culturing slices in the presence of Rap310 from α-Syn mice both during their transition period from normal to impaired states (4-6 months), as well as slices that are from animals in which cognitive function has declined, we could determine if maintenance or improvement of dendritic survival is imparted by the presence of Rap310. Live imaging could also be utilized to determine if this change is related to rod disappearance by using the rod reporter (Mi et al., 2013).

The question also arises as to what is the active form of alpha-synuclein within the PFF preparation? Previously it was shown that soluble dimers of amyloid beta and not the insoluble fibrils found in plaques are the most synaptotoxic species and these are the ones that induce rod formation through PrP^C and NOX. Sonication of fibrils before their use might alter the dynamic equilibrium between monomers, oligomers, and fibrils, if indeed such a reversal of amyloid forms is possible. It has also been demonstrated that

soluble species of Aβ interact with alpha-synuclein to promote its oligomerization rather than fibril formation (Candreva et al., 2020). We have obtained a large batch of monomeric alpha-synuclein and in the future we will fractionate it during the fibril assembly process to see if monomers or small oligomers have higher rod inducing activity than fibrils. Furthermore, the rod-inducing activity of Aβ might arise from the formation of dityrosine cross-linked dimers through Y10 of the peptide (see Chapter 6). It is of interest to note that alpha-synuclein also has the potential to form dityrosine links at Y39 and both are mediated by low levels of copper (Abeyawardhane et al., 2018). Peptides of Aβ with Y10F substitution do not induce rods. Would this also occur in Y39F alpha-synuclein? Future studies will try and address this issue.

Finally, it was our intention to utilize methods we developed in Chapter 3 to quantify dendritic spines in the absence and presence of PFF and to determine if Rap310 or specific X4 and R5 antagonists will protect spines. Hopefully, we can soon obtain some preliminary results from these ongoing experiments.

References

Abeyawardhane DL, Fernández RD, Heitger DR, Crozier MK, Wolver JC, Lucas HR. (2018) Copper Induced Radical Dimerization of α-Synuclein Requires Histidine. *J Am Chem Soc*. 2018;140(49):17086-17094. doi:10.1021/jacs.8b08947

Adamowicz DH, Roy S, Salmon DP, et al. (2017) Hippocampal α-Synuclein in Dementia with Lewy Bodies Contributes to Memory Impairment and Is Consistent with Spread of Pathology. *J Neurosci*. 2017;37(7):1675-1684. doi:10.1523/JNEUROSCI.3047-16.2016

Appel-Cresswell S, et al. (2013) Alpha-synuclein p.H50Q, a novel pathogenic mutation for Parkinson's disease. Mov Disord. 2013; 28:811–3.

Araki K, Yagi N, Aoyama K, Choong CJ, Hayakawa H, Fujimura H, Nagai Y, Goto Y, Mochizuki H. (2019) Parkinson's disease is a type of amyloidosis featuring accumulation of amyloid fibrils of α-synuclein. Proc Natl Acad Sci U S A. 2019 Sep 3;116(36):17963-17969. doi: 10.1073/pnas.1906124116.

Baba M, Nakajo S, Tu PH, et al. (1998) Aggregation of alpha-synuclein in Lewy bodies of sporadic Parkinson's disease and dementia with Lewy bodies. *Am J Pathol*. 1998;152(4):879-884.

Bamburg JR, Bernstein BW. (2016) Actin dynamics and cofilin-actin rods in alzheimer disease. *Cytoskeleton (Hoboken)*. 2016;73(9):477-497. doi:10.1002/cm.21282

Bamburg, J. R., & Bloom, G. S. (2009). Cytoskeletal pathologies of Alzheimer disease. Cell motility and the cytoskeleton, 66(8), 635–649. https://doi.org/10.1002/cm.20388

Book A, Guella I, Candido T, et al. (2018) A Meta-Analysis of α-Synuclein Multiplication in Familial Parkinsonism. *Front Neurol*. 2018;9:1021. Published 2018 Dec 11. doi:10.3389/fneur.2018.01021

Burré, J., Sharma, M., Tsetsenis, T., Buchman, V., Etherton, M. R., & Südhof, T. C. (2010). Alpha-synuclein promotes SNARE-complex assembly in vivo and in vitro. Science (New York, N.Y.), 329(5999), 1663–1667. https://doi.org/10.1126/science.1195227

Byrne EJ, Lennox GG, Godwin-Austen RB, Jefferson D, et al. (1991) Dementia associated with cortical Lewy bodies: Proposed clinical diagnostic criteria. Dementia. 1991; 2(5):283–284.

Candreva J, Chau E, Rice ME, Kim JR. (2020) Interactions between Soluble Species of β-Amyloid and α-Synuclein Promote Oligomerization while Inhibiting Fibrillization. *Biochemistry*. 2020;59(4):425-435. doi:10.1021/acs.biochem.9b00655

Chesselet MF, Richter F, Zhu C, Magen I, Watson MB, Subramaniam SR. (2012) A progressive mouse model of Parkinson's disease: the Thy1-aSyn ("Line 61") mice. *Neurotherapeutics*. 2012;9(2):297-314. doi:10.1007/s13311-012-0104-2

Cristóvão, A. C., Guhathakurta, S., Bok, E., Je, G., Yoo, S. D., Choi, D. H., & Kim, Y. S. (2012). NADPH oxidase 1 mediates α-synucleinopathy in Parkinson's disease. The Journal of neuroscience : the official journal of the Society for Neuroscience, 32(42

De Cecco, E., & Legname, G. (2018). The role of the prion protein in the internalization of α-synuclein amyloids. Prion, 12(1), 23–27. https://doi.org/10.1080/19336896.2017.1423186

Eliezer D1, K. E. (2001). Conformational properties of alpha-synuclein in its free and lipid-associated states. *J Mol Biol*, 1061-7

Emmanouilidou, E., Melachroinou, K., Roumeliotis, T., Garbis, S. D., Ntzouni, M., Margaritis, L. H., Stefanis, L., & Vekrellis, K.. (2010). Cell-produced alpha-synuclein is secreted in a calcium-dependent manner by exosomes and impacts neuronal survival. T

Fang, F., Yang, W., Florio, J. B., Rockenstein, E., Spencer, B., Orain, X. M., Dong, S. X., Li, H., Chen, X., Sung, K., Rissman, R. A., Masliah, E., Ding, J., & Wu, C. (2017). Synuclein impairs trafficking and signaling of BDNF in a mouse model of Parkinson's disease. Scientific reports, 7(1), 3868. https://doi.org/10.1038/s41598-017-04232-4

Fares MB, et al. (2014) The novel Parkinson's disease linked mutation G51D attenuates in vitro aggregation and membrane binding of alpha-synuclein, and enhances its secretion and nuclear localization in cells. Hum Mol Genet. 2014; 23:4491–509.

Ferreira DG, Temido-Ferreira M, Vicente Miranda H, et al. (2017) α-synuclein interacts with PrP^C to induce cognitive impairment through mGluR5 and NMDAR2B. *Nat Neurosci*. 2017;20(11):1569-1579. doi:10.1038/nn.4648

Galvagnion C, et al. (2015) Lipid vesicles trigger alpha-synuclein aggregation by stimulating primary nucleation. Nat Chem Biol. 2015; 11:229–U101.

Guerrero-Ferreira R, Kovacik L, Ni D, Stahlberg H. (2020) New Insights on the Structure of alpha Synuclein Fibrils Using Cryo-electron Microscopy. Curr Opin Neurobiol. 2020 Feb 26;61:89-95. doi: 10.1016/j.conb.2020.01.014

Herms J, Dorostkar MM. (2016) Dendritic Spine Pathology in Neurodegenerative Diseases. *Annu Rev Pathol*. 2016;11:221-250. doi:10.1146/annurev-pathol-012615-044216

Hou, L., Bao, X., Zang, C., Yang, H., Sun, F., Che, Y., Wu, X., Li, S., Zhang, D., & Wang, Q. (2018). Integrin CD11b mediates α-synuclein-induced activation of NADPH oxidase through a Rho-dependent pathway. Redox biology, 14, 600–608. https://doi.org/10.1

Kiely AP, Ling H, Asi YT, et al. (2015) Distinct clinical and neuropathological features of G51D SNCA mutation cases compared with SNCA duplication and H50Q mutation. *Mol Neurodegener*. 2015;10:41. Published 2015 Aug 27. doi:10.1186/s13024-015-0038-3

Kim, W. S., Kågedal, K., & Halliday, G. M. (2014). Alpha-synuclein biology in Lewy body diseases. Alzheimer's research & therapy, 6(5), 73. https://doi.org/10.1186/s13195-014-0073-2

Kitada T, Asakawa S, Hattori N, et al. (1998) Mutations in the parkin gene cause autosomal recessive juvenile parkinsonism. *Nature*. 1998;392(6676):605-608. doi:10.1038/33416

Konno, T., Ross, O. A., Puschmann, A., Dickson, D. W., & Wszolek, Z. K. (2016). Autosomal dominant Parkinson's disease caused by SNCA duplications. Parkinsonism & related disorders, 22 Suppl 1(Suppl 1), S1–S6. https://doi.org/10.1016/j.parkreldis.2015.09.

Lesage S, Anheim M, Letournel F, et al. (2013) G51D α-synuclein mutation causes a novel parkinsonian-pyramidal syndrome. *Ann Neurol*. 2013;73(4):459-471. doi:10.1002/ana.23894

Spillantini MG, Crowther RA, Jakes R, Hasegawa M, Goedert M. (1998) alpha-Synuclein in filamentous inclusions of Lewy bodies from Parkinson's disease and dementia with lewy bodies. *Proc Natl Acad Sci U S A*. 1998;95(11):6469-6473. doi:10.1073/pnas.95.11.6469

Meade, R.M., Fairlie, D.P. & Mason, J.M. (2019) Alpha-synuclein structure and Parkinson's disease – lessons and emerging principles. Mol Neurodegeneration 14, 29 (2019). https://doi.org/10.1186/s13024-019-0329-1

Mi J, Shaw AE, Pak CW, et al. (2013) A genetically encoded reporter for real-time imaging of cofilin-actin rods in living neurons. *PLoS One*. 2013;8(12):e83609. Published 2013 Dec 31. doi:10.1371/journal.pone.0083609

Minamide LS, Striegl AM, Boyle JA, Meberg PJ, Bamburg JR. (2000) Neurodegenerative stimuli induce persistent ADF/cofilin-actin rods that disrupt distal neurite function. *Nat Cell Biol*. 2000;2(9):628-636. doi:10.1038/35023579

Minamide LS, Maiti S, Boyle JA, et al. (2010) Isolation and characterization of cytoplasmic cofilin-actin rods. *J Biol Chem*. 2010;285(8):5450-5460. doi:10.1074/jbc.M109.063768

Nuvolone M, Hermann M, Sorce S, et al. (2016) Strictly co-isogenic C57BL/6J-Prnp-/- mice: A rigorous resource for prion science. *J Exp Med*. 2016;213(3):313-327. doi:10.1084/jem.20151610

Patterson JR, Polinski NK, Duffy MF, et al. (2019) Generation of Alpha-Synuclein Preformed Fibrils from Monomers and Use In Vivo. *J Vis Exp*. 2019;(148):10.3791/59758. Published 2019 Jun 2. doi:10.3791/59758

Polymeropoulos MH, Lavedan C, Leroy E, et al. (1997) Mutation in the alpha-synuclein gene identified in families with Parkinson's disease. *Science*. 1997;276(5321):2045-2047. doi:10.1126/science.276.5321.2045

Shaw AE, Bamburg JR. (2017) Peptide regulation of cofilin activity in the CNS: A novel therapeutic approach for treatment of multiple neurological disorders. *Pharmacol Ther*. 2017;175:17-27. doi:10.1016/j.pharmthera.2017.02.031

Singh Y, Sharpe PC, Hoang HN, et al. Amyloid formation from an α-helix peptide bundle is seeded by 3(10)-helix aggregates. (2011) *Chemistry*. 2011;17(1):151-160. doi:10.1002/chem.201002500

Tomiyama T, Nagata T, Shimada H, Teroka R, Fukushima A, Kanemitsu H, Takuma H, Kuwano R, Imagawa M, Ataka S. (2008). A new Aβ variant favoring oligomerization in Alzheimer's type dementia. Ann Neurol, 63:377-387.

W R Gibb, A. J. (1988). The relevance of the Lewy body to the pathogenesis of idiopathic Parkinson's disease. *Journal of Neurology, Neurosurgery & Psychiatry* , 51,6.

Walsh KP, Minamide LS, Kane SJ, Shaw AE, Brown DR, Pulford B, et al. (2014) Amyloid-β and Proinflammatory Cytokines Utilize a Prion Protein-Dependent Pathway to Activate NADPH Oxidase and Induce Cofilin-Actin Rods in Hippocampal Neurons. PLoS ONE, 9(4): e

Woo JA, Liu T, Fang CC, et al. (2019) Activated cofilin exacerbates tau pathology by impairing tau-mediated microtubule dynamics. *Commun Biol*. 2019;2:112. Published 2019 Mar 22. doi:10.1038/s42003-019-0359-9

Woo JA, Boggess T, Uhlar C, et al. (2015) RanBP9 at the intersection between cofilin and Aβ pathologies: rescue of neurodegenerative changes by RanBP9 reduction. *Cell Death Dis*. 2015;6(3):1676. Published 2015 Mar 5. doi:10.1038/cddis.2015.37

Xu, L., & Pu, J. (2016) Alpha-Synuclein in Parkinson's Disease: From Pathogenetic Dysfunction to Potential Clinical Application. Parkinson's disease, 2016, 1720621. https://doi.org/10.1155/2016/1720621

Yoshino H, Hirano M, Stoessl AJ, et al. (2017) Homozygous alpha-synuclein p.A53V in familial Parkinson's disease. *Neurobiol Aging*. 2017;57:248.e7-248.e12. doi:10.1016/j.neurobiolaging.2017.05.022

Zarranz JJ, Alegre J, Gómez-Esteban JC, et al. (2004) The new mutation, E46K, of alpha-synuclein causes Parkinson and Lewy body dementia. *Ann Neurol*. 2004;55(2):164-173. doi:10.1002/ana.10795

Zavodszky E, et al. (2014) Mutation in VPS35 associated with Parkinson's disease impairs WASH complex association and inhibits autophagy. Nat Commun. 2014; https://doi.org/10.1038/ncomms4828., 5:16.

Zhang Y, Pak C, Han Y, et al. (2013) Rapid single-step induction of functional neurons from human pluripotent stem cells. *Neuron*. 2013;78(5):785-798. doi:10.1016/j.neuron.2013.05.029

Zhong, Z., Grasso, L., Sibilla, C., Stevens, T. J., Barry, N., & Bertolotti, A. (2018). Prion-like protein aggregates exploit the RHO GTPase to cofilin-1 signaling pathway to enter cells. The EMBO journal, 37(6), e97822. https://doi.org/10.15252/embj.2017

Zimprich A, Biskup S, Leitner P, et al. (2004) Mutations in LRRK2 cause autosomal-dominant parkinsonism with pleomorphic pathology. *Neuron*. 2004;44(4):601-607. doi:10.1016/j.neuron.2004.11.005

CHAPTER 6

AMYLOID BETA DIMER/TRIMER-INDUCED COFILIN-ACTIN ROD PATHOLOGY AND DENDRITIC SPINE LOSS IS MEDIATED BY CXCR4 AND CCR5 RECEPTORS AND REVERSED BY RECEPTOR ANTAGONISTS

Introduction

Extracellular plaques and intracellular tangles in human brain were first discovered by Alois Alzheimer in 1907 and have since been the established hallmarks of Alzheimer's Disease (AD) (Nelson et al., 2009). The discovery of the amyloid-β peptide (Aβ) as the major component of plaques and the discoveries that familial forms of AD arose from mutations in the pathway for amyloid-β (Aβ) over production or decreased clearance from the brain, led to the amyloid hypothesis of AD, which has undergone many revisions since it was first proposed in 1992 (Hardy and Higgins, 1992; Hardy, 2017), but which is still generally accepted today (Selkoe and Hardy, 2016). Contributing to the revision of the original hypothesis is the finding that plaque burden has poor correlation with cognitive dysfunction (Tsartsalis et al., 2018), which is more associated with the presence of soluble oligomeric forms of Aβ, especially dimer (Shankar et al., 2008; Mc Donald et al, 2010; Jin et al., 2011). Furthermore, plaques are not found in the brains of subjects with an Alzheimer-like dementia caused by an Aβ variant missing glutamate at residue 22 (ΔE22), which leads to a soluble species of Aβ that favors rapid dimerization and then oligomerization without plaque formation (Tomiyama et al., 2008). This mutated Aβ

variant is found within a cohort of Japanese families; affected individuals undergo severe dementia but lack the elevated amounts of Aβ peptides usually associated with AD. The AβΔE22 inhibits LTP in vivo (Takuma et al., 2008). Furthermore, small soluble oligomers of Aβ extracted from the brains of AD subjects, particularly oligomers containing the dimer/trimers (Aβd/t), are the most synaptotoxic, reducing hippocampal dendritic spine densities in culture when used at 5 nM (Shankar et al., 2008). Laboratory rodents (mice and rats) do not develop AD, but the amino acid sequences of Aβ between human and lab rodents (mice and rats) differ in only 3 amino acids: R5G, Y10F and H13R, respectively. These three residues in human Aβ contribute to the formation of a dityrosine dimer in a Cu^{2+} catalyzed reaction with molecular oxygen (Atwood et al., 2004) and it could be this specific form of Aβ that contributes to the oligomer subtypes that possess the greatest synaptic toxicity (Knight et al., 2016).

Because laboratory rodents do not naturally develop AD, mouse models have been made in which familial AD mutant forms of human APP along with mutant forms of its γ-secretase processing presenilin subunits are expressed. In these mice, age-related cognitive deficits do occur. These deficits can be reduced or eliminated by inhibiting expression of one of several different proteins thought to be binding partners of Aβ (Benilova and De Strooper, 2013), many or all of which might be linked through a common pathway that requires the presence of cellular prion protein (PrP^C) (Laurén et al., 2009; Gimbel et al., 2010). Synaptic damage by Aβ appears to be mediated by cross-linked regions of PrP^C (Bate and Williams, 2011). This common pathway leads to an underappreciated pathological change, the formation within neurites of rod-shaped cofilin-actin filament bundles (rods) (Minamide et al., 2000).

Oligomers of Aβ, especially Aβd/t, affects the actin cytoskeleton through cell signaling pathways (Davis et al., 2011). The actin cytoskeleton, through assembly and disassembly mechanisms, is necessary for synapse formation, stabilization, and elimination (Korobova and Svitkina, 2010). Cofilin, a major actin dynamizing protein, is inactive in binding actin when phosphorylated on serine 3 and becomes active when dephosphorylated (Morgan et al., 1993; Agnew et al., 1995; Moriyama et al., 1996). LIM Kinase 1 (LIMK1), the major kinase phosphorylating cofilin ser3, is bound to the plasma membrane through palmitoylation (George et al., 2015) and is activated by members of the p21-activated kinase family (PAK) (Arber et al., 1998; Yang et al., 1998; Soosairajah et al., 2005). Slingshot-1 (SSH1), is a p-cofilin phosphatase (Niwa et al., 2002) that requires binding to F-actin for its activity (Nagata-Ohashi et al., 2004; Soosairajah et al., 2005). Another cofilin-specific phosphatase, chronophin (CIN) is also found in brain (Gohla et al., 2005) and regulates cofilin activity in some dendritic spines (Kim et al., 2016). The dynamic balance between phospho and dephospho forms of cofilin control its spatial regulation critical for synapse function (Bamburg and Bernstein, 2016). Both LIMK1 and SSH1 play essential roles in synapse morphology (Sarmiere and Bamburg, 2002; Zhou et al., 2012; Simhadri et al., 2017; Wang et al., 2005) as well as in synaptic function in memory (Wang et al., 2013; Lunardi et al., 2018). Oligomers of Aβ alter cofilin phosphorylation in synaptosomes, but often in opposite directions (e.g. Rush et al., 2018; Kommaddi et al., 2018), strongly suggesting that many other proteins that work along with cofilin to modulate actin dynamics in dendritic spines help maintain a balance in actin assembly (Shaw and Bamburg, 2017). Indeed, large changes in cofilin-mediated cellular actin dynamics have been observed in the absence of any change in the ratio of phospho-

to dephospho-cofilin (Meberg et al., 1998). Local phosphoregulation is coupled with cofilin sequestering on F-actin, binding to and controlled release from monomeric G-actin through nucleotide exchange mechanisms (and thus dependent on local ATP pool), as well as binding and release from dynamic pools of membrane phosphatidylinositol phosphates (Bamburg and Bernstein, 2016).

In addition to its regulation of actin dynamics, cofilin can be found associated with rod-shaped bundles of actin filaments (rods) within neurites of stressed neurons (Minamide et al., 2000). Aβ oligomers induce formation of rods (Maloney et al, 2005), which contain only dephosphorylated (active) cofilin. In Aβ-treated neurons there is no global change in cofilin/phospho-cofilin (Maloney et al., 2005; Walsh et al., 2014) suggesting localized accumulation of active cofilin into rods through production of ROS which is needed to cross-link F-actin-bound cofilin via disulfide bond formation (Bernstein et al., 2012). Localized cofilin dephosphorylation through SSH1 is mediated by integrins and the scaffolding protein RanBP9 (Woo et al., 2015), or in spines perhaps via Ca^{2+} signaling through the protein phosphatase calcineurin (aka PP2B), which removes an inhibitory phosphate from SSH1 (Wang et al., 2005). Acute release of active CIN from its cellular binding partner hsp90, leads to a rapid increase in dephosphorylated cofilin and the formation of rods. Since CIN binding to hsp90 is ATP-dependent, this release is one mechanism by which energy depletion can induce rods (Huang et al., 2008). Restoring the pool of phosphorylated cofilin in neurons from several different mouse models of neurodegenerative disorders prevented the stress-induced rod formation and rescued synaptic function measured both in vitro and in vivo (Shaw and Bamburg, 2017).

Cofilin severing of actin filaments is enhanced by WDR1 (aka Aip1), which specifically aids in filament severing between regions of F-actin that have no cofilin and those regions saturated with cofilin, which binds cooperatively along F-actin (Hayden et al., 1993; McGough et al., 1997; Hayakawa et al., 2019). Rods probably form from pieces of cofilin-saturated actin filaments that are not fully depolymerized because of insufficient amounts or activity of another protein, CAP1 (Moriyama and Yahara, 2002). Aip1 and CAP1 were shown many years ago to enhance filament dynamics in the presence of cofilin (Balcer et al., 2003). CAP1 is phosphoregulated (Zhou et al., 2012) and it has recently been shown that phosphorylation regulates oligomerization of CAP1 which tremendously enhances its ability to disassemble the cofilin-saturated pieces of F-actin (Purde et al., 2019; Zhang et al., 2020). Thus, many cellular mechanisms come into play to both spatially and temporally modulate cofilin-actin filament depolymerization. Delays in any of these processes coupled with local elevation in reactive oxygen species (ROS), can lead to the intermolecular cofilin-disulfide bonds that stabilize rods (Bernstein et al., 2012).

Higher numbers of rods along with amorphous aggregates of dense cofilin immunostaining have been observed in postmortem hippocampi and entorhinal cortex of AD human subjects compared to cognitively normal age matched control groups (Rahman et al, 2014). We have observed a significant increase in rods occurring in early AD (unpublished results of Minamide et al.). Although rods were found around most amyloid plaques in AD brain (Minamide et al., 2000), they are also prevalent in many other areas, suggesting it is not the plaques *per se* that give rise to the rods (Maloney and Bamburg, 2007).

AD-like cognitive deficits that are hippocampal-based, such as contextual fear conditioning, occur in mice expressing human APP containing familial AD mutations, sometimes along with AD-associated mutations in human presenilins, components of γ-secretase, and human tau (Lewis et al., 2000; Hall and Roberson, 2011; Woo et al., 2015; Woo et al., 2019). The γ-secretase is the protease responsible for the intramembrane cleavage of the Aβ peptide from the single-pass transmembrane amyloid precursor protein (APP). When AD mice are cross-bred with cofilin-hemizygous mice to eliminate one copy of the cofilin gene, cofilin expression is reduced by 50%, and the mice no longer develop hippocampal dependent contextual fear conditioning deficits (Woo et al., 2015A; Woo et al., 2015B, Woo et al., 2019), suggesting that their learning/memory deficits are cofilin-dependent. Hippocampal slices from the tau mouse line P301L, a mutation involved in frontal temporal dementia and neurofibrillary tangle formation, show reduced expression of presynaptic proteins, and decreased LTP when stimulating the CA3 neurons and recording from CA1 pyramidal neurons (Lewis et al., 2000; Woo et al., 2019). This LTP defect was abolished in hippocampal slices that express the phosphomimic cofilin S3E or if slices came from mice that were crossed with cofilin hemizygous mice (Woo et al., 2019), again suggesting that active cofilin plays a role in AD induced synaptic depression. Furthermore, in an AD mouse model in which expression of RanBP9, an upstream component of SSH-1L activation is reduced by 50%, rod formation is reduced along with restoration of contextual fear conditioning in the mice and the ability of brain slices from the mice to undergo LTP in vitro (Woo et al., 2015A). Thus, in the absence of other compensatory changes to modulate cofilin-mediated actin dynamics, excess active

cofilin contributes to cognitive decline. Rod formation correlates with this decline but whether rods are the major cause of the Aβ-initiated decline has yet to be determined.

We previously demonstrated that incubating Aβd/t with rodent postnatal hippocampal slices for 48 h induced cofilin actin rods in the dentate gyrus (DG) and mossy fibers (MF) of the hippocampus (Davis et al., 2011). We further demonstrated that rod formation induced in dissociated rat and mouse hippocampal neurons treated with Aβd/t, synthetic $A\beta_{1\text{-}42}$ oligomers, or any of several different proinflammatory cytokines is dependent on the expression of PrP^C and the activation of NADPH oxidase (NOX), a producer of ROS (Walsh et al., 2014). Because we have shown in Chapter 4 that the HIV gp120 protein induces rods in neurons through a PrPc- and NOX-dependent pathway utilizing CXCR4 (and perhaps CCR5) receptors, and in Chapter 5 that sonicated α-Syn fibrils do the same, here we examined if: 1) the neuronal rod response to Aβd/t is also mediated by CXCR4/CCR5 receptors, 2) all of the rod-inducing agents target the identical rod responsive neuronal population, and 3) RAP310, the peptide antagonist of the CXCR4 and CCR5 receptors, will reverse and/or block rod formation induced by Aβd/t. In addition, we examine Aβd/t-induced rod formation in hippocampal slices from various ages of mice, 4 days, 4 month, 7 months and 10.5 months, the location of rods that form within the slices, and we quantified the rod response in wild type (WT), α-Syn overexpressing, PrPc-null and p47-null adult mice. Finally, we have initiated an examination of the effects of Aβd/t on dendritic spines and the ability of the CXCR4/CCR5 peptide antagonist RAP310 to protect spines from Aβd/t-induced loss. Images have been collected for this study but analysis is ongoing and will not be included in this thesis.

Methods

Animals: All animals were handled according to National Research Council's Guidelines to Care and Use of Laboratory Animals as approved by the Colorado State University Institutional Animal Care and Use Committee protocols 17-7541A, 17-7411A and 18-7779A. The lines of mice used are: Thy1-alpha-synuclein Line61 mice (Chesselet et al., 2012); WT C57BL6/DBA2 50:50 background as breeding stock for the Line61 mice; p47 null mice ($p47^{phox\ -/-}$) JAX stock number 027331 B6N.129S2-Ncf1tm1Shl/J); PrP^{C} null mice ($PrP^{-/-}$ TALEN; (Nuvolone et al., 2016)); C57BL6 wild type mice. Breeders for Line61 and p47-null mice were generously provided by Dr. Ray Swanson, University of California, San Francisco. $PrP^{-/-}$ mice were generously provided by Mark Zabel, Prion Research Center, CVMBS, CSU.

Cultures of dissociated hippocampal neurons: Frozen stocks of neurons were prepared as described in Chapter 3 from E16.5 embryos of timed pregnant mice. For short term cultures (DIV7), neurons from frozen stocks in 50% FBS and 10% DMSO were diluted at least 1:6 with HNB medium and plated at 30,000 cells per well on PDL-coated coverslips in wells of 24 well plates as described in Chapter 3. After 2 hr for attachment, medium was removed and replaced with 1 ml of fresh medium. Medium was changed on DIV 2 and 5, with treatments on DIV 6 and fixation 16 hr later, on DIV 7.

For long term cultures (>DIV 20), neurons were diluted at least 1:6 in HNB and plated at 62,500 cells per PDL-coated well using the center 8 wells of a 24 well glass bottom plate (Cellvis P24-1.5H-N, Lot#: 190828). After 2 h, medium was removed and replaced with 1 ml of overnight glial conditioned complete HNB (GCM). Cells were fed every other day with freshly harvested GCM (20-24 h conditioning). No results will be presented from

these cultures but images have been collected and will be analyzed post-submission of this thesis.

*Preparation of glial conditioned medi*um: Glial cells were prepared from brains of P1 mouse pups following the procedure of (Meberg and Miller, 2003). Aliquots of cells in medium containing 10% DMSO were frozen and stored in liquid nitrogen until needed. To prepare GCM, a vial of glial cells was quickly thawed, cells centrifuged at 400xg for 4 min and suspended in glial cultured medium (DMEM+10% FBS with pen/strep). Cells were plated onto a 10 cm tissue culture dish and allowed to grow to about 60-70% confluency at which point medium was removed, cultures washed with complete HNB and then incubated with 10 ml of complete HNB overnight. Glia stop growing in HNB and the same plate can be used for up to 3 weeks to provide GCM for long term neuronal cultures. GCM is always used immediately after harvesting and not stored.

Adult mouse hippocampal slice cultures: Dissection and culturing of adult brain slices was performed as described in Chapter 3. Ages of mice were approximately 4, 7 and 10.5 months. Duration of time from euthanasia to culture never spanned more than 2 hrs with brains and slices kept cold during this entire period. Each mouse yielded at least 48 slices. Slices were cultured for at least DIV 7 in GCM prior to starting treatments and some were fixed on DIV 0 and DIV 7 for comparison of morphology. Medium was changed every other day.

Specifics for each age group. Mice at 4 months: Cultures of hippocampal slices (48, 2/coverslip) were obtained from 2 male alpha-synuclein mice and an identical number from 2 male WT mice. Freshly harvested glial conditioned medium (GCM) was changed completely every other day. Mice at 7 months: Cultures of hippocampal slices (48,

2/coverslip) were obtained from 2 male Line 61 WT mice. In addition, 24 slices of each genotype were obtained from two $p47^{PHOX-/-}$, two $PrP^{-/-}$, and two WT C57DB/J6 (genotype control). The GCM was harvested from glial cultures and for some experiments, held overnight at 4° C prior to changing on slice cultures every other day. Mice at 10.5 months: Cultures of hippocampal slices (48, 2/coverslip) were obtained from 2 male Line 61 WT mice. The added glial conditioned medium (GCM) was used fresh and changed completely every other day.

Preparation of human Aβd/t from culture medium of a secreting cell line: 7PA2 CHO cells (Walsh et al., 2002), a gift from Dennis Selkoe, BWH, Harvard University, were cultured in 10 cm dishes as previously described (Welzel et al., 2014). Medium (10 ml) containing horse serum was replaced with 10 ml of serum-free DMEM 16 hrs before its harvesting and concentrating to 1 ml in an Amicon Ultracel 3K centrifugal filter using a Beckmann 7 table centrifuge at 4° C at 4,000xg for ~45minutes or until concentrated to 1ml. Many plates of medium can be collected and concentrated and the 1 ml aliquots quick frozen in liquid nitrogen for subsequent chromatography.

A 1 ml fraction of concentrated medium is loaded onto a column of Superdex 300 (GE) equilibrated with filtered and degassed 50 mM ammonium acetate buffer, pH 8.5 at 4° C. The elution was performed on an FPLC at a pumped flow rate of 0.5 ml/min, collecting 1ml fractions. Several 1 ml aliquots of medium can be loaded in sequence and the fraction collector reset at tube one to collect the products of many preparations in the same array of fraction tubes. To identify the fractions with the highest Aβd/t concentrations, 0.2 ml of each fraction was used on a Western blot to localize Aβ species. If single preps are done from 1 ml concentrated medium, 20% of each fraction is utilized

in Western blots, but if 10 x1 ml preps are fractionated repetitively in the same tubes, the loss is only 2%.

Western blotting: Lyophilized 200 µl fractions are resuspended in 10 µl 1x Tris/Tricine Sample prep buffer (0.5 M Tris pH 6.8, 5% SDS, 40% Glycerol, 18% H_2O, 2% 2-mercaptoethanol, trace of methylene blue) and loaded onto a 17.5% Tris-Tricine gel (Bio-Rad) along with a 2x protein standard (Kaldoscope Polypeptide Standard Cat 161-0325) and a standard of monomeric $A\beta_{1-42}$ (Anaspec). Running buffer is 100 mM Tris, 100 mM Tricine, 0.1% SDS). Proteins are transferred to nitrocellulose for 3 hr at 300 amps. Nitrocellulose is then boiled in PBS for 10 min, washed once in TBS and then blocked for 1 hr (2% BSA Fraction V in 1x TBS). Primary antibody for human Aβ (mouse anti-human Aβ 1-16, 6E10, used at 1:1000 in 1% BSA, 0.1% Tween, in 1x TBS) is incubated overnight at 4° C. The membrane is then washed 10x over the course of an hour and incubated with secondary antibody (goat anti-mouse Dylight 680) at 1:10,000 in secondary wash solution (1% BSA, 0.1% Tween, 0.01% SDS in 1x TBS) for 2 h at room temp. The blot is then washed in TBS-Tween for an hour with 10 washes, transferred to TBS, and washed twice, and imaged on an IR-laser scanning system (LiCor Odyssey). Fractions containing the dimer/trimer (three fractions) were combined, an aliquot removed for quantitative blotting, and the remainder freeze dried, suspended in water and freeze dried a second time to remove traces of the volatile buffer. The aliquot of the combined fraction was run using the same Western blotting method but was also loaded with standards of 1.5, 3, 6 and 12 ng of synthetic $A\beta_{1-42}$. Images were analyzed using ImageJ to obtain Aβd/t amounts with respect to the standard curve of $A\beta_{1-42}$ (concentration is expressed in monomer equivalents).

Treatments of slices: All slices were cultured for at least 7 DIV prior to treatment, which lasted for 4 days with a change of medium and treatment additive on day two. The combined Aβd/t fractions that represented between 80 and 98% of the total d/t in the culture medium (80% if only 1 prep was fractionated and 20% was used for gel analysis to 98% if 10 preps were combined) were suspended in complete glial conditioned medium (complete HNB incubated overnight on glial cells) to approximate the amount of Aβd/t in the 7PA2 medium (referred to as 1X). This amount is approximately 1 nM (4.5 ng/ml) (see results). Treatments used for slices in 600 µl of GCM or Aβd/t-containing GCM included: maraviroc, an inhibitor of CCR5 (Veljkovic et al., 2015), dissolved to 20 mg/ml in 70% ethanol, with a dilution to 50 ug/ml in PBS before a 1:1000 dilution to 50 ng/ml in culture; AMD3100, an inhibitor of CXCR4 receptors (Wang et al., 2020), dissolved to 5 mg/ml in PBS and diluted to 50 ug/ml before addition to cultures at 50 ng/ml; Rap310 (all D amino acid octapeptide ASTTTNYT, Creative BioPeptides, Inc.), diluted from a 10^{-6} M stock in water to 10^{-9} M in GCM and used at a 1:100 dilution in cultures to obtain a final concentration of 10^{-11} M.

Immunostaining was performed as described in chapter 3. Antigens and their respective antibodies are: cofilin, affinity purified rabbit 1439 antibody (Shaw et al;, 2004); GFAP, mouse monoclonal antibody (Fisher MA5-15086); Iba1, goat monoclonal antibody (generous gift from Ray Swanson, UCSF); Map2, chicken antibody (Abcam cat# ab92434). Secondary antibodies (Thermo-Fisher) were raised in goat, except for the Iba1, which was a donkey anti-goat secondary antibody. Chromatin was stained with DAPI, added either with secondary antibodies or with the Prolong Diamond Antifade.

Specifics for staining in each set of slices: Post-natal slices: DIV 12 treated slices immunostained for cofilin, GFAP, Iba1. 4-month slices: DIV 0 and DIV 7 slices were immunostained for cofilin, Map2, and GFAP. DIV 12 slices were immunostained for cofilin, GFAP, and Iba1. 7 -month slices: DIV 0 and DIV 7 slices were immunostained for cofilin, Map2, and Iba1. DIV 12 treated slices were immunostained for cofilin. 10.5- month slices: All slices were immunostained for cofilin, and Map2.

Cultures of dissociated neurons were immunostained for cofilin and co-stained with DAPI.

Labeling of Dendritic Spines: DiA microcrystal labeling of random neurons cultured 21 DIV on glass bottom 24 well dishes was performed as described in Chapter 3. Only the middle 8 wells of a 24 well plate were used. In all wells prior to treatment, labeled neurons with stretches of dendrites in which spines could be visualized were imaged on the Keyence microscope. Labeled neurons were identified by scanning with a 20x objective and positions identified that were then imaged with a 100x oil objective in a z-stack of 24 planes with 1 µm steps. Labeled cells were either left untreated or treated with 1x Aβd/t, gp120 or PFF and the exact same positions imaged 16-18 hr later. In some experiments, RAP310 was used along with the rod-inducing treatment and in others it was added 24 hr after the rod inducer and cultures imaged again a day later.

Microscopy and image analysis for rods: Plated neurons were imaged on the Keyence microscope with a 40x air objective as described in Chapter 3. Neurons in cultures of dissociated cells were manually counted in stitched images of the fields and rods were counted using the unbiased semi-automated procedure described in Chapter 3 to obtain rod index values (rods/neuron). To obtain percent neurons with rods we manually scored

coverslips on the Nikon Diaphot 300 microscope using the 60x Nikon plan apo oil objective (NA 1.4).

Slices were imaged on the Keyence microscope with a 40x air objective as described in chapter 3 for mapping the location of cofilin pathology. Rod quantification was performed using the Olympus Spinning Disk Confocal 60x oil objective. All fields and rods were counted using the unbiased semi-automated procedure described in Chapter 3.

Results

Isolation and characterization of Aβd/t. Previous work from our laboratory demonstrated that the Aβd/t fraction was >1000 fold more active in rod-induction than was the typically used synthetic Aβ oligomer preparation. However, only a single preparation of the Aβd/t had been previously quantified for Aβ content (Davis et al., 2011). Here we performed multiple preparations of Aβd/t to obtain a large pool of material for many experiments and then used quantitative immunostaining with standards of monomeric synthetic Aβ, calculated by weight of peptide and purity, to determine the actual concentration of dimer/trimer in monomeric equivalents. The concentration obtained shows that medium harvested from an overnight incubation from a single 10 cm dish of 70% confluent 7PA2 cells contains 45 ng of Aβd/t or 4.5 ng/ml (1 nM) which is defined as the 1X concentration (Figure 6.1 A, B). We then used dissociated mouse hippocampal neuronal cultures for dose response measurements to find the minimal amount of Aβd/t needed to obtain the maximum rod response (Figure 6.1 C). Confirming our previous work, the maximum % of

neurons forming rods in response to Aβd/t is 25% and is induced by the 1X concentration (1 nM).

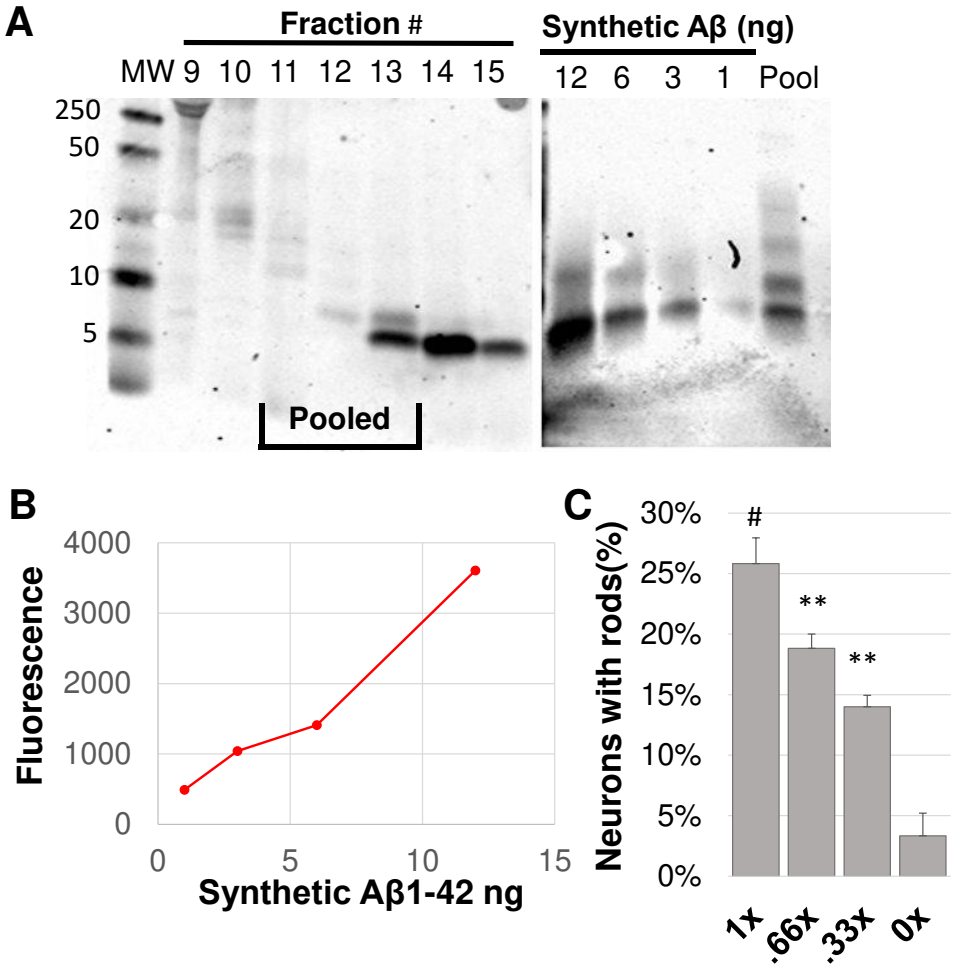

Figure 6.1. Fractionation, quantification and activity of Aβd/t from medium of 7PA2 cells. (A) Western blot of fractions from FPLC gel filtration column stained for human amyloid-β with mouse 6E10 monoclonal antibody. Pooled fractions contained about 50% monomer, which is not rod inducing as determined from tests on fractions of monomer alone (Davis et al., 2011). These were run on a western blot against standards of synthetic Aβ1-42. (B) Standard curve of total fluorescence intensity of stained standard versus amount loaded based on weighed starting material. Amounts of Aβ in fractions were calculated based upon monomer equivalents. (C) Dose-response showing percent neurons forming rods from pooled fractions of Aβd/t expressed in terms of 7PA2 medium amounts as 1X (1 nM). (n=3). P values from one-way Student's T-test. Relative to 0x: 1x p=0.003, 0.66x p= 0.005, 0.33x p=0.009. Relative to 1x: 0.66x p=0.027. Relative to 0.66x: 0.33x p=0.022.

Aβd/t-induced rod localization in adult and postnatal WT slices. Previously our lab had shown that Aβd/t used at 1X for 48 hrs induced rods in postnatal slices cultured at the air/liquid interface on membranes. The location of the rods in the slices was determined after fixation and immunostaining using fiduciary marks and a stretch and fit algorithm to try and align various regions from multiple slices (Davis et al., 2011). Both the dentate gyrus (DG) and mossy fiber tract (MF) were most abundant in rods. In the present study, we performed complete 3D imaging of adult brain slices from 10.5- month mice that had been treated with 1X Aβd/t for 4 days. Specific regions were selected for high resolution confocal 3D imaging for rod quantification using the regions defined in Chapter 3, Figure 3.7. Very significant increases in rod formation were evident in all ages of adult mice and the DG and MF of adult slices were prime areas for rods (Figure 6.2).

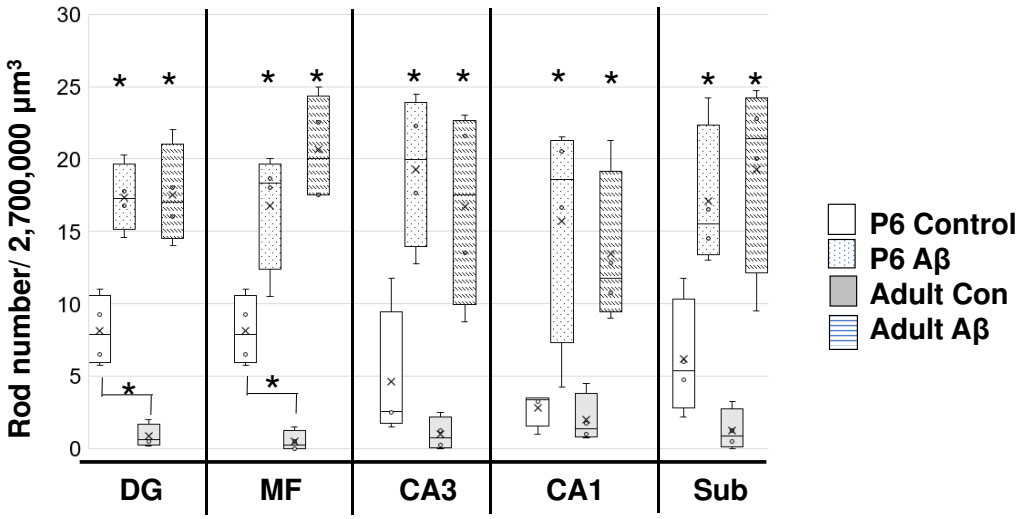

Figure 6.2 Localization of rods in postnatal and adult slices. 3D Stitched images of the entire hippocampus from postnatal (P6) and 10 month adult slices showed the same pattern of Aβd/t-induced rod formation. However, P6 slices had apparent higher levels of rods in the DG and MF untreated controls compared to adult slices. (n=4; *p<0.05 between Aβ-treated and control of same age or between untreated P6 and adult).

However, in addition we found significant rod formation in the subiculum and the Cornu Ammonis 1 and 3 (CA1,CA3) regions (Figure 6.2). Although the locations of rods were similar between postnatal and adult slices treated with Aβd/t, we were surprised to find

the greater numbers of rods in the postnatal control slices compared to adults. This will be addressed in more detail in our discussion below.

Antagonists of CCR5 and CXCR4 in slices and cultures of dissociated mouse neurons block rod formation induced by Aβd/t. Results presented elsewhere in this thesis already suggest a common pathway for rod formation from the inducers studied, namely gp120, α-Syn PFF, and Aβd/t. To see if CXCR4, and/or CCR5 receptors are involved in this neuronal signaling pathway for Aβd/t, we tested the ability of Rap310, the X4 and R5 antagonist, to block Aβd/t-induced rod formation in adult slices (Figure 6.3 A,B). Rap310 at 10^{-11} M blocks rod formation from Aβd/t.

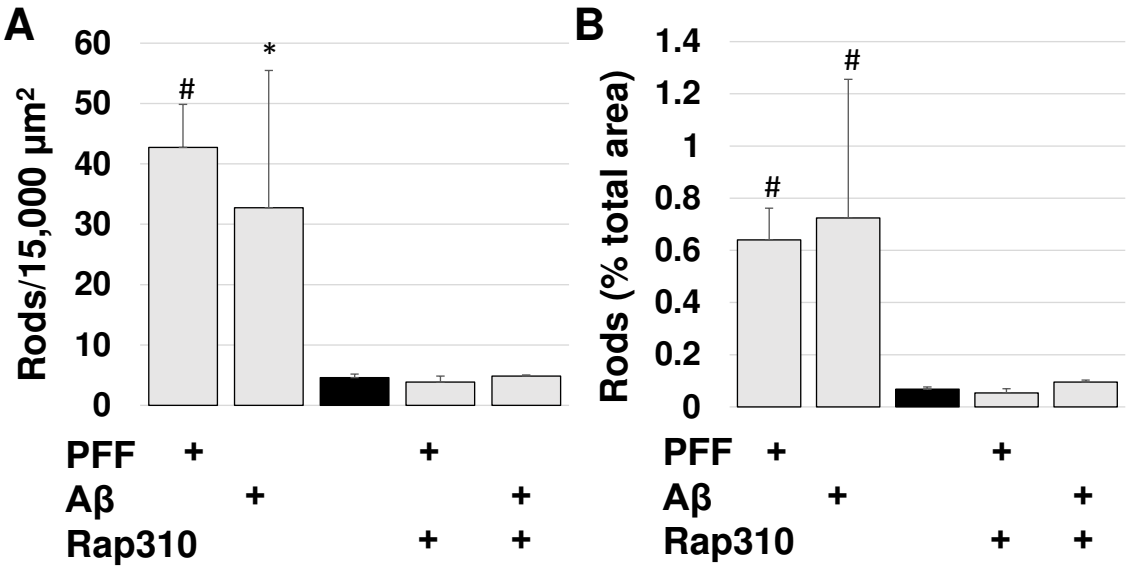

Figure 6.3 RAP 310 inhibits and reverses rod formation in adult brain slices. Hippocampal slices from 10 month WT mouse untreated (black bar) or treated with PFF or Aβ for 4 days in the presence or absence Rap310 at 10 pM for the last two days of stressor treatment. (A) Number of rods in the DG per 60x confocal field. (n=4. Comparison between untreated and: Aβ *p=0.049; PFF #p=0.0005, Rap310 NS.). (B) Rod area as a percent of total per 60x confocal field. (n=4, Comparison between untreated and: Aβ #p=0.0052, PFF #p=0.0008, +Rap310 NS. ANOVA with post hoc Student's T-test.

Discussion

In this chapter we exclusively used pooled dimer and trimer-containing fractions of Aβ which contained about 50% monomer. Previous studies using monomer only fractions from the gel filtration column showed that these were not rod-inducing (Davis et al, 2011). Thus, our effective concentration of the presumed active species (Aβd/t) is about 500 pM. We confirmed that Aβd/t induces rods in both cultured neurons and hippocampal slices through the same PrP^C and NOX-dependent pathway as is used by gp120 and PFF. Furthermore, antagonists of the X4 and R5 receptors block rod formation from Aβd/t.

The only major surprise from the results observed here were the elevated rod numbers quantified by our unbiased and semi-automated method in untreated postnatal slices compared to their adult counterparts. We believe this can be easily explained by considering the quantification method. In dissociated neuronal cultures we eliminated the contribution to rod counts made by bundles of cofilin-stained actin in growth cones that had very different dynamic properties from rods (Chapter 3). Since growth cones are rarely found in adult brain slices, we did not apply any subtraction method for removing such structures in the adult slice quantification algorithm. We feel that it is likely that there are still abundant growth cones in postnatal slices that contribute to the high "apparent" rod numbers by their inclusion. Previous work on effects of Aβ on brain slices used only postnatal slices and thus rod quantification and rod localization might have been biased by inclusion of rod-like staining of growth cone cofilin-actin structures. Although we did confirm that the DG and MF regions in Aβ-treated postnatal brain slices previously found to be most abundant in rods were also rich in rods in treated adult slices, other regions of

the adult hippocampus seemed to show a robust rod response as well. Yet in figure 3.7 we show 4 month WT slices treated with Aβ have specific rod localization to the DG and MF suggesting that the older slices in this present study may be more susceptible to rod formation in all regions.

In preliminary results for which statistics are not yet completed, it appears that slices expressing alpha-synuclein are more susceptible to rod formation from Aβd/t compared to WT slices. This finding, if confirmed by statistical analysis, is of importance because of the potential that in PDD patients, rod formation may be occurring through Aβ-enhancement of α-Syn signaling, both of stimulate rod formation through the CCR5 and CXCR4 pathway.

In progress are studies quantifying dendritic spines in slices and neuronal cultures treated with Aβd/t, PFF and CXCR4 and CCR5 inhibitors to determine if there is any additive effects of rod inducers and spines can be protected from the effects of either or both using X4 and R5 inhibitors.

References

Agnew BJ, Minamide LS, Bamburg JR. (1995) Reactivation of phosphorylated actin depolymerizing factor and identification of the regulatory site. *J Biol Chem*. 1995;270(29):17582-17587. doi:10.1074/jbc.270.29.17582

Arber S, Barbayannis FA, Hanser H, et al. (1998) Regulation of actin dynamics through phosphorylation of cofilin by LIM-kinase. *Nature*. 1998;393(6687):805-809. doi:10.1038/3172

Atwood CS, Perry G, Zeng H, Kato Y, Jones WD, Ling K-Q, Huang X, Moir RD, Wang D, Sayre LM. (2004). Copper mediated dityrosine cross-linking of Alzheimer's amyloid-beta. *Biochemistry,* 43:560-568.

Bamburg JR, Bernstein BW. (2016) Actin dynamics and cofilin-actin rods in Alzheimer disease. *Cytoskeleton (Hoboken)*. 2016;73(9):477-497. doi:10.1002/cm.21282

Bate C, Williams A. (2011) Amyloid-β-induced synapse damage is mediated via cross-linkage of cellular prion proteins. *J Biol Chem*. 2011;286(44):37955-37963. doi:10.1074/jbc.M111.248724

Benilova I, De Strooper B. (2013) Neuroscience. Promiscuous Alzheimer's amyloid: yet another partner. *Science*. 2013;341(6152):1354-1355. doi:10.1126/science.1244166

Bernstein BW, Shaw AE, Minamide LS, Pak CW, Bamburg JR. (2012) Incorporation of cofilin into rods depends on disulfide intermolecular bonds: implications for actin regulation and neurodegenerative disease. *J Neurosci*. 2012;32(19):6670-6681. doi:10.1523/JNEUROSCI.6020-11.2012

Bertling E, Hotulainen P, Mattila PK, Matilainen T, Salminen M, Lappalainen P. (2004) Cyclase-associated protein 1 (CAP1) promotes cofilin-induced actin dynamics in mammalian nonmuscle cells. *Mol Biol Cell*. 2004;15(5):2324-2334. doi:10.1091/mbc.e04-01-0048

Chesselet MF, Richter F, Zhu C, Magen I, Watson MB, Subramaniam SR. (2012) A progressive mouse model of Parkinson's disease: the Thy1-aSyn ("Line 61") mice. *Neurotherapeutics*. 2012;9(2):297-314. doi:10.1007/s13311-012-0104-2

Davis RC, Marsden IT, Maloney MT, et al. (2011) Amyloid beta dimers/trimers potently induce cofilin-actin rods that are inhibited by maintaining cofilin-phosphorylation. *Mol Neurodegener*. 2011;6:10. Published 2011 Jan 24. doi:10.1186/1750-1326-6-10

George J, Soares C, Montersino A, Beique JC, Thomas GM. (2015) Palmitoylation of LIM Kinase-1 ensures spine-specific actin polymerization and morphological plasticity. *Elife*. 2015;4:e06327. Published 2015 Apr 17. doi:10.7554/eLife.06327

Gimbel DA, Nygaard HB, Coffey EE, et al. (2010) Memory impairment in transgenic Alzheimer mice requires cellular prion protein. *J Neurosci*. 2010;30(18):6367-6374. doi:10.1523/JNEUROSCI.0395-10.2010

Gohla A, Birkenfeld J, Bokoch GM. (2005) Chronophin, a novel HAD-type serine protein phosphatase, regulates cofilin-dependent actin dynamics. *Nat Cell Biol*. 2005;7(1):21-29. doi:10.1038/ncb1201

Hall AM, Roberson ED. (2012) Mouse models of Alzheimer's disease. *Brain Res Bull*. 2012;88(1):3-12. doi:10.1016/j.brainresbull.2011.11.017

Hardy J. (2017) The discovery of Alzheimer-causing mutations in the APP gene and the formulation of the "amyloid cascade hypothesis". *FEBS J*. 2017;284(7):1040-1044. doi:10.1111/febs.14004

Hardy JA, Higgins GA. (1992) Alzheimer's disease: the amyloid cascade hypothesis. *Science*. 1992;256(5054):184-185. doi:10.1126/science.1566067

Hayakawa K, Sekiguchi C, Sokabe M, Ono S, Tatsumi H. (2019) Real-Time Single-Molecule Kinetic Analyses of AIP1-Enhanced Actin Filament Severing in the Presence of Cofilin. *J Mol Biol*. 2019;431(2):308-322. doi:10.1016/j.jmb.2018.11.010

Hayden SM, Miller PS, Brauweiler A, Bamburg JR. (1993) Analysis of the interactions of actin depolymerizing factor with G- and F-actin. *Biochemistry*. 1993;32(38):9994-10004. doi:10.1021/bi00089a015

Huang TY, Minamide LS, Bamburg JR, Bokoch GM. (2008) Chronophin mediates an ATP-sensing mechanism for cofilin dephosphorylation and neuronal cofilin-actin rod formation. *Dev Cell*. 2008;15(5):691-703. doi:10.1016/j.devcel.2008.09.017

Jin M, Shepardson N, Yang T, Chen G, Walsh D, Selkoe DJ. (2011) Soluble amyloid beta-protein dimers isolated from Alzheimer cortex directly induce Tau hyperphosphorylation and neuritic degeneration. Proc Natl Acad Sci U S A. 2011;108(14):5819-5824. doi:10.1073/pnas.1017033108

Kim JE, Kim YJ, Lee DS, et al. (2016) PLPP/CIN regulates bidirectional synaptic plasticity via GluN2A interaction with postsynaptic proteins. *Sci Rep*. 2016;6:26576. Published 2016 May 23. doi:10.1038/srep26576

Knight EM, Kim SH, Kottwitz JC, et al. (2016) Effective anti-Alzheimer Aβ therapy involves depletion of specific Aβ oligomer subtypes. *Neurol Neuroimmunol Neuroinflamm*. 2016;3(3):e237. Published 2016 May 10. doi:10.1212/NXI.0000000000000237

Kommaddi RP, Das D, Karunakaran S, et al. (2018) Aβ mediates F-actin disassembly in dendritic spines leading to cognitive deficits in Alzheimer's disease. *J Neurosci*. 2018;38(5):1085-1099. doi:10.1523/JNEUROSCI.2127-17.2017

Korobova F, Svitkina T. (2010) Molecular architecture of synaptic actin cytoskeleton in hippocampal neurons reveals a mechanism of dendritic spine morphogenesis. *Mol Biol Cell*. 2010;21(1):165-176. doi:10.1091/mbc.e09-07-0596

Laurén J, Gimbel DA, Nygaard HB, Gilbert JW, Strittmatter SM. (2009) Cellular prion protein mediates impairment of synaptic plasticity by amyloid-beta oligomers. *Nature*. 2009;457(7233):1128-1132. doi:10.1038/nature07761

Lewis J, McGowan E, Rockwood J, et al. (2000) Neurofibrillary tangles, amyotrophy and progressive motor disturbance in mice expressing mutant (P301L) tau protein [published correction appears in Nat Genet 2000 Sep;26(1):127]. *Nat Genet*. 2000;25(4):402-405. doi:10.1038/78078

Lunardi P, Sachser RM, Sierra RO, et al. (2018) Effects of Hippocampal LIMK Inhibition on Memory Acquisition, Consolidation, Retrieval, Reconsolidation, and Extinction. *Mol Neurobiol*. 2018;55(2):958-967. doi:10.1007/s12035-016-0361-x

Maloney, M. T., & Bamburg, J. R. (2007). Cofilin-mediated neurodegeneration in alzheimer's disease and other amyloidopathies. *Molecular Neurobiology*, 35(1), 21-43

Maloney MT, Minamide LS, Kinley AW, Boyle JA, Bamburg JR. (2005) Beta-secretase-cleaved amyloid precursor protein accumulates at actin inclusions induced in neurons by stress or amyloid beta: a feedforward mechanism for Alzheimer's disease [published correction appears in J Neurosci. 2006 Jan 4;26(1):354]. *J Neurosci*. 2005;25(49):11313-11321. doi:10.1523/JNEUROSCI.3711-05.2005

Mc Donald JM, Savva GM, Brayne C, et al. (2010) The presence of sodium dodecyl sulphate-stable Abeta dimers is strongly associated with Alzheimer-type dementia. Brain. 2010;133(Pt 5):1328-1341. doi:10.1093/brain/awq065

McGough A, Pope B, Chiu W, Weeds A. (1997) Cofilin changes the twist of F-actin: implications for actin filament dynamics and cellular function. *J Cell Biol*. 1997;138(4):771-781. doi:10.1083/jcb.138.4.771

Meberg PJ, Miller MW. (2003) Culturing hippocampal and cortical neurons. *Methods Cell Biol*. 2003;71:111-127. doi:10.1016/s0091-679x(03)01007-0

Meberg PJ, Ono S, Minamide LS, Takahashi M, Bamburg JR. (1998) Actin depolymerizing factor and cofilin phosphorylation dynamics: response to signals that regulate neurite extension. *Cell Motil Cytoskeleton*. 1998;39(2):172-190. doi:10.1002/(SICI)1097-0169(1998)39:2<172::AID-CM8>3.0.CO;2-8

Minamide LS, Striegl AM, Boyle JA, Meberg PJ, Bamburg JR. (2000) Neurodegenerative stimuli induce persistent ADF/cofilin-actin rods that disrupt distal neurite function. *Nat Cell Biol*. 2000;2(9):628-636. doi:10.1038/35023579

Minamide LS, Maiti S, Boyle JA, et al. (2010) Isolation and characterization of cytoplasmic cofilin-actin rods. *J Biol Chem*. 2010;285(8):5450-5460. doi:10.1074/jbc.M109.063768

Morgan TE, Lockerbie RO, Minamide LS, Browning MD, Bamburg JR. (1993) Isolation and characterization of a regulated form of actin depolymerizing factor. *J Cell Biol*. 1993;122(3):623-633. doi:10.1083/jcb.122.3.623

Moriyama K, Yahara I. (2002) Human CAP1 is a key factor in the recycling of cofilin and actin for rapid actin turnover. *J Cell Sci*. 2002;115(Pt 8):1591-1601.

Moriyama K, Iida K, Yahara I. (2002) Phosphorylation of Ser-3 of cofilin regulates its essential function on actin. *Genes Cells*. 1996;1(1):73-86. doi:10.1046/j.1365-2443.1996.05005.x

Nagata-Ohashi K, Ohta Y, Goto K, et al. (2004) A pathway of neuregulin-induced activation of cofilin-phosphatase Slingshot and cofilin in lamellipodia. *J Cell Biol*. 2004;165(4):465-471. doi:10.1083/jcb.200401136

Nelson PT, Braak H, Markesbery WR. (2009) Neuropathology and cognitive impairment in Alzheimer disease: a complex but coherent relationship. *J Neuropathol Exp Neurol*. 2009;68(1):1-14. doi:10.1097/NEN.0b013e3181919a48

Nuvolone M, Hermann M, Sorce S, et al. (2016) Strictly co-isogenic C57BL/6J-Prnp-/- mice: A rigorous resource for prion science. *J Exp Med*. 2016;213(3):313-327. doi:10.1084/jem.20151610

Purde V, Busch F, Kudryashova E, Wysocki VH, Kudryashov DS. (2019) Oligomerization Affects the Ability of Human Cyclase-Associated Proteins 1 and 2 to Promote Actin Severing by Cofilins. *Int J Mol Sci*. 2019;20(22):5647. Published 2019 Nov 12. doi:10.3390/ijms20225647

Rahman T, Davies DS, Tannenberg RK, et al. (2014) Cofilin rods and aggregates concur with tau pathology and the development of Alzheimer's disease. *J Alzheimers Dis*. 2014;42(4):1443-1460. doi:10.3233/JAD-140393

Rush T, Martinez-Hernandez J, Dollmeyer M, et al. (2018) Synaptotoxicity in Alzheimer's Disease Involved a Dysregulation of Actin Cytoskeleton Dynamics through Cofilin 1 Phosphorylation. *J Neurosci*. 2018;38(48):10349-10361. doi:10.1523/JNEUROSCI.1409-18.2018

Sarmiere PD, Bamburg JR. (2002) Head, neck, and spines: a role for LIMK-1 in the hippocampus. *Neuron*. 2002;35(1):3-5. doi:10.1016/s0896-6273(02)00759-6

Selkoe DJ, Hardy J. (2016) The amyloid hypothesis of Alzheimer's disease at 25 years. *EMBO Mol Med*. 2016;8(6):595-608. Published 2016 Jun 1. doi:10.15252/emmm.201606210

Shankar GM, Li S, Mehta TH, et al. (2008) Amyloid-beta protein dimers isolated directly from Alzheimer's brains impair synaptic plasticity and memory. *Nat Med*. 2008;14(8):837-842. doi:10.1038/nm1782

Shaw AE, Bamburg JR. (2017) Peptide regulation of cofilin activity in the CNS: A novel therapeutic approach for treatment of multiple neurological disorders. *Pharmacol Ther*. 2017;175:17-27. doi:10.1016/j.pharmthera.2017.02.031

Simhadri PK, Malwade R, Vanka R, Nakka VP, Kuppusamy G, Babu PP. (2017) Dysregulation of LIMK-1/cofilin-1 pathway: A possible basis for alteration of neuronal morphology in experimental cerebral malaria. *Ann Neurol*. 2017;82(3):429-443. doi:10.1002/ana.25028

Soosairajah J, Maiti S, Wiggan O, et al. (2005) Interplay between components of a novel LIM kinase-slingshot phosphatase complex regulates cofilin. *EMBO J*. 2005;24(3):473-486. doi:10.1038/sj.emboj.7600543

Takuma H, Teraoka R, Mori H, Tomiyama T.(2008). Amyloid-β E22Δvariant induces synaptic alteration in mouse hippocampal slices. *NeuroReport,* 19:615–619.

Tomiyama T, Nagata T, Shimada H, Teroka R, Fukushima A, Kanemitsu H, Takuma H, Kuwano R, Imagawa M, Ataka S. (2008). A new Aβ variant favoring oligomerization in Alzheimer's type dementia. *Ann Neurol,* 63:377-387.

Tsartsalis,S., Xekardaki,A., Hof,P.R., Kovari,E., Bouras, C. (2018). Early Alzheimer-type lesions in cognitively normal subjects. *Neurobio Aging*, 62:34-44

Veljkovic N, Vucicevic J, Tassini S, Glisic S, Veljkovic V, Radi M. (2015) Preclinical discovery and development of maraviroc for the treatment of HIV. *Expert Opin Drug Discov*. 2015;10(6):671-684. doi:10.1517/17460441.2015.1041497

Walsh DM, Klyubin I, Fadeeva JV, et al. (2002) Naturally secreted oligomers of amyloid beta protein potently inhibit hippocampal long-term potentiation in vivo. *Nature*. 2002;416(6880):535-539. doi:10.1038/416535a

Walsh KP, Minamide LS, Kane SJ, et al. (2014) Amyloid-β and proinflammatory cytokines utilize a prion protein-dependent pathway to activate NADPH oxidase and induce cofilin-actin rods in hippocampal neurons. *PLoS One*. 2014;9(4):e95995. Published 2014 Apr 23. doi:10.1371/journal.pone.0095995

Wang J, Tannous BA, Poznansky MC, Chen H. (2020) CXCR4 antagonist AMD3100 (plerixafor): From an impurity to a therapeutic agent [published online ahead of print, 2020 Jun 13]. *Pharmacol Res*. 2020;159:105010. doi:10.1016/j.phrs.2020.105010

Wang Y, Shibasaki F, Mizuno K. (2005) Calcium signal-induced cofilin dephosphorylation is mediated by Slingshot via calcineurin. *J Biol Chem*. 2005;280(13):12683-12689. doi:10.1074/jbc.M411494200

Wang Y, Dong Q, Xu XF, et al. (2013) Phosphorylation of cofilin regulates extinction of conditioned aversive memory via AMPAR trafficking. *J Neurosci*. 2013;33(15):6423-6433. doi:10.1523/JNEUROSCI.5107-12.2013

Welzel AT, Maggio JE, Shankar GM, et al. (2014) Secreted amyloid β-proteins in a cell culture model include N-terminally extended peptides that impair synaptic plasticity. *Biochemistry*. 2014;53(24):3908-3921. doi:10.1021/bi5003053

Woo JA, Boggess T, Uhlar C, et al. (2015A) RanBP9 at the intersection between cofilin and Aβ pathologies: rescue of neurodegenerative changes by RanBP9 reduction. *Cell Death Dis*. 2015B;6(3):1676. Published 2015 Mar 5. doi:10.1038/cddis.2015.37

Woo JA, Zhao X, Khan H, et al. (2015B) Slingshot-Cofilin activation mediates mitochondrial and synaptic dysfunction via Aβ ligation to β1-integrin conformers. *Cell Death Differ*. 2015A;22(6):1069-1070. doi:10.1038/cdd.2015.41

Woo JA, Liu T, Fang CC, et al. (2019) Activated cofilin exacerbates tau pathology by impairing tau-mediated microtubule dynamics. *Commun Biol*. 2019;2:112. Published 2019 Mar 22. doi:10.1038/s42003-019-0359-9

Yang N, Higuchi O, Ohashi K, et al. (1998) Cofilin phosphorylation by LIM-kinase 1 and its role in Rac-mediated actin reorganization. *Nature*. 1998;393(6687):809-812. doi:10.1038/31735

Zhang H, Ramsey A, Xiao Y, et al. (2020) Dynamic Phosphorylation and Dephosphorylation of Cyclase-Associated Protein 1 by Antagonistic Signaling through Cyclin-Dependent Kinase 5 and cAMP Are Critical for the Protein Functions in Actin Filament Disassembly and Cell Adhesion. *Mol Cell Biol*. 2020;40(4):e00282-19. Published 2020 Jan 30. doi:10.1128/MCB.00282-19

Zhou GL, Zhang H, Wu H, Ghai P, Field J. (2014) Phosphorylation of the cytoskeletal protein CAP1 controls its association with cofilin and actin. *J Cell Sci*. 2014;127(Pt 23):5052-5065. doi:10.1242/jcs.156059

Zhou L, Jones EV, Murai KK. (2012) EphA signaling promotes actin-based dendritic spine remodeling through slingshot phosphatase. *J Biol Chem*. 2012;287(12):9346-9359. doi:10.1074/jbc.M111.302802

CHAPTER 7

CONCLUSIONS AND FUTURE DIRECTIONS

We barely understand the biology of cognition, which makes studying neurodegeneration and the loss of cognition difficult. This thesis describes methods to improve the study of neurodegeneration at the cell and molecular level and utilizes these novel methods to address long standing questions in AD, PD, and HAND. Using rodent models and causative inducers of neurodegeneration, we show that cofilin rods form in these diseases through a common pathway requiring PrP^c, NOX, CXCR4, and CCR5. We propose that this is a common pathway to cognitive disorders in the hippocampus and that we have developed valuable techniques for studying in culture and slices, cell and molecular changes that may lead to dementia.

Future Directions

The culturing of adult brain slices for maintaining dendrites is extremely labor intensive and requiring daily observations of glia cultures, to ensure diverse cell types are present and cultures are healthy. (I have a song called happy glia which does wonders for the cultures). It has previously been established that glia conditioning medium can enhance culture vitality (Conde Guerri et al., 1989), but the literature on the proper use of glia conditioned medium for long-term neuronal maintenance is unclear. In our experience only fresh glia conditioned medium maintained dendritic branches in adult slices. In one set of experiments glia conditioned medium was used after 24 h at 4^o C and the staining

of dendrites for Map2 showed more fragmented dendrites at earlier time-points. My mistake in believing literature saying GCM can be stored at 4° C is resulting in us having to repeat the experiments done on 7 month old mice to have more confidence in our results.

Recently it has been shown that the CCR5 receptor plays a major role in stroke recovery. Human trials using maraviroc immediately after stroke significantly improved cognitive outcomes. The CCR5 receptor is highly expressed in microglia and macrophages and plays a role in immune cell activation and signaling for cytokine production. Interestingly, while we can immunostain for both CCR5 and CXCR4 on the surface of dissociated cultured rodent neurons, it is unclear if human neurons express CCR5. Human ES cells differentiated into excitatory glutamatergic neurons express CXCR4 mRNA at DIV 0 but even by DIV 46, no expression of R5 is observed (Zhang et al., 2013). The CXCR4 receptor plays a role in the migration and morphology of neurons of the hippocampus and its endogenous ligand CXCL12, also known as SDF-1alpha, is an inhibitor of the receptor that would be expected to inhibit rod formation but probably mediates cofilin-based signaling through phospho-regulation of cofilin. We do not know if human neurons form rods in response to gp120, α-Syn, and Aβ, although rods are a pathology of human AD brain. We are currently growing human ES cells and differentiating them into cortical-like neurons (2) to determine if rods will form in response to the disease-related stressors. This work will require testing rod formation at different DIV because of the slow development of the differentiated human neurons. If rods form than CXCR4 maybe the neuronal specific receptor signaling rod formation.

Our dissociated cultured neurons do not have cells that stain for a microglia marker. Previous studies in our lab showed cytokine production within the neuronal cultures remained significantly below rod-inducing levels, highly suggesting that the pathway we have uncovered is in essence neuronal specific but it does not eliminate the possibility of astrocytes contributing to rods in culture or microglia contributing to the rods we see in vivo.

In chapter 5 we showed that as α-Syn expressing mice aged, and in slices cultured from them in vitro, more cofilin rods formed per length dendrite during aging. We also observed the staining of dendrites for Map2 disappeared by DIV 7 in slices from α-Syn mice at 7 or 10.5 months of age. These observations have led us to want to address the possibility that rod formation through the CXCR4 and CCR5 pathway mediates synaptic decline induced by gp120, α-Syn, and Aβ. By culturing α-Syn slices from mice > 6 months of age with Rap310, we will examine dendrite loss that occurs between DIV 0 to DIV 7 and determine if it can be blocked. In addition utilizing the modified roller tube method, we hope to culture adult brain slices that are randomly and sparsely labeled with DiA and do repetitive localization of the same dendrites during culture with gp120, α-Syn, or Aβ before and after addition of Rap310. Finally, I would like to perform long-term live imaging experiments in DIV 21 dissociated neurons. We are imaging dendritic spines, labeled with DiA, and using a rod-reporter, cofilin-R21Q mRFP expressed from lenti particles to visualize rods. We hope to be able to follow the same dendritic spines before and up to 16 hours after addition of gp120, α-Syn, or Aβ. Finally, we will be adding Rap310 for an additional 16 hours and image the same fields to see if rods that form can be reversed and if spines can recover. Additionally, we are collaborating with Marcia Liz on a grant to

do behavioral studies using Rap310 to preserve cognition in aging α-Syn mice. This thesis work has addressed some questions but truly just opened doors for many other questions to be addressed.

References

Conde Guerri B, Sinués Porta E, Arrazola Schlamilch M, Comuñas González F, Calatayud Maldonado V. (1989) Effects of glia-conditioned medium on primary cultures of central neurons. *Histol Histopathol*. 1989;4(2):217-222.

Zhang, Y., Pak, C., Han, Y., Ahlenius, H., Zhang, Z., Chanda, S., Marro, S., Patzke, C., Acuna, C., Covy, J., Xu, W., Yang, N., Danko, T., Chen, L., Wernig, M., & Südhof, T. C. (2013). Rapid single-step induction of functional neurons from human pluripotent stem cells. *Neuron*, *78*(5), 785–798. https://doi.org/10.1016/j.neuron.2013.05.029

SUPPLEMENTARY MATERIAL

CHAPTER 3

3.S1. ImageJ language script for dissociate culture. Line 23 allows for adjustment of shape perameters. Line 21 allows for adjustment of threshold sensitivity to size of rods and intensity of rod staining. Numbers on each line are not included in the ImageJ script.

```
1. //dapi
2. dir=getDirectory("Choose a Directory");
3. run("Image Sequence...", "open=[dir] number=1 starting=2");
4. run("8-bit");
5. Dapi = getImageID();
6. selectImage(Dapi);
7. rename("Dapicount");
8. //setMinAndMax(2, 26);
9. run("Find Maxima...", "prominence=25 strict output=[Maxima Within Tolerance]");
10. run("Watershed");
11. run("Analyze Particles...", "size=0.024-10.00 circularity=0.40-1.00 show=Overlay summarize");
12. //rods
13. run("Image Sequence...", "open=[dir] number=1 starting=1");
14. run("8-bit");
15. rods = getImageID();
16. selectImage(rods);
17. rename("rodcount");
18. run("Gaussian Blur...", "sigma=1");
19. run("Convolve...", "text1=[-1 -1 -1 -1 -1\n-1 -1 -1 -1 -1\n-1 -1 50 -1 -1\n-1 -1 -1 -1 -1\n-1 -1 -1 -1 -
    1\n] normalize");
20. run("Subtract Background...", "rolling=8");
21. run("Auto Local Threshold", "method=Bernsen radius=15 parameter_1=40 parameter_2=0
    white");
22. run("Watershed");
23. run("Analyze Particles...", "size=0.002-0.03 circularity=0.00-0.75 show=Masks summarize");
24. //growth cone exclusion
25. run("Image Sequence...", "open=[Dir] starting=3 increment=3 sort");
26. run("Auto Local Threshold", "method=Bernsen radius=15 parameter_1=40 parameter_2=0
    white");
27. run("Dilate");
28. run("Analyze Particles...", "size=0-10 show=Overlay");
29. growthcones = getImageID();
```

```
30. rename ("growthcones");
31. //back to rods
32. imageCalculator("Subtract", growthcones, rods);
33. run("Analyze Particles...", "size=0.002-0.02 circularity=0.00-0.70 summarize display clear");
34. run("Convert to Mask");
35. rename("Final Rod Image");
```

3. S2. ImageJ language script for slice culture. Line 26 allows for adjustment of threshold sensitivity to size of rod and intensity of staining. Line 31 allows for adjustment of size and shape parameters. This code required both the Dapi channel image and cofilin channel image to be in the same folder.

```
1.  dir= getDirectory("Choose a Directory");
2.  count = 1;
3.  listFiles(dir);
4.  function listFiles(dir) {
5.  list = getFileList(dir);
6.  for (i=0; i<list.length; i++) {
7.  if (endsWith(list[i], "/"))
        a.  listFiles(""+dir+list[i]);
8.  else
9.  open(dir+list[i]);
    }
    }
10. run("Images to Stack", "name=Stack title=[] use");
11. makeRectangle(36, 36, 3972, 3012);
12. run("Duplicate...", "duplicate");
13. run("8-bit");
14. run("16-bit");
15. saveAs("Tiff", dir );
16. selections = getNumber("how many selections do you want to create?", 36);
17. roiManager("Reset");
18. makeRectangle(2256, 780, 216, 260);
19. for(s=1; s<=selections; s++) {
20. waitForUser("Create Selection " + s);
21. run("Add to Manager");
    }
22. close();
23. run("Image Sequence...", "open=[dir] number=1 starting=1 increment=1 convert sort");
24. run("16-bit");
25. run("8-bit");
```

```
26. run("Auto Local Threshold", "method=Median radius=10 parameter_1=-10 parameter_2=0
    white");
27. //duplicates ROI's and processes with analyze particles
28. imgID=getImageID();
29. numROIs= roiManager("Count");
30. for (j=0; j<numROIs; j++)
    {
        a. selectImage(imgID);
        b. roiManager("select",j);
        c. run("Duplicate...", "duplicate");
31. run("Fill Holes");
32. run("Analyze Particles...", "size=0.0001-0.001 circularity=0.00-1.00 show=Masks clear
    summarize");
            }
33. roiManager("Save",dir+"ROIs.zip");
```

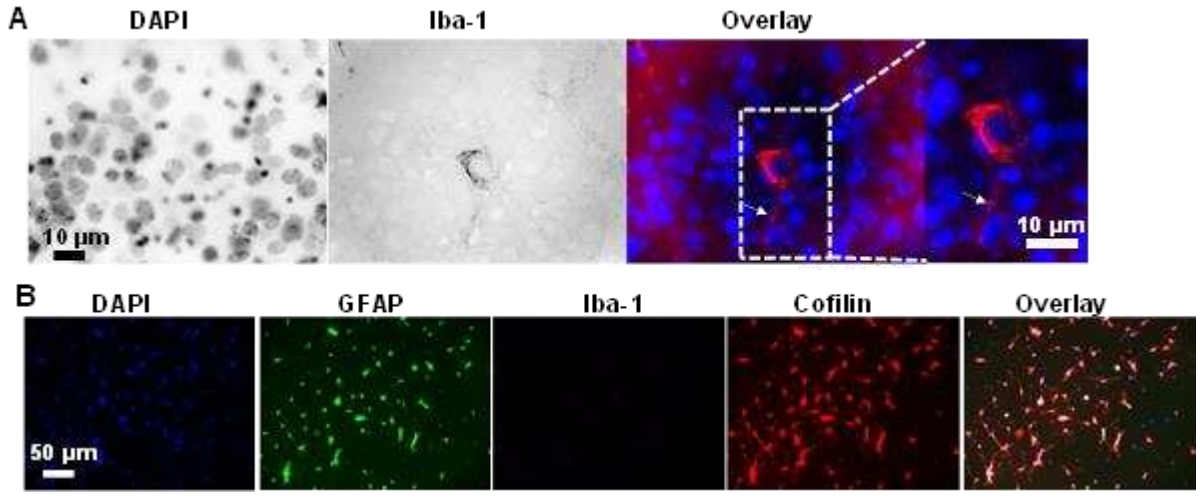

Figure S4.1. Cultures of Dissociated Neurons have no Microglia but contain Astrocytes (GFAP positive). (A) Characterization of microglial staining in adult brain slice with Iba-1 antibody. Slice shown was permeabilized with 100% methanol but identical staining was also found in slices in which the citrate buffer antigen retrieval was performed. Iba-1 immunostained components with the cytoplasm of a microglia with a DAPI stained nucleus. Ramified extensions of the microglia are visible (arrow in overlaid images). Captured with 100x objective on confocal microscope but cells were easily visible with 20x objective. (B) Images from fixed and immunostained cultures of mouse hippocampal neurons at DIV 7. Fixation and immunostaining was the same as for the slice in A. Images are obtained using 20x objective on confocal microscope and show the same field of cells stained for chromatin (DAPI), GFAP, Iba-1, and cofilin, with an overlay of all the images. No Iba-1 staining was observed indicating cultures were devoid of microglia (confirmed by scanning with 60x and 100x objectives as well. GFAP positive cells comprised about 40% of total DAPI nuclei within this particular preparation.

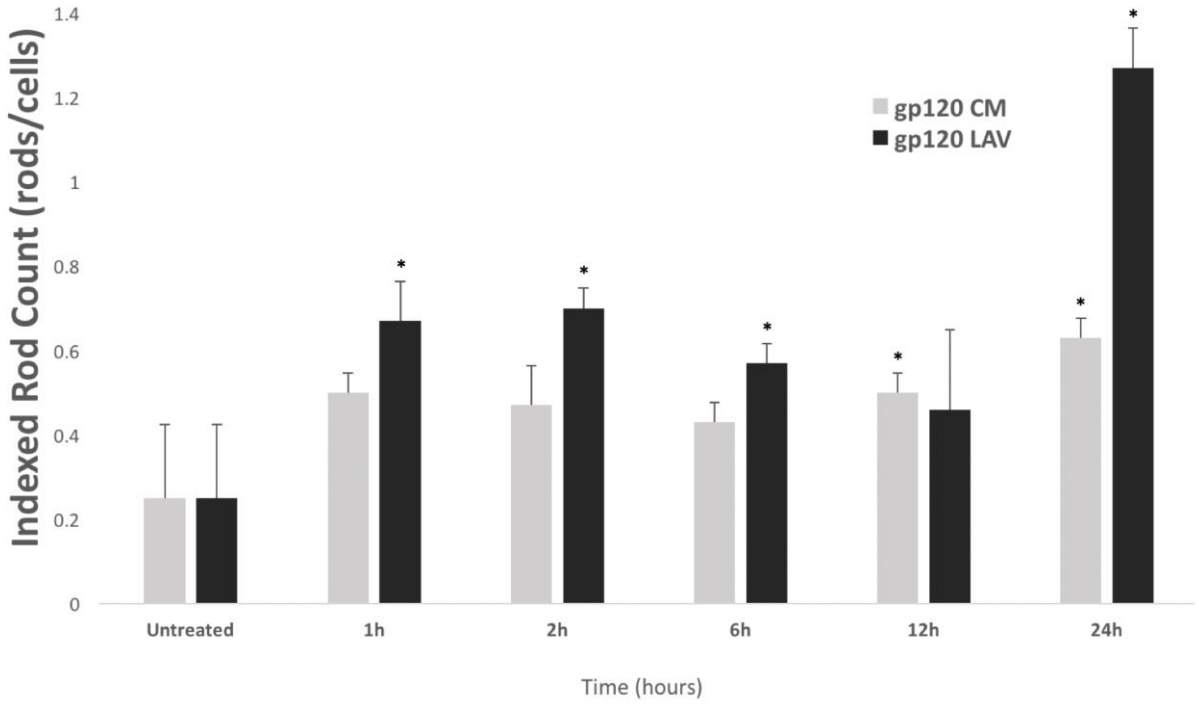

Supplemental Figure S4.2. Time Course of gp120-induced Rod Formation in E18 Rat Cortical Neurons. Rat E18 cortical neurons were grown on coverslips for 6 DIV and treated with 250 pM R5-tropic $gp120_{CM}$ and X4-tropic $gp120_{IIIB}$ for indicated time then fixed, immunostained for cofilin, and imaged. While each of the gp120 strains tested induced rod formation, X4-tropic gp120 induced a more potent response, reaching significance above control at 1 hour post-exposure.

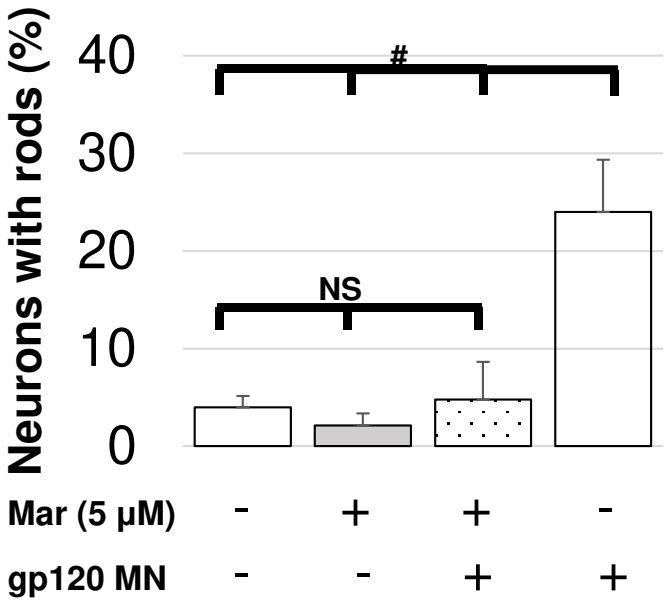

Supplemental Figure S4.3. Maraviroc inhibits dual tropic gp120 rod induction. Cultures of dissociated E18 rat neurons DIV 6 were teared for 16 h with dual-tropic gp120MN in the absence of presence of maraviroc. Although the concentration of maraviroc used here is relatively high (5 µM), it did not appear to be cytotoxic for the 16 hr of exposure during treatment with gp120 MN (500 pM). n=3. Significance (#) relative to gp120 MN of $p<0.005$ from one-way ANOVA, post hoc Tukey's analysis, using JMP Statistics software. NS = no significant difference relative to untreated.

MONOMERS **PFF**

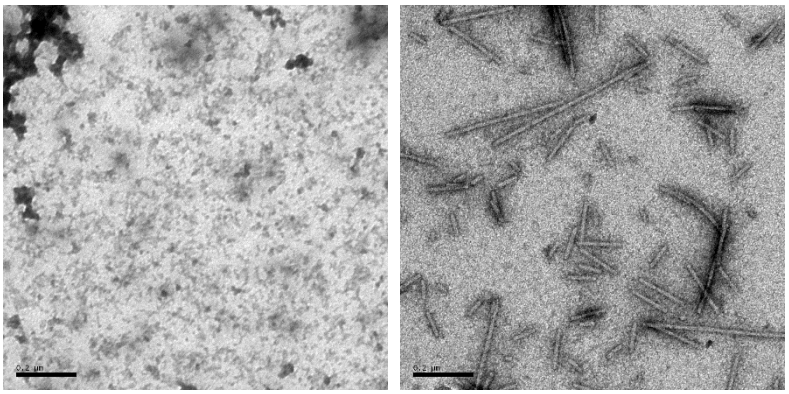

Supplemental Figure S5.1 Negative stained images of human α-Syn monomers (left) and PFF (right) taken immediately after bath sonication with A JEM-100CX II transmission electron microscope (JEOL Ltd., Tokyo, Japan).Scale bar = 0.2 μm